

**The Large-Scale Geostrophic Flow-Field
and Eddy Variability
as seen from the
TOPEX/Poseidon and Jason-1
Tandem Mission**

Dissertation
zur Erlangung des Doktorgrades
der Naturwissenschaften
im Department Geowissenschaften
der Universität Hamburg
vorgelegt von Martin G. Scharffenberg aus Jena

Hamburg, 2010

Als Dissertation angenommen vom
Department Geowissenschaften der Universität Hamburg
Auf Grund der Gutachten von

Prof. Dr. Detlef Stammer
und
Dr. Armin Köhl

Hamburg, den 23.04.2010

Professor Dr. Jürgen Oßenbrügge
(Leiter des Departments Geowissenschaften)

Abstract

Geostrophic surface velocity anomalies are used to analyze the annual variations of the large-scale geostrophic currents and of the eddy kinetic energy (EKE) field of the ocean circulation. The underlying geostrophic currents were estimated from the Jason-1-TOPEX/Poseidon (JTP) tandem altimetric sea surface height (SSH) measurements using the “parallel-track-approach” with a 6.2 km along-track resolution. However, due to the given separation of the tracks of the two satellites, only large mesoscale eddies are resolved by the tandem measurements. The analysis covers the entire 3-year period of the tandem mission (109 repeat cycles) from September, 2002, to September, 2005. The high resolution along-track availability of the geostrophic velocity estimates allows for a spacial mapping of all quantities on a $2^\circ \times 1^\circ$ grid, resulting in a doubled mapping resolution. The ocean circulation is shown to have a slightly higher meridional variability by 10 to 20 % in mid latitudes, while in the tropics the EKE field is dominated by the variability of the mostly zonal current field which clarifies that in some regions it can be important to assume anisotropy. Very complex structures emerge in the ratio of EKE and mean kinetic energy (MKE). However, the ratio is shown to be a lower bound estimate. The investigation of the seasonal flow changes reveals annual variations of all major current systems, particularly of the zonal flow-field in low latitudes. There, they lead to zonal jet-like structures on the annual cycle in the southern Pacific, Atlantic, and Indian Ocean. In mid and high latitudes, indications of a seasonally modulated strength of the Sverdrup circulation emerge from the analysis. Noticeable in mid- and high latitudes are large changes in the wind-driven barotropic circulation that are not represented in other altimetric velocity products. The EKE field also shows changes in its amplitude on the annual period. In low latitudes, these can be explained by seasonally modulated currents. The strongest signals appear in the Gulf of Tehuantepec close to the Central American continent and in the Great Whirl region. On the annual period (as well as for the 3-year mean EKE), the Indian Ocean is the most energetic basin. The frequency and wavenumber spectra are shown for both geostrophic velocity components and for the EKE on global and regional scales. New insights are obtained due to the separate consideration of both velocity components such as a slightly higher energy level for the meridional component in the frequency range below 100 days over the entire extra-tropical ocean. Furthermore, strikingly universal frequency-slopes are found for all extra-tropical regions, though containing different power spectral densities (PSD). On the aliasing frequencies of the M_2 and S_2 tides, peaks exist in some regions on the continental shelves that suggest an insufficient correction of the tidal signal from the FES2004 tidal model. For the wavenumber spectra, the resolution of the tandem mission becomes evident for wavelengths shorter than 100 - 200 km. Nevertheless, new features appear for longer wavelengths such as the steeper slope for the zonal velocity component compared to the meridional. Besides the differences between the velocity components, nearly equal slopes are found within the wavenumber spectra of all extra-tropical regions (excluding the meridional component of the low energy regions). The slopes of the EKE wavenumber spectra indicate that the surface quasi geostrophic (SQG) turbulence theory is a better explanation than the quasi geostrophic (QG) theory for the satellite data.

Table of Contents

Abstract	I
Table of Contents	III
List of Figures	V
1. Introduction	1
1.1. State of Research	1
1.2. Scientific Goals	4
1.3. Outline of this Thesis	5
2. Data and Errors	7
2.1. Introduction	7
2.2. The Jason-1 TOPEX/Poseidon Tandem Mission	8
2.2.1. JTP - Data	9
2.2.2. JTP - Errors	12
2.3. The OSCAR Model	15
2.4. The Oleander Project	16
2.5. The Mean Dynamic Topography	17
2.6. Summary	19
3. Basic Statistics	21
3.1. Introduction	21
3.2. RMS SSH Variability	21
3.3. RMS Geostrophic Velocity Variability	23
3.4. Probability Density Function	24
3.5. Isotropy	28
3.6. EKE Field	30
3.7. Ratio EKE/MKE	33
3.8. Summary	34
4. The Seasonal Cycle	37
4.1. Introduction	37
4.2. Seasonal Changes of the Flow-Field	37
4.2.1. Seasonal Harmonic Analysis	37
4.2.2. Seasonal Zonal Jets	45
4.2.3. Comparison with ADCP data from MV Oleander	51
4.3. The Seasonal Signal of the Eddy Kinetic Energy	53
4.4. Summary	58

5. The Spectral distribution	63
5.1. Introduction	63
5.2. Frequency Spectra	65
5.2.1. Global and Basin Wide Frequency Spectra	65
5.2.2. Regional Frequency Spectra	70
5.3. Wavenumber Spectra	76
5.3.1. Global and Basin Wide Wavenumber Spectra	77
5.3.2. Regional Wavenumber Spectra	80
5.4. The aliasing frequencies of the M_2 and S_2 tides	88
5.5. Summary	91
6. Conclusions and Outlook	95
References	101
A. Main Equations	111
A.1. Geostrophic Velocities	111
A.2. Seasonal Harmonic Analysis	113
A.3. Lomb Periodogram	114
B. Glossary	117
C. Constants and Variables	119

List of Figures

2.1. Global bathymetry metric map with depth contours every 1000 m. The yellow lines separate the different basins into the Pacific, Atlantic and Indian Ocean, as well as into their eastern and western parts.	7
2.2. Virtual ground track (grey) on which the geostrophic velocities were calculated using the SSH data available from the JTP tandem mission. Exemplarily the TOPEX/Poseidon (red) and Jason-1 (blue) ground-tracks are shown for ARC 1 and 2.	8
2.3. (a) Schematic of the geometry used to compute orthogonal geostrophic velocity components on the interleaving track from SSH measurements provided along the two tracks to the east and west. (b) Schematic illustrating the orientation of the orthogonal velocity components obtained from the along-track data and their rotation into a local Cartesian coordinate system with zonal and meridional orientation (after STAMMER AND DIETERICH, 1999). Bottom left panel: the distances $D_{1,2}$ and $D_{3,4}$ between the SSH measurements that are used for the geostrophic velocity calculation and their variation over latitude.	9
2.4. Filter wavelength of the Loess filter $L(\phi)$ from Equation 2.7. The filter length scale is smaller than 100 km poleward and rises to more than 1500 km at 1° around the equator.	10
2.5. Number of velocity measurements (prior to Loess-smoothing) calculated for each JTP along-track point and subsequently averaged on a $2^\circ \times 1^\circ$ grid for the 109 repeat cycles covering the period September 30, 2002, to September 14, 2005, that were processed in this study.	11
2.6. Error of zonal and meridional geostrophic velocity components estimated from JTP data at each along-track point and averaged on a $2^\circ \times 1^\circ$ grid. See text for details on the computation of the error.	13
2.7. Error variance of zonal and meridional geostrophic velocity components estimated from JTP data at each along-track point and averaged on a $2^\circ \times 1^\circ$ grid. See text for details on the computation of the error variances.	14
2.8. Mean dynamic topography (top; RIO AND HERNANDEZ, 2004) with a $0.5^\circ \times 0.5^\circ$ resolution and the resulting mean flow-field (bottom) gridded onto $2^\circ \times 1^\circ$ boxes. (Includes Altimetry (1993-1999), Geoid Models EGM96 and EIGEN-2, Lagrangian Buoys (1992-1999) and Hydrographic Profiles (1993-2000).)	17
2.9. Mean u (top) and v -velocity-components (bottom). The mean of each $2^\circ \times 1^\circ$ grid box was calculated from the 1° SSH-gradients in u - and v -direction around each 0.5° grid point.	18

3.1.	Standard deviation of η' calculated for each JTP along-track point (top) and difference of standard deviation from JTP (top) and standard deviation from Jason-1 alone (bottom), averaged on a $2^\circ \times 1^\circ$ grid and calculated without Loess-smoothing.	22
3.2.	Standard deviation of the geostrophic velocity estimates for the zonal u (top) and meridional v (bottom) component calculated for each JTP along-track point and averaged on a $2^\circ \times 1^\circ$ grid. The color scale for both figures is the same.	23
3.3.	Variance of the geostrophic velocity estimates for the zonal u (top) and meridional v (bottom) component calculated for each JTP along-track point and averaged on a $2^\circ \times 1^\circ$ grid. The color scale for both figures is the same.	24
3.4.	(Top, left) Global probability density function distribution of the zonal (bold) and meridional (thin) geostrophic velocity components in m/s along with the exponential (dashed) and Gaussian fit (dotted) to the zonal PDF. (Top, right) Global distribution of probability density function width in m/s . (Bottom) Same global probability density function distribution as above but normalized by the standard deviation (Fig. 3.2) along with the Gaussian fit to the zonal PDF (dotted).	25
3.5.	Probability density function distribution of the zonal (top) and meridional (middle) geostrophic velocity components [m/s] for $10^\circ \times 10^\circ$ subregions. (Bottom) The distribution of probability density function width [m/s]. The top right insets give the axis ranges of the displayed PDFs.	26
3.6.	Same probability density function distribution as in Fig. 3.5 but weighted by the STD of the geostrophic velocity components (Fig. 3.2). The top right insets give the axis ranges of the displayed PDFs.	27
3.7.	Isotropy of the JTP data $\langle v'^2 \rangle - \langle u'^2 \rangle$ normalized by $\langle v'^2 \rangle + \langle u'^2 \rangle$ (top) and Isotropy from the 15-year long OSCAR data-set $\langle v'^2 \rangle - \langle u'^2 \rangle$ normalized by $\langle v'^2 \rangle + \langle u'^2 \rangle$, (October 21, 1992, to December 26, 2007, bottom). Here u' and v' denote the zonal and meridional geostrophic velocity anomalies, respectively. For both panels the isotropy was calculated for the mean of each $2^\circ \times 1^\circ$ grid cell.	29
3.8.	Zonal mean normalized isotropy for JTP (blue) and OSCAR (red). For positive/negative values the meridional component is smaller/larger than the zonal component.	30
3.9.	(Top) EKE [cm^2/s^2] calculated from the three-year long JTP velocity time series for each along-track point and gridded subsequently on a $2^\circ \times 1^\circ$ grid. (Bottom) OSCAR EKE field, covering the same period, but calculated on a $2^\circ \times 1^\circ$ spatial grid. Scales are logarithmic in both panels.	31
3.10.	Difference between JTP and OSCAR EKE fields in (Fig. 3.9). Scale is logarithmic.	32
3.11.	(Top) Mean Kinetic Energy (MKE) computed from the RIO AND HERNANDEZ (2004) Mean Dynamic Topography (MDTP) for each $2^\circ \times 1^\circ$ grid cell. (Bottom) Ratio of EKE from JTP (Fig. 3.9 , top) and MKE, filtered with a $6^\circ \times 4^\circ$ running mean.	34
4.1.	JTP amplitudes of the annual signal for the u (top) and v (bottom) geostrophic velocity anomaly components, calculated for the mean of each $2^\circ \times 1^\circ$ grid cell.	38

4.2.	JTP phases of the annual signal for the u (top) and v (bottom) geostrophic velocity anomaly components calculated for the mean of each $2^\circ \times 1^\circ$ grid cell. Zero degrees of the phases corresponds to January 1st.	39
4.3.	Amplitudes of the annual signal for the u (top) and v (bottom) geostrophic velocity anomaly components from OSCAR (15 years) calculated for the mean of each $2^\circ \times 1^\circ$ grid cell.	40
4.4.	Phases of the annual signal of the u (top) and v (bottom) geostrophic velocity anomaly components from OSCAR (15 years) calculated for the mean of each $2^\circ \times 1^\circ$ grid cell. Zero degrees of the phases corresponds to January 1st. . .	41
4.5.	Percentages of the annual amplitude at the standard deviation of the flow-field, calculated for each $2^\circ \times 1^\circ$ grid cell, for the zonal (top) and meridional (bottom) geostrophic velocity components.	42
4.6.	Percentages held by the annual amplitude at the standard deviation of the OSCAR flow-field (15 years), calculated for each $2^\circ \times 1^\circ$ grid cell, for the zonal (top) and meridional (bottom) geostrophic velocity components. . . .	43
4.7.	Zonally averaged percentages held by the annual amplitude at the STD of the geostrophic JTP (blue) and OSCAR (red) velocities for the meridional (top) and zonal (bottom) component.	44
4.8.	Annual anomalies of the geostrophic velocity zonally averaged over 10° longitude for September. The annually varying geostrophic flow-fields are shown in Fig.4.9 for the marked sections.	45
4.9.	Zonal averages over 10° longitude of the annually varying geostrophic flow-field from JTP for the western boundary current regions of the Pacific, Atlantic (next page top) and Indian Ocean (next page bottom) that are indicated in the black boxes of Fig. 4.8 . The grey dashed lines indicate transitions between adjacent boxes.	46
4.9.	Continued.	47
4.10.	Latitude-time sections of the annually varying zonal mean geostrophic flow-field anomalies, averaged over the western (120° W - 154° W) and the eastern (154° W - 66° W) parts of the Pacific; over the western (66° W - 30° W) and the eastern (30° W - 30° E) parts of the Atlantic (next page); and over the western (30° E - 72° E) and the eastern (72° E - 120° E) parts of the Indian Ocean (after next page). See Fig. 2.1 for a map including the basin separation.	48
4.10.	Continued.	49
4.10.	Continued.	50
4.11.	Comparison of the annual flow-field from the geostrophic velocity anomalies for JTP (blue), OSCAR (15 years, red), and Oleander ADCP ship data (black) in the vicinity of the Gulf Stream region. Shown is a snapshot of the seasonal cycle from all three estimates. The ADCP data was chosen from a depth of 100 m which gives the closest fit to the JTP and Oleander data sets and is well out of the Ekman-layer to avoid the wind-driven variability.	51
4.12.	A direct comparison between the three estimates is shown in the right panels for site [a] and left panels for site [b] that are marked in Fig. 4.11	52
4.13.	Amplitude of the seasonal cycle for the EKE estimated from the JTP time series (top) and the OSCAR data (15 years, bottom). The scale is logarithmic for both panels. The black line in the top panel is the path of the latitude-time-diagram shown in Fig. 4.18	54
4.14.	Phase of the seasonal cycle for the EKE estimated from the JTP data (top), and the OSCAR time series (15 years, bottom). Zero degrees of the phases correspond to January 1st.	55

4.15. Zonal-mean annual EKE from JTP averaged over the latitude bands 120° W - 154° W, 154° W - 66° W, 66° W - 30° W, 30° W - 30° E, 30° E - 72° E, 72° E - 120° E, from left to right. See Fig. 2.1 for a map of the separated basins. The color of the bars indicate the phases of the annual signal.	56
4.16. Percentages held by the annual EKE amplitude at the standard deviation of the EKE for JTP (top) and OSCAR (15 years, bottom). Both calculated for the mean of each 2° × 1° grid cell.	57
4.17. Zonally averaged percentages held by the annual EKE amplitude at the STD of the EKE, for JTP (blue) and OSCAR (15 years, red).	58
4.18. Latitude-time-diagram of the annual EKE variations estimated from JTP data in the Indian Ocean (see black section in Fig. 4.13 , top). Here, the white lines correspond to the black dots on the section-line of Fig. 4.13 (top). For display purposes, the one-year time series of the annual harmonic is shown twice.	59
5.1. Frequency spectra for zonal (u) and meridional (v) velocity components in the main thermocline at Kiel276. With courtesy of MÜLLER AND SIEDLER (1992, after their Fig. 13).	63
5.2. Zonal-wavenumber spectra of zonal velocity (solid line) and meridional velocity (dash-dotted line). After Fig. 17 of ZANG AND WUNSCH (2001).	64
5.3. Global-averaged frequency spectra (left) of the geostrophic velocity components [$cm^2/s^2/cpd$] and (right) of the EKE [$cm^4/s^4/cpd$]. The annual frequency is marked in all plots as thin black line denoting 365 days. The left hand figure contains both velocity components with the u -component shown as bold and the v -component as thin line.	66
5.4. Global-averaged frequency spectra from the geostrophic velocity components [$cm^2/s^2/cpd$] for the OSCAR data set (black). For the three years covering the same period as JTP (left) and for the complete 15-year OSCAR period (right). The red spectra display the JTP data from Fig. 5.3 (left).	67
5.5. Basin wide averaged frequency spectra for geostrophic velocity estimates [$cm^2/s^2/cpd$] (left) and EKE [$cm^4/s^4/cpd$] (right) for the Pacific (top), Atlantic (middle) and Indian Ocean (bottom). Note the different scale for the bottom right panel.	69
5.6. Map with mean frequency spectra of the geostrophic u and v velocity component [$cm^2/s^2/cpd$] (top and middle) and the EKE [$cm^4/s^4/cpd$] (bottom). See text for the calculation of the spectra. The top right insets give the axis ranges of the displayed spectra.	71
5.7. Frequency spectra of globally averaged 10° zonal bands for different latitudes, left for the southern and right for the northern hemisphere. As in Fig. 5.3 for the geostrophic u and v velocity components [$cm^2/s^2/cpd$] (left) and the EKE [$cm^4/s^4/cpd$] (right).	73
5.8. Map of the 10° × 10° areas over which the frequency (Fig. 5.9) and wavenumber spectra (Fig. 5.17) were averaged for different regional regimes according to their RMS SSH variability. For the very low energy regions with $\sigma_{SSH} < 6$ cm (small grey dots), the bulk of the oceans with $6 \text{ cm} < \sigma_{SSH} < 15$ cm (dark grey dots), the high energy areas with $\sigma_{SSH} > 15$ cm (black dots) and the tropical oceans between 10° S and 10° N (open circles).	74

5.9. Regional averaged frequency spectra of the geostrophic u and v velocity components [$cm^2/s^2/cpd$] (left) and of the EKE [$cm^4/s^4/cpd$] (right), for the tropical oceans (blue), the low energy regions (light grey), the bulk of the ocean (dark grey) and the high energy areas (black). Their respective geographical regions are marked in Fig. 5.8 as open circles, small light grey-, dark grey- and large black-dots.	74
5.10. Geostrophic velocity frequency spectrum [$cm^2/s^2/cpd$] of $5^\circ \times 5^\circ$ area in the North Atlantic.	75
5.11. As Fig. 5.12 (left), but without Loess smoothing applied to the SSH measurements.	77
5.12. Global-averaged wavenumber spectra of the geostrophic velocity components [$cm^2/s^2/cpkm$] (left) and of the EKE [$cm^4/s^4/cpkm$] (right). The left hand figure contains both velocity components with the u -component shown as bold and the v -component as thin line. The spectra were calculated for each arc segment spanning 10° in latitude. See text for details.	78
5.13. Basin wide averaged wavenumber spectra for geostrophic velocity estimates [$cm^2/s^2/cpkm$] (left) and EKE [$cm^4/s^4/cpkm$] (right) for the Pacific (top), Atlantic (middle) and Indian Ocean (bottom). Note the different scale for the bottom right panel.	79
5.14. Mean wavenumber spectra of the geostrophic u - and v -velocity component [$cm^2/s^2/cpkm$] (top, middle) and for the EKE [$cm^4/s^4/cpkm$] (bottom). See text for calculation of the spectra. Top right insets give the axis ranges of the displayed spectra.	81
5.15. Wavenumber spectra of 10° global averaged zonal bands for different latitudes. Left for the southern and right for the northern hemisphere. As in Fig. 5.12 , for the geostrophic u - and v -velocity components [$cm^2/s^2/cpkm$] (left) and the EKE [$cm^4/s^4/cpkm$] (right).	83
5.16. Track-segment-length for the different 10° latitude ranges that was used for the calculation of the wavenumber spectra (right) and (left) an estimate of a “Rhines” scale (Eq. 5.1).	84
5.17. Regional averaged wavenumber spectra of the geostrophic u and v velocity components [$cm^2/s^2/cpkm$] (left) and of the EKE [$cm^4/s^4/cpkm$] (right), for the tropical oceans (blue), the low energy regions (light grey), the bulk of the ocean (dark grey) and the high energy areas (black). Their respective geographical regions are marked in Fig. 5.8 as open circles, small light grey-, dark grey- and large black-dots, respectively.	84
5.18. Averaged wavenumber spectra from all $10^\circ \times 10^\circ$ areas in the latitude band of 30° N and 40° N in the North Atlantic (see Fig. 5.14), for the zonal (left) and meridional (right) geostrophic velocity component [$cm^2/s^2/cpkm$]. The center longitudes of the $10^\circ \times 10^\circ$ boxes are indicated in the figure.	86
5.19. $10^\circ \times 10^\circ$ averaged wavenumber spectra for geostrophic velocity estimates [$cm^2/s^2/cpkm$] (left) and EKE [$cm^4/s^4/cpkm$] (right) for the Kuroshio (top), Gulf Stream (middle) and Agulhas Retroflexion (bottom).	87
5.20. Differences [cm] of the M_2 tide from the HAMTIDE and FES2004 models. The largest differences occur on the North-Brazilian shelf.	88
5.21. Same figure as Fig. 5.3 (left). The arrows indicate the periods of 62.1 and 58.7 days which are the aliasing periods of the M_2 and S_2 tides for the JTP satellites.	88

5.22.	PSD peak-height of the geostrophic velocity spectra (see Fig. 5.6) at the period of 62.1 days (which is the aliasing period for the M_2 tide), for the zonal (top) and meridional (bottom) velocity components [$cm^2/s^2/cpd$]. Shown are regions with a clear peak at the aliasing period of the M_2 tide. The letters from a - f correspond to the spectra in Fig. 5.23 . Note the logarithmic scale.	89
5.23.	$10^\circ \times 10^\circ$ averaged frequency spectra for geostrophic velocity estimates [$cm^2/s^2/cpkm$] for (left) a Alaskan Stream, b Yellow Sea, c Argentine Shelf and (right) d Bay of Biscay - European Shelf, e Amazon Shelf and f Abrolhos Bank east of Brazil. The spectra belong to the regions a - f in Fig. 5.22 . The regression slope of the period range 45 - 100 days is indicated as blue and the according noise-level as red lines.	90
A.1.	Eddy scale [km] from STAMMER (1997a, Fig. 22) (right axis) and Rossby Number (A.5) calculated for geostrophic velocities of 10 cm/s, 20 cm/s and 50 cm/s (compare also Fig. 3.2) from the equator to 55° N (left axis). . . .	112

1. Introduction

The ocean is one of the important parts of the Earth's climate system next to the atmosphere and the land masses. As all parts of the climate system interact with each other and are causes and consequences at the same time, understanding the driving mechanisms behind each component is necessary in order to conquer questions about our past, present and future climate. Knowing that the ocean covers about 70% of the Earth, its particular importance becomes evident.

The scales in the ocean reach from seconds to the lifetime of the ocean (ZANG AND WUNSCH, 2001) and from millimeters to 10,000s of kilometers where the circumference of the Earth itself marks the cutoff wavelength. Furthermore, there is a tight relationship between all scales of motion in time and space as a consequence of the turbulent nature of oceanic flows (FERRARI AND WUNSCH, 2009). Due to this complexity of the ocean variability manifold approaches exist to capture the wide range of motion on all scales.

Methods used reach from point measurements within moorings to mooring arrays, from ship measurements along sections, drifters, floats and gliders to tomography and satellite based measurements of the ocean. With these methods, the interior ocean and its surface processes can be quantified within the resolution of the respective instruments. However, in spite of the large number of different measurement approaches, some scales of ocean variability still cannot be resolved at all at present.

Within this picture, an interesting role is attributed to satellite based measurements as they are able to capture a large variety of spatial scales with a reasonable time sampling. Among other applications for satellite altimetry¹, the need to continuously monitor ocean currents and transport is one of the primary drivers for uninterrupted altimetric missions. After more than 17 successful years, starting with the famous TOPEX/Poseidon (T/P) mission in September, 1992, altimetry is now generally accepted as one of the key elements of the ocean observing system that is suitable to monitor the ocean circulation and its variability, especially its energetic "mesoscale" eddy field.

The following section will provide an overview of the state of research relevant for this thesis.

1.1. State of Research

Satellite altimetry is now a part of the global ocean observing system whose roots go back to the Skylab (1973) and GEOS3 (1975) satellites. However, the first mission that provided useful data was Seasat in 1978. After that, a number of satellite altimeters have been in orbit such as Geosat (1986-1988), ERS1 (1991-2000), TOPEX/Poseidon (1992-2006), ERS2 (1995-present), GFO (1998-2008), Jason-1 (2001-present), ENVISAT (2002-present) and Jason-2 (2008-present). The huge increase in knowledge about ocean variability that emerged from altimetric sea surface height (SSH) measurements includes many

¹Altimeter measurements are explained in Chapter 2

aspects of the turbulent and large-scale flow-field, such as planetary waves as well as the seasonal cycle of the basin-scale circulation and the heat content of the ocean (the reader is referred to FU AND CAZENAIVE (2001), for a detailed summary).

Despite its enormous success, most of the progress emerging from altimetry is based on SSH fields (e. g. ZLOTNICKI ET AL., 1989; VAZQUEZ ET AL., 1990; PARK AND GAMBÉRONI, 1995; CHELTON AND SCHLAX, 1996; GREENSLADE ET AL., 1997). Direct applications to the ocean’s flow-field are limited to only a few studies and assimilation-based approaches (JOHNSON ET AL., 1992; STEWART ET AL., 1993; STAMMER, 1997a; LEBEN AND POWELL, 2003). This is because, until recently, the computation of horizontal geostrophic currents from along-track altimetric data was, on the one hand, limited to cross-over points, where two components of the flow-field can be inferred from the intersecting descending and ascending tracks. In combination, those two independent and non-synchronous estimates can subsequently be rotated into Cartesian flow components in zonal and meridional direction (see MORROW ET AL., 1994). However, cross-over locations are sparse in space and since the two components are not available simultaneously, a significant error is associated with this way of determining ocean currents, especially in regions of rapid changes. On the other hand, the geostrophic velocity can be calculated solely in cross-track direction while using the along-track slopes of SSH. With that approach, only the cross-track velocity component is available but with the assumption of isotropy it is possible to calculate for example an estimate for the eddy kinetic energy (EKE; WUNSCH AND STAMMER, 1998) or cross-track wavenumber spectra LE TRAON AND ROUQUET (1990). An advantage of that method are the small distances across which the geostrophic velocities are calculated. Alternatively, objective analysis combining SSH anomalies from various satellite missions into spatially and temporally regular fields of SSH anomalies (AVISO, Archiving, Validation and Interpretation of Satellite Oceanographic data) can be used to compute geostrophic currents in zonal and meridional direction (DUCET ET AL., 2000; CHELTON ET AL., 2007). The arising problem is that the underlying SSH anomaly fields are constructed by filtering altimetric data in space and time, e. g. using data covering several weeks in time, which results in the elimination of fast barotropic signals from the SSH analysis on periods less than two months. From a practical point of view, data have to be collected over several weeks before SSH analysis and current fields can be available, implying that near-realtime applications of the flow-field are difficult.

Many of the disadvantages of previously available methods that were used to compute ocean geostrophic currents from altimetric data can be avoided by using the “parallel-track-method” which can be applied when satellite data is available quasi-simultaneously along two parallel satellite tracks as previously described by STAMMER AND DIETERICH (1999) and LEEUWENBURGH AND STAMMER (2002). While using this method, geostrophic current vectors can be computed with a spatial resolution of 6.2 km along a virtual track that is interleaving the altimetric SSH tracks. Noticeably, those results can be available quasi-instantaneously to the SSH measurement as fast as about three hours after the measurements were taken and therewith turning a tandem altimeter constellation into a space-born current meter. The principle could be used with any future altimeter constellation, but applies especially to a wide-swath altimeter technology.

Fortunately, the approach to use a tandem constellation for the estimation of ocean velocity was already applicable during the tandem-phase of the TOPEX/Poseidon and Jason-1 missions. The tandem-phase lasted about three years, during which T/P was shifted westward to cover a new track directly interleaving its previous track, which then was continued by Jason-1. STAMMER AND THEISS (2004) already demonstrated the usefulness of the parallel-track velocity approach based on data from the first months of the mission. With three com-

plete years of data now available from the entire Jason-1 - TOPEX/Poseidon (JTP) tandem mission, those data need to be used for more detailed studies of the ocean flow-field. While the covered time is still short for a quantitative investigation of eddy characteristics and statistics, the data can be used for many other basic investigations of the flow-field and its variability.

A specific aim of this thesis is to use the tandem velocity data to investigate changes of the large-scale, basin wide flow-field occurring on the annual cycle. At the same time, the changes of the eddy kinetic energy (EKE) also occurring on the annual cycle are of interest. Knowledge of both is part of a basic description of the general ocean circulation but is lacking in detail besides some regional descriptions. Regional studies about the seasonally changing flow-field have previously been discussed e. g. by BUSALACCHI AND O'BRIEN (1980); REVERDIN ET AL. (1994) in the tropical Pacific, DONG AND KELLY (2003) in the Middle Atlantic Bight, FUENZALIDA ET AL. (2008) in the Humboldt Current and KNUTSEN ET AL. (2005, velocity and EKE) in the North Eastern Atlantic and seasonal changes of the EKE have been investigated e. g. by DICKSON ET AL. (1982) in the North Atlantic, KELLY ET AL. (1998) in the California Current, WUNSCH AND STAMMER (1998); STAMMER AND WUNSCH (1999); DUCET ET AL. (2000) globally, QIU (1999); QIU AND CHEN (2004) in the North Pacific Subtropical Countercurrent, DUCET AND TRAON (2001) in the Gulf Stream and Kuroshio region and STAMMER ET AL. (2001); EDEN AND BÖNING (2002) in the north Atlantic and Labrador Sea, respectively. As an example, an in-depth-knowledge of annual changes of the large-scale ocean circulation will shed further light on the dynamics of the large-scale gyre circulation and its driving mechanism and also on the response mechanism of the ocean circulation to changes in the forcing and to changes of boundary current transports. Knowledge of the temporal changes of the EKE will allow, among other things, for a better understanding of the mechanism of creating and dissipating EKE. For example, eddy stirring is a key element of the meridional overturning circulation of the ocean (FERRARI AND WUNSCH, 2009).

Zonally coherent structures have previously been found to exist throughout the ocean in eddy permitting ocean general circulation models (SEMTNER JR. AND CHERVIN, 1992; WEBB, 2000; NAKANO AND HASUMI, 2005). Observations support the model results of zonal jet-like structures for instance from satellite measurements (MAXIMENKO ET AL., 2005), acoustic float data in the equatorial Atlantic (OLLITRAULT ET AL., 2006), ERS1 and QuickSCAT wind fields (KESSLER AND GOURDEAU, 2006) and Expendable Bathythermograph (XBT) and float data (MAXIMENKO ET AL., 2008). There has been a long discussion about the formation mechanisms of such zonal jet-like features, containing the beta-plane turbulence (RHINES, 1994; DANILOV AND GURARIE, 2004; NADIGA, 2006), including the mixing of potential vorticity (BALDWIN ET AL., 2007) and the destabilization of mixed Rossby gravity waves (HUA ET AL., 2008). However, a random field of mesoscale eddies (SCHLAX AND CHELTON, 2008) is able to produce striped features instead of averaging rapidly to zero. The interpretation of quasi-zonal jets may therefore be premature. Nevertheless, eddies indeed can follow preferred pathways (MAXIMENKO ET AL., 2005, 2008; SCOTT ET AL., 2008) and the jet properties can differ between the subtropical and sub-polar gyres (KAMENKOVICH ET AL., 2009). Zonal jets appear while averaging the velocity fields in time (over a few years), indicating that they denote persistent signals in the ocean circulation. However, nothing is known about any temporal modulation or behavior, which will be addressed in this thesis in terms of the seasonally changing flow-field.

The broadband energy distribution of the ocean circulation can be visualized by its frequency and wavenumber description. Before the advent of satellite based measurements, spectra have been calculated in the frequency space as it was impractical to capture the

spatial scales needed to calculate wavenumber spectra. However, since Seasat this missing link is now part of the basic description of the ocean circulation. FU (1983) have been the first to calculate global wavenumber spectra of SSH and EKE and thereby paved the way to a deeper knowledge of the turbulent flow-field of the ocean. Subsequently, Geosat offered the possibility for a wide range of spectral analyses. These comprise, amongst other things, the description of SSH wavenumber spectra in the North Atlantic (LE TRAON AND ROUQUET, 1990; STAMMER AND BÖNING, 1992), frequency-wavenumber spectra in the South Atlantic Subtropical Gyre (LE TRAON AND MINSTER, 1993) and Brazil Malvinas Confluence region (PROVOST AND LE TRAON, 1993) and frequency spectra (VAZQUEZ ET AL., 1990) in the Gulf Stream region. However, due to the intrinsic uncertainties in the Geosat estimates, the interpretation has been speculative and controversial (see LE TRAON, 1993; STAMMER AND BÖNING, 1993). With the launch of the TOPEX/Poseidon satellite, the accuracy has been improved (LE TRAON ET AL., 1994), mainly due to the reduced orbit error of the satellite so that a reevaluation of many aspects becomes necessary. Hence, WUNSCH AND STAMMER (1995) constructed the first global frequency-wavenumber spectrum of SSH variability and STAMMER (1997a) provided a detailed description of the global characteristics of ocean variability in the frequency and wavenumber domain for SSH, slope and cross-track geostrophic velocities, while showing some universal aspects of the ocean variability. A first guess model for a general frequency-wavenumber spectrum has been deduced by ZANG AND WUNSCH (2001) using a variety of different measurements, including altimetry, as well as the first constructed wavenumber spectrum for both geostrophic velocity components. Furthermore, the discussion about frequency and wavenumber spectra is essentially related to the question of the underlying turbulence that causes their given relations. The surface quasi-geostrophic (SQG) turbulence theory (BLUMEN, 1978; HELD ET AL., 1995) has been proposed to describe the boundary layer dynamics in a more appropriate framework than the quasi-geostrophic (QG) theory. Therein, the dynamic is entirely driven by the density evolution of the boundary as a counterpart to the QG turbulence theory whose properties are relatively unaffected by boundary constraints. LAPEYERE AND KLEIN (2006) revisited the question of the upper ocean layer dynamics in terms of SQG. Within the ongoing discussion (CAPET ET AL., 2008; LE TRAON ET AL., 2008; KLEIN ET AL., 2008; TULLOCH AND SMITH, 2009; LAPEYRE, 2009) it is shown that the SQG theory can serve as a much better framework for the description of the upper ocean “mesoscale” dynamics. But as questions remain concerning the generality of the results (FERRARI AND WUNSCH, 2010), it is necessary to verify whether the directly observed wavenumber spectra of geostrophic velocities which have been missing until now can be explained by either one of the theories.

1.2. Scientific Goals

The aim of this thesis is to emphasize the important increase in knowledge that can be gained by measuring geostrophic velocity anomalies with a tandem altimeter satellite mission or any comparable satellite constellation. Due to the instantaneous measurement of both velocity components it is therewith possible to describe the ocean flow-field without the assumption of isotropy. Therefore, the SSH measurements of the Jason-1 - TOPEX/Poseidon tandem mission are used to calculate both components of the geostrophic velocity field covering the 3-year period between September 30, 2002, and September 14, 2005. As the coverage of the JTP satellites is nearly global (only latitudes north and south of 66° are omitted), the data set allows for a global description of the geostrophic flow-field and at the same time for regional comparisons.

In this context the thesis focuses on the following questions:

- How do the measurement setup and its spacial resolution influence the accuracy of the calculated geostrophic velocities?
- Can the existing picture of the variability in the oceanic flow- and EKE-field be improved by using the geostrophic velocity estimates of the JTP tandem mission? To what degree does anisotropy have to be considered as being essential within the ocean circulation and is there a resulting need to account for the anisotropic oceanic flow-field throughout the study?
- What new insights can be gained regarding the regional differences in the global distribution of the seasonal signals for the geostrophic velocity estimates and the EKE? How significant are the seasonal signals compared to the total variance? Are the seasonal signals robust for the shortness of the time series and do they show real oceanic signals? Does evidence exist for a change of the large-scale gyre circulation as well as for changes in the wind forcing?
- How do the global and regional spectra as they are now available for both velocity components contribute to a more detailed understanding of the eddy dynamics? Do differences exist in the frequency and wavenumber spectral behavior between the zonal and meridional geostrophic velocity component and to what extent are they influenced by the resolved scales of the JTP tandem mission? Is there an indication for a universal frequency and wavenumber spectrum and how do the wavenumber spectra fit in the discussion about geostrophic turbulence ?

With these goals the importance of satellite based estimates of the oceanic circulation will be addressed as the space born measurements provide the opportunity to capture the upper ocean circulation and its variability on a global scale and with a sufficient temporal resolution.

1.3. Outline of this Thesis

This thesis is organized as follows:

Chapter 2 introduces the JTP tandem mission data set and the resulting geostrophic velocity estimates. The calculation steps of achieving geostrophic velocities from the SSH data are explained and the corresponding error analysis is carried out. Further explained are the data sets of the Ocean Surface Current Analyses - Real time (OSCAR, JOHNSON ET AL., 2007) data set, the MV Oleander project (ROSSBY AND GOTTLIEB, 1998) and the mean dynamic topography (MDTP, RIO AND HERNANDEZ, 2004) that are used for comparison within this study.

Chapter 3 presents basic statistics that are applied to the geostrophic velocity estimates of the JTP tandem mission. The statistics comprise the global root mean square (RMS) SSH variability, a description of global and local probability density functions (PDF), and an assessment of the isotropy field. Moreover, the global EKE field and the relation of eddy and mean kinetic energy (MKE) are evaluated.

Chapter 4 then focusses on seasonal changes of the JTP flow-field and of the EKE. The seasonal part of the geostrophic velocities and of the EKE are compared with seasonal

changes derived from the OSCAR data set. Concerning the flow-field, seasonal zonal jets are discussed that become evident on the global seasonal signal. Additionally, the seasonal flow-field is compared with similar information available from the MV Oleander data set (ROSSBY AND GOTTLIEB, 1998).

Chapters 2, 3 and 4 contributed to SCHARFFENBERG AND STAMMER (2010).

Chapter 5 discusses the frequency and wavenumber spectra of the geostrophic velocity estimates and EKE of the JTP tandem mission data set. Global spectra as well as basin wide spectra are discussed and related to previous estimates. Furthermore, regional spectra are calculated to highlight the different energetic regions of the turbulent ocean circulation.

The main findings and conclusions of the thesis are then summarized in Chapter 6 and an outlook on future research goals concerning tandem mission data from past (JTP) and future satellites and satellites already in orbit (Jason-1 and Jason-2) is given.

In the appendix, the main basic equations used within this study are defined, including the calculation procedure to obtain geostrophic velocity estimates from the simultaneously derived along-track SSH measurements. Furthermore, the harmonic analysis using a least squares fit of the seasonal modulated signal to the time series is explained as well as the Lomb Periodogram used to calculate the spectra instead of a fast fourier transformation (FFT).

2. Data and Errors

2.1. Introduction

The TOPEX/Poseidon (T/P) satellite as well as its successors Jason-1 and Jason-2 are altimeter satellites that measure the height of the satellite above the ground. The height measurements can be achieved by estimating the height between satellite and the sea surface. The radar altimeters onboard the satellite transmit a short pulse of high frequency microwave radiation toward the sea surface where part of the pulse is reflected. The travel time of the pulse from the satellite to the sea surface and back is precisely determined (see CHELTON ET AL., 2001, in FU AND CAZENAVE, 2001). With an exactly known satellite orbit, geoid and reference ellipsoid as well as several corrections that need to be applied for instance for the tropospheric and ionospheric corrections, the sea surface height (SSH) can be calculated. For a detailed description of satellite altimetry techniques and applications the reader is referred to FU AND CAZENAVE (2001).

The T/P mission, launched on August 10, in 1992, was designed to avoid most tidal aliasing periods. To satisfy the constraints given by the tidal aliasing periods and yet cover most parts of the ocean, an inclination of 66° was selected. As the temporal and spatial resolution of a single satellite mission are in direct competition, a repeat period of 9.9156 days was chosen (nominally referred to as a 10-day repeat period, see FU ET AL., 1994). This results in a cross-track separation of 316 km at the equator. **Figure 2.1** shows the part of the

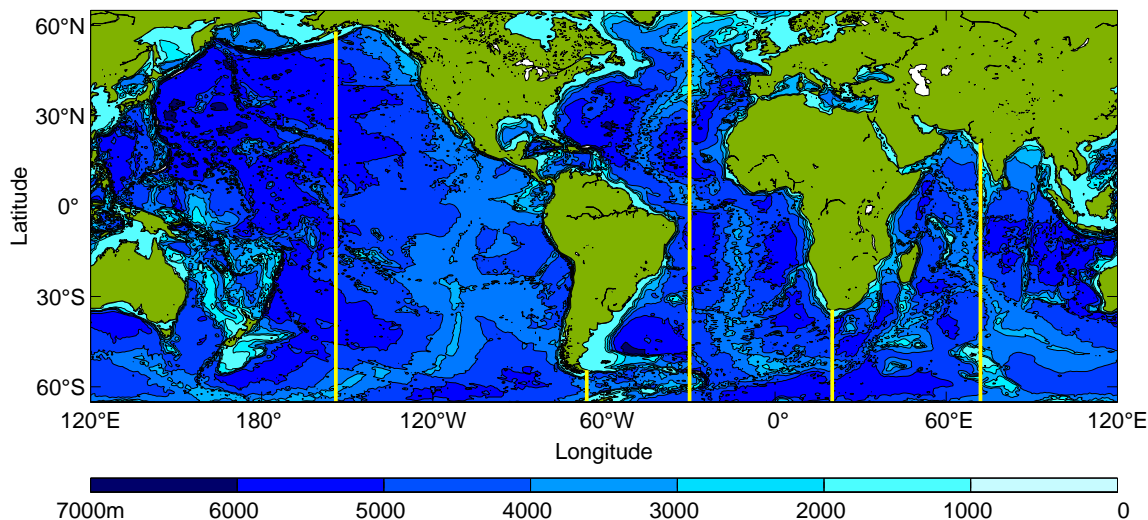


Figure 2.1.: Global bathymetry metric map with depth contours every 1000 m. The yellow lines separate the different basins into the Pacific, Atlantic and Indian Ocean, as well as into their eastern and western parts.

world that is covered by the T/P and hence the JTP satellites from 65°S to 65°N . For an easy location of scientific quantities in the successive chapters the figure indicates the topographic features of the ocean bottom. For several scientific questions in Chapters 4 and 5 it is appropriate to separate the world ocean into its basins. Therefor the yellow lines in **Fig. 2.1** indicate the separation into the Pacific, Atlantic and Indian Ocean and also divide the basins into their eastern and western parts.

The aim of this chapter is to introduce the JTP tandem mission and the resulting data set. An error propagation is provided to verify the uncertainties in the geostrophic velocity estimates. Furthermore, the OSCAR model (JOHNSON ET AL., 2007) is introduced that was used for comparisons with the JTP data set within this study. Other models as the Estimating the Circulation and Climate of the Ocean Model (ECCO2; MENEMENLIS ET AL., 2008) and the Los Alamos National Lab distribution of Parallel Ocean Program (POP) general circulation model (MALTRUD AND MCCLEAN, 2005) were compared with the JTP data as well, but are not shown and discussed here because the OSCAR model yielded the closest results to the JTP estimates. In the following, the data handling of the Acoustic Doppler Current Profiler (ADCP) in situ data, measured by the the Oleander Project (ROSSBY AND ZHANG, 2001), is described. It was used as ground truth measurement comparison with the JTP data. Finally, a description of the Mean Dynamic Topography (MDTP; RIO AND HERNANDEZ, 2004) and the resulting mean flow-field is given.

2.2. The Jason-1 TOPEX/Poseidon Tandem Mission

After the launch of Jason-1 into the same orbit as T/P on December 7, 2001, both satellites had a calibration phase during which they flew behind each other with a one minute time separation. This configuration simplified the cross-calibration of both systems. Beginning on August 15, 2002, after one month of maneuvers, T/P was moved to the west into a different orbit, half way between the original tracks (1.4173° track separation), providing a double space-time sampling of Jason-1 and T/P and offering new science perspectives.

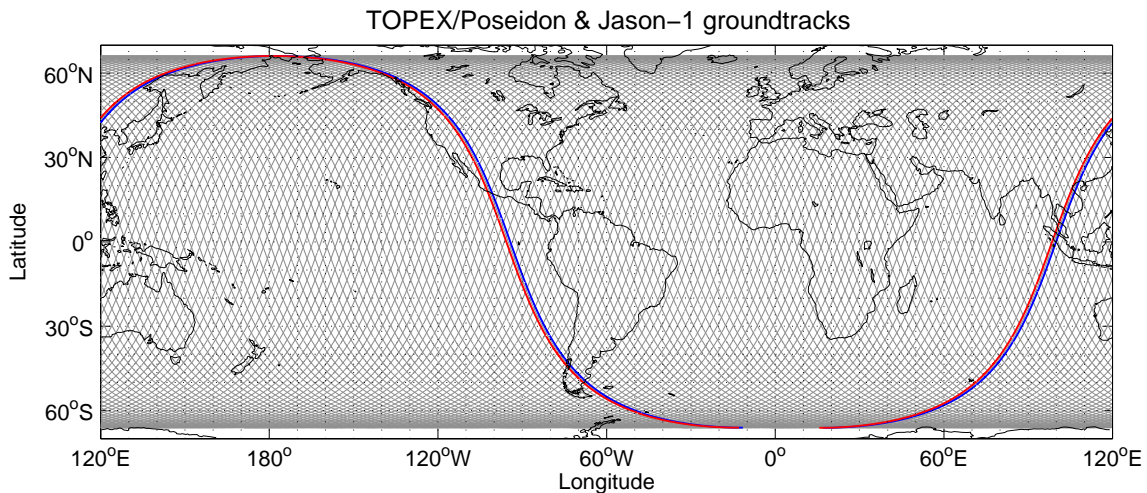


Figure 2.2.: Virtual ground track (grey) on which the geostrophic velocities were calculated using the SSH data available from the JTP tandem mission. Exemplarily the TOPEX/Poseidon (red) and Jason-1 (blue) ground-tracks are shown for ARC 1 and 2.

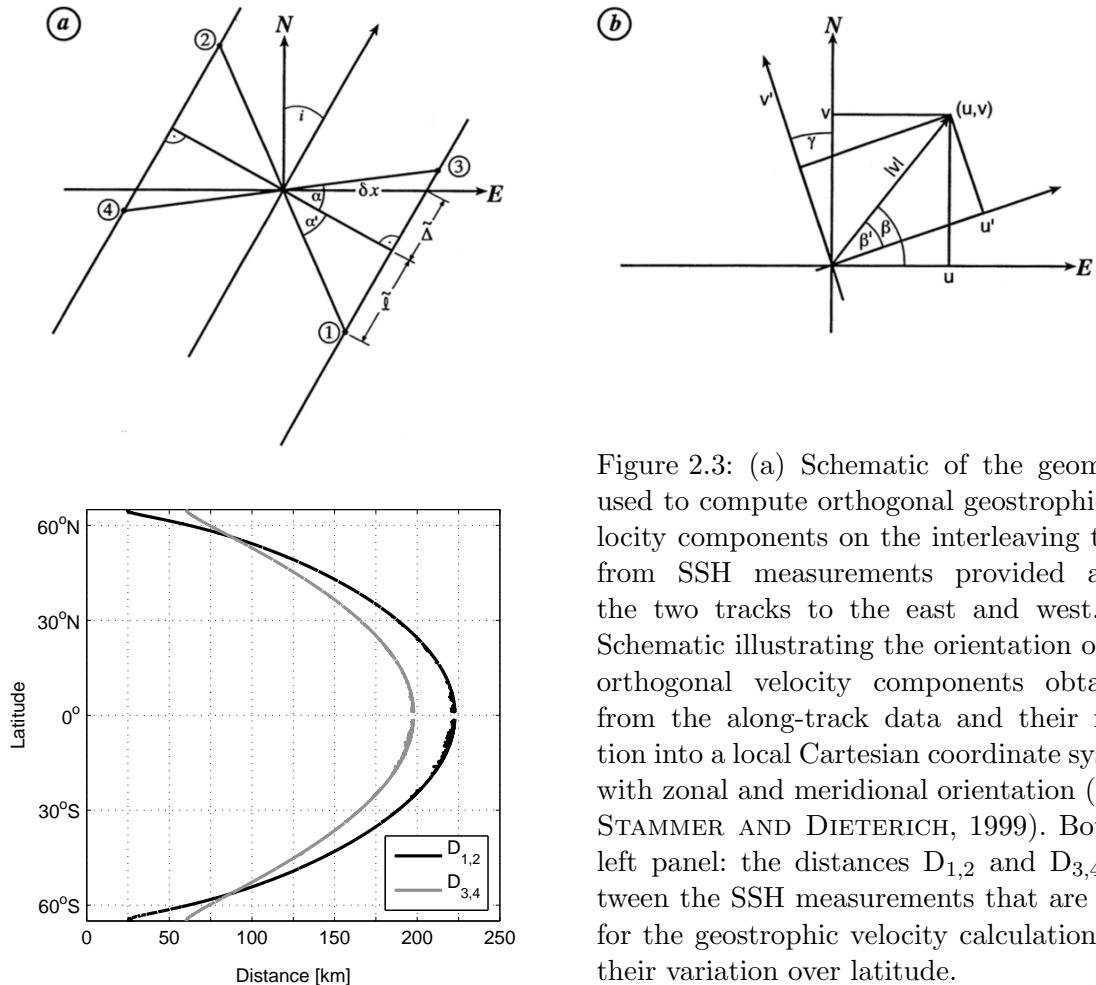


Figure 2.3: (a) Schematic of the geometry used to compute orthogonal geostrophic velocity components on the interleaving track from SSH measurements provided along the two tracks to the east and west. (b) Schematic illustrating the orientation of the orthogonal velocity components obtained from the along-track data and their rotation into a local Cartesian coordinate system with zonal and meridional orientation (after STAMMER AND DIETERICH, 1999). Bottom left panel: the distances $D_{1,2}$ and $D_{3,4}$ between the SSH measurements that are used for the geostrophic velocity calculation and their variation over latitude.

2.2.1. JTP - Data

In this analysis, the “parallel-track-method” is applied to compute horizontal geostrophic ocean currents along a virtual velocity path interleaving the JTP tracks. The global coverage of the virtual velocity path for one repeat cycle is shown in **Fig. 2.2** (grey). For ARCs 1 and 2 the tracks of the T/P (red) and Jason-1 (blue) satellites are marked as well. The analysis is based on the complete 3-year tandem data set covering the period between September 30, 2002, and September 14, 2005 (the end of the successful T/P mission). With this technique, velocity estimates are obtained with an along-track resolution of 6.2 km from the two parallel and simultaneously obtained SSH observations, using SSH gradients in two nearly orthogonal directions. Details of the computation are described by STAMMER AND DIETERICH (1999) and LEEUWENBURGH AND STAMMER (2002). STAMMER AND THEISS (2004) applied the method to the first month of data available from the JTP tandem mission. Here, their approach is essentially followed with only a few modifications introduced.

During the JTP mission, both satellites were flown quasi-simultaneously along two parallel ground tracks, separated by 157 km at the equator. The horizontal geostrophic flow-field can then be computed from the resulting SSH measurements by using SSH data from the

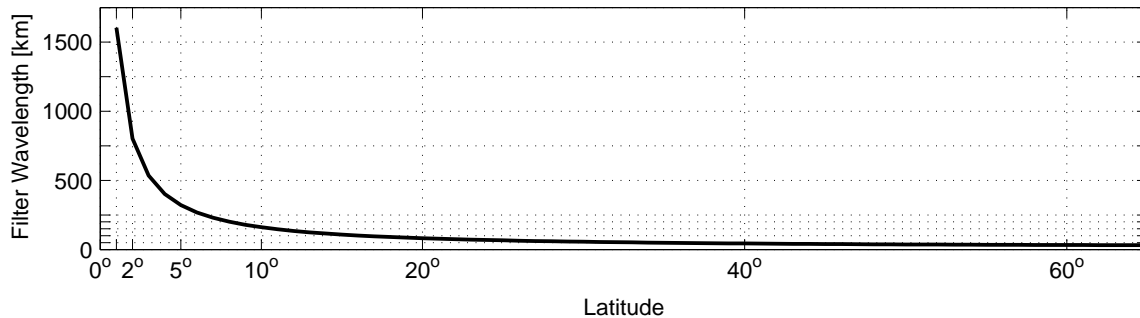


Figure 2.4.: Filter wavelength of the Loess filter $L(\phi)$ from Equation 2.7. The filter length scale is smaller than 100 km poleward and rises to more than 1500 km at 1° around the equator.

following along-track positions as outlined schematically in **Fig. 2.3**:

$$x_1 = \tilde{\Delta} + \tilde{l} \quad (2.1)$$

$$x_2 = -(\tilde{\Delta} + \tilde{l}) \quad (2.2)$$

$$x_3 = \tilde{\Delta} - \tilde{l} \quad (2.3)$$

$$x_4 = -\tilde{\Delta} + \tilde{l}. \quad (2.4)$$

See **Fig. 2.3 a** for an explanation of the symbols used (the diagram is simplified for display purposes; the actual computations take the sphericity into account). Two orthogonal velocity components \tilde{u} and \tilde{v} can then be obtained at the central track position using the geostrophic relation¹:

$$\tilde{u} = -\frac{g}{f'} \frac{(\eta'_1(x_1) - \eta'_2(x_2))}{D_{1,2}} \quad (2.5)$$

$$\tilde{v} = \frac{g}{f'} \frac{(\eta'_3(x_3) - \eta'_4(x_4))}{D_{3,4}}, \quad (2.6)$$

with $D_{1,2}$ and $D_{3,4}$ being the geographical distance between the two location pairs (x_1, x_2) and (x_3, x_4) , respectively, g the gravitational acceleration, and f' the Coriolis parameter, being evaluated at the central velocity position. A rotation of this set of velocity components (\tilde{u}, \tilde{v}) by an angle γ relative to north in space (compare **Fig. 2.3 b**) finally yields a velocity vector of the velocity anomalies u' and v' in a Cartesian reference frame with zonal and meridional orientation.

Conceptually, the computation involves the following steps: (1) A 3-year time mean SSH value is computed at every along-track position and removed from each individual repeat cycle to produce a data set of along-track time varying SSH anomalies $\eta' = \eta - \bar{\eta}$. (2) Orbit errors can create long-wavelength differences in along-track direction between the adjacent JTP values which would appear as spatially coherent (along-track) velocity errors for each arc. To avoid this error, a zonal difference was computed at every along-track position for each pair of tracks and a $1/\text{revolution}$ sin-wave and bias were subsequently fitted to the

¹The calculation of the geostrophic velocities is explained in detail in appendix A.1.

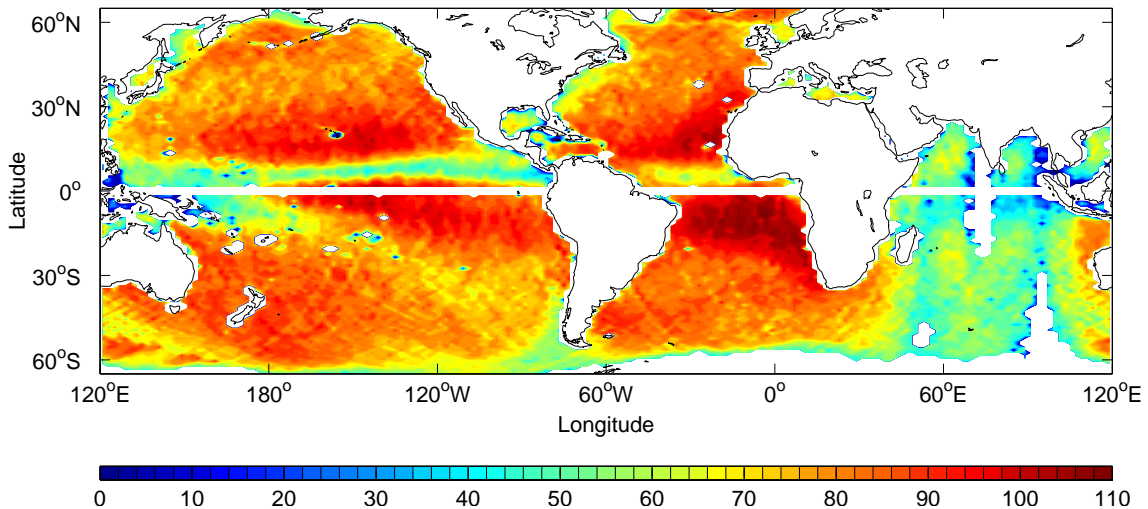


Figure 2.5.: Number of velocity measurements (prior to Loess-smoothing) calculated for each JTP along-track point and subsequently averaged on a $2^\circ \times 1^\circ$ grid for the 109 repeat cycles covering the period September 30, 2002, to September 14, 2005, that were processed in this study.

differences over each entire arc and removed from the original SSH anomalies. With this step, any zonally coherent error between the two tracks (such as biases between two sensors on board the two satellites) was eliminated as well. (3) Finally, to minimize the effect of noise in the η' data, the SSH anomalies were filtered in along-track direction prior to the velocity computation. For this purpose, a Loess filter (SCHLAX AND CHELTON, 1992) was applied before geostrophic velocities were calculated as described by STAMMER AND THEISS (2004). To be comparable with the eddy scale analyzed by STAMMER (1997a), the filter wavelength L was set to be a function of latitude according to

$$L(\phi) = \frac{28 \text{ km}}{|\sin(\phi)|}. \quad (2.7)$$

As can be seen in **Fig. 2.4**, the resulting filter wavelength of $L(\phi)$ is smaller than 100 km poleward of 20° latitude and rises to more than 1500 km as close as 1° N and S of the equator. Using the bias-corrected and Loess-smoothed η' data, geostrophic velocity anomalies (u' , v') were computed from SSH gradients between the two tracks in two directions outside the latitudinal band of $\pm 1^\circ$ and were subsequently used to compute fields of the EKE. Moreover, the degree of isotropy of the eddy variability and the seasonal cycle of the large-scale flow-field as well as of the EKE fields were investigated. All computations of velocity statistics were performed locally at the along-track velocity positions and results were then gridded on a $2^\circ \times 1^\circ$ geographic grid (in longitude and latitude, respectively). An exception to this approach was followed during the computation of the annual signal of the large-scale flow-field: the annual harmonic was least-squares fitted to (u' , v') values after averaging them across $2^\circ \times 1^\circ$ grid boxes to reduce the influence of noise on the estimate of the annual harmonic.

The geographical distribution of along-track calculated velocity data available during the JTP tandem mission is displayed in **Fig. 2.5** after averaging the number of velocity estimates over $2^\circ \times 1^\circ$ boxes. The maximum number of velocity estimates at each along-track velocity position is 109. In the Intertropical Convergence Zone (ITCZ) as well as in several other

regions characterized by increased precipitation, the data coverage is reduced due to heavy rain that absorbs the energy of the radar pulse. Over most parts of the Indian Ocean, upstream of Drake Passage, and over the Gulf Stream (GS) up to 50% of the data are missing due to the loss of storing capacity of the data recording system on board the T/P satellite. The basin wide averages for the geostrophic velocity over the Pacific, Atlantic and Indian Ocean amount to 64.5, 71.3 and 47.8 samples in time, respectively.

2.2.2. JTP - Errors

To specify the formal uncertainties of the resulting velocity estimates, a formal error propagation approach was used which is described in detail by BRATH (2007) and BRATH ET AL. (under revision). This error computation includes the altimeter noise, uncertainties in corrections of atmospheric path delays, sea-state related biases, and orbit errors. During the computation, the global Root Mean Square (RMS) accuracy of the SSH measurements is taken to be $\Delta\eta = 4.2$ cm (1σ) over one-second-averages for typical sea-state conditions for both satellites according to MENARD ET AL. (2003) and LEULIETTE ET AL. (2004). The error of the SSH-anomalies $\Delta\eta'$ of both satellites is then given as

$$\Delta\eta' = \sqrt{\Delta\eta^2 + \frac{\sigma_{\eta'}^2}{N}}, \quad (2.8)$$

with $\sigma_{\eta'}$ being the standard deviation over the 3-year period of the unsmoothed SSH anomalies (see **Fig. 3.1**) and N the number of samples. The second term accounts for uncertainties in the time-mean SSH and its influence on the SSH anomaly. The error resulting for each component estimated at the virtual velocity position is provided by

$$\Delta\tilde{u} = -\frac{g}{f} \frac{\sqrt{\Delta\eta_1'^2 + \Delta\eta_2'^2}}{D_{1,2}}, \quad (2.9)$$

$$\Delta\tilde{v} = \frac{g}{f} \frac{\sqrt{\Delta\eta_3'^2 + \Delta\eta_4'^2}}{D_{3,4}}. \quad (2.10)$$

The error for the smoothed velocity anomaly estimates after rotation into a Cartesian reference frame can be written as

$$\Delta u = \sqrt{(\Delta U \cos\gamma)^2 + (U \sin\gamma \cdot \Delta\gamma)^2}, \quad (2.11)$$

$$\Delta v = \sqrt{(\Delta U \sin\gamma)^2 + (U \cos\gamma \cdot \Delta\gamma)^2}. \quad (2.12)$$

Here U and ΔU are the absolute values of the velocity anomalies and their errors, and γ and $\Delta\gamma$ the direction of the velocity anomaly and its error, respectively.

The resulting errors of zonal geostrophic velocity anomalies (**Fig. 2.6**) for the zonal and meridional flow component clearly display a pronounced latitudinal dependence, leading to enhanced errors due to a decreasing Coriolis parameter in low latitudes and due to a decreasing track spacing approaching the poleward turning latitudes. Furthermore, the errors are slightly enhanced in areas of large variability associated with western boundary currents where the standard deviation of the SSH measurements (see **Fig. 3.1**) dominates the resulting velocity error.

LEEUWENBURGH AND STAMMER (2002) previously investigated errors (in terms of error-to-signal variance ratios) of tandem velocities empirically based on model results². The

²They used a three day interval output of the 1/10° North Atlantic run of the Los Alamos Parallel Ocean Program (SMITH ET AL., 2000).

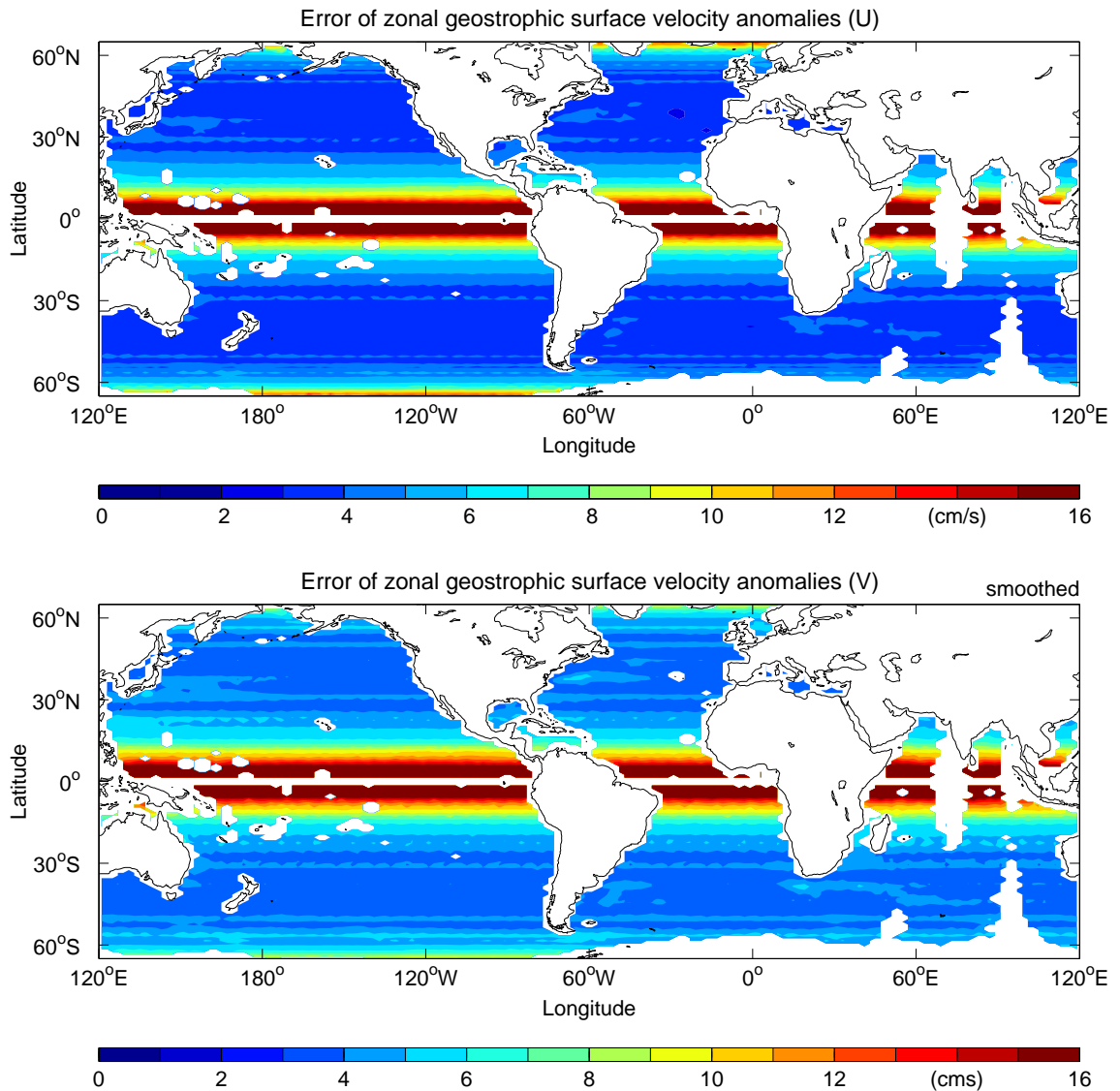


Figure 2.6.: Error of zonal and meridional geostrophic velocity components estimated from JTP data at each along-track point and averaged on a $2^\circ \times 1^\circ$ grid. See text for details on the computation of the error.

error-to-signal variance ratio is defined as

$$EV(\vec{u}) = \frac{\text{var}(\Delta\vec{u}) \cdot 100}{\text{var}(\vec{u})} \quad (2.13)$$

with $\text{var}(\vec{u})$ the variance of the zonal and meridional velocity component. In the GS region, their error variances (for the zonal and meridional velocity component) expressed as percentages of signal variance were in the order of 45 % - 60 % for different error budgets and smoothing length scales, including data as well as sampling errors. According to their estimates, using an instrument noise of 2 cm, the formal error computation presented here, which only includes the data errors but no sampling error along with the assumption of 4.2 cm instrument noise, lead to error variances in the GS region of 7.2 % and 7.6 % for

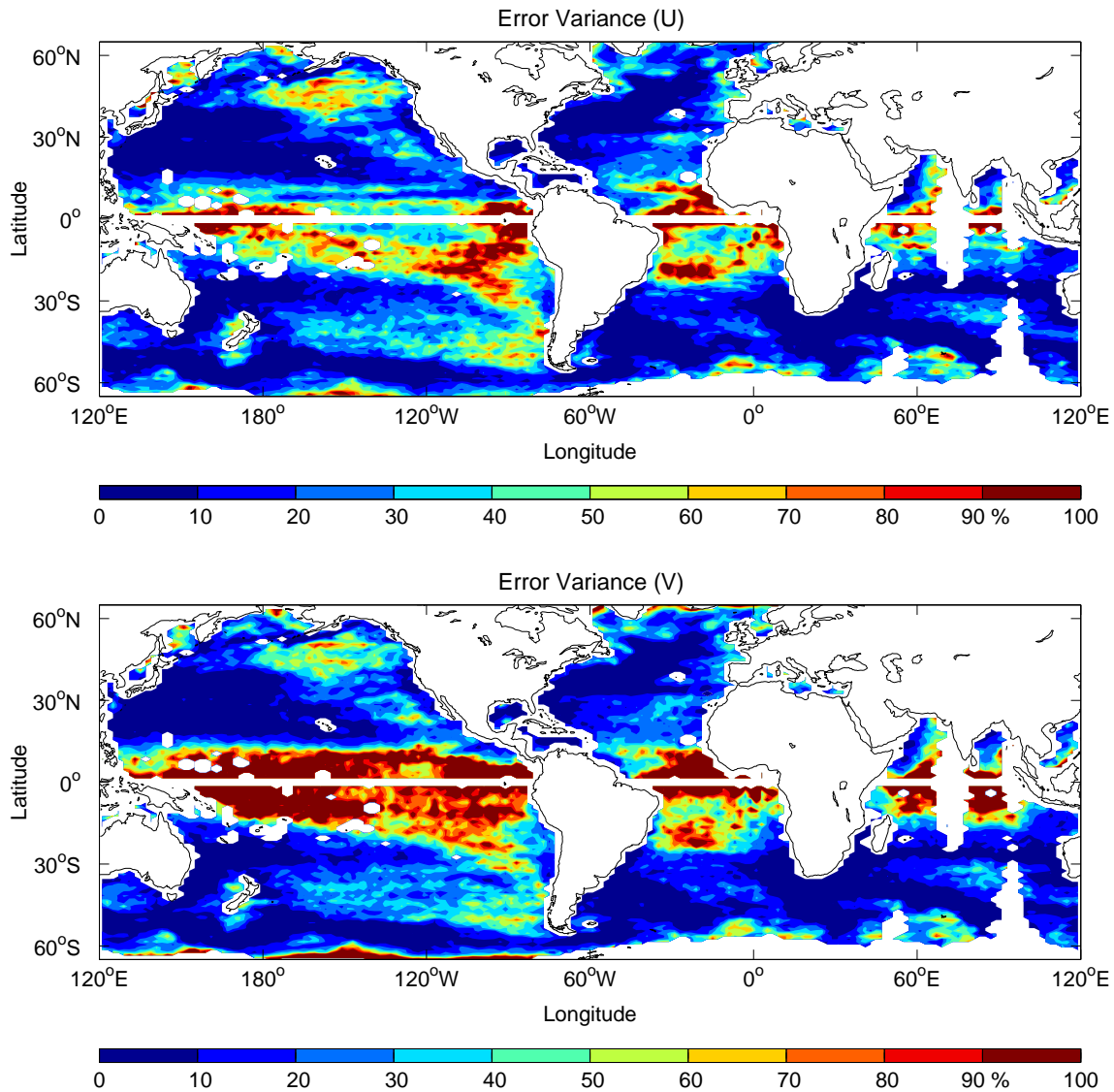


Figure 2.7.: Error variance of zonal and meridional geostrophic velocity components estimated from JTP data at each along-track point and averaged on a $2^\circ \times 1^\circ$ grid. See text for details on the computation of the error variances.

the zonal and meridional component, respectively. Hence, the errors shown here only represent the difference between the error variance budgets of both the sampling error (their **Fig. 3**) and the sampling error plus data error (their **Fig. 4** and **5**). The global maps of the error variances calculated from the JTP tandem mission velocities are shown in **Fig. 2.7** and are used to calculate the error variances over the same four regions in the Atlantic as previously done by LEEUWENBURGH AND STAMMER (2002). Those regions are the Subpolar region (SP; $53^\circ - 66^\circ$ N, $65^\circ - 0^\circ$ W), the Gulf Stream (GS; $30^\circ - 50^\circ$ N, $80^\circ - 40^\circ$ W), the Subtropical region (ST; $10^\circ - 30^\circ$ N, $50^\circ - 20^\circ$ W), and the Equatorial region (EQ; $0^\circ - 10^\circ$ N, $60^\circ - 0^\circ$ W). Their error variances (their **Fig. 5**) were the following (for U/V component and a track spacing of 1.5° concerning the actual track spacing of the JTP tandem mission): SP ($\sim 85/\sim 80\%$), GS ($\sim 55/\sim 50\%$), ST ($55/50-90\%$) and EQ ($\sim 25/30-70\%$). The mean error variances over the same regions from the JTP data but excluding any sampling error

(**Fig. 2.7**) are, respectively: SP (26/37%), GS (7/8%), ST (33/30%) and EQ (68/108%). Furthermore, the empirical errors (LEEUEWENBURGH AND STAMMER, 2002) in highly energetic regions, such as the boundary currents, were generally much larger but represented only a small fraction of the local variability. Besides, increased levels of uncertainty were also found towards the equator due to a decreasing Coriolis parameter and at high latitudes due to a decreasing track spacing. However, in comparison to their empirical results, the formal error computation presented here appears promising with errors smaller than 6 cm/s over most parts of the ocean for both velocity components (**Fig. 2.7**) and global mean error variances of 27.8% and 37.15% for the zonal and meridional component, respectively.

It is unfortunate that the tandem mission was optimized for SSH resolution and not for the sampling of the geostrophic flow-field. As a result, the track spacing of 157 km at the equator leads to an under-sampling of the small-scale structures of the flow-field. This is even enhanced by the fact that SSH gradients are computed here across distances that are even longer than the nominal track separation. Because of this limitation, only the characteristics of the flow-field on wavelengths in the order of 200 km or larger can be computed here, with a respective reduction toward the turning latitudes of the satellites (see Section 5.3). This needs to be kept in mind while interpreting later results as well as the error fields shown in **Fig. 2.6**. These fields do not include the omitted flow features on scales smaller than what can be resolved here, but show an estimate of uncertainty at scales resolved by the tandem mission set-up. The reader is referred to SCHLAX AND CHELTON (2003) for an extensive discussion of an error analysis that includes unresolved features. They calculated not only the measurement errors that are shown here but also the sampling errors using covariance matrices of velocity estimates and SSH measurements and using the nominal decorrelation scales based on the global zonal average of the Rossby radius. The authors conclude that the sampling (omission) error is significant if not the largest source of errors for the parallel track method using a 1.5° track separation.

2.3. The OSCAR Model

The Ocean Surface Current Analyses - Real time (OSCAR³) data set (see JOHNSON ET AL., 2007, for more details) comprises the T/P (October 1992-June 2002) and Jason-1 (July 2002-present) SSHs (LAGERLOEF ET AL., 1999). The scatterometer winds are provided by the Special Sensor Microwave Imager (SSM/I; October 1991-September 2001) and the QuikSCAT gridded winds by the Center for Ocean-Atmospheric Prediction Studies (COAPS; August 2001-present). Furthermore, both Advanced Very High Resolution Radiometer (AVHRR) and in situ Sea Surface Temperatures (SST; BONJEAN AND LAGERLOEF, 2002) data are used. The OSCAR currents are calculated every five days from previously gridded SSH, wind and SST that represent approximately the surrounding ten days of data. The final velocity field then is a combination of geostrophic, Ekman-Stommel and thermal-wind currents. This needs to be kept in mind while comparing the OSCAR velocities and the velocity from JTP. Besides, due to the spacial and temporal filtering of the OSCAR data the fast barotropic motions are filtered out. In previous studies, different authors applied an error propagation to the expected measurement errors of the satellite data throughout the calculation and interpolation using either reasonable assumptions about the space and timescales of the SSH and the velocity field (LE TRAON AND DIBARBOURE, 1999; DUCET ET AL., 2000; SCHLAX AND CHELTON, 2003) or the output of a general circulation model (LEEUEWENBURGH AND STAMMER, 2002). In contrast, the OSCAR model was tested

³Downloaded from <http://www.oscar.noaa.gov/>.

against an exhaustive collection of available ground-based velocity data to examine the ability of the data set to reproduce the temporal and spacial variability of real ocean currents (JOHNSON ET AL., 2007). Velocity data was supplied for instance by surface drifters, moored current meters and Acoustic Doppler Current Profiler (ADCP).

The OSCAR data set provides reasonably accurate time variability of zonal currents only in the near-equatorial region but has its limitations poleward of 10° latitude where amplitudes of the velocity variability diminish unrealistically. Moreover, the variability of meridional currents seems poorly estimated at all latitudes that can be confirmed from the comparison of JTP and OSCAR velocities in Section 3.5.

The OSCAR data set available to us comprises geostrophic velocity anomalies $((u_O(t), v_O(t)))$ available on a $1^\circ \times 1^\circ$ grid, covering the period from October 21, 1992, to December 26, 2007 (1094 fields). The calculations were performed on the $1^\circ \times 1^\circ$ grid and subsequently gridded onto the $2^\circ \times 1^\circ$ grid on which JTP results are available. For a direct comparison between JTP and OSCAR velocities, only 211 OSCAR fields covering the same time period as JTP were used (three years). Comparisons between the JTP and OSCAR velocities are carried out for the isotropy in Section 3.5 and for the EKE-field in Section 3.6. Further discussed were the seasonal velocities including the seasonal variations of the EKE in Chapter 4 and the global frequency spectra in Section 5.2.1.

2.4. The Oleander Project

The ADCP program of the MV Oleander has been in continuous operation since fall 1992, providing ADCP velocity measurements on a weekly basis along a nominal path connecting Hamilton-Bermuda with the U.S. main land (Port Elizabeth, New Jersey). Details of the Oleander ADCP program are provided by ROSSBY AND GOTTLIEB (1998) and ROSSBY AND ZHANG (2001). See FLAGG ET AL. (1998) for technical aspects and <http://www.po.gso.uri.edu/rafos/research/ole/> for a detailed description and all publications of the Oleander program. The Oleander-ADCP data (available on the Joint Archive for Shipboard ADCP data ftp://ilikai.soest.hawaii.edu/caldwell_pub/adcp/INVNTORY/oleander.html) that has already been gridded in space and depth has until recently only been available from 1992 until August 2004, limiting the period of direct overlap with JTP data to the period from September 30, 2002, to August 14, 2004. (Since recently, the complete data set until the present is available at <http://po.msfc.sunysb.edu/Oleander/> but is not part of this analysis.)

Due to the short time series, the results of the annual harmonic obtained from three years of JTP data were compared with those obtained from two years of Oleander-ADCP data both starting September 2002. For the comparison with the geostrophic JTP velocities, the Oleander results from a depth of 100 m were used to minimize the ageostrophic contributions from the Ekman layer to the Oleander observations. To determine a mean velocity from the not-exactly repeating Oleander data prior to the harmonic analysis, a 2° mean around the Oleander track points closest to the gridded JTP estimates was obtained and removed from the individual ADCP velocity anomalies. The annual harmonics of the gridded ADCP velocity anomalies were then computed in the same way as it was done for the JTP data (see Section 4.2.3).

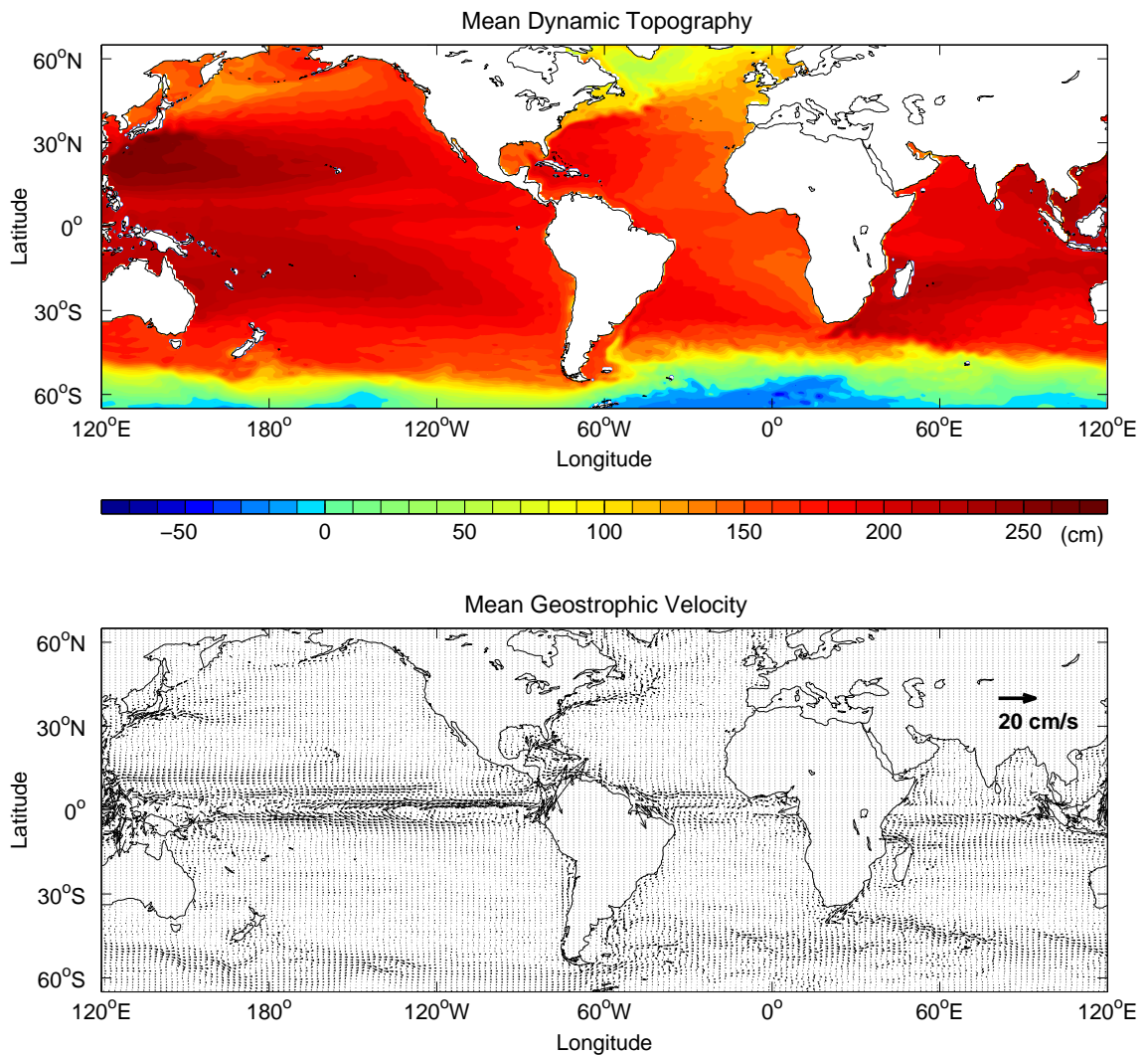


Figure 2.8.: Mean dynamic topography (top; RIO AND HERNANDEZ, 2004) with a $0.5^\circ \times 0.5^\circ$ resolution and the resulting mean flow-field (bottom) gridded onto $2^\circ \times 1^\circ$ boxes. (Includes Altimetry (1993-1999), Geoid Models EGM96 and EIGEN-2, Lagrangian Buoys (1992-1999) and Hydrographic Profiles (1993-2000).)

2.5. The Mean Dynamic Topography

The Mean Dynamic Topography (MDTP) from RIO AND HERNANDEZ (2004) is used in this study to evaluate the ratio of Eddy Kinetic Energy (EKE) to the Mean Kinetic Energy (MKE) in Section 3.7. The Rio2004-MDTP consists of Altimetry measurements during the period between 1993 and 1999 using four satellites: Geodetic Satellite (Geosat), European Remote Sensing Satellite (ERS) - 1/2, and TOPEX/Poseidon. Moreover, the Geoid Model EGM96 (LEMOINE ET AL., 1998) was used for the sea surface heights at the continental shelves and the EIGEN-2 (REIGBER ET AL., 2003) geoid model to determine a previous MDTP. Additional in situ data was used from Lagrangian Buoys (1992-1999) from the World Ocean Circulation Experiment (WOCE) and from the Tropical Ocean and Global Atmosphere (TOGA) Surface Velocity Program (SVP). Collected Hydrographic Profiles

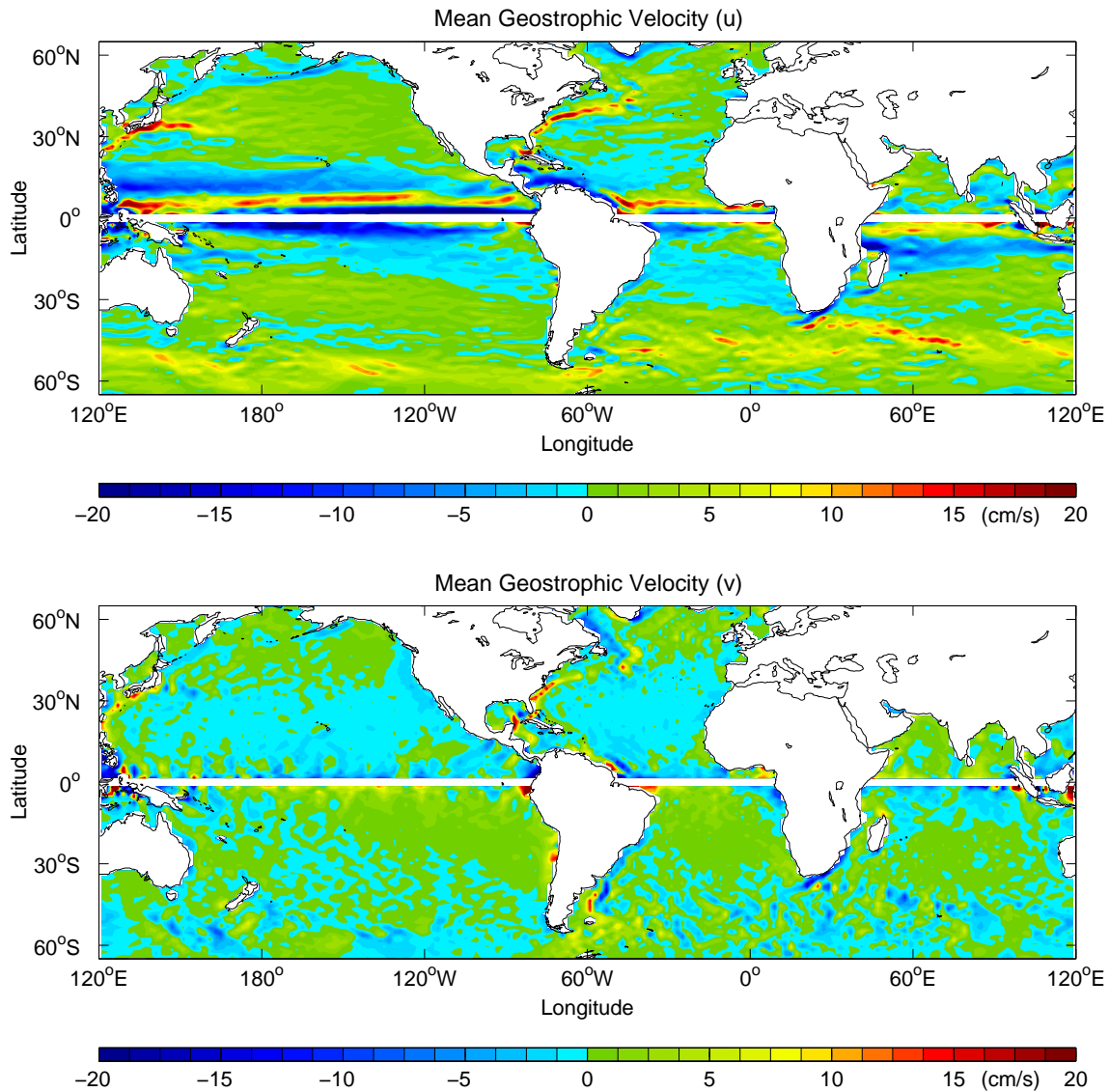


Figure 2.9.: Mean u (top) and v -velocity-components (bottom). The mean of each $2^\circ \times 1^\circ$ grid box was calculated from the 1° SSH-gradients in u - and v -direction around each 0.5° grid point.

(1993-2000) distributed via Système d'Informations Scientifiques pour la Mer (SISMER) from the Institut Français de Recherche pour l'Exploration de la MER (IFREMER) were used as well. **Fig. 2.8** shows the MDTP (top) with an original resolution of $0.5^\circ \times 0.5^\circ$ and the resulting mean flow-field (bottom) that was calculated on the same $0.5^\circ \times 0.5^\circ$ grid from 1° SSH-gradients in u - and v -direction around each 0.5° grid point. Subsequently, the flow-field was averaged on the same $2^\circ \times 1^\circ$ grid as the JTP results. In **Fig. 2.8** (bottom), the strong mean-equatorial currents become visible as well as the mean-boundary-currents. Among many other features of the global circulation, the mean pathways of the Antarctic Circumpolar Current (ACC) are easily determinable.

To gain insight into the respective zonal and meridional mean geostrophic velocity components separately, both are shown in **Fig. 2.9** top and bottom, respectively. In zonal direction,

the equatorial currents, the strong boundary currents, the Agulhas Retroflexion and the ACC are most pronounced whereas in meridional direction the mean currents have a far more patchy structure and show strongest velocities in the boundary current regions (close to the shelves), in the Brazil Malvinas Confluence region, in some equatorial regions as the Indonesian through-flow and in the West Greenland Current (WGC) and offshore the Grand Banks.

2.6. Summary

In this chapter, a detailed description of the calculation procedure to retrieve the geostrophic velocity anomaly estimates from the Jason-1 - TOPEX/Poseidon tandem mission “parallel-track-approach” is given. It has been the first satellite based observing system to retrieve geostrophic velocity estimates instantaneously for both velocity components. As every observing system has its shortcomings, the limitations of the JTP tandem mission setup are demonstrated. Those are namely the distance between the SSH measurements, the temporal sampling and the measurement error of the SSH signal. Due to the track spacing of both satellites, the distances used for the calculation of the geostrophic velocities are as large as 225 km close to the equator. Therefore, smaller spatial scales are resolved by the tandem mission. A formal error propagation demonstrates that over most parts of the ocean the geostrophic velocity anomalies could be calculated with an error smaller than 6 cm/s for both velocity components. However, the error rises to as much as 12 cm/s poleward of 60° and to more than 20 cm/s approaching the equator from 15° N and S.

The OSCAR data set that will be compared with the JTP results throughout this study was explained. It is known that the OSCAR data set poorly reproduces the off-equatorial meridional currents. As ground truth comparison to the JTP and OSCAR results, the ADCP data from the container ship MV Oleander is used and has been introduced briefly in this chapter. While using a MDTP, the resulting mean geostrophic flow-field is computed from which the MKE is then calculated and compared with the EKE.

3. Basic Statistics

3.1. Introduction

To start the analysis of the velocity data, first a few basic statistical descriptions of the SSH and of the velocity fields will be summarized before entering a more focused analysis of the annual cycle in the flow and the EKE fields in Chapter 4. The ocean is in steady motion on spatial scales from millimeters to 10,000 km and on timescales from seconds to years (FERRARI AND WUNSCH, 2009). Therefore a complete description of the ocean circulation is rather challenging. However, with data sets like the JTP tandem mission, with which it is possible to not only gain insight into the global scale SSH field but also into a global estimate of geostrophic velocities, another puzzle-piece of the ocean-circulation-picture can be added within its own temporal (JTP repeat period of 9.9156 days) and spatial limits (6.2 km along-track sampling with a track spacing of 157 km at the equator).

The temporal variability can be described by the RMS variability or standard deviation (STD). Sections 3.2 and 3.3 deal with the RMS SSH and geostrophic velocity variability, respectively. For the velocity fields, the variance is shown as well. The Probability Density Functions (PDF) in Section 3.4 give an idea of how the estimated geostrophic velocities are distributed concerning their strength and frequency of occurrence in the global ocean. Prior to the tandem mission, geostrophic velocities were calculated in cross-track direction of the satellite path. Under the assumption of isotropy, the Eddy Kinetic Energy (EKE) could then be calculated. Whether the assumption of an isotropic flow-field is valid or not will be discussed in Section 3.5. Finally, the mean EKE of the global ocean and the ratio of EKE to Mean Kinetic Energy (MKE) are reevaluated for the JTP data in Sections 3.6 and 3.7, respectively. Hence this chapter gives an overview of important statistical quantities of the geostrophic ocean circulation from the JTP tandem mission point of view.

3.2. RMS SSH Variability

The RMS SSH field was shown before in several publications (e. g., WUNSCH AND STAMMER, 1998) from substantially longer altimetric time series. A similar field is shown here, albeit from the much shorter 3-year long time series of the tandem mission, to put results into perspective with those obtained from much longer time series, and to thereby indicate the data quality of the tandem mission. Moreover, because T/P was shifted laterally halfway between the standard T/P SSH tracks, the zonal resolution of the SSH field resulting from the JTP tandem mission is twice as good as that existing before from T/P alone. This leads to a much better spatial resolution of ocean SSH variability. **Fig. 3.1** shows in its top panel respective results computed from the unsmoothed¹ η' field calculated for each JTP along-track point and averaged on a $2^\circ \times 1^\circ$ grid. Note that the field extends all the way to the continental margin and includes shelf sea areas, regions that were often excluded previously. The inclusion of the shelf regions was maintained throughout the work. Because

¹No Loess filter (see Equation 2.7 and **Fig. 2.4**) was applied for the calculation.

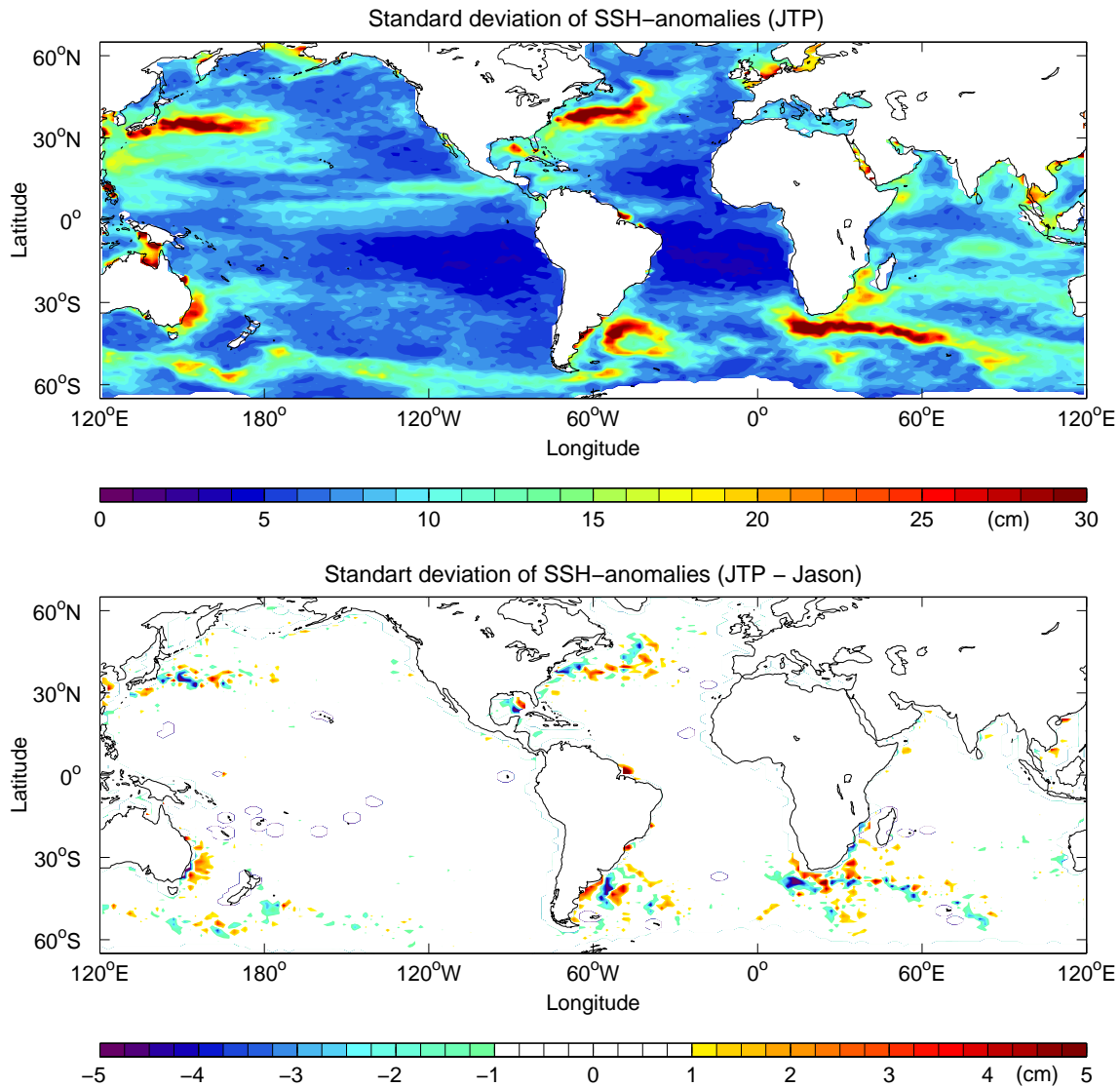


Figure 3.1.: Standard deviation of η' calculated for each JTP along-track point (top) and difference of standard deviation from JTP (top) and standard deviation from Jason-1 alone (bottom), averaged on a $2^\circ \times 1^\circ$ grid and calculated without Loess-smoothing.

of the short duration of the tandem mission, not all ocean variability is represented in the map. As an example, the large interannual tropical variability, shown in previous results due to El Niño Southern Oscillation (ENSO) events, was not captured by the 3-year sampling period. Instead, the figure mostly represents short term variability due to ocean eddies and the seasonal cycle of the flow-field which is represented now with improved meridional resolution. Owing to the better spatial resolution, the field provides enhanced insight into spatial structures of the eddy activity. In this context, it should be noted that there is a particularly high basic variability level in the Indian Ocean relative to the other two oceans. Furthermore, complex variability structures exist outside the western boundary currents, especially in the eastern basins and in the tropical oceans.

To indicate the benefit from the denser spatial sampling, the bottom panel of **Fig. 3.1**

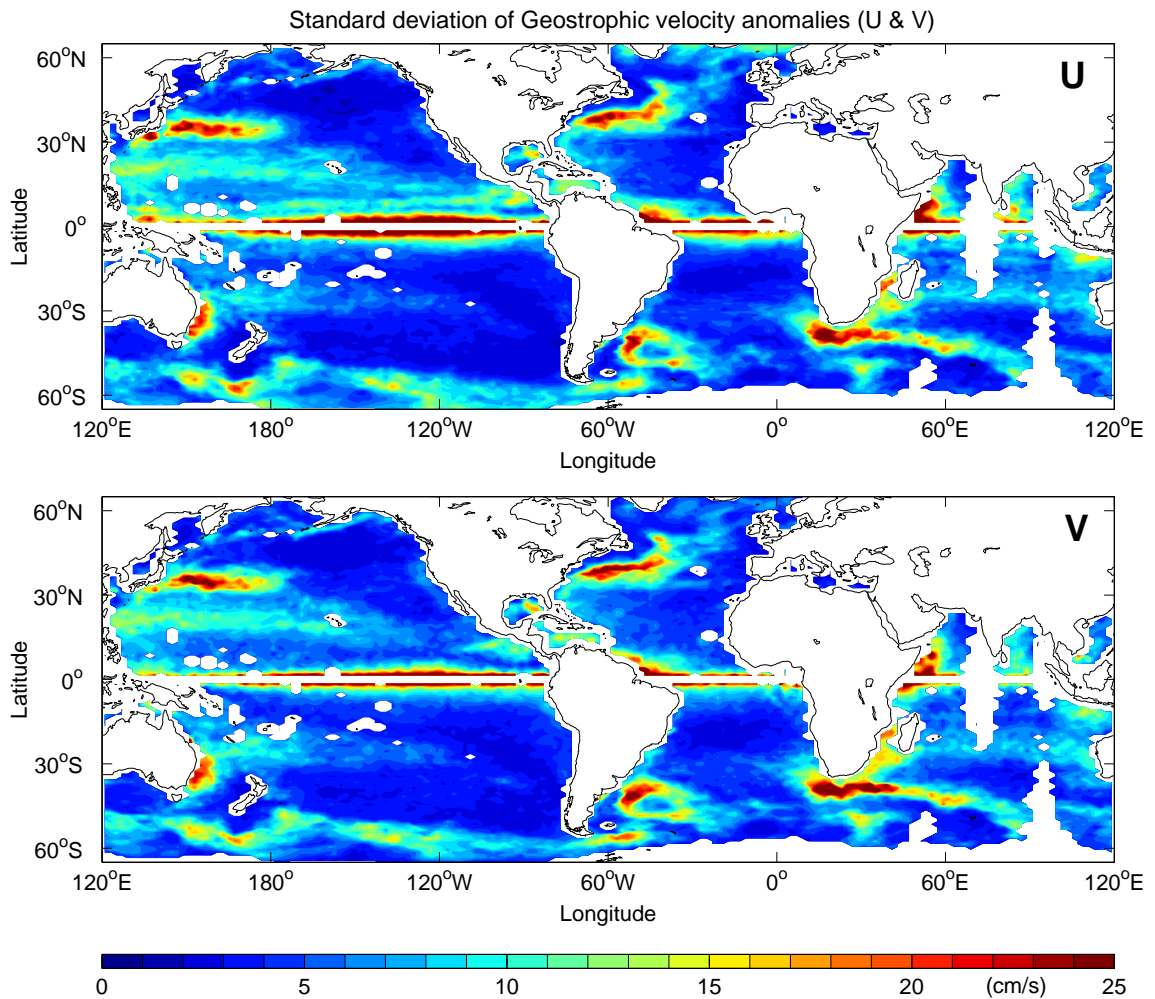


Figure 3.2.: Standard deviation of the geostrophic velocity estimates for the zonal u (top) and meridional v (bottom) component calculated for each JTP along-track point and averaged on a $2^\circ \times 1^\circ$ grid. The color scale for both figures is the same.

shows the difference between the RMS SSH variability estimated from the tandem mission data and the variability estimated from Jason-1 data only, over the same period. Large differences (up to a few centimeters) exist along all major current systems, highlighting the need for denser spatial coverage of SSH data particularly in those regions.

3.3. RMS Geostrophic Velocity Variability

To complete the description of variability, **Fig. 3.2** provides the standard deviation of the zonal and meridional velocity estimates that were calculated on the interleaving virtual velocity track. While comparing the standard deviations of SSH and geostrophic velocities, a difference can be seen at the equator showing large STDs for the geostrophic velocity estimates. Here, the STD of the zonal compared to the meridional geostrophic velocity is stronger at the equator due to the strong equatorial currents in zonal direction. Differences between both velocity components occur over the complete ocean and represent the isotropy

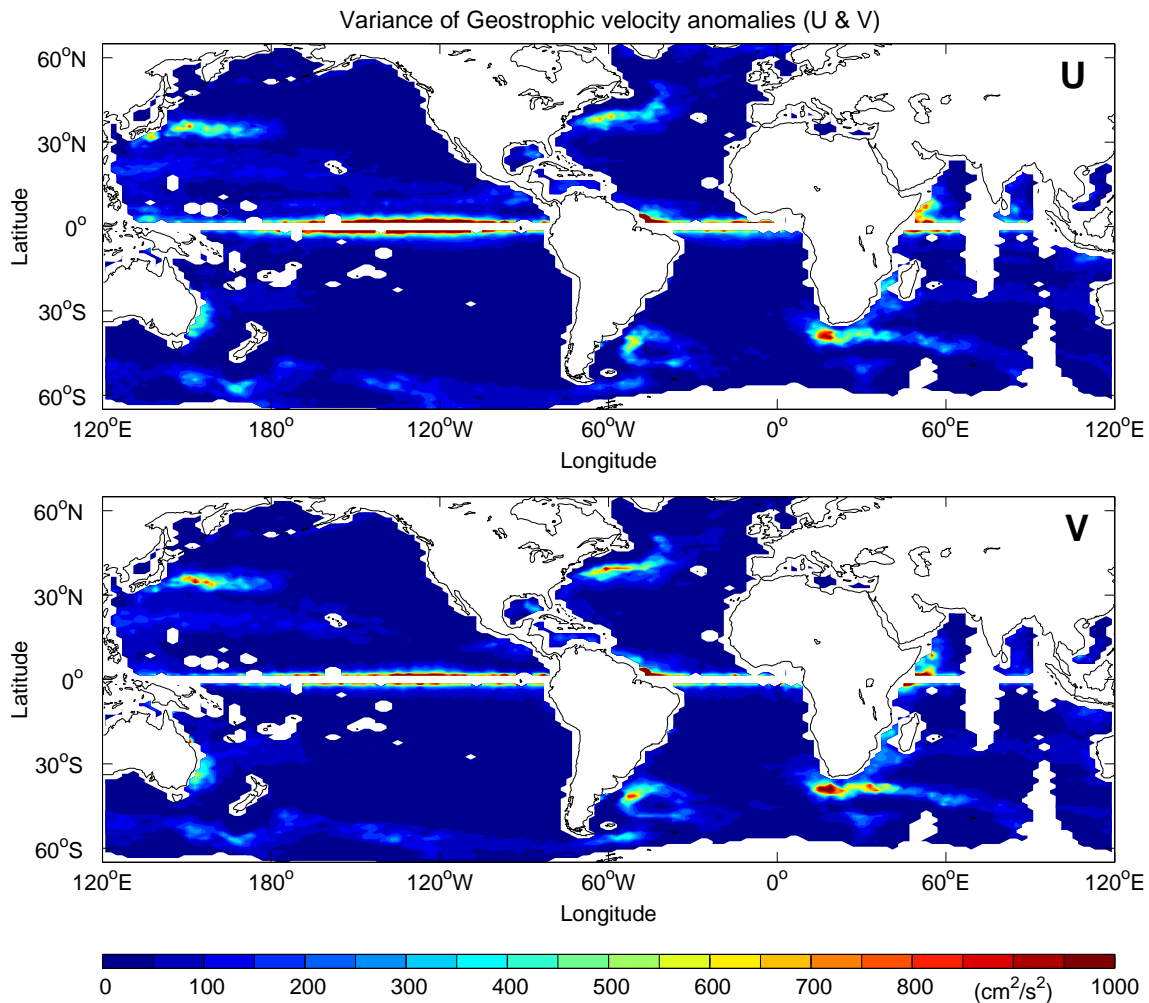


Figure 3.3.: Variance of the geostrophic velocity estimates for the zonal u (top) and meridional v (bottom) component calculated for each JTP along-track point and averaged on a $2^\circ \times 1^\circ$ grid. The color scale for both figures is the same.

field that is discussed in Section 3.5.

In **Fig. 3.3** the variance of the geostrophic velocity estimates for the zonal (top) and meridional (bottom) geostrophic velocity estimates are shown. As the variance is the square of the STD, **figures 3.2** and **3.3** comprise the same structures, however, the variance of the geostrophic velocities is the measure of the amount of variation within the geostrophic velocity values and thus takes into account all possible values and their probabilities or weightings. The largest variances occur in the equatorial ocean. The Agulhas Retroflexion region holds the most pronounced variances among the big current systems.

3.4. Probability Density Function

Probability Density Functions (PDF) are a basic statistical tool to describe turbulent motions. The JTP data set presents the first satellite observing system to clarify the shape

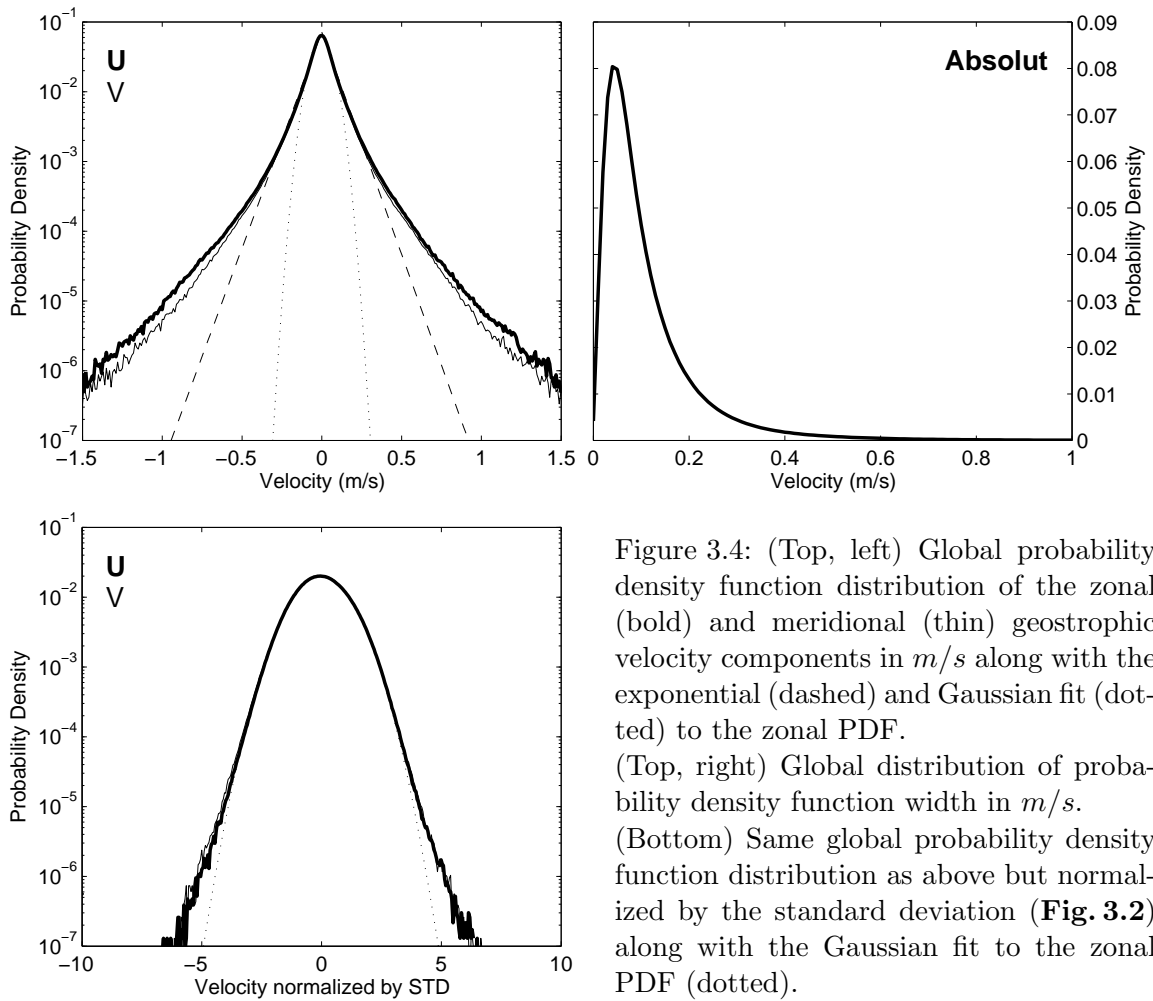


Figure 3.4: (Top, left) Global probability density function distribution of the zonal (bold) and meridional (thin) geostrophic velocity components in m/s along with the exponential (dashed) and Gaussian fit (dotted) to the zonal PDF.

(Top, right) Global distribution of probability density function width in m/s .

(Bottom) Same global probability density function distribution as above but normalized by the standard deviation (**Fig. 3.2**) along with the Gaussian fit to the zonal PDF (dotted).

of oceanic geostrophic velocity PDFs without the assumption of isotropy, as it had to be done for previous studies (LLEWELLYN SMITH AND GILLE, 1998; GILLE AND SMITH, 2000; SCHORGHOFER AND GILLE, 2002). Hence, the PDFs are available for both velocity components. Additionally, it is now possible to calculate the PDF width (w -PDF), which is equivalent to the RMS velocity or the EKE, from both geostrophic velocity components.

Histograms of all along-track time series were calculated. These histograms were summed over all $2^\circ \times 1^\circ$ boxes and normalized by their amount within each box as well as normalized by their bin width. The same was done for a $10^\circ \times 10^\circ$ resolution and for global PDFs of both geostrophic velocity components (u , v) and the width of the distribution (w -PDFs).

The global distribution of the velocity PDFs is displayed in **Fig. 3.4**. In the top left panel the PDF distribution of both velocity components is shown. The PDFs are calculated from geostrophic velocity anomalies (the mean velocity has already been removed), and thus the PDFs are centered around zero. A wider shape can be found for the zonal component due to the larger variability in the zonal direction. An exponential (dashed) as well as an Gaussian fit (dotted) to the zonal PDF are included in the panel. Both velocity components rather resemble an exponential than a Gaussian shape as expected from previous studies by LLEWELLYN SMITH AND GILLE (1998) and GILLE AND SMITH (2000). The shape of the global PDF is more exponential as a consequence of the significant variance of EKE over the whole world ocean (compare **Fig. 3.9**, top). LLEWELLYN SMITH AND GILLE (1998)

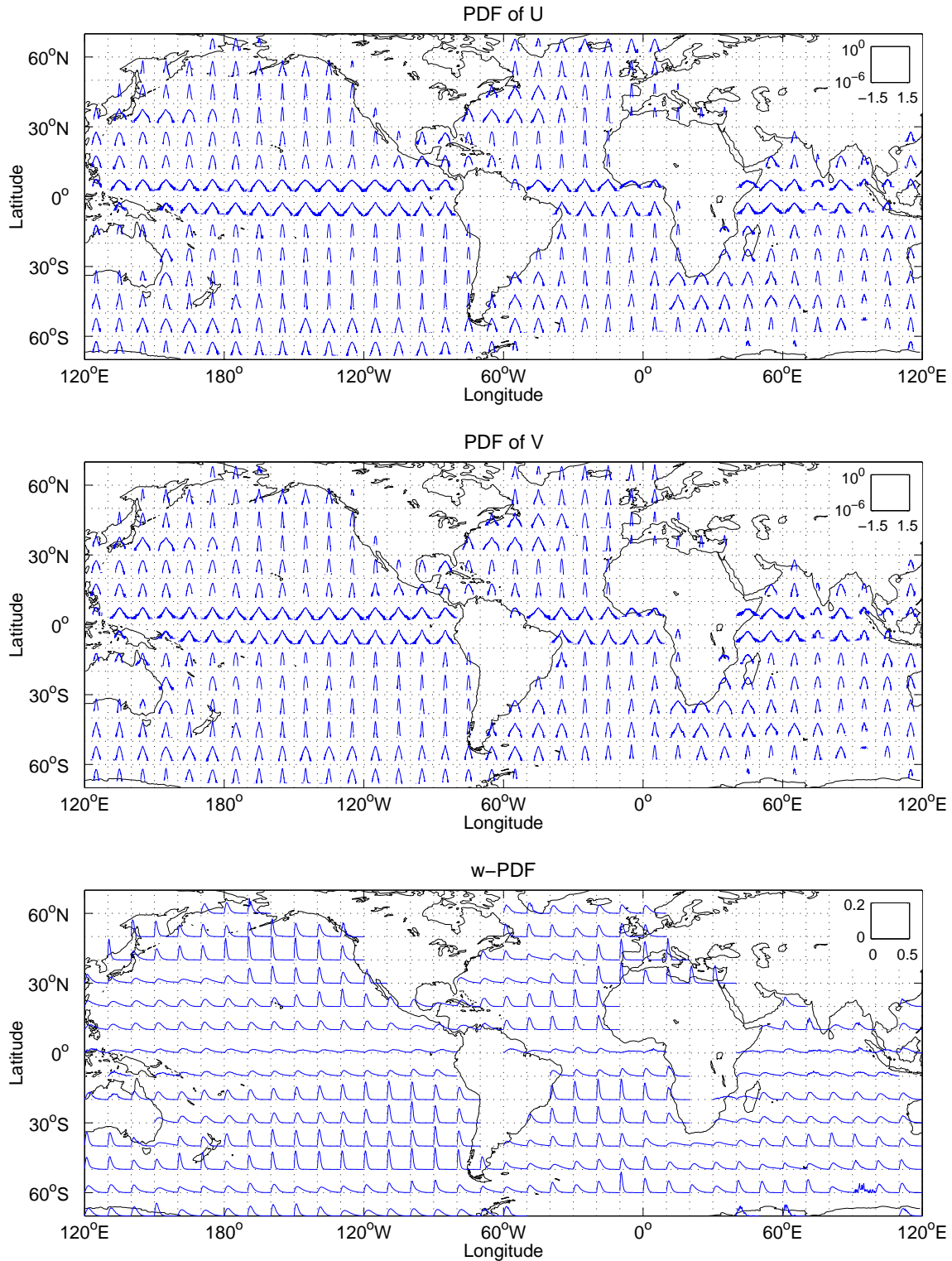


Figure 3.5.: Probability density function distribution of the zonal (top) and meridional (middle) geostrophic velocity components [m/s] for $10^\circ \times 10^\circ$ subregions. (Bottom) The distribution of probability density function width [m/s]. The top right insets give the axis ranges of the displayed PDFs.

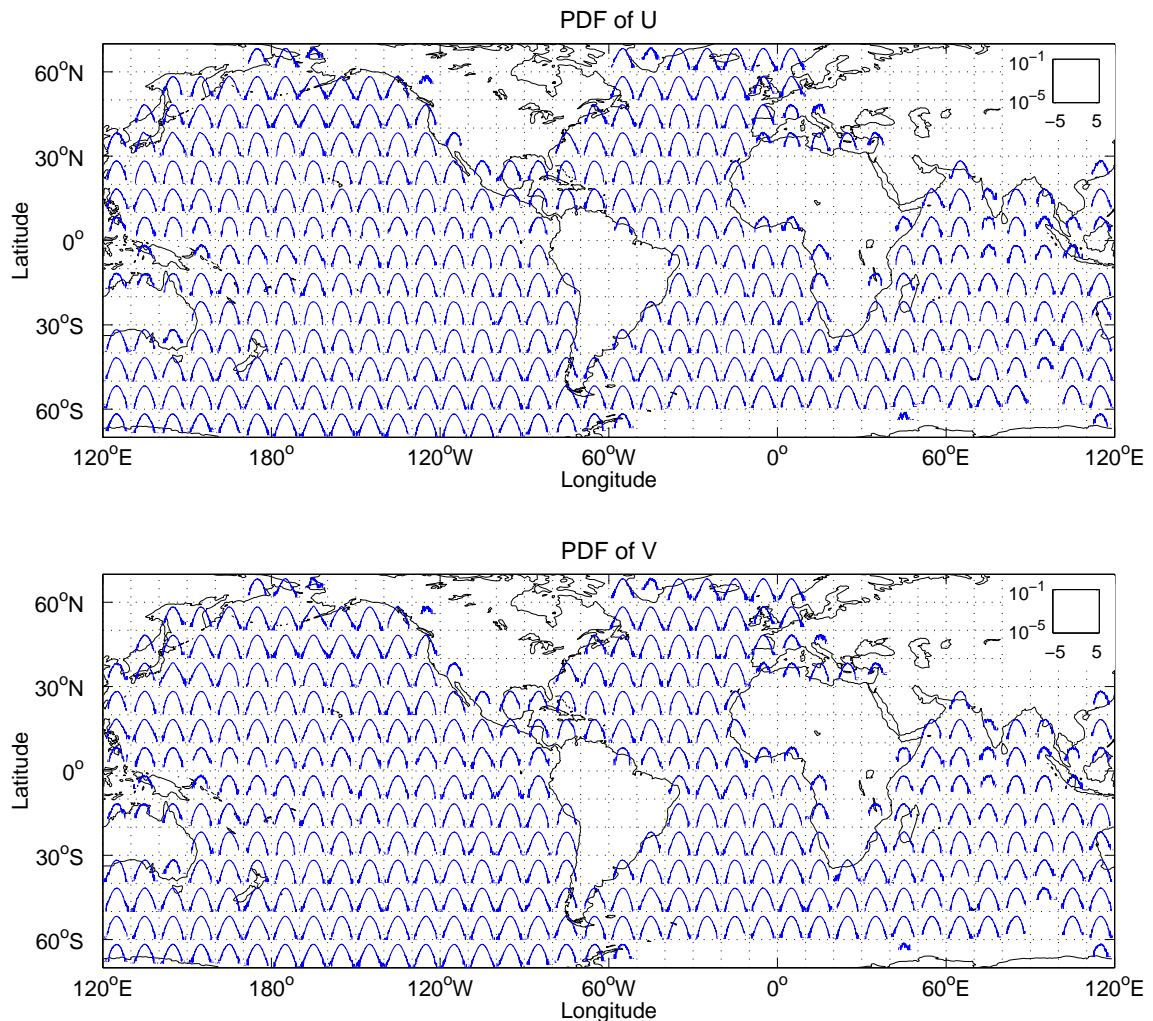


Figure 3.6.: Same probability density function distribution as in **Fig. 3.5** but weighted by the STD of the geostrophic velocity components (**Fig. 3.2**). The top right insets give the axis ranges of the displayed PDFs.

and GILLE AND SMITH (2000) previously explained the different shapes of PDFs that cover different size regions with the varying PDF-width or varying EKE within the respective regions. In **Fig. 3.5**, the geostrophic velocity PDF distributions for the zonal (top) and meridional (middle) velocity components are shown for all available $10^\circ \times 10^\circ$ subregions. As can be seen, the shape of the PDF distributions varies significantly over the global ocean. The scales for each subplot in the map are shown in the small top right insets of the map. In regions where the EKE (see **Fig. 3.9**, top) does not vary significantly over a $10^\circ \times 10^\circ$ grid box, the according PDF has a close to Gaussian shape, whereas for $10^\circ \times 10^\circ$ boxes with a strongly changing EKE strength, the shape of the PDF is found to be clearly exponential. (Compare the dotted and dashed curve in **Fig. 3.4**, top, right) Strongly varying EKE can be found e.g. in the whole equatorial region, in the Kuroshio and Gulf Stream region as well as in the Agulhas Retroflexion, Brazil Malvinas Confluence and in parts of the ACC. SCHORGHOFER AND GILLE (2002, their **Fig. 2**) proposed that large coherent eddies play only a minor role in generating their observed statistics from T/P cross-track velocities. While concentrating on **Fig. 3.5** (top, middle), the PDFs from JTP give no evidence either

for a shape suggesting that large coherent eddies play an important role.

The global distribution of probability density function width [m/s] (w -PDF) is displayed in **Fig. 3.4** (top, right). As has been discussed in LLEWELLYN SMITH AND GILLE (1998); GILLE AND SMITH (2000) the width of the PDF is varying throughout the ocean. It is wider in regions of high variability and high EKE, and narrower in regions where the variability is low. To illustrate the spatial variation of the w -PDFs, in **Fig. 3.5** (bottom) all available $10^\circ \times 10^\circ$ averaged w -PDFs are shown. In high energy regions the PDF width is wider whereas in regions of low variability the width of the PDF is narrow and confined to absolute velocities smaller than 20 cm/s. Within an analysis CHU (2008) show w -PDFs of the upper tropical Pacific (0-50 m) at two stations of the Tropical Atmosphere Ocean array (TAO). The TAO-PDFs have the same order of magnitude as those estimated from the JTP velocities. As can be seen in **Fig. 3.5** (bottom), the PDFs in the equatorial regions show PDF-widths in the order of 0.02 whereas e.g. in the North Pacific they can reach values up to 0.2 which is a difference of an order of magnitude, showing that the velocities and their variability are much smaller.

A Gaussian shape of the PDF distribution can be gained when normalizing the geostrophic velocity anomalies with their STD from **Fig. 3.2** (top). The accordingly normalized PDF distributions of the $10^\circ \times 10^\circ$ subregions are displayed in **Fig. 3.6** for the zonal (top) and meridional (bottom) velocity components. It is evident that the PDF distribution within each $10^\circ \times 10^\circ$ region has a Gaussian shape and thus the normalized global PDF distribution in the lower panel of **Fig. 3.4** has to have a Gaussian shape as well. Therefore, the Gaussian fit to the zonal PDF (dotted) is shown exemplarily.

The normalized PDF distributions can be compared with normalized PDFs from in situ data of subsurface floats in the North Atlantic (BRACCO ET AL., 2000) which show a similar Gaussian shape as in **Fig. 3.4** and **3.6** (bottom). However, when averaging all PDF distributions from the subsurface floats that were not normalized by their STD, a clear exponential shape as in **Fig. 3.4** (top, left) appears.

3.5. Isotropy

A question of long-lasting concern is that of the isotropy of the ocean eddy field. In the past, only few data sets were available to obtain answers (WUNSCH, 1997; DUCET ET AL., 2000). As an example, WUNSCH (1997) investigated this question based on the available global ocean mooring data set and concluded that outside western boundary current regions the mesoscale eddy variability would be essentially isotropic. Closer to western boundary currents such as the GS, barotropic variability, associated with the recirculation of the GS, gains importance (about 30% of the observed variability) and can lead to preferred directions of variability.

The question of isotropy of the ocean eddy field is revisited using the JTP velocity data set. For that purpose, an isotropy coefficient (HUANG ET AL., 2007) was computed at every along-track position of the tandem velocity field that is defined as

$$ISO = \frac{\langle v'^2 \rangle - \langle u'^2 \rangle}{\langle v'^2 \rangle + \langle u'^2 \rangle}. \quad (3.1)$$

The resulting field, as it follows from the 3-year long JTP time series, is shown in **Fig. 3.7** (top). Albeit noisy due to the short duration of the data set, the figure indicates a slightly higher meridional variability in mid latitudes (by 10 to 20%). The opposite is true for the

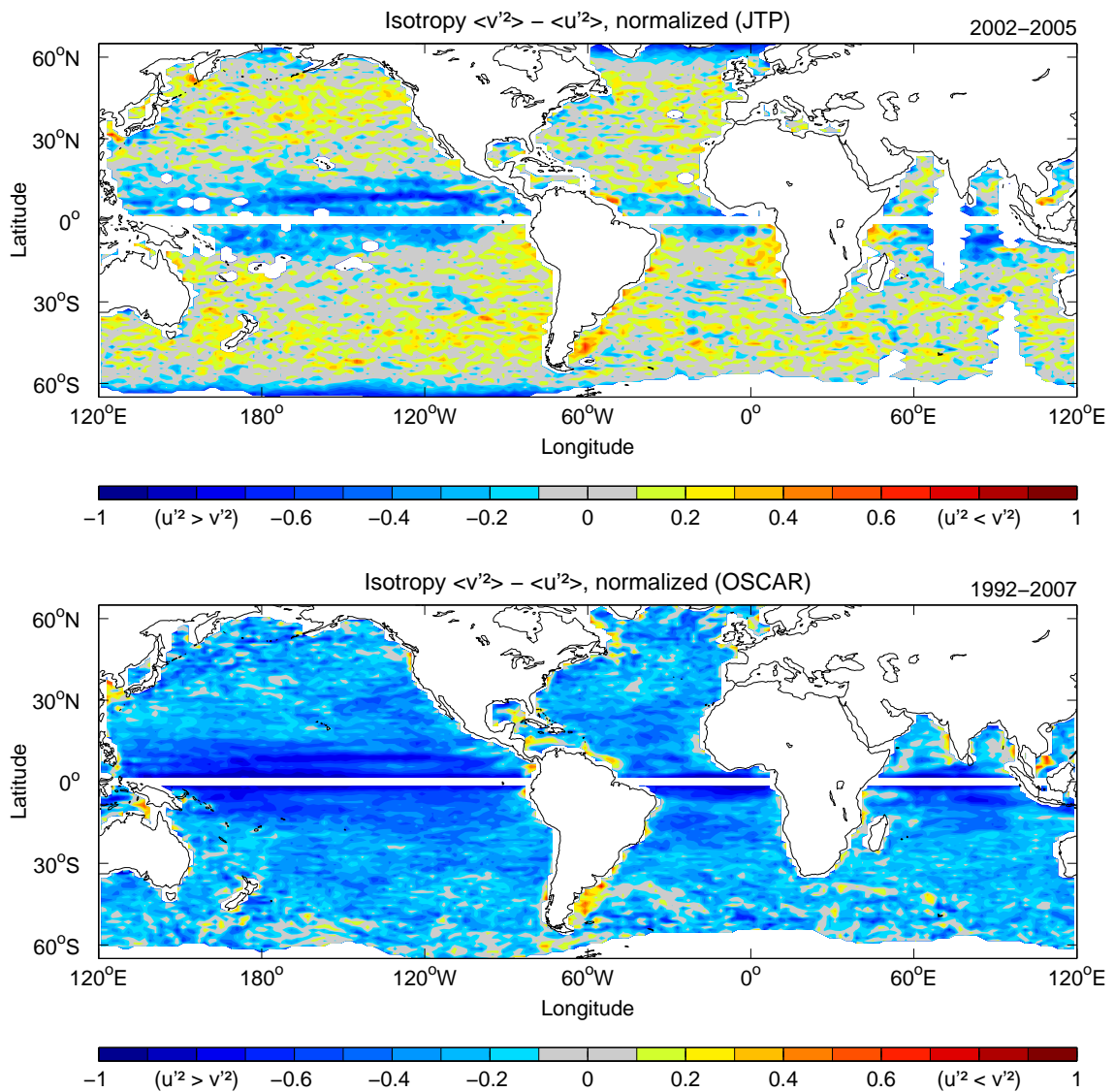


Figure 3.7.: Isotropy of the JTP data $\langle v'^2 \rangle - \langle u'^2 \rangle$ normalized by $\langle v'^2 \rangle + \langle u'^2 \rangle$ (top) and Isotropy from the 15-year long OSCAR data-set $\langle v'^2 \rangle - \langle u'^2 \rangle$ normalized by $\langle v'^2 \rangle + \langle u'^2 \rangle$, (October 21, 1992, to December 26, 2007, bottom). Here u' and v' denote the zonal and meridional geostrophic velocity anomalies, respectively. For both panels the isotropy was calculated for the mean of each $2^\circ \times 1^\circ$ grid cell.

tropics where much of the EKE field is dominated by the variability of the mostly zonal current field. Except for the high latitudes, these estimates generally agree with DUCET ET AL. (2000) and with the regions defined in HUANG ET AL. (2007). In high latitudes, the error of the zonal velocity component might dominate, although the figure was corrected for uncertainties. In contrast, a similar field, but computed from the longer 15-year OSCAR data set (1992-2007; **Fig. 3.7**, bottom), shows an enhanced zonal variability. The same tendency holds for OSCAR results representing the JTP period. Only a few exceptions can be found at locations where the meridional variability is also enhanced in the OSCAR results. Notably, those are located along the South American Continent and along the California Current.

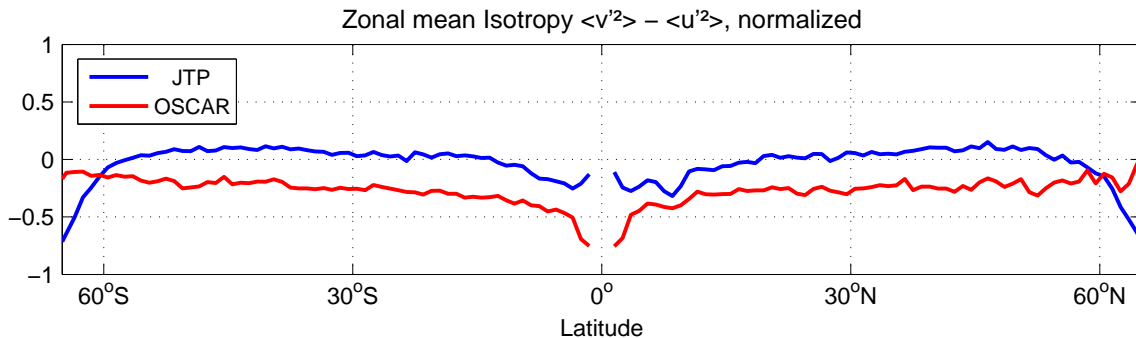


Figure 3.8.: Zonal mean normalized isotropy for JTP (blue) and OSCAR (red). For positive/negative values the meridional component is smaller/larger than the zonal component.

A summary of the isotropy of the eddy variability present in the JTP and OSCAR data is shown in **Fig. 3.8**, showing zonal averages of both isotropy fields. The figure shows a slight enhancement of meridional variability in the JTP data set outside the tropical band and the high latitudes and indicates a substantially lower meridional than zonal variability present in the OSCAR data set. JOHNSON ET AL. (2007) provide a comparison of OSCAR currents with in situ data from moored current meters, drifters, and shipboard current profilers. The analysis indicates that OSCAR provides reasonably accurate time variability of zonal currents only in the near-equatorial region. Poleward of 10° latitude, amplitudes of the velocity variability decrease unrealistically. Moreover, the variability of meridional currents seems poorly estimated at all latitudes. The results from the JTP tandem mission confirm those earlier conclusions by JOHNSON ET AL. (2007).

3.6. EKE Field

In this section, the eddy kinetic energy (EKE) of the world ocean is analyzed. First, the mean EKE field for the 3-year period is discussed. Then, the focus is set to their seasonal variations. These calculations reveal the regions of seasonally changing eddy variability. A field of the Eddy Kinetic Energy (EKE) was calculated from the two velocity components (u' , v') available from the parallel-tracks over the entire 3-year period at each along-track position according to

$$EKE = \frac{1}{2} (u'^2 + v'^2), \quad (3.2)$$

where u' and v' are the velocity anomalies. Then, results were gridded on a $2^\circ \times 1^\circ$ grid (**Fig. 3.9**, top). As for the SSH field, all major current systems are again clearly visible and in addition many regional aspects are pronounced. As an example, a split of enhanced EKE values is observed around the Hawaiian Island Chain (HOLLAND AND MITCHUM, 2001) and a general enhancement of the EKE field west of the Hawaiian Islands. A similar structure appears in the South Pacific. Moreover, enhancements in EKE can be found all along the western U.S. coast and from there along the North Pacific Current toward the Kuroshio. High amplitudes of EKE are likewise visible along the Aleuten Chain where DOUGLASS ET AL. (2006) found a variation of the Aleuten Current in Expendable Bathythermograph (XBT) and model simulations and CRAWFORD ET AL. (2000) found multi-year meanders and eddies in the Alaskan Stream from T/P altimeter data. The pronounced detail of

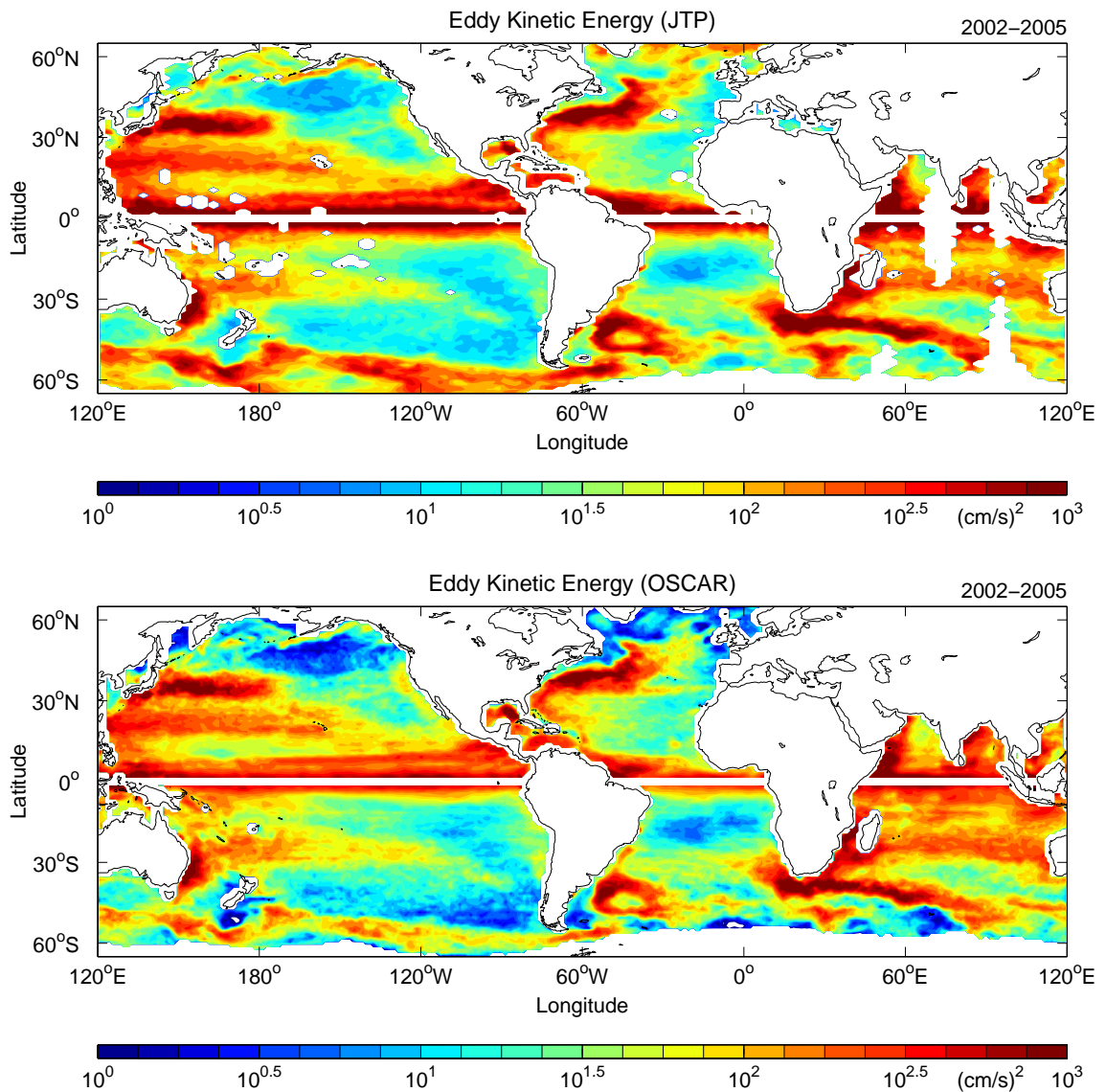


Figure 3.9.: (Top) EKE [cm^2/s^2] calculated from the three-year long JTP velocity time series for each along-track point and gridded subsequently on a $2^\circ \times 1^\circ$ grid. (Bottom) OSCAR EKE field, covering the same period, but calculated on a $2^\circ \times 1^\circ$ spatial grid. Scales are logarithmic in both panels.

EKE along the entire ACC has to be noted as well, including the Agulhas region, with all topographic structures clearly highlighted in the field. In the eastern Pacific, enhanced EKE amplitudes can be found especially close to the Central American continent where the strong winds (Tehuano) through the Isthmus of Tehuantepec cause substantial variability in the ocean (ROMERO-CENTENO ET AL., 2003; WILLET ET AL., 2006; PALACIOS AND BOGRAD, 2005). In the Atlantic, the Azores Current and complex structures along the North Atlantic Current are visible, among several known local structures in the subpolar basin. The Indian Ocean shows the highest values of EKE, especially along 25° S. In the northern Indian Ocean, both the Arabian Sea and the Gulf of Bengal are characterized by substantial eddy variability (BIROL AND MORROW, 2003).

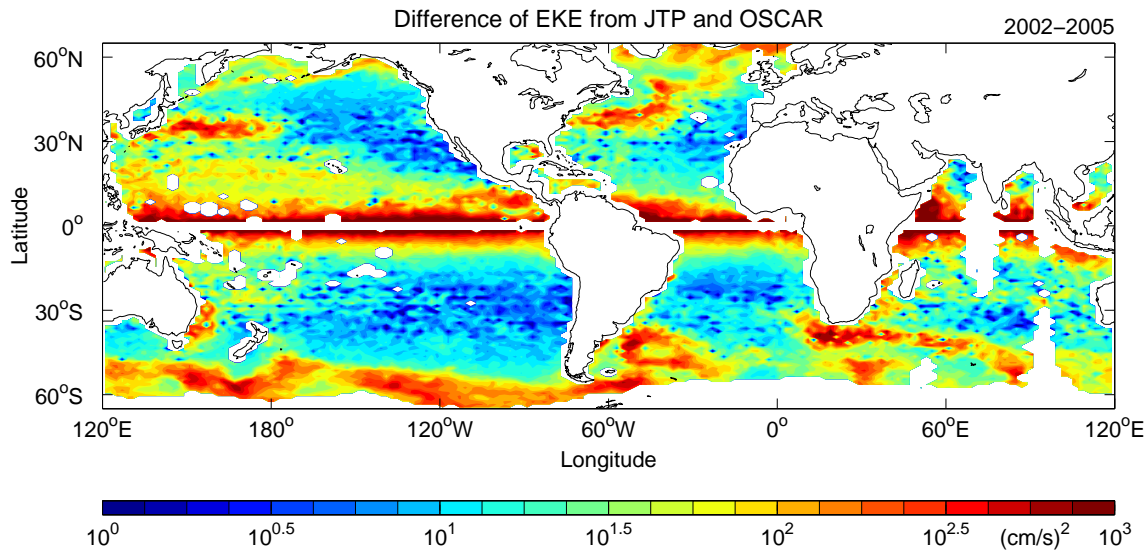


Figure 3.10.: Difference between JTP and OSCAR EKE fields in (**Fig. 3.9**). Scale is logarithmic.

Without the parallel track approach, the EKE was calculated before from the cross-track geostrophic velocity anomalies under the assumption of isotropy (see: WHITE AND HEYWOOD, 1995; STAMMER, 1997a; BRANDT ET AL., 2004; STAMMER ET AL., 2006). While comparing the JTP results with EKE_{CT} (cross-track) estimates from different satellites and various satellite configurations covering different time-periods, it can be found that results in the high energy regions are of the same order of magnitude. However, the EKE_{JTP} (eq. 3.2) results appear smaller in low energy regions due to the relatively large track separation and the associated filter effect. Within these spatial scales, regions of known anisotropic conditions can now be displayed with higher accuracy. Nevertheless, the overall structures are comparable.

For a further test of the eddy variability inferred from the JTP data, a comparison of the EKE field is shown in **Fig. 3.9** (top) with similar results obtained from the OSCAR data set (see Section 2.3 for a detailed description). The OSCAR data set available to us comprises geostrophic velocity anomalies ($u_O(t), v_O(t)$) available on a $1^\circ \times 1^\circ$ grid covering the period from October 21, 1992, to December 26, 2007, every 5 days (1094 fields). For a comparison with JTP results, an EKE field from the OSCAR data covering the JTP data period (211 OSCAR fields) was computed. The EKE field was calculated on the original OSCAR $1^\circ \times 1^\circ$ grid, and results were gridded subsequently on the same $2^\circ \times 1^\circ$ geographical grid on which JTP results are available (**Fig. 3.9**, bottom). Overall, results compare well with those obtained from the JTP tandem mission velocities. However, there are some significant differences which are highlighted in (**Fig. 3.10**). Most noticeably, JTP results are generally higher in amplitude than OSCAR-based estimates due to filtering. This is most obvious along major current systems, like the Kuroshio, the North Atlantic Current or the ACC, where the tandem results are higher by 100 - 500 cm^2s^{-2} . Even higher differences (up to 1000 cm^2s^{-2}) can be found in the tropics. Equally important, JTP results lead to much higher EKE in high latitudes. Most likely, this is due to the fact that the JTP results contain barotropic motions of the flow-field which are filtered out in the OSCAR product by the temporal smoothing of the data; the same holds for the AVISO product (DUCET ET AL.,

2000). STAMMER ET AL. (2000) analyzed the high-frequency barotropic variability and its contribution to SSH. Their results already showed a significant contribution of barotropic processes to high-latitude ocean variability. Differences between JTP and OSCAR are smallest in the low-energy regions of the eastern subtropical basins. However, spurious banded structures occur in the difference fields which seem to emerge from the OSCAR data set. It is important to recall that the JTP results are a lower bound of the estimate of EKE which implies that the OSCAR analysis as well as others based on an objective analysis lead to a significant underestimation of the eddy flow-field.

3.7. Ratio EKE/MKE

Another long-lasting question is that of the ratio between EKE and Mean Kinetic Energy (MKE) with

$$MKE = \frac{1}{2} (\bar{u}^2 + \bar{v}^2), \quad (3.3)$$

where \bar{u} and \bar{v} are the time-mean velocity components. In the past, the EKE and MKE fields were shown by WYRTKI ET AL. (1976) and EMERY (1983) and the ratio between EKE and MKE was estimated before by QIU ET AL. (1991) for the Kuroshio extension. Here, the JTP results were used together with a MKE computed from the RIO AND HERNANDEZ (2004) Mean Dynamic Topography (MDTP) field to recompute the ratio between EKE and MKE. As shown in **Fig. 3.11** (top), high values of MKE can be found all along the Kuroshio (compare: QIU ET AL., 1991) and the GS axes, along the East Greenland Current and in the Labrador Sea Rim Current, the Azores Current and in the tropical oceans. Along the ACC, the MKE is enhanced only at a few locations and along several frontal structures.

The ratio between EKE and MKE is shown in **Fig. 3.11**, bottom. Regions of reduced EKE/MKE ratio are aligned along regions of enhanced MKE, where the ratio is typically of the order of 10. In the northern hemisphere, regions of high values of EKE/MKE are covering the western subtropical Pacific, the western subtropical Atlantic to the eastern side north of the Azores Current, the eddy high way in the South Atlantic from the Agulhas region to South America and across the subtropical South Pacific, and the entire southern Indian Ocean. In most of those areas a ratio of 10^2 - 10^3 can be found. QIU ET AL. (1991) found a EKE/MKE ratio in the Kuroshio extension of 1.5-2.0 using Geodetic Satellite (Geosat) altimeter data. The JTP results suggest a ratio of 10-15 in the Kuroshio extension between 140° and 150° E. However, values increase poleward and equatorward, where factors of 10^2 - 10^3 are common. On global average, a ratio of about 6.5 of EKE/MKE is obtained. However, the RIO AND HERNANDEZ (2004) MDTP is a smooth field due to the analysis procedure. Accordingly, the MKE shown here has to be considered a lower bound of the MKE of the ocean circulation. New fields of the mean dynamic SSH and of the MKE will be available soon after the launch of the European satellite GOCE (Gravity-field and steady-state Ocean Circulation Explorer). It will be important to recompute the MKE field then, based on GOCE results, and to revisit the question of the ratio between EKE and MKE. On the other hand, the EKE field estimated here from the parallel tracks is a lower bound as well (compare: SCHLAX AND CHELTON, 2003) and the exact ratio has to be computed from future data expected from the wide-swath altimeter mission of very-high resolution numerical simulations.

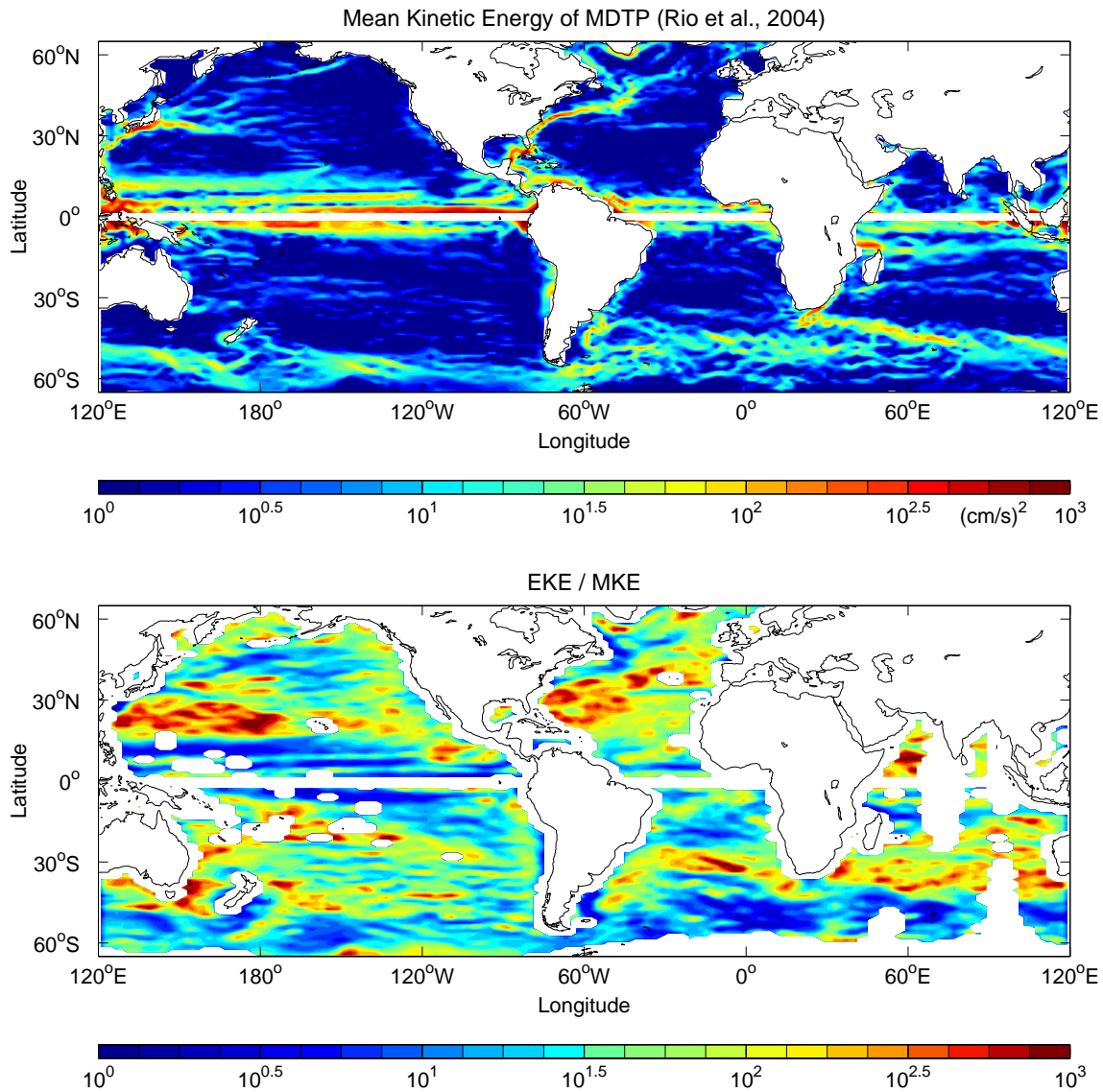


Figure 3.11.: (Top) Mean Kinetic Energy (MKE) computed from the RIO AND HERNANDEZ (2004) Mean Dynamic Topography (MDTP) for each $2^\circ \times 1^\circ$ grid cell. (Bottom) Ratio of EKE from JTP (**Fig. 3.9**, top) and MKE, filtered with a $6^\circ \times 4^\circ$ running mean.

3.8. Summary

This chapter deals with basic statistical descriptions of the SSH and of the velocity fields. It gives an overview of the general variability and its spatial variation within the JTP geostrophic velocity data set.

As an effort of the JTP tandem configuration, a doubled resolution of the SSH measurements is gained, that leads to a more detailed description of the STD distribution. Thereby the meridional resolution is improved by a factor of two. However, due to the short duration of the time series, not all ocean phenomena (e.g. ENSO events) are captured. The tandem mission therefore shows the short term variability due to ocean eddies and the seasonal cycle

of the flow-field. Next to the expected high variability within the big current systems as the western boundary currents, the Agulhas Retroflexion, and the Brazil Malvinas Confluence, a generally higher variability in the whole Indian Ocean is detected.

When the STD of SSH and of geostrophic velocities are compared at the equator, larger STDs appear for the geostrophic velocity estimates. Moreover, the stronger zonal equatorial currents lead to a stronger zonal STD at the equator. The most pronounced variances among the big current systems are found in the Agulhas Retroflexion region.

The JTP tandem mission was the first satellite observing system that could clarify the shape of oceanic geostrophic velocity PDFs without the assumption of isotropy. The global PDF has a clear exponential shape as a consequence of the significant variance of EKE or PDF-width over the global ocean. Hence small regions can have Gaussian shapes but averaged over larger regions with varying PDF-width or varying EKE the shape would get more exponential. The shape of the JTP PDFs indicates that large coherent eddies did not play an important role for the observed distributions. A comparison with PDFs from in situ data (TAO array) yield the same order of magnitude of 0.02 for the PDF-width, though after normalizing the PDFs with the STD of the geostrophic velocity estimates all PDFs have Gaussian shapes. Therefore, the normalized global PDF is Gaussian as well.

The isotropy field resulting from the JTP tandem mission is still noisy due to a time series of only three years. A slight enhancement of the meridional variability is found in mid latitudes, outside the tropical region and the high latitudes. The mostly zonal current field dominates the variability there. The OSCAR velocities show a substantially lower meridional than zonal variability. The results from the JTP tandem mission confirm the earlier conclusions that the variability of the meridional OSCAR currents seem to be poorly estimated.

The 3-year mean EKE field clearly displays all major current systems. Furthermore, in the Pacific, a general enhancement of the EKE field is found west of the Hawaiian Islands, all along the western U. S. coast and from there along the North Pacific Current towards the Kuroshio. In the eastern equatorial Pacific, strong winds (Tehuano) through the Isthmus of Tehuantepec cause substantial variability and hence EKE. In the Atlantic, the Azores Current and complex structures along the North Atlantic Current are visible. The Indian Ocean shows the highest values of EKE, especially in the equatorial and GW region. In the northern Indian Ocean, the Arabian Sea and the Gulf of Bengal are characterized by substantial EKE, whereas in the southern Indian Ocean high values of EKE are found all along 25° S. Finally, pronounced details of EKE can be noted along the entire ACC including the Agulhas region.

The JTP EKE amplitudes are generally higher than the OSCAR-based estimates due to the temporal smoothing of the OSCAR data. Differences of up to 500 and 1000 cm^2s^{-2} are found along the major current systems and in the tropics, respectively.

EKE from the tandem mission is compared to EKE estimates that assumed isotropy. The comparison shows that the overall structures were comparable and of the same order of magnitude in high energy regions but are smaller in low energy regions due to the relatively large track separation of the JTP tandem mission and the associated filter effect. However, within these spatial scales the regions of known anisotropic conditions are displayed with higher accuracy.

It is important to note that the JTP results are a lower bound of the EKE estimate which implies that the OSCAR analysis as well as others based on an objective analysis lead to a significant underestimation of the eddy flow-field.

The ratio of EKE to MKE is recomputed. Reduced ratios are aligned along regions of enhanced MKE where the ratio is typically in the order of 10, whereas regions of high EKE

to MKE have ratios of $10^2 - 10^3$ and are located in the western subtropical North Pacific, in the western subtropical North Atlantic and reaching from there to the eastern side north of the Azores Current, within the eddy high way in the South Atlantic (from the Agulhas region towards South America), across the subtropical South Pacific and the entire southern Indian Ocean. A global averaged ratio of about 6.5 is obtained.

However, it is necessary to note that the MDTP is a smooth field due to the analysis procedure and therefore the MKE has to be considered a lower bound of MKE of the ocean circulation. New fields of mean dynamic SSH have to be calculated from the European satellite GOCE. With a more accurate MDTP, the ratio of EKE/MKE can then be recomputed. Additionally, the EKE calculated from the JTP tandem mission parallel track method is a lower bound as well, due to its wide track spacing and the unresolved small scaled eddies. A more complete estimate can be computed from future data expected from the wide-swath Surface Water Ocean Topography (SWOT) satellite mission (FU AND RODRIGUEZ, 2004; FU AND FERRARI, 2008) and the use of very-high resolution numerical simulations.

Hence the global geostrophic velocity anomaly estimates computed from the JTP tandem mission improve and sustain, within their spatial and temporal limitations, the picture of the variability of the geostrophic velocity and EKE field, because it has been the first satellite observing system to retrieve both geostrophic velocity components instantaneously and without assuming isotropy.

4. The Seasonal Cycle

4.1. Introduction

A central topic investigated in this study concerns the variations of the large-scale flow-field on the annual time scale. The annual signal is one of the major signals in the world ocean. Therefore, it is useful to determine its amplitudes and phases to describe the variations that can be explained by the annual cycle alone. There exist a vast amount of studies that concentrate on the annual cycle. However, those studies cover almost exclusively regional scales. With the JTP tandem mission it is now possible to calculate the seasonal cycle of the geostrophic velocity field and of the EKE field from a set of 109 gridded maps covering almost three years of data. It may be questionable to calculate an annual signal from only three years of data, however, the JTP results already yield very robust results compared with the 15 year long OSCAR time series. Interesting patterns occur on the seasonal cycle that demonstrate for example the importance of the seasonal cycle in the equatorial regions of the world ocean. Striking phase patterns occur that indicate the Rossby wave propagation in the tropical regions as previously shown by the use of sea level anomalies by CHELTON AND SCHLAX (1996).

In Section 4.2.1, the seasonal changes of the geostrophic flow-field derived from the JTP tandem mission are described and related to those obtained from the 15 year long OSCAR time series. As zonal jets emerge on the annual cycle of the JTP data, Section 4.2.2 deals with these zonal structures. A test against in situ Acoustic Doppler Current Profiler (ADCP) data is provided in Section 4.2.3. The ADCP data is measured from the MV Oleander along a ship track repeated on a regular basis between Bermuda and the U.S. main land. The seasonal signal of the EKE is then discussed in Section 4.3.

4.2. Seasonal Changes of the Flow-Field

4.2.1. Seasonal Harmonic Analysis

To investigate the annual cycle in the JTP flow-field, first the along-track velocity components were averaged in $2^\circ \times 1^\circ$ geographic boxes to reduce noise effects. Subsequently, an annual harmonic was least-squares fitted independently to each velocity component (see appendix A.2 for a detailed description of the harmonic analysis). The resulting amplitudes of a geographically varying seasonal cycle in the zonal (u) and meridional (v) components of the flow-field, shown in **Fig. 4.1**, indicate enhanced amplitudes of annual changes of the flow-field along the major current systems. Especially high amplitudes can be found in the u -component all along the low latitude currents which reverse on the seasonal cycle. In the Arabian Sea the Great Whirl (GW) stands out (SCHOTT AND MCCREARY JR., 2001). A similar structure appears in the Gulf of Bengal associated with the Sri Lanka Dome (SLD; VINAYACHANDRAN AND YAMAGATA, 1998; VINAYACHANDRAN ET AL., 1999). Amplitudes of the annual cycle in the u -component reach values larger than 10 cm/s in the

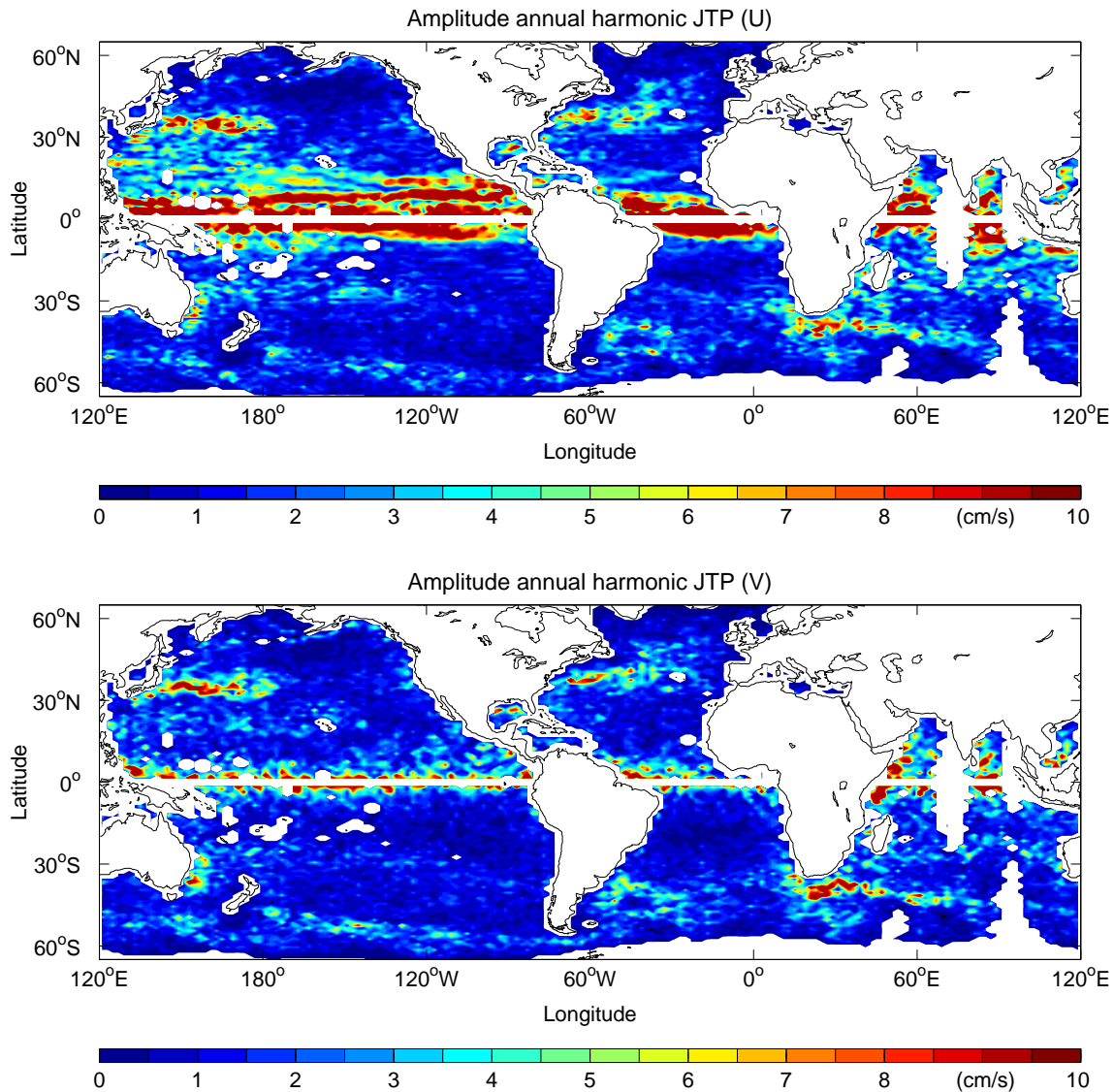


Figure 4.1.: JTP amplitudes of the annual signal for the u (top) and v (bottom) geostrophic velocity anomaly components, calculated for the mean of each $2^\circ \times 1^\circ$ grid cell.

equatorial Pacific, the Kuroshio, and Agulhas Current. Similar amplitudes can be found for the v -component in the Kuroshio and Agulhas Current.

Phases of the annual harmonics of u - and v -components, shown in **Fig. 4.2**, reveal zonally coherent changes of the flow-field in zonal direction associated with seasonal reversals of the flow-field there. Poleward of 10° latitude, the phase lines of the seasonal changes of the u -component start to tilt in a way one would expect from annual Rossby waves crossing the ocean from east to west. Respective results are visible in all ocean basins. Further poleward, tilting phase lines are still visible, but phase structures are getting increasingly more complex. In particular, superimposed to phase lines tilting from north east to south west in the northern hemisphere (as they would be expected from Rossby waves) phase lines appear that tilt the opposite way, especially in the southern hemisphere. The extent to which they represent real physical phenomena is unknown at this point. However, preliminary

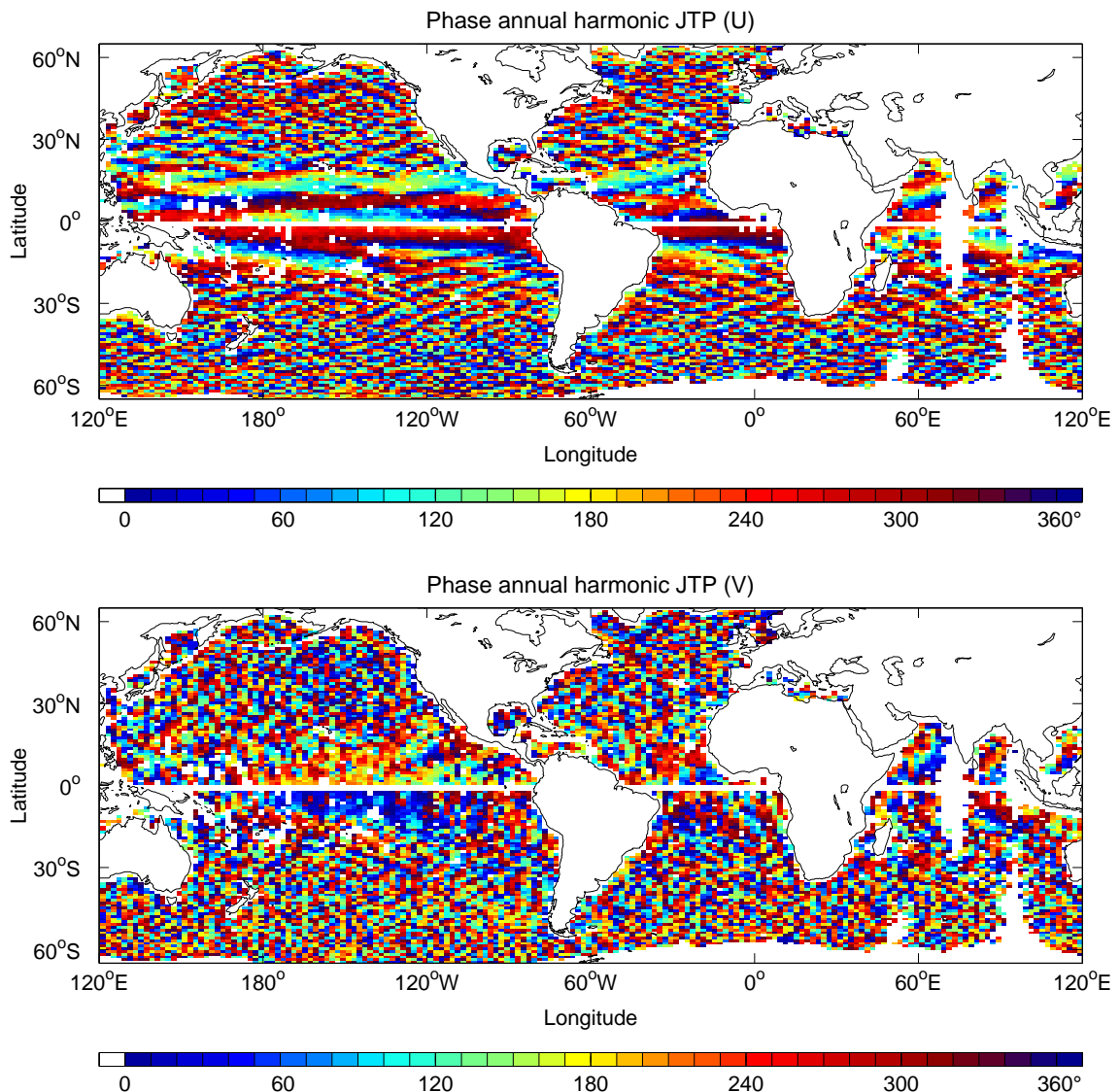


Figure 4.2.: JTP phases of the annual signal for the u (top) and v (bottom) geostrophic velocity anomaly components calculated for the mean of each $2^\circ \times 1^\circ$ grid cell. Zero degrees of the phases corresponds to January 1st.

studies reveal that they are present also in longer model simulations as can be seen in **Fig. 4.3** (top) for the 15-year long OSCAR time series. The appearance there suggests that they are not just an artifact of noise in a relatively short time series. A detailed analysis of underlying physical processes has to be subject of a future study.

In terms of the v -component, changes in the phases of the annual cycle again suggest zonally coherent changes of the flow-field along slanted lines. In contrast with the zonal flow component, changes of the meridional flow-field on the seasonal time scale appear on a larger meridional wave number, causing a large fraction of the eastern tropical Pacific to change its meridional flow. The same holds for the Indian Ocean on both sides of the equator, but is not as clear in the Atlantic. In contrast with the phase of the zonal flow component, the phase of the v -component shows mostly scatter in mid- and high latitudes,

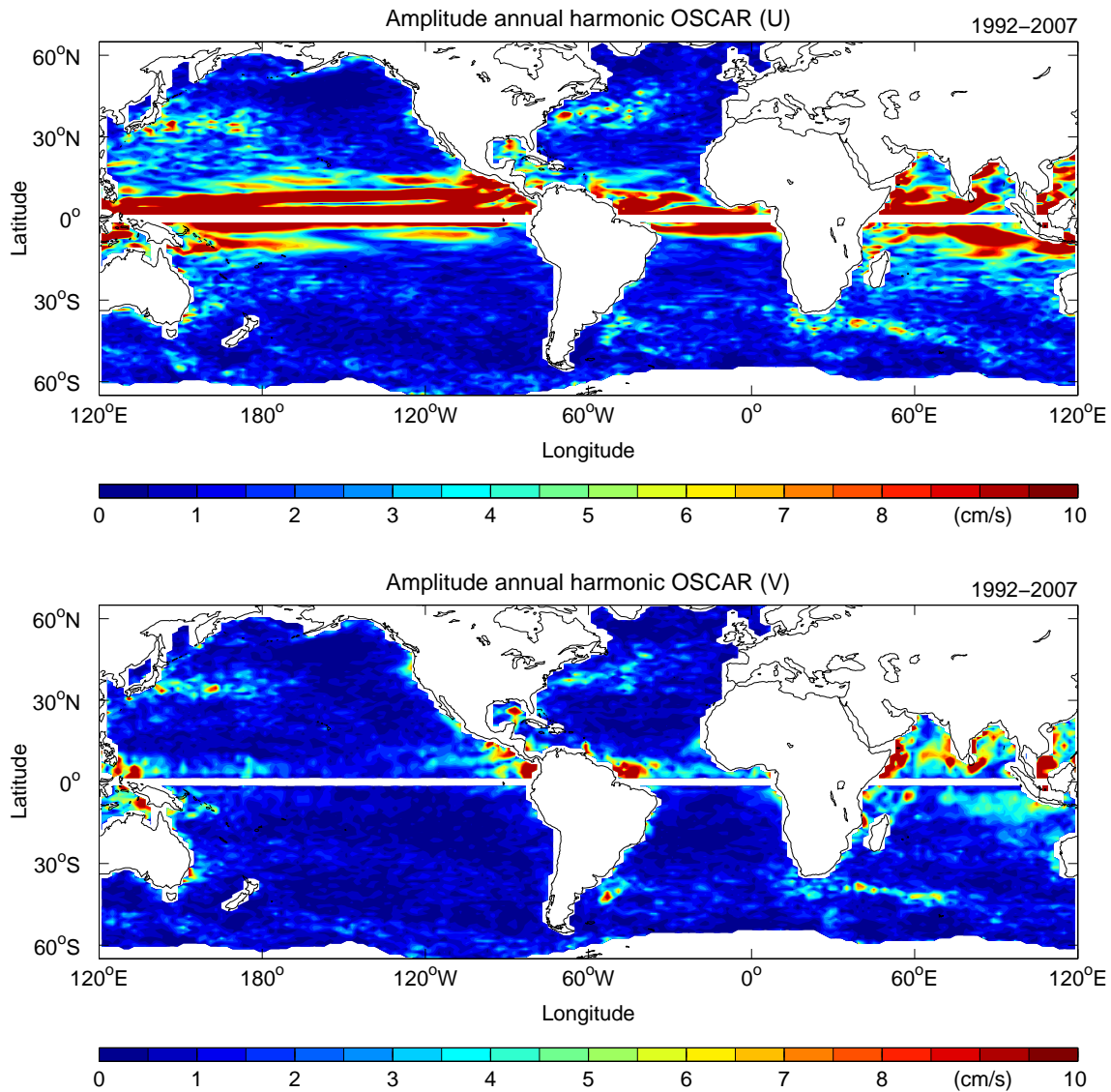


Figure 4.3.: Amplitudes of the annual signal for the u (top) and v (bottom) geostrophic velocity anomaly components from OSCAR (15 years) calculated for the mean of each $2^\circ \times 1^\circ$ grid cell.

and it is not really possible to determine any spatial structures there as in a purely random eddy field. However, in principle this could be due to the short time series analyzed here and the still dominating eddy noise.

To identify the impact of the shortness of the time series on the estimate of the annual harmonic the annual changes of the flow-field were estimated by using the 15-year long OSCAR data set. Resulting amplitudes in the zonal and meridional components are largely consistent with those estimated from the JTP data (**Fig. 4.3**). However, amplitudes in the low latitudes are larger, reaching 30 cm/s in many places. Largest differences can be seen in the Indian Ocean where the JTP sampling is weakest (compare **Fig. 2.5**).

In both analyses, large amplitude changes of the zonal flow-field in the Indian Ocean are

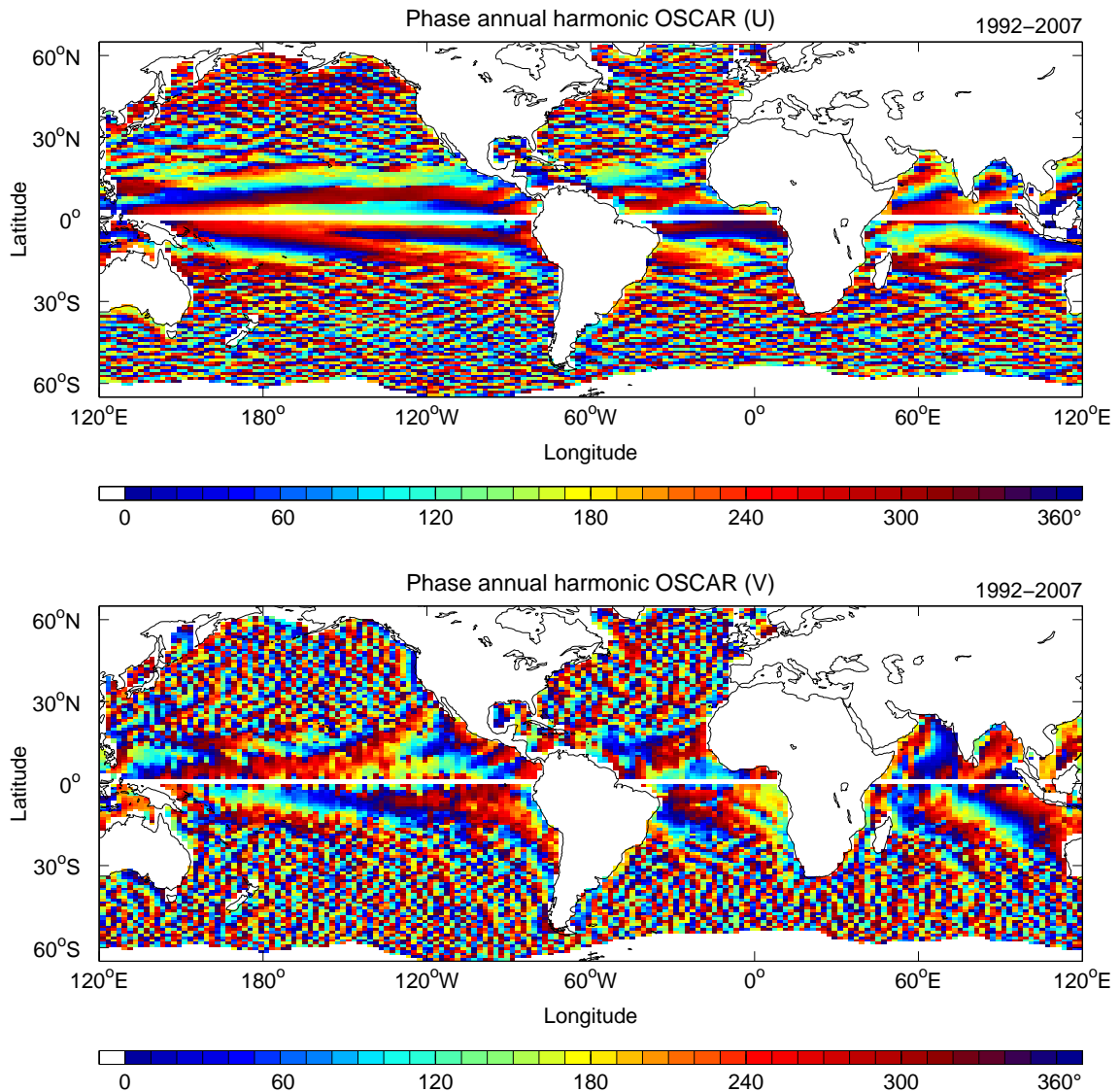


Figure 4.4.: Phases of the annual signal of the u (top) and v (bottom) geostrophic velocity anomaly components from OSCAR (15 years) calculated for the mean of each $2^\circ \times 1^\circ$ grid cell. Zero degrees of the phases corresponds to January 1st.

associated with the South Equatorial Counter Current (SECC), besides the South Java Current. It stretches from about 5° S in the western part of the basin to 15° S in the eastern part of the Indian Ocean. Moreover, the GW in the Arabian Sea and the SLD in the Gulf of Bengal are visible as enhanced seasonal changes of the meridional flow component. In the equatorial Atlantic, large seasonal variations in amplitude occur in the northern branch of the South Equatorial Current (nSEC) and the underlying North Equatorial Undercurrent (NEUC). The North Equatorial Counter Current (NECC) and the nSEC show the largest seasonal variations in the North Pacific.

Enhanced meridional flow variations on the annual period are found in the tropical Indian Ocean and for the tropical Atlantic north of the equator. Further enhanced seasonal changes of the v -component are associated with the North Brazil Current rings in the Atlantic and in the eastern Pacific with the Costa Rica Dome (CRD), the Tehuantepec Bowl (TB) and the

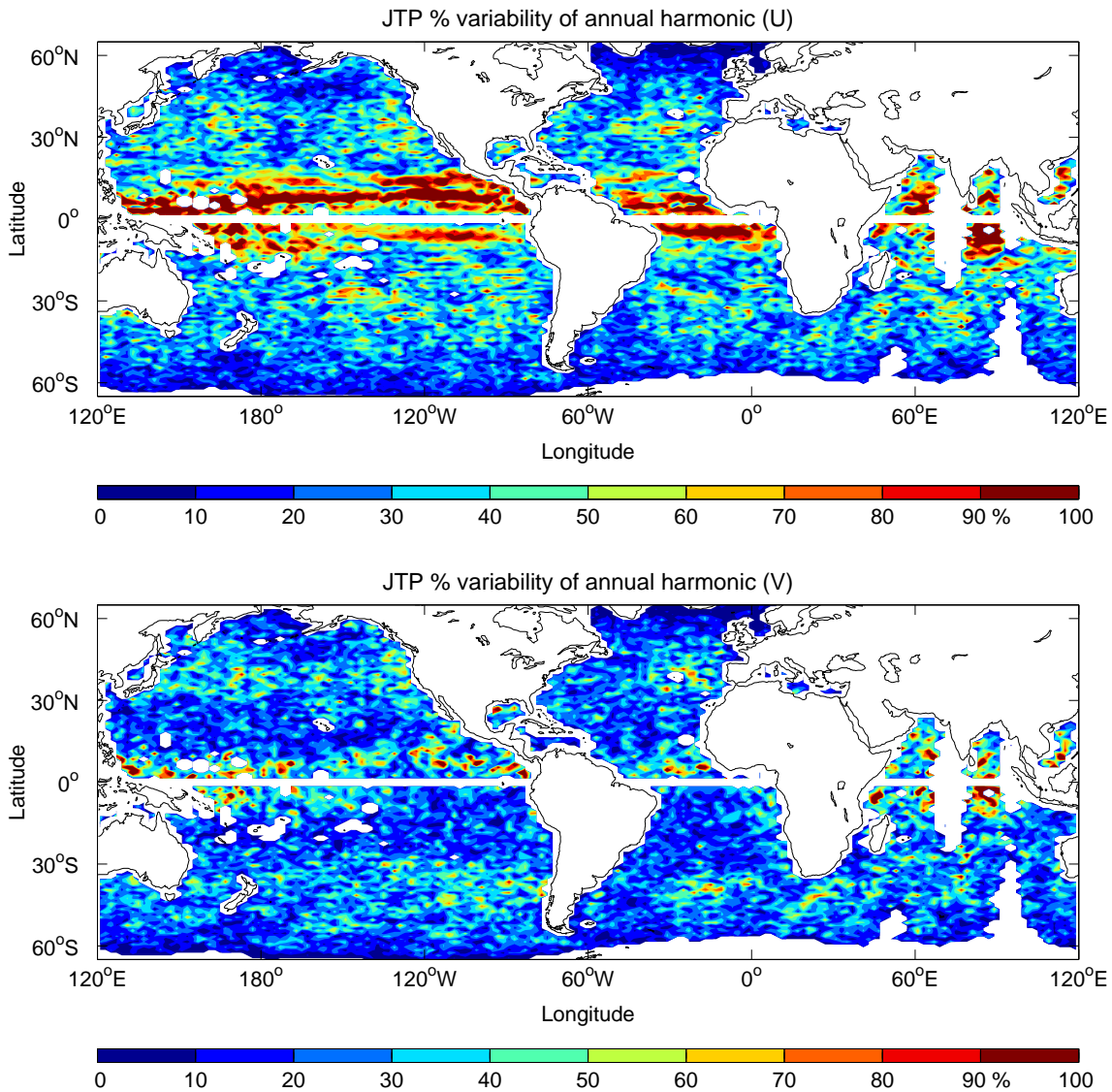


Figure 4.5.: Percentages of the annual amplitude at the standard deviation of the flow-field, calculated for each $2^\circ \times 1^\circ$ grid cell, for the zonal (top) and meridional (bottom) geostrophic velocity components.

upwelling region of the Equatorial Undercurrent (EUC) that is feeding the South Equatorial Current (SEC). In the western Pacific, the Halmahera Eddy north of New Guinea shows an enhanced signal. In general, the meridional component of the annual OSCAR amplitude is smaller than the meridional amplitudes of JTP, which is most obvious in the ACC region, the GS and the Kuroshio.

Turning to the annual phase maps of the u and v flow components in **Fig. 4.4**, the OSCAR results confirm those results seen above based on JTP but show clearer spatial structures due to the underlying longer time series. This holds especially for the v -component, which now also suggests spatially coherent phase structures in mid latitudes of all ocean basins.

As the amplitudes of the seasonal cycle in the geostrophic velocities reflect to some extent the distribution of the EKE fields, it can be assumed that the fit of the annual harmonic is

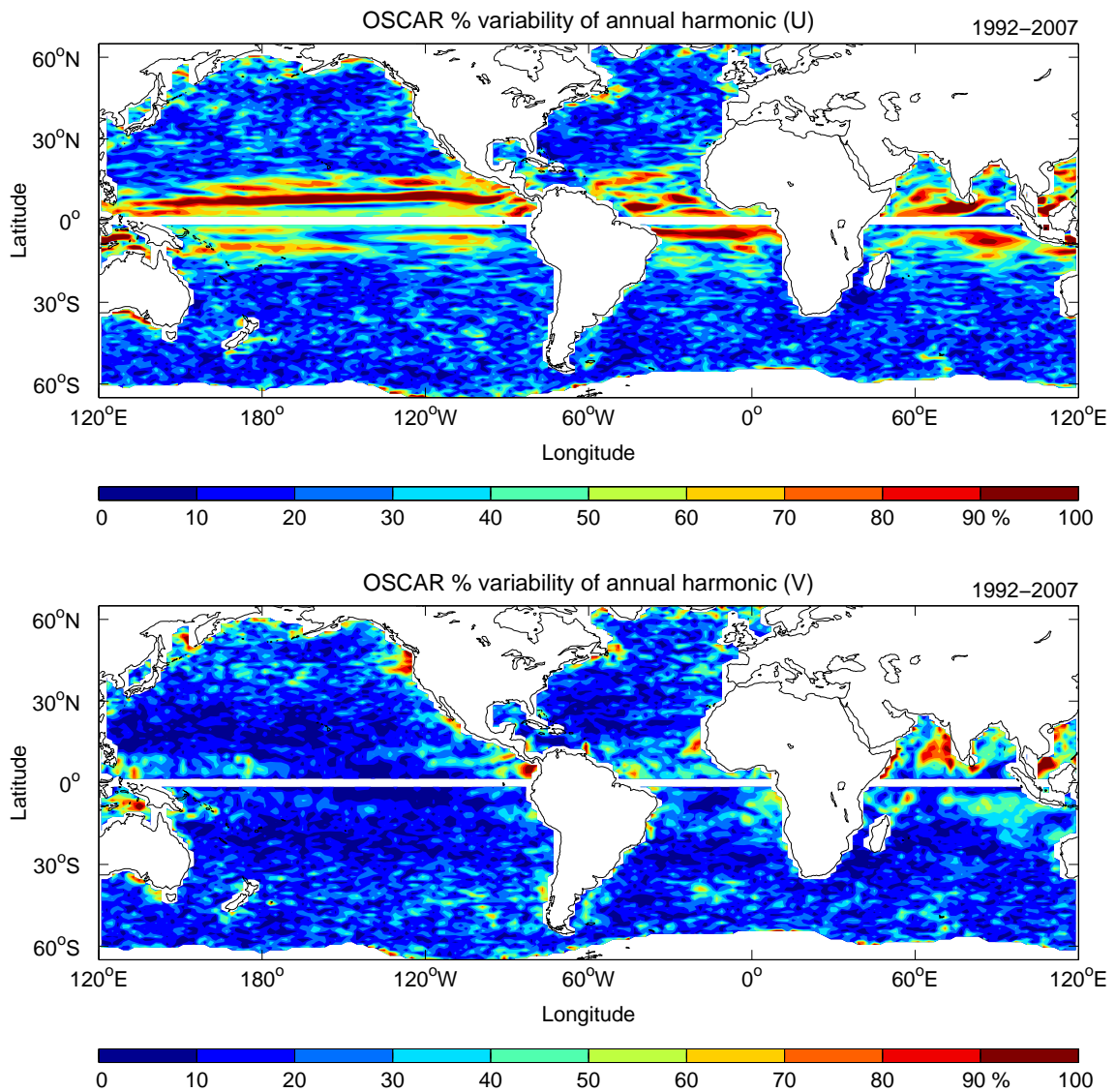


Figure 4.6.: Percentages held by the annual amplitude at the standard deviation of the OSCAR flow-field (15 years), calculated for each $2^\circ \times 1^\circ$ grid cell, for the zonal (top) and meridional (bottom) geostrophic velocity components.

just selecting the annual variability out of an otherwise broad spectrum; i.e., it cannot be assumed that the regions of enhanced amplitude of the seasonal cycle correspond to peaks in the spectral energy distribution on the annual period. To test the relative significance of the the annual harmonic of the flow-field, the percentages of total variability present on the seasonal cycle in the JTP and OSCAR data are show in **Fig. 4.5** and **Fig. 4.6**, respectively.

Clearly outstanding are the percentages of the u -component of the seasonally reversing currents in low latitudes, reaching maximum percentages in the Atlantic south of the equator. Low latitude percentages appear higher in the OSCAR results suggesting an underrepresentation of the general variability in that data set. Percentages of the annual u -component variability are also enhanced in the eastern basins of the mid latitudes in the JTP results.

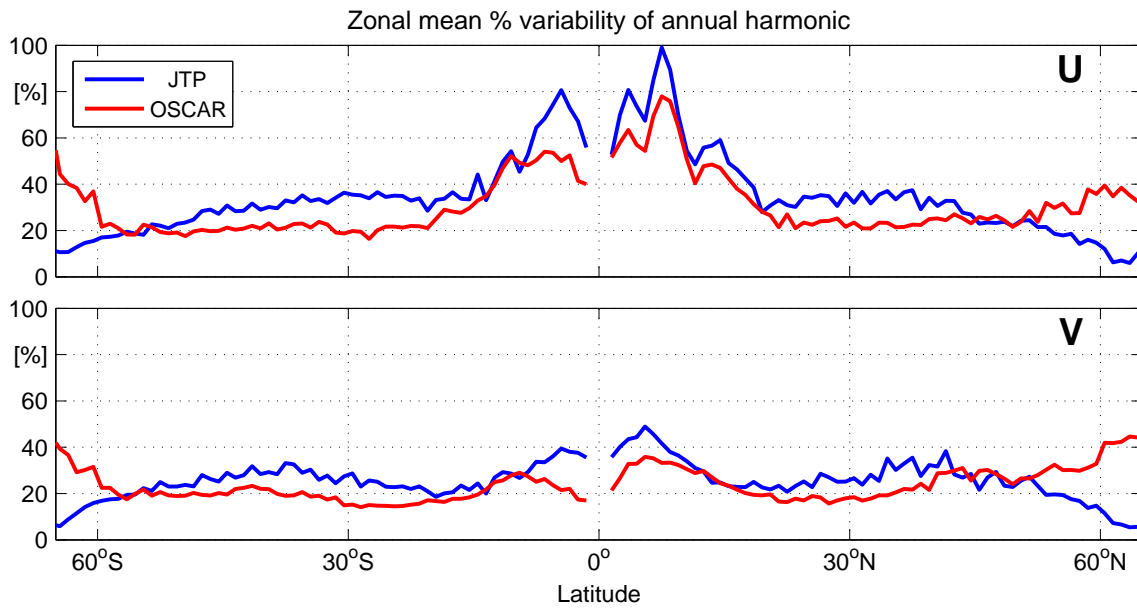


Figure 4.7.: Zonally averaged percentages held by the annual amplitude at the STD of the geostrophic JTP (blue) and OSCAR (red) velocities for the meridional (top) and zonal (bottom) component.

The same holds for the annual variability of the meridional flow-field which shows enhanced percentages primarily in mid latitudes. That appears even clearer in **Fig. 4.7** where zonal averages of the percentages at the total STD from both data sets are shown. The figure clearly illustrates the enhanced percentages of annual variability in both components in mid latitudes: Between 20° and 50° amplitudes for the zonal and between 30° and 50° amplitudes for the meridional components are $\sim 35\%$ for JTP and $\sim 20\%$ for OSCAR. A clear difference is evident in the maximum percentages of the zonal component at 30° N and of the meridional component at 40° N. A similar difference exists in the southern hemisphere but is shifted somewhat toward the equator. Poleward of 50° latitude the percentages in the JTP results decrease substantially while in the OSCAR results they increase to 40% . Differences between both data sets are again due to the lack of the high-frequency barotropic variability in the OSCAR results close to the equator where special assumptions went into the OSCAR analysis (JOHNSON ET AL., 2007).

Changes of the flow-field in mid latitudes on the annual period can be rationalized in terms of a changing Sverdrup circulation in response to a changing wind stress field. In previous studies, MESTAS-NUÑEZ ET AL. (1991) and STAMMER (1997b) have investigated the seasonal cycle of the Sverdrup circulation in the Pacific and have shown that large-scale changes in SSH to some extent can be explained through a time-varying Sverdrup relation. It appears that here again the effect of the changing gyre circulation can be seen but now directly in the flow-field. It suggests that the basin wide gyre circulation is varying in response to a changing wind forcing on the annual cycle. However, this seems to show more clearly in the large-scale circulation than in the boundary currents where the eddy variability dominates the general variability.

KESSLER (2006) investigated the annual cycle of the geostrophic circulation of the eastern tropical Pacific. The conclusions drawn by the authors are consistent with findings from

the JTP analysis. In particular, in both studies a maximum eastward velocity of the NECC is found in November when it feeds the North Equatorial Current (NEC) moving to the west. The eastern EUC shoaling occurs when local easterly winds are weakest as part of a basin wide phenomenon that begins in the far east in March and reaches the dateline in August due to the westward-propagating annual cycle of zonal wind along the equator. The nSEC is strongest in the second half of the year in both estimates. The weakest SEC can be found just south of the equator caused by southerly cross-equatorial winds causing enhanced upwelling in that region. The maximum of the Peruvian coastal upwelling occurs in August-September with maximum south-westerly winds in June. The north-eastward annual maximum of the geostrophic JTP velocities occurs in April-May at the time when the upwelling starts.

4.2.2. Seasonal Zonal Jets

In the previous section, pronounced zonal structures could be seen in the annual harmonic flow-field both in terms of amplitude and phase (**Figs. 4.1 - 4.4**). Now the geographic structures of the seasonally varying geostrophic flow-field will be analyzed in detail as they result from the JTP data set. To minimize the impact of local noise on the estimate and to thereby highlight the large-scale structures, the JTP results were averaged over 10° zonal bands. The resulting annual harmonic flow-field for September is shown in **Fig. 4.8** which reveals predominantly zonal structures, particularly in the low latitudes and in the western Pacific. As noted before, there are some gaps in the Indian Ocean due to the low JTP sampling there. But from what is shown, zonal bands of the seasonally varying flow-field are visible as well. In the North Pacific large amplitudes of the annual flow changes are present primarily in the western subtropical gyre west of the Hawaiian Islands. In contrast, changes of the flow-field on the annual cycle in the Atlantic cover the entire basin.

Based on earlier gridded T/P data, STAMMER AND WUNSCH (1994) have computed seasonal anomalies of the flow-field for March and September. **Fig. 4.8** can be compared with

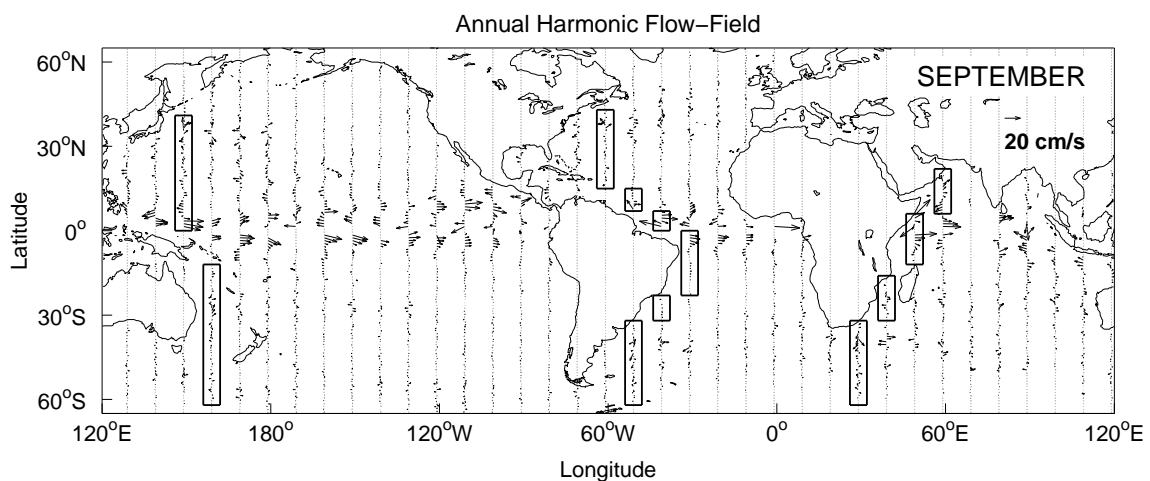


Figure 4.8.: Annual anomalies of the geostrophic velocity zonally averaged over 10° longitude for September. The annually varying geostrophic flow-fields are shown in **Fig.4.9** for the marked sections.

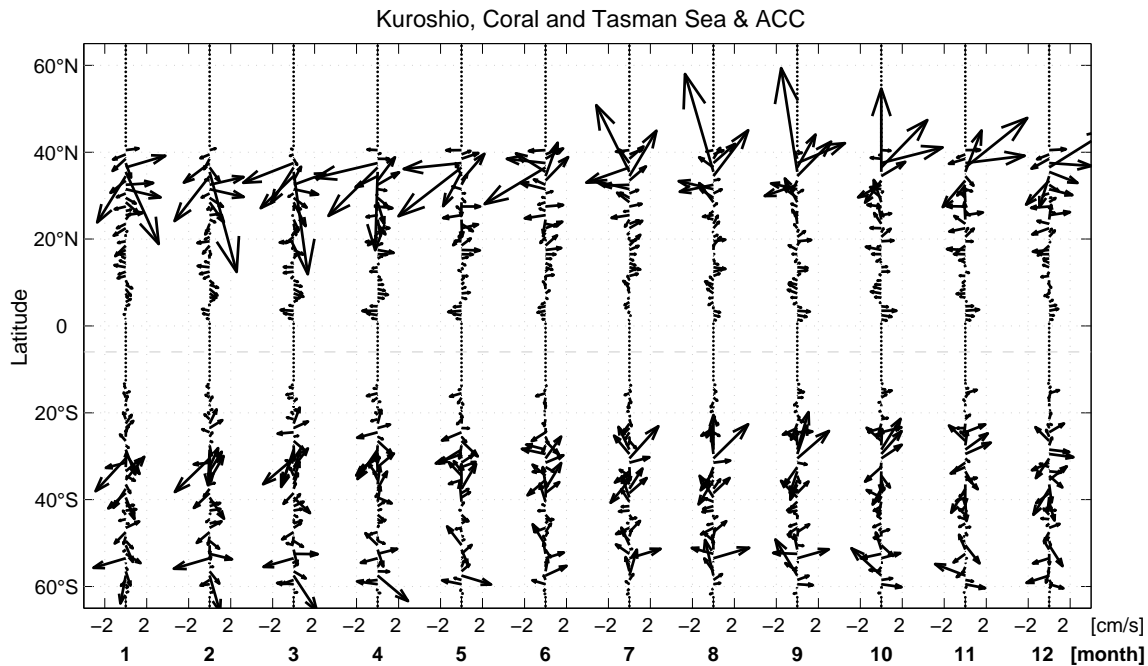


Figure 4.9.: Zonal averages over 10° longitude of the annually varying geostrophic flow-field from JTP for the western boundary current regions of the Pacific, Atlantic (next page top) and Indian Ocean (next page bottom) that are indicated in the black boxes of **Fig. 4.8**. The grey dashed lines indicate transitions between adjacent boxes.

their **Fig. 6 b**, at least in the Atlantic Ocean. In general terms, the figures agree. However, **Fig. 4.8** shows much more detail of the seasonal flow changes. In the tropical Atlantic, the annual cycle of the NECC is indicated, giving maximum eastward transport during autumn and minimum (essentially zero) eastward flow during spring. The NEC shows the opposite behavior. The changes of the GS and North Atlantic Current can also be compared with earlier altimetric studies by KELLY AND GILLE (1990) and ZLOTNICKI (1991). As an example, KELLY AND GILLE (1990) estimated the maximum surface velocity and the surface transport using Geosat data. Maximum surface velocities were typically between 1.2 and 2.0 cm/s and an analysis of the average annual signal in transport showed maximum values in the late fall and minimum transport in the late spring. While the phasing appears close to the findings from JTP, amplitudes revealed here are larger by a factor of three.

The seasonal changes of currents in the tropical Pacific were investigated by YU AND MCPHADEN (1999) from the Tropical Atmosphere Ocean array (TAO). They find maximum amplitudes in the eastern and central Pacific with more than 30 cm/s at 160° E- 110° W. Their phases at 5° S of the equator agree with the JTP results whereas at 5° N the phases for the eastern part are shifted by about 180° . JOHNSON ET AL. (2002) used hydrographic and ADCP data from 172 synoptic sections taken in the tropical Pacific to calculate seasonal transports. JTP reveals an only slightly different picture of the annual cycle. At 165° W the NECC peaks in December-January. The nSEC peaks in early November for JTP rather than in December as for the ADCP data. The sSEC has its maximum in February-April in both results at 165° W. However, the ADCP data reveals a weak seasonal cycle in the central Pacific with maximum values at 110° W in October-December whereas the JTP results show their maximum in March while having a rather strong annual signal. In the

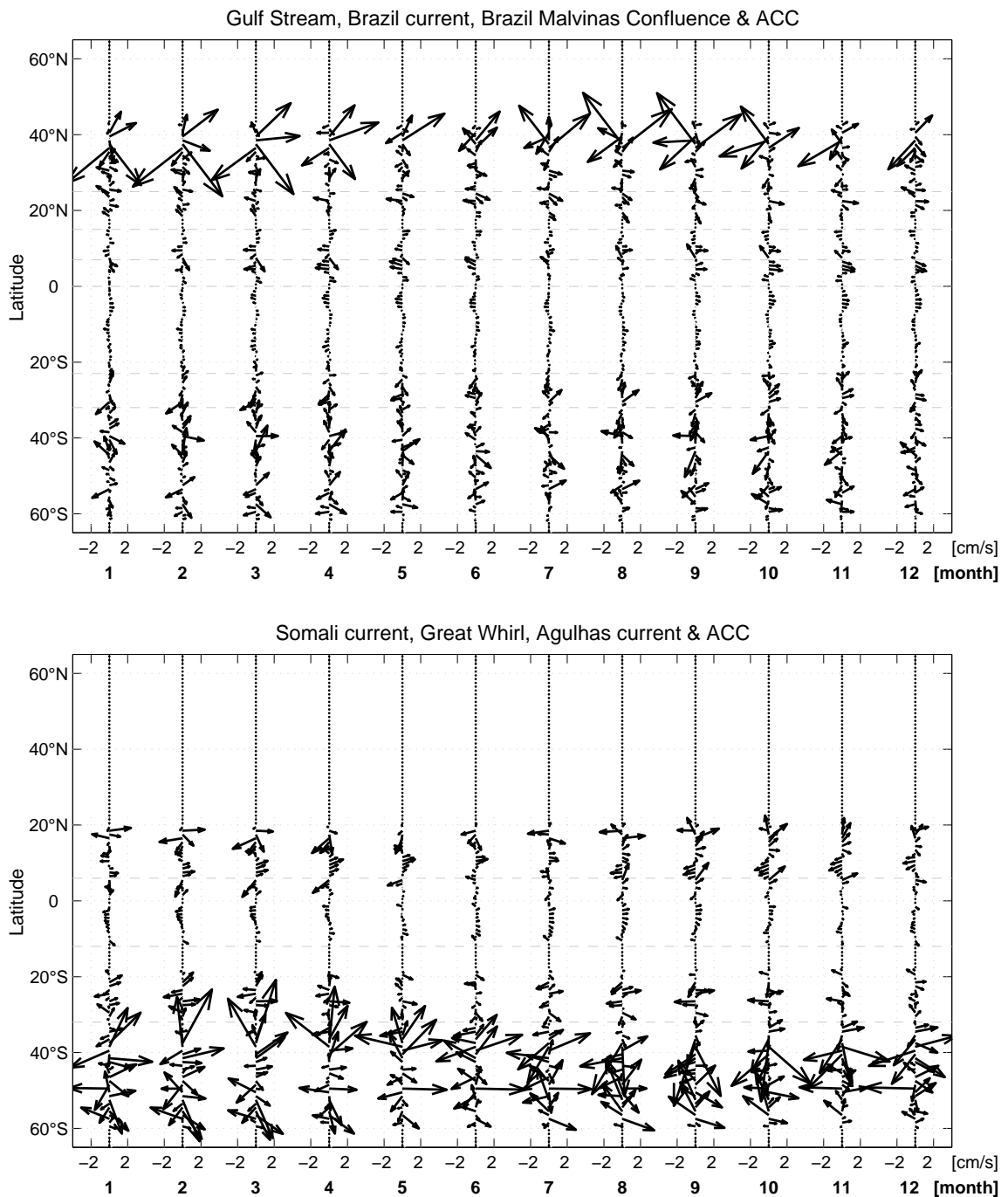


Figure 4.9.: Continued.

central Pacific at 155° W, the nSEC appears strongest in December and the NECC peaks in October consistent with the JTP results. At 110° W, the SEC with its maximum in October and the NECC peaking in August also agree in both results.

In the Kuroshio, QIU (1992) found seasonal transport variations with a maximum occurring in July and August which coincides with the annual maximum of the JTP velocity data. CHEN AND QIU (2004) show that the seasonal velocities of the SECC have their maximum

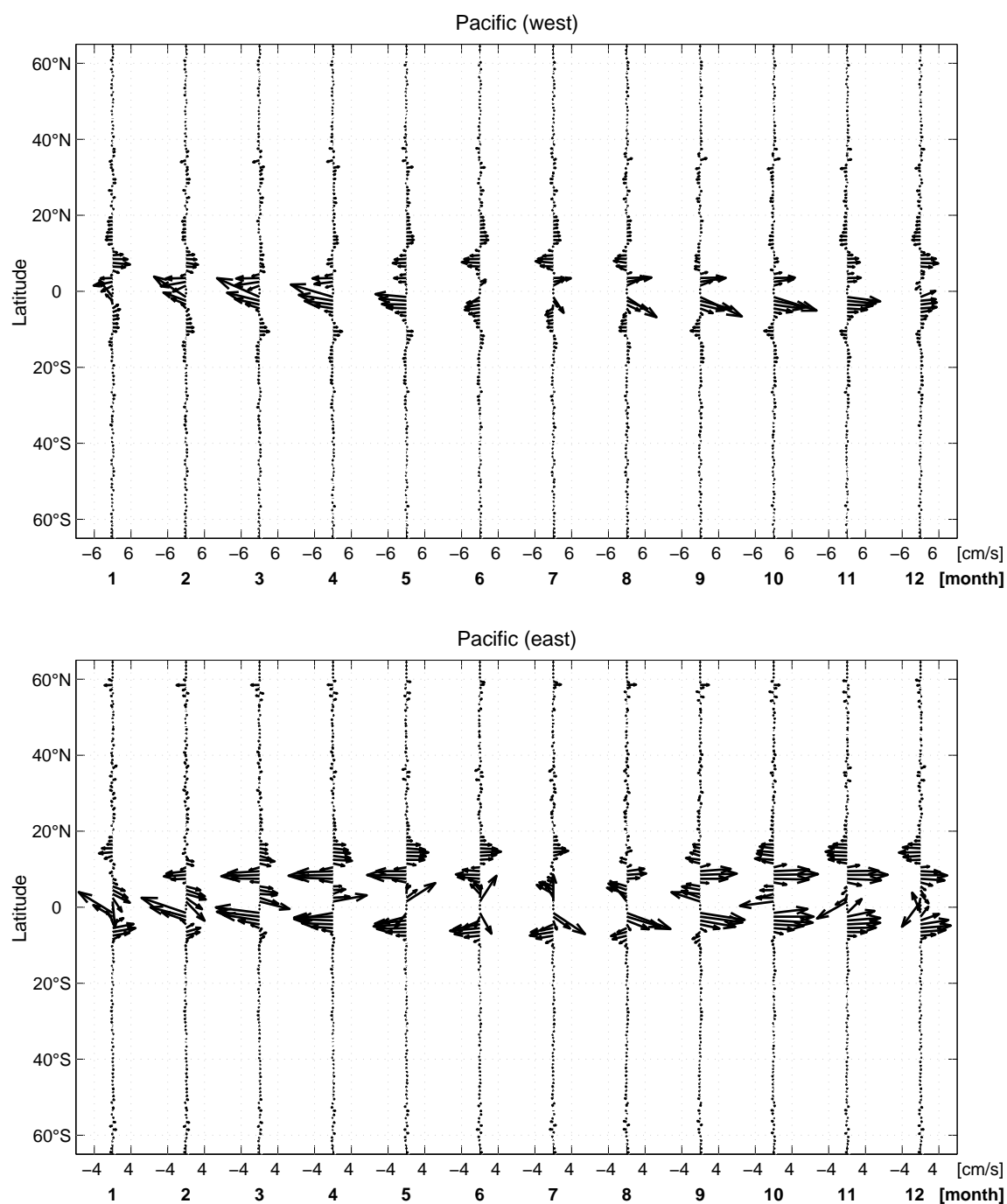


Figure 4.10.: Latitude-time sections of the annually varying zonal mean geostrophic flow-field anomalies, averaged over the western (120°W - 154°W) and the eastern (154°W - 66°W) parts of the Pacific; over the western (66°W - 30°W) and the eastern (30°W - 30°E) parts of the Atlantic (next page); and over the western (30°E - 72°E) and the eastern (72°E - 120°E) parts of the Indian Ocean (after next page). See **Fig. 2.1** for a map including the basin separation.

in March. That can be confirmed by the JTP results and is related to two types of forced Rossby waves north and south of 10°S .

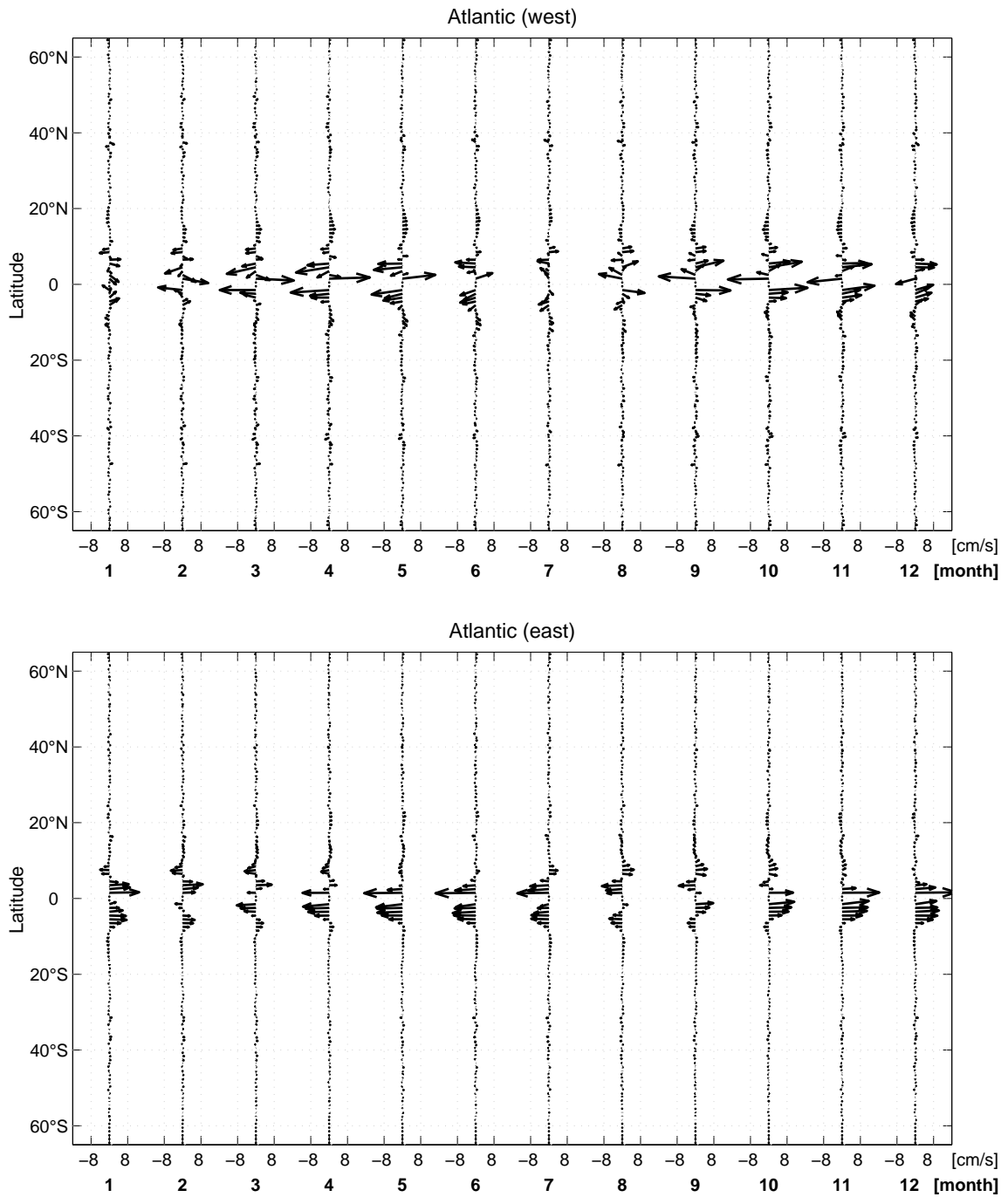


Figure 4.10.: Continued.

To highlight the current variations of the western basins, the latitude-time series along latitude slices marked in **Fig. 4.8** are shown in **Fig. 4.9**, but now as latitude-time plots from the western Pacific, the western Atlantic and the western Indian Ocean. All three sections were scaled by $\sin(\phi)$ (with ϕ being latitude) to visually enhance the flow variations in mid- and high latitudes relative to the otherwise dominating amplitudes in the lower latitudes. The GS appears to be modulated on the annual period. A similar picture emerges for the Kuroshio. Further equatorward, changes in the flow-field appear zonally banded with fairly

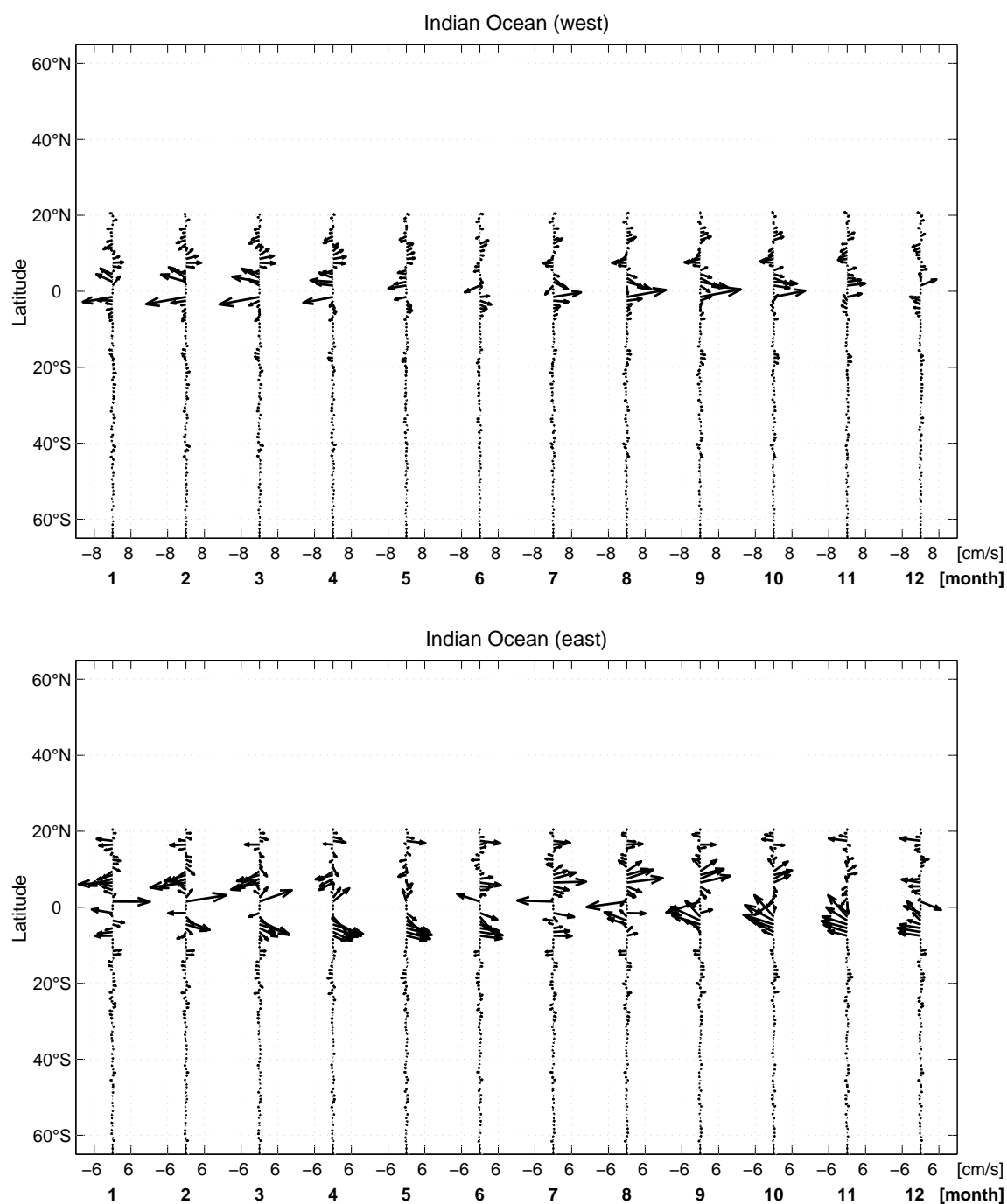


Figure 4.10.: Continued.

high meridional wavenumbers (in the order of $5^\circ - 10^\circ$). This holds especially in the western Pacific. Changes of the mid latitudes in the southern hemisphere appear more complex and show more meridional excursions, both possibly due to the topographic influence on the circulation. In the Indian Ocean, the flow changes north of 15° S are primarily related to the known changes of the Somali Current and the GW and associated changes in the zonal flow-field, e. g. the SECC. Further south, changes of the flow-field are dominated by the Agulhas or ACC systems. The same holds for the other basins, suggesting that some

regional changes of the ACC might be present but not necessarily on a large zonal scale.

Finally, **Fig. 4.10** shows latitude-time sections of the seasonal flow variations, but now averaged over the western and eastern parts of each ocean basin which are indicated in **Fig. 2.1**. Again a dominance of the seasonal flow changes in low latitudes is obvious, with smaller amplitudes of seasonal flow variations also visible in the western basin associated with changes of the gyre circulation. In general, seasonal flow changes along the ACC appear small. The tropical Atlantic has maximum counter currents in September - October on both sides of the equator. A flow in the opposite direction can be found around 3° N. The latter is missing in the eastern part of the basin, where the seasonal flow changes appear to reach across the equator. The maximum of the NECC occurs in September - October. A similar but weaker feature appears also south of the equator. While the seasonal flow changes in the Atlantic appear to be mostly zonal, this does not hold for the Pacific where a clear seasonal convergence/divergence on the equator can be observed. The seasonal flow changes are in phase between western and eastern Pacific, leading to enhanced downwelling on the equator in January - March and enhanced upwelling six months later. In addition, changes in the gyre circulation of the western Pacific with complex meridional (banded) structures are seen clearly. In the Indian Ocean, the annual reversal of the typical flow structures (compare SCHOTT AND MCCREARY JR., 2001, their **Figs. 8** and **9**) can be found with enhanced amplitudes dominating the entire northern Indian Ocean.

4.2.3. Comparison with ADCP data from MV Oleander

In the above results substantial regional variations can be seen in the annual changes of the flow-field, especially near the GS and other western boundary currents. This seems to hold both for the JTP and the longer OSCAR data sets. Are those regional aspects representing

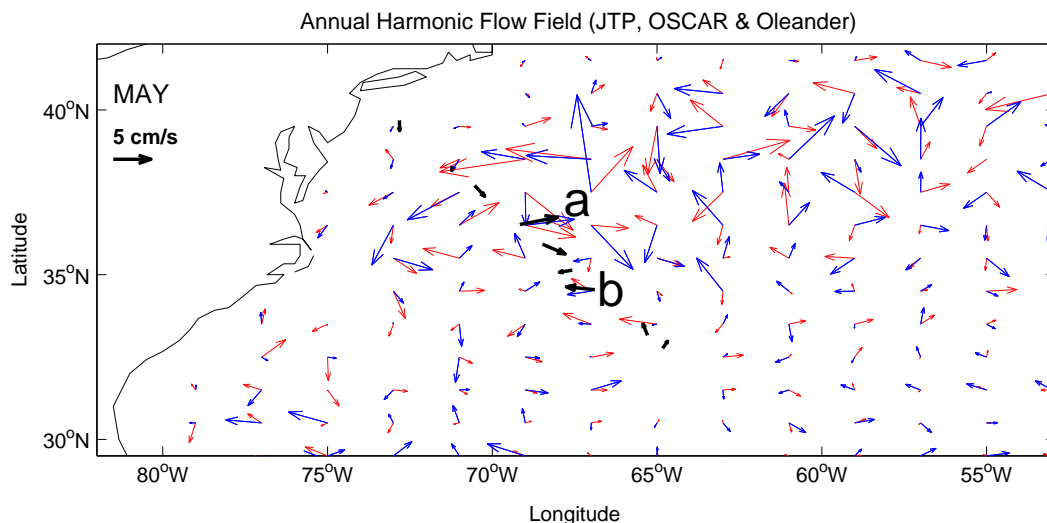


Figure 4.11.: Comparison of the annual flow-field from the geostrophic velocity anomalies for JTP (blue), OSCAR (15 years, red), and Oleander ADCP ship data (black) in the vicinity of the Gulf Stream region. Shown is a snapshot of the seasonal cycle from all three estimates. The ADCP data was chosen from a depth of 100 m which gives the closest fit to the JTP and Oleander data sets and is well out of the Ekman-layer to avoid the wind-driven variability.

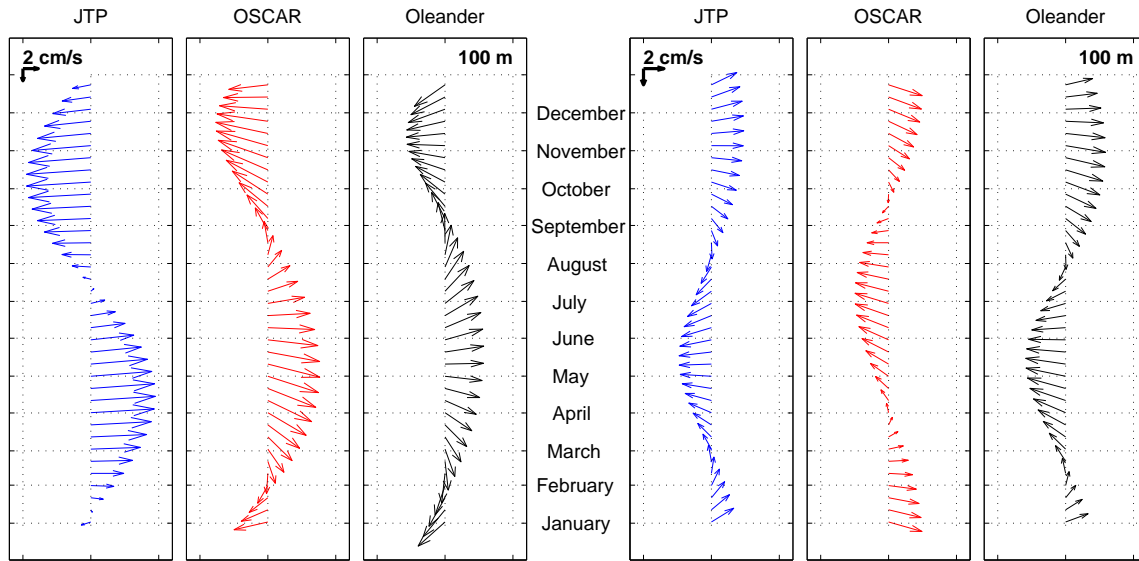


Figure 4.12.: A direct comparison between the three estimates is shown in the right panels for site [a] and left panels for site [b] that are marked in **Fig. 4.11**.

the ocean or are they rather an artifact of the data sets? To answer this question the extra information available from the MV Olenader ADCP data will be used (see Section 2.4 for a description of the data). Details of the Oleander ADCP program are provided by ROSSBY AND GOTTLIEB (1998) and ROSSBY AND ZHANG (2001). Oleander-ADCP data has until recently been available only from 1992 until August 2004, limiting the period of direct overlap with JTP data to the period from September 30, 2002, to August 14, 2004. Due to the short time series, the results of the annual harmonic obtained from three years of JTP data are compared with those obtained from two years of Oleander-ADCP data both starting September 2002.

For a direct comparison of the annual harmonic flow-field in all three data sets, **Fig. 4.11** shows their seasonal geostrophic velocity anomalies for May in the vicinity of the GS region. For the comparison the Oleander results were used from a depth of 100 m to minimize the ageostrophic contributions from the Ekman layer to the Oleander observations. Additionally, they lead to the best fit with JTP results. The figure clearly confirms the large spatial inhomogeneity in the estimates of the annual flow cycle in the JTP, in the Oleander and in the much longer (15 years) OSCAR results. Although the results are not identical, they show consistent results in the spatial variability. Due to the differing periods, the phases are not identical. To highlight this, **Fig. 4.12** shows two time series of the seasonal cycle, representing points *a* and *b* in **Fig. 4.11**. A reasonable agreement is found between their phases, amplitudes and directions of rotation. The amplitudes of the annual signal from the JTP and Oleander data have the same order of magnitude in the core region of the GS whereas in regions with less variability the Oleander velocities are much larger than the JTP estimates. ROSSBY AND GOTTLIEB (1998) found a seasonal velocity dependence of 0.01 m/s with a minimum in early winter that is supported by the JTP data.

With the aid of the in situ ADCP data from the MV Oleander it could be demonstrated that the regional annual variations in the GS region within the JTP data set represent real ocean processes and are not an artifact of the JTP time series.

4.3. The Seasonal Signal of the Eddy Kinetic Energy

Previously, STAMMER AND WUNSCH (1999) and STAMMER ET AL. (2006) investigated the extent to which EKE amplitudes are changing on the annual cycle using along-track T/P data. To do so, the cross-track geostrophic velocity was used to compute the EKE field under the assumption of isotropy. In the following, the JTP data set is used to revisit the question of a seasonally changing large-scale eddy field. To this end, the EKE was calculated as described in Section 3.6 but now for each repeat cycle (10 day period) separately. Subsequently, each repeat cycle was averaged on a $2^\circ \times 1^\circ$ grid and an annual harmonic was least-squares fitted as described in appendix A.2. The annual amplitudes of the EKE are displayed in **Fig. 4.13** (top) for the JTP estimates. The same computations based on EKE fields averaged over two month periods led to similar results as those calculated over all repeat cycles. All major current systems stand out in the amplitude field of seasonal EKE variations alongside strong seasonal signals in the Gulf of Tehuantepec and along the entire equatorial Pacific, Atlantic and Indian Ocean. The variations of a similar estimate based on the 15-year long OSCAR time series in **Fig. 4.13** (bottom) show even more clearly in the Indian Ocean. The OSCAR EKE amplitudes are smoother than those from JTP due to the longer time series. The largest amplitudes occur in the GW-region.

The phase fields of the seasonal cycle for the EKE from the JTP (top) and OSCAR (15 years, bottom) data sets are shown in **Fig. 4.14**. While both results essentially agree in low and mid latitudes, the OSCAR results are smoother in space due to the longer extent of the time series. Significant difference in the resulting phase fields exists in high latitudes, especially in the subpolar North Pacific and North Atlantic basins. Here the JTP data show a maximum of EKE early in the year in agreement with STAMMER AND WUNSCH (1999) and STAMMER ET AL. (2001). In the subpolar North Atlantic, STAMMER ET AL. (2001) identified those variations with the contribution of direct wind forcing to the eddy variability. These are not seen in the OSCAR results. Again, the OSCAR data set is lacking any barotropic variability. In the same way, the maximum of EKE along the ACC and in large parts of the southern ocean occurs in the southern winter along with the maximum of the wind stress forcing, while in the OSCAR results the maximum occurs rather in southern summer.

To highlight the seasonal variations in EKE, **Fig. 4.15** shows basin-wide zonal averages of the annual harmonic EKE amplitude and corresponding phase. Compare **Fig. 2.1** for the location of the separated basins. **Fig. 4.15** can be discussed in the same way as **Figs. 4.13** and **4.14**. As before, a substantial seasonal variation of the EKE field can be seen along zonal stripes in the western Pacific. In contrast, the eastern Pacific shows highest seasonal EKE variation in low latitudes, but also in the Alaskan Current and in the ACC region. In the Atlantic, seasonal variations in EKE are even larger than in the Pacific Ocean. This holds for the tropical Atlantic, but likewise for the GS region. Enhanced seasonal variations of the EKE field can also be seen in the vicinity of the Malvinas Current, and, less pronounced, near the Agulhas Retroflexion. The amplitudes in the South Atlantic are not as large as those in the North Atlantic. Finally, the Indian Ocean shows the highest variability of EKE as compared to the other two basins. In the western part, the equatorial region as well as the GW region are most pronounced. Further large amplitudes can be found at $20\text{--}30^\circ\text{S}$ in the South Indian Ocean Countercurrent (SICC; see **Figs. 4.13** (top) and **Fig. 4.18**) and at 40°S in the Agulhas Retroflexion. The eastern part of the Indian Ocean has again the largest amplitudes at the equator. However, a large annual signal occurs in the northern Bay of Bengal. As in the western part, the pronounced annual signal around 25°S is visible in the eastern part as well. At 50°S the ACC can be detected.

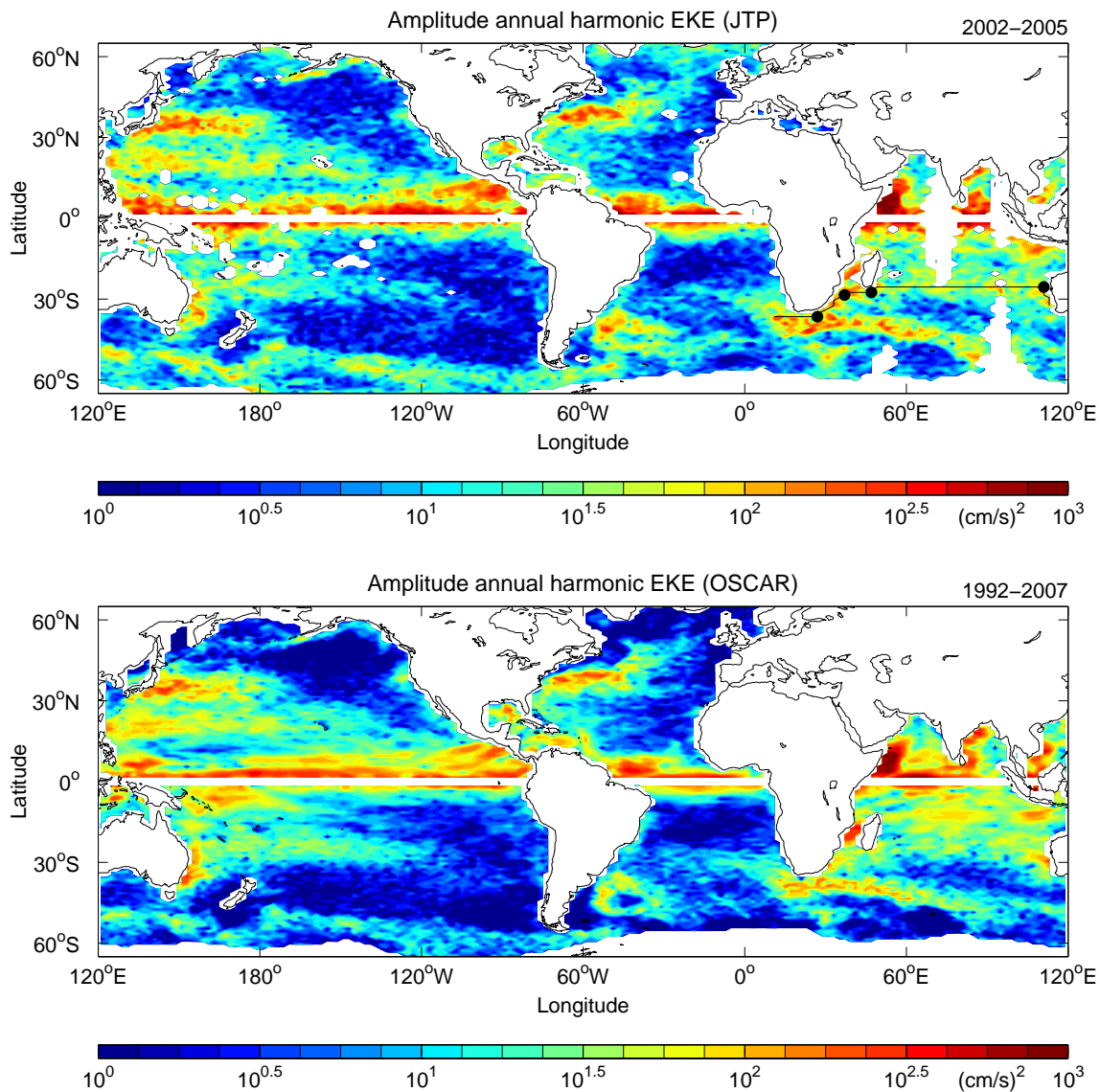


Figure 4.13.: Amplitude of the seasonal cycle for the EKE estimated from the JTP time series (top) and the OSCAR data (15 years, bottom). The scale is logarithmic for both panels. The black line in the top panel is the path of the latitude-time-diagram shown in Fig. 4.18.

To shed light on the significance of the seasonal signal for the EKE, the percentages of the EKE at the total variability, normalized by the standard deviation of the EKE, are shown in Fig. 4.16 for JTP (top), and OSCAR (15 years, bottom), respectively. For both, only few regions exist where the seasonal cycle exceeds 50% in total variability. The regions are namely the Gulf of Tehuantepec in the Pacific, the North Brazil Current and, even more strongly, the NECC in the Atlantic, and the GW and parts of the Leeuwin Current in the Indian Ocean. Further high percentages can be found for the JTP EKE in the northern branch of the Pacific SEC, the NEC, parts of the California Current, patches westward of Hawaii and the Bering Sea. Elsewhere, a very patchy structure exist. Except for the Indian Ocean, the annual OSCAR EKE has a distinctly lower percentage in variability than JTP.

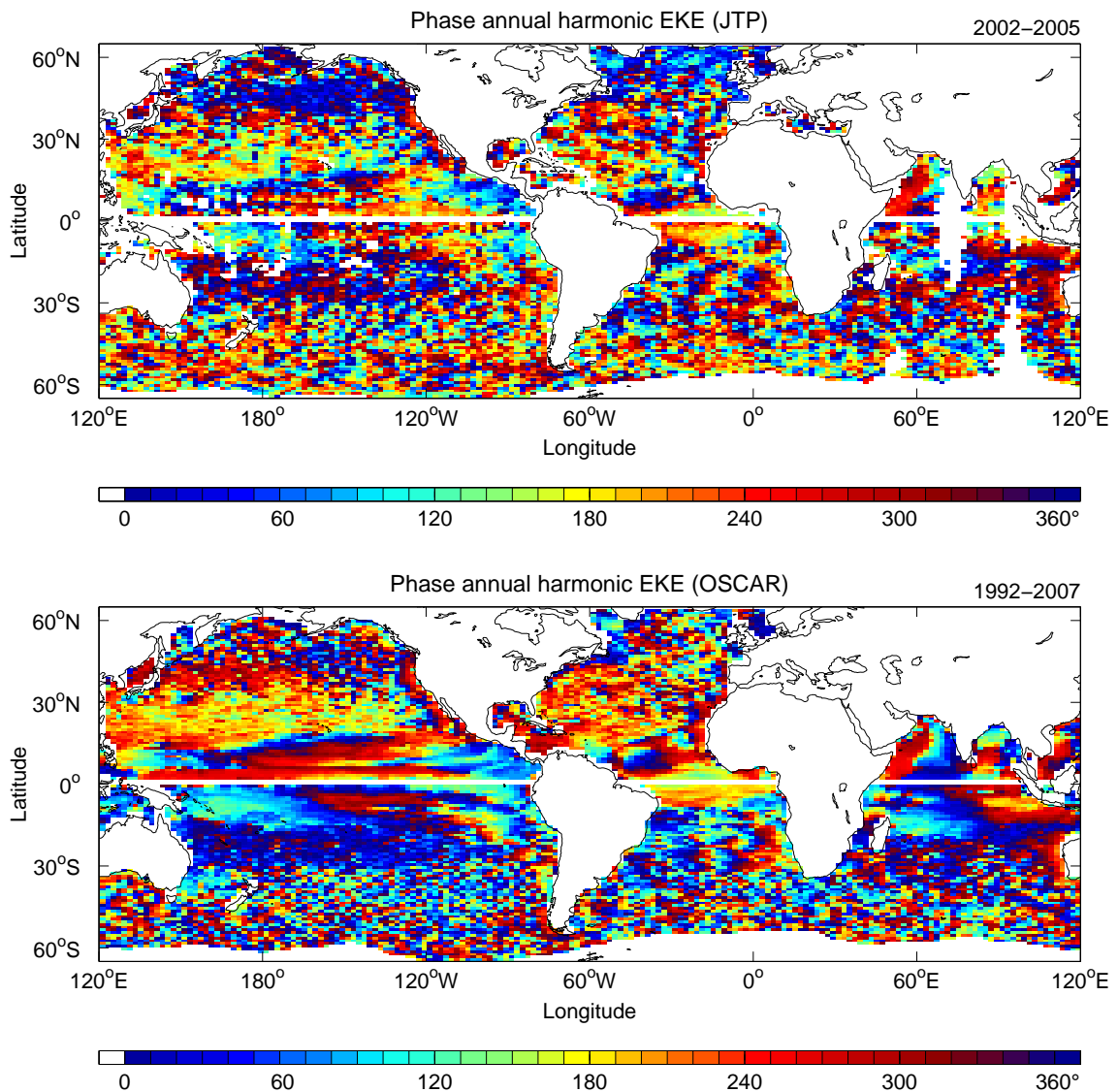


Figure 4.14.: Phase of the seasonal cycle for the EKE estimated from the JTP data (top), and the OSCAR time series (15 years, bottom). Zero degrees of the phases correspond to January 1st.

The largest percentage variations exist in the Indian Ocean where OSCAR percentages exceed JTP by up to 20%. Enhanced variations can be found in low latitudes for OSCAR. From **Fig. 4.17** it appears that zonal averages of the percentage fields are larger for JTP, except for latitudes south of 60° S. Both averages of the percentages are in better agreement in low latitudes equatorward of 20° N and S and are generally larger for the northern hemisphere.

From the JTP results a seasonal EKE signal is evident between Australia and Madagascar that evolves in the Leeuwin Current west of Australia in July which corresponds to the seasonal maximum of the Leeuwin Current ranging from March-May on the shelf and from June-August farther seaward (SMITH ET AL., 1991; GODFREY AND RIDGWAY, 1985;

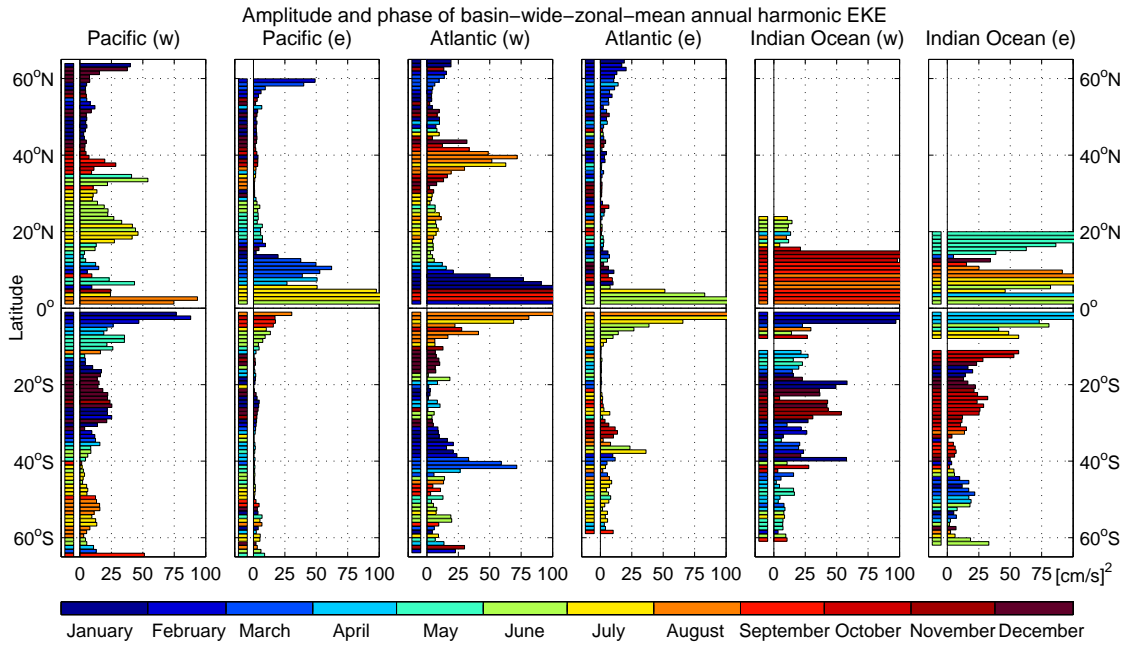


Figure 4.15.: Zonal-mean annual EKE from JTP averaged over the latitude bands 120° W - 154° W, 154° W - 66° W, 66° W - 30° W, 30° W - 30° E, 30° E - 72° E, 72° E - 120° E, from left to right. See **Fig. 2.1** for a map of the separated basins. The color of the bars indicate the phases of the annual signal.

FENG ET AL., 2003). To highlight this evolution, **Fig. 4.18** shows the annual EKE as it evolves in time along the corresponding black section shown in **Fig. 4.13** (top). It is obvious from **Fig. 4.18** that an enhanced EKE signal seems to move westward across the Indian Ocean until it reaches the ninety-east ridge in October. These findings are consistent with BIROL AND MORROW (2003, their **Fig. 3**) showing an offshore Rossby wave propagation to the west from the suggested region of planetary wave generation at a broad latitude range off western Australia. West of the ninety-east ridge, the enhanced EKE appears over the whole west Indian Ocean instantaneously in October-November at 25° S where the planetary wave and eddy flow pattern are embedded within the SICC east of Madagascar (SIEDLER ET AL., 2006). This suggests a strengthening of the whole eddy field in the SICC during October - November. A possible explanation for the occurrence of the annual signal over the west Indian Ocean at 25° S is given by PALASTANGA ET AL. (2007). Their model results show that the areas of maximum vertical shear in the flow system of the SICC and the underlying SEC are baroclinically unstable and correspond surprisingly well to estimations of the wavenumber spectra from altimetry and hydrography. With the Southeast Madagascar Current (SEMC) the signal then moves south until it gets to the Agulhas Retroflection in February. On its way down the African coast it joins the strong signal of seasonal EKE originating in the Mozambique Channel that is propagating south with the Mozambique Channel flow. DE RUIJTER ET AL. (2002) and SCHOUTEN ET AL. (2003) found a constant train of about four eddies per year in the Mozambique Channel, triggered (see RIDDERINKHOF AND DE RUIJTER, 2003) by Rossby waves propagating from the east rather than an enhanced seasonal cycle.

The JTP results appear consistent with DE RUIJTER ET AL. (2002) who postulated the sensitivity of Agulhas eddy shedding to anomalies propagating from the Indonesian through

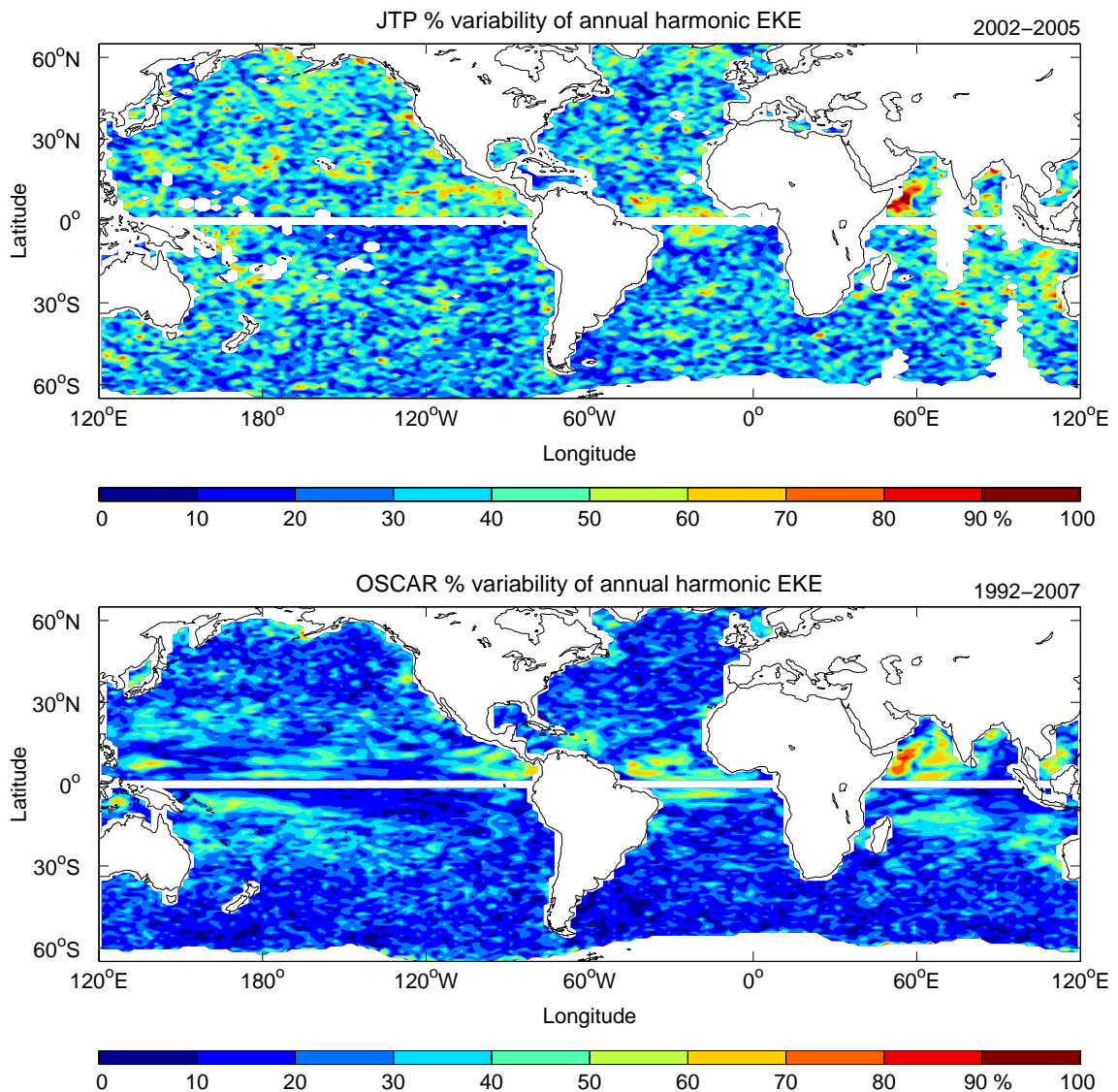


Figure 4.16.: Percentages held by the annual EKE amplitude at the standard deviation of the EKE for JTP (top) and OSCAR (15 years, bottom). Both calculated for the mean of each $2^\circ \times 1^\circ$ grid cell.

flow across the Indian Ocean where the Rossby waves at the northern tip of Madagascar trigger the generation of eddies that will form the Mozambique Current moving south and from there on into the Agulhas region. However, an additional pathway from the Indonesian through flow towards the Agulhas region can be seen. Coastal propagating waves at the east Australian coast could be the source for mid-latitude baroclinic Rossby waves (BIROL AND MORROW, 2003) crossing the Indian Ocean at 25° S within the SICC (SIEDLER ET AL., 2006). The signal joins the EMC and continues to the African coast joining the Mozambique Current and Agulhas Current. An alternative interpretation of the westward propagating features could be that they are large non-linear eddies as discussed in detail by CHELTON ET AL. (2007).

The JTP analysis of the annual EKE in the Mozambique Channel coincides with the

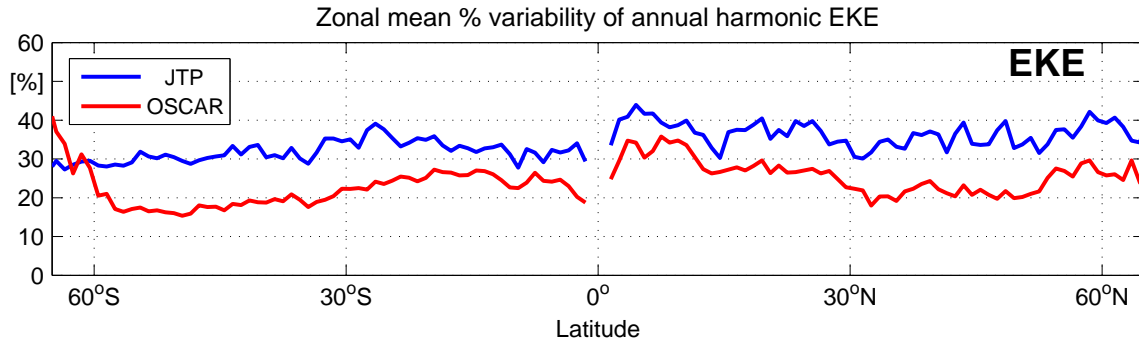


Figure 4.17.: Zonally averaged percentages held by the annual EKE amplitude at the STD of the EKE, for JTP (blue) and OSCAR (15 years, red).

minimum southward flow from March-May in the POP time series for 1985-1995 from MALTRUD ET AL. (1998, see their **Fig. 9**). However, the maximum of southward flow that they see from July-September does not correspond with the maximum of annual EKE at the northern entrance in November-December where the North East Madagascar Current (NEMC) reaches the Mozambique Channel. No connection can be found between the seasonal EKE signal of the SEMC and the NEMC. As pointed out in SCHOTT AND MCCREARY JR. (2001), the SEMC has no seasonal cycle in terms of transport. However, SWALLOW ET AL. (1988) estimated a seasonal transport variation of the NEMC with a maximum in August-September and a minimum in January-February that coincides with the annual EKE found in the JTP data set. Looking further north, the GW is evident with its strong seasonal cycle showing the maximum during the summer monsoon from July-October.

In the southern Pacific ocean, QIU AND CHEN (2004) calculated the seasonal modulations of the EKE using T/P and ERS-1/2 altimeter data. Their seasonal variations of the South Tropical Countercurrent (STCC) can be confirmed by the JTP data set with amplitudes of $50 \text{ cm}^2/\text{s}^2$ and a maximum in November-January. The SECC shows higher energies in their estimates with about $100 \text{ cm}^2/\text{s}^2$ and a maximum in March-April compared to maximal $50 \text{ cm}^2/\text{s}^2$ from JTP with a maximum rather in May-June. The ACC on the other hand show slightly higher EKE values in the JTP EKE with a maximum of $50 \text{ cm}^2/\text{s}^2$. The seasonal cycle of the EKE within the East Australian Current (EAC) coincides in magnitude (mean over $15^\circ \times 15^\circ$ box of $50 \text{ cm}^2/\text{s}^2$ and up to $150 \text{ cm}^2/\text{s}^2$ for JTP) and phase for both estimates with the maximum occurring in February compared to December-February for JTP. Accordingly, RIDGWAY AND GODFREY (1997, their **Fig. 8**) showed before that the EAC anticyclonic eddies are stronger in summer than in winter. The OSCAR results again show a slight overestimation in low latitudes and an underestimation in higher latitudes as proposed before in JOHNSON ET AL. (2007).

4.4. Summary

One of the major temporal signals in the global ocean is found on the annual cycle. In this chapter the seasonal changes of the flow-field are calculated in terms of their amplitudes and phases. The geostrophic velocity anomaly estimates of the JTP tandem mission are the first

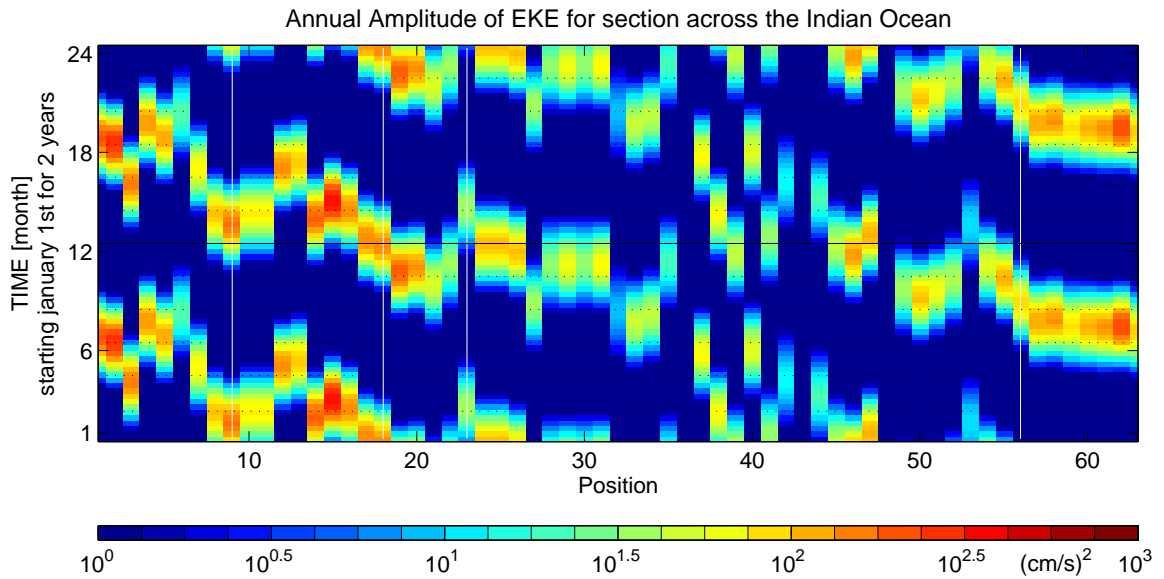


Figure 4.18.: Latitude-time-diagram of the annual EKE variations estimated from JTP data in the Indian Ocean (see black section in **Fig. 4.13**, top). Here, the white lines correspond to the black dots on the section-line of **Fig. 4.13** (top). For display purposes, the one-year time series of the annual harmonic is shown twice.

data set allowing for the along track calculation of ocean signals without the assumption of isotropy. Hence, a more accurate global picture of the annual cycle compared with previous estimates assuming isotropy could be drawn in this study. It is necessary to note that the large scale structures for both the JTP velocities and estimates assuming isotropy are comparable. However, on the regional scale, large differences occur.

In the amplitude fields all major current systems are visible. The largest amplitudes reach, in the u -component, velocities larger than 10 cm/s in the low latitude currents (which reverse on the seasonal cycle) as well as in the Kuroshio, and Agulhas Current. Similar amplitudes are found for the v -component in the Kuroshio and Agulhas Current only.

Tilting phase lines are found in all ocean basins at the u -component poleward of 10° latitude, as one would expect from annual Rossby waves crossing the ocean from east to west. Further poleward, the phase lines become increasingly more complex. Additionally, phase lines appear that tilt the opposite way (as expected from Rossby waves). Whether they represent real physical phenomena is unknown and needs to be subject of a future study. However, they are as well evident in longer model simulations as the 15-year long OSCAR time series. In contrast, changes in the v -component appear on a larger meridional wavenumber within the eastern tropical Pacific and Indian Ocean, and show mostly scatter in mid- and high latitudes as would be expected for a purely random eddy field, probably due to the short time series.

The impact of the short length of the time series is investigated through the comparison with the 15-year OSCAR time series. Resulting amplitudes in the zonal and meridional components are largely consistent whereas the phases of the longer OSCAR time series show clearer spatial structures especially in the v -component in mid latitudes.

An outstanding significant percentage held by the annual cycle at the total variability is found for the u -component in low latitudes. Slightly enhanced percentages of annual vari-

ability are found for both components in mid latitudes with poleward shifted maxima of the meridional components. The changes of the flow-field in mid latitudes on the annual cycle are rationalized in terms of a changing Sverdrup circulation in response to a changing wind stress field.

Predominantly zonal structures are shown to appear particularly in the low latitudes and in the western Pacific. Those zonal jet like structures are in good agreement with previous studies of satellite (GS and North Atlantic Current, Kuroshio), model (SECC) and in situ data (tropical Pacific), both in their phases and amplitudes.

A clear dominance of the seasonal flow changes in low latitudes exist and the seasonal flow changes along the ACC are generally small. The Atlantic shows mostly zonal seasonal flow changes, whereas in the Pacific a clear seasonal convergence/divergence is observed on the equator, that leads to enhanced downwelling in January - March and enhanced upwelling six month later. Further complex meridional banded structures appear in the western Pacific due to changes in the gyre circulation. Consistent with previous results in the Indian Ocean, annual reversals of typical flow structures are found.

A regional test of satellite derived annual flow changes against annual flow changes derived from in situ ADCP data measured by the MV Oleander is performed. It shows reasonable agreement between their phases and amplitudes in the core region of the GS, even though the time series differ in length. However, the ADCP data yield higher velocities in regions with less variability. It is demonstrated that regional annual variations in the GS region within the JTP data set represent real ocean processes and are not an artifact of the relatively short JTP time series.

Within the seasonal changes of EKE, all major current systems stand out in magnitude along strong signals in the Gulf of Tehuantepec and along the entire equatorial Pacific, Atlantic and Indian Ocean. The same estimates for the 15-year long OSCAR time series are smoother due to the longer time series and are in essentially in agreement. However, a difference is found in the phase fields in the subpolar North Pacific and North Atlantic basins, where the JTP results have their maximum early in the year consistent with the direct wind forcing that is not seen in the OSCAR results. The same is found along the ACC and large parts of the southern ocean, where the maximum of the JTP amplitudes occurs in the southern winter along with the maximum of the wind stress forcing, while in the OSCAR results the maximum occurs rather in southern summer, again due to the lack of the barotropic variability in that data set.

Basin wide averages show zonal structures within the seasonal variations of the EKE field that are most pronounced in the equatorial regions of the separated basins. However, enhanced basin wide seasonal variations emerge as well in the Alaskan Current and the western subtropical Pacific, the GS and in the vicinity of the Malvinas Current in the Atlantic, the GW, the Bay of Bengal, the SICC and less pronounced in the Agulhas- and in the whole ACC region in the Indian Ocean.

The significance of the seasonal signal within the EKE held at the total variability is largest in the Gulf of Tehuantepec in the Pacific, the North Brazil Current and the NECC in the Atlantic, and in the GW and parts of the Leeuwin Current in the Indian Ocean. Elsewhere, a very patchy structure exist. The OSCAR results again yield distinctly lower percentages held at the total variability than JTP. In general, both show larger percentages for the northern hemisphere.

An obvious westward moving annual EKE signal is detected at 25° S in the Indian Ocean. It is discussed in terms of westward Rossby wave propagation, most likely generated at the western Australian shelf. An explanation for instantaneous occurrence of the annual signal

in the western Indian Ocean could be the previously suggested (PALASTANGA ET AL., 2007) baroclinic instability in regions of large vertical shear along the SICC-SEC system. Hence, the Rossby waves could strengthen the eddy field within the SICC. However, an alternative interpretation could be that they are large, non-linear eddies (CHELTON ET AL., 2007). Within the SEMC the signal then moves to the African coast joining the Mozambique Current until it gets to the Agulhas Retroflexion. Further north, the GW is evident with its strong seasonal cycle showing the maximum during the summer monsoon from July-October.

Further comparisons in the Madagascar Current show differences in the data sets, whereas comparisons in the STCC and the SECC (T/P data) as well as in the EAC (XBT data) reveal reasonable consistency in the annual signal.

The annual EKE derived from the OSCAR velocities again show a slight overestimation in low latitudes and an underestimation in higher latitudes relative to JTP.

Concluding, the seasonal changes of the flow-field and of the EKE field derived from the JTP tandem mission fit largely within the depicted regional studies, greatly add to a global overview of the changes that occur on the seasonal time scale and help to visualize their regional significance and distribution.

5. The Spectral distribution

5.1. Introduction

The spectral distribution in the frequency and in the wavenumber domain of the geostrophic flow-field and of the resulting EKE retrieved from the JTP tandem mission will be presented in this chapter. As the oceanic variability covers a wide frequency spectrum, the description of the seasonal cycle as in Chapter 4 contains important information but only reflects a small part of the oceanic variability. In contrast, the spectral frequency distribution can demonstrate the significance of the annual cycle within the complete frequency range covered by the JTP satellite mission.

As the oceanic variability comprises all temporal and spacial scales, the spectral distribution clarifies the impact of the different scales within the complete energy distribution. Therefore, it would be desirable to investigate very long time series sampled at high frequencies with spatial distributions from millimeters to thousands of kilometers. As both a high spatial and temporal resolution at the same time is not operable, one needs to combine different attempts to measure the oceanic circulation as recently proposed by FERRARI AND WUNSCH (2010).

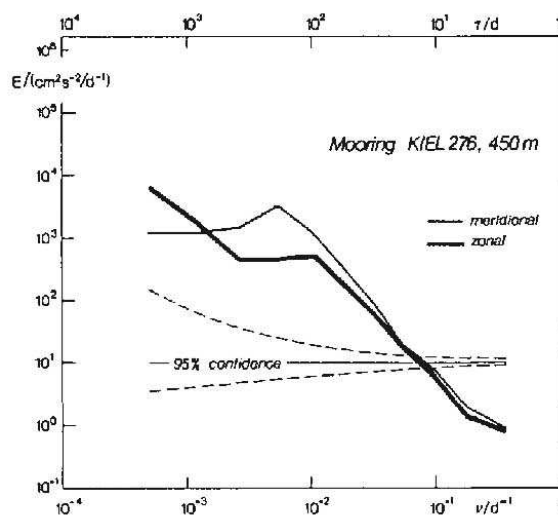


Figure 5.1.: Frequency spectra for zonal (u) and meridional (v) velocity components in the main thermocline at Kiel276. With courtesy of MÜLLER AND SIEDLER (1992, after their Fig. 13).

the purpose of obtaining wavenumber spectra. Therefore, another attempt can be made for the upper oceanic circulation by the use of satellite based measurements of e.g. SSH. Pioneering work has been done by FU (1983) who calculated wavenumber spectra of

One such attempt are point measurements from moored current meters or ADCPs that allow a spectral frequency description of the ocean circulation. A huge amount of such records exists but as mentioned in FERRARI AND WUNSCH (2009), an exhaustive study is not intended. However, FERRARI AND WUNSCH (2009) exemplarily demonstrate the ability of such records to contribute to the understanding of the oceanic circulation on scales from hours to about half a year. The inertial frequency as well as tidal signals become evident in their analysis. However, longer time series exist as the Kiel276 mooring in the North Atlantic that allows frequency spectra to be calculated up to the annual frequency (MÜLLER AND SIEDLER, 1992, Fig. 5.1). However, it is not practicable to establish and sustain moored observations for

SSH and kinetic energy using Seasat data and in a detailed analysis of LE TRAON AND ROUQUET (1990) with Geosat data. Using T/P data, STAMMER (1997a) analyzed in detail the frequency and wavenumber spectra of SSH and cross-track geostrophic velocities, whereas ZANG AND WUNSCH (2001, see **Fig. 5.2**) produced a first guess model for a general frequency-wavenumber spectrum for the open ocean circulation deduced from altimetry, moored current and temperature sensors, acoustic tomography and XBTs. Recently, an alternative dynamical explanation compared to the quasi geostrophic (QG) theory has been revisited by LAPEYERE AND KLEIN (2006) based on the surface quasi geostrophic (SQG) turbulence theory proposed by BLUMEN (1978) and HELD ET AL. (1995). This ongoing discussion (LE TRAON ET AL., 2008; TULLOCH AND SMITH, 2009; LAPEYRE, 2009; FERRARI AND WUNSCH, 2010) needs to be continued throughout the different data acquisition types, including JTP.

With the use of the “parallel-track-method” from the JTP tandem mission it has been possible for the first time to calculate the frequency and wavenumber spectra for the zonal and meridional geostrophic velocity components separately and for the resulting EKE along the virtual velocity track. These calculations could be performed without the assumption of isotropy. Up to now, the determination of the wavenumber spectra of geostrophic velocity has been difficult (ZANG AND WUNSCH, 2001) and could only be achieved by using along-track SSH slopes along with the assumption of an isotropic ocean circulation, through the use of model results or through the calculation of the geostrophic velocities from gridded SSH fields.

For the “parallel-track-approach”, one has to keep in mind that the geostrophic velocities were calculated over distances of up to 220 km at the equator, and thus the smaller scale features of the flow-field cannot be resolved. However, within the sampled scales the geostrophic velocities provide the opportunity to calculate frequency spectra for each data-point along the JTP virtual ground track as well as along-track wavenumber spectra for the EKE and for both geostrophic velocity components separately. Thus, another obstacle could be faced (FERRARI AND WUNSCH, 2009) to obtain a nearly global (65° S-65° N) description of the frequency and wavenumber spectra.

A couple of questions will be addressed throughout this chapter. How is the energy distributed on regional scales across the global ocean in the frequency and wavenumber domain? Can any similarities be found within the spectral distributions as proposed before by STAMMER (1997a) or do different dynamical regions show completely different behavior? What are the significant differences between the ocean basins? Is there any latitudinal dependence evident within the frequency and wavenumber spectra? How and where is the annual cycle important? Do any further differences exist between the JTP spectra and those previously estimated under the assumption of isotropy?

To tackle these questions this chapter is structured as follows: After a short introduction of the frequency spectra calculation in Section 5.2, the global velocity and EKE frequency

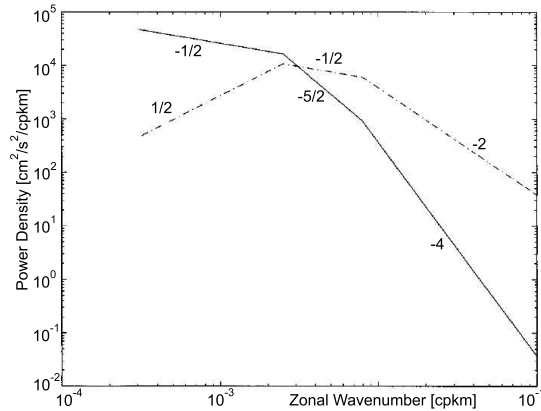


Figure 5.2.: Zonal-wavenumber spectra of zonal velocity (solid line) and meridional velocity (dash-dotted line). After **Fig. 17** of ZANG AND WUNSCH (2001).

spectra will be discussed in Section 5.2.1 to give an overview about the global frequency (wavenumber) characteristics, as those are a fundamental element in the description of the ocean circulation (WUNSCH AND STAMMER, 1995). The discussion of the different slopes from former studies (e. g. STAMMER, 1997a) is continued and the spectral distribution for the complete Atlantic, Pacific and Indian Ocean demonstrates the differences between the three basins.

To obtain a global overview of the spectral frequency distribution across $10^\circ \times 10^\circ$ regions in Section 5.2.2, the spectra from all subregions are implemented within a global map. Additionally, the zonal and meridional changes across a basin are demonstrated.

Proceeding to even more regional spacial scales, the JTP frequency spectra are compared to spectra derived from in situ data obtained from the Kiel276 mooring in the North Atlantic Canary Basin.

The spectral description is continued with the global wavenumber spectra in Section 5.3. Again, an overview of the global wavenumber characteristics and a comparison of the JTP wavenumber spectra with previous estimates by ZANG AND WUNSCH (2001) is given. The basin wide (Atlantic, Pacific and Indian Ocean) wavenumber spectra are also discussed. The along-track wavenumber spectra averaged over all available $10^\circ \times 10^\circ$ areas are shown in Section 5.3.2. As for the frequency spectra, zonal and meridional sections are displayed, explaining the spectral wavenumber changes across a basin.

Section 5.4 displays enhanced Power Spectral Densities (PSD) at frequencies of about 60 days that correspond to the tidal aliasing frequencies for the M_2 and S_2 constituents. It is discussed whether these signals can originate from tidal signals that have not been removed sufficiently.

5.2. Frequency Spectra

To quantify the importance of the seasonal signal discussed in Chapter 4, and even more to get an overview of the frequency characteristics on a global and regional scale, the frequency spectra of both the geostrophic velocity estimates and of the EKE are discussed within this section. The frequency spectra were calculated for each along-track position using the Lomb periodogram. The details of computation are discussed in Appendix A.3. The frequency f is given as $f = 1/T$, with T denoting the period. Due to the oversampling, the length of the resulting periodograms comprises 218 frequencies. After the calculation, the spectra were gridded onto $2^\circ \times 1^\circ$, $5^\circ \times 5^\circ$ and $10^\circ \times 10^\circ$ grid boxes.

5.2.1. Global and Basin Wide Frequency Spectra

Globally averaged spectra of both frequency and wavenumber are a fundamental part in the description of the ocean circulation and its variability. WUNSCH AND STAMMER (1995) were the first to calculate global frequency and wavenumber spectra of sea surface height and slope using the T/P dataset from December 1992 to December 1994. In a later study, STAMMER (1997a) used three years of T/P data (December 1992 to November 1995) to calculate the frequency and wavenumber spectra of sea surface height, slope and geostrophic velocity.

Figure 5.3 displays the global mean frequency spectra of the Loess smoothed geostrophic velocity anomalies (left) and of EKE (right), with the annual period marked as thin black line denoting 365 days. The left hand figure contains both velocity components with the

u -component always shown as bold and the v -component as thin line. As mentioned above, the PSDs of geostrophic velocity estimates ($cm^2/s^2/cpd$) and EKE ($cm^4/s^4/cpd$) are shown as a function of frequency in days.

Starting with the geostrophic velocities (**Fig. 5.3**, left), the highest PSDs can be found on the annual period followed by the half year period. At about 60 days, two small peaks can be found denoting aliasing effects of the M_2 and S_2 tides that are further discussed in Section 5.4. At periods longer than $\frac{1}{2}$ year, the zonal velocity component contains more energy compared to the meridional and the year- and $\frac{1}{2}$ -year frequencies are far more pronounced. For the geostrophic velocities, a relation of $f^{-3/2}$ can be found for periods between 60 and 180 days a slightly steeper relation for periods shorter than 60 days. Within the range of 180 and 365 days, a slope of $f^{-1/2}$ can be found for the zonal velocity component whereas for the meridional velocity component, the slope between the semiannual and annual frequencies is slightly flatter. For longer periods the spectrum turns more into a white spectrum with a tendency to a blue spectrum for periods longer than three years. (See **Fig. 5.4**, below.)

The EKE frequency spectrum (**Fig. 5.3**, right) shows a clear peak at the annual period and the 3-year period while only a small peak is visible for the half year period. A relation of $f^{-3/2}$ is obtained for periods shorter than 100 days and of f^{-1} for periods ranging from 100 up to 365 days. For longer periods, a white spectrum can be found up to periods of three years. Ignoring the annual peak, a slope of $f^{-2/5}$ can be fitted to the EKE frequency spectrum for periods between 200 and 1000 days. The lowest frequencies end in a nearly blue low-frequency-tail of the spectrum. The decay of energy for periods longer than three years may be an artifact due to the shortness of the time series as can be seen from **Fig. 5.4**. When comparing the spectra derived from the 3- and 15-year OSCAR time series (left and right), it becomes evident that the spectra lose energy at the low frequency end.

The JTP SSH measurements were smoothed with a Loess filter as described in Section 2.2.1 (Equation 2.7 and **Fig. 2.4**). According to the latitudinal change of the filter length scale $L(\phi)$, the measured JTP signal was smoothed and thus a certain part of the high frequency energy was removed. While comparing the geostrophic velocity and EKE spectra derived from the Loess smoothed JTP data with the unsmoothed data (not shown) it becomes

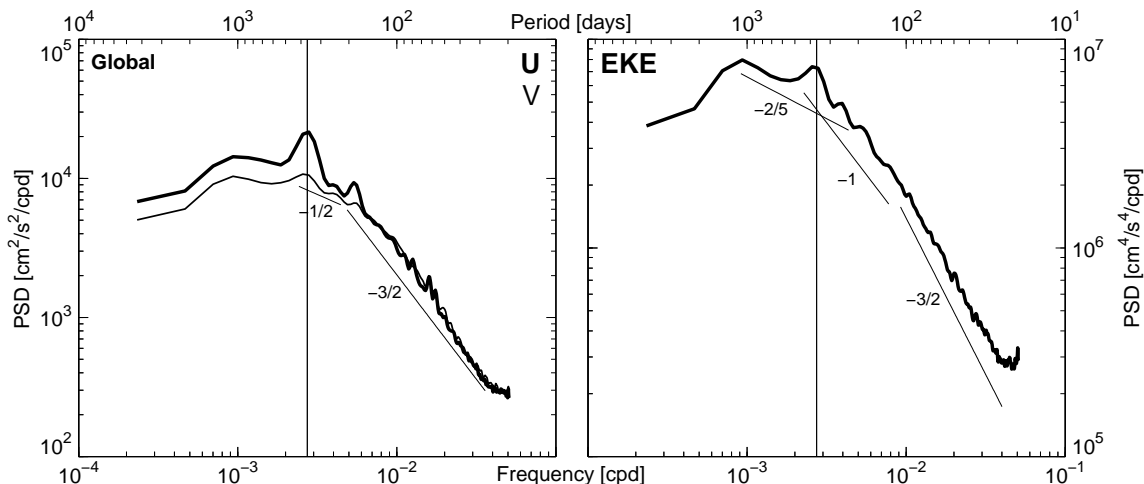


Figure 5.3.: Global-averaged frequency spectra (left) of the geostrophic velocity components [$cm^2/s^2/cpd$] and (right) of the EKE [$cm^4/s^4/cpd$]. The annual frequency is marked in all plots as thin black line denoting 365 days. The left hand figure contains both velocity components with the u -component shown as bold and the v -component as thin line.

evident that the Loess smoothed spectrum lose energy over the complete frequency range. For periods longer than a year only a small amount of energy was removed on a nearly constant level, while for higher frequencies the spectra becomes slightly but increasingly red. This results in an only slight reduction of the annual and semiannual peaks for the spectra of the geostrophic velocity components, whereas the two tidal aliasing peaks around 60 days are far more reduced for the Loess smoothed data. The effect of the Loess filter is even more pronounced for the wavenumber spectra in Section 5.3.

Comparing the smoothed global geostrophic velocity spectra from the JTP data, **Fig. 5.3**, with spectra obtained from the OSCAR data set, **Fig. 5.4**, an overall agreement becomes evident. The OSCAR data set was introduced in Section 2.3. The spectra are shown for a 3-year period covering the same time frame as JTP (**Fig. 5.4**, left) and for the complete 15-year OSCAR time series (**Fig. 5.4**, right). In both panels the JTP spectra for zonal and meridional velocity components are shown in red color for an easy comparison. Both panels demonstrate the under/over-representation of the meridional/zonal velocity component for periods longer/shorter than 100 days. The peaks for the annual and semi-annual periods are more pronounced for the 3-year OSCAR period than for JTP and, as expected for a longer time-series, become very sharp for the complete 15-year OSCAR data set. For periods longer than a year up to ten years, the spectrum stays white indicating that the decline in the JTP velocity spectrum for periods longer than three years could be an artifact from the length of the time series for all spectra shown here.

Now the basin-wide¹ averaged frequency spectra (**Fig. 5.5**) will be compared with the global mean spectra and with each other.

Starting with the Pacific (**Fig. 5.5**, top), the zonal velocity component is nearly equal to the global mean while the meridional component has smaller PSDs for the annual and for longer periods. Hence the EKE spectrum for the Pacific contains only slightly less energy than the global EKE spectrum.

In the Atlantic (**Fig. 5.5**, middle), both spectra for the geostrophic velocity components

¹Compare **Fig. 2.1** for the location of the separate basins.

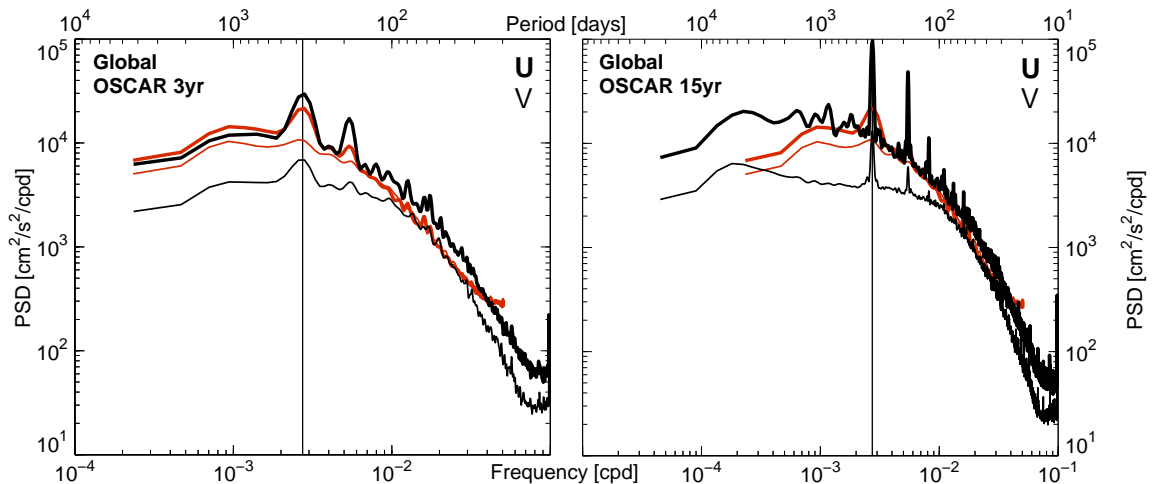


Figure 5.4.: Global-averaged frequency spectra from the geostrophic velocity components [$cm^2/s^2/cpd$] for the OSCAR data set (black). For the three years covering the same period as JTP (left) and for the complete 15-year OSCAR period (right). The red spectra display the JTP data from **Fig. 5.3** (left).

contain less energy than the global spectra for periods longer than half year and, moreover, the meridional velocity component is slightly enhanced on shorter periods. This results in an EKE spectrum that contains less energy compared to the global EKE spectrum on periods longer than 100 days.

Partly following from the scarce data coverage² (see **Fig. 2.5**, bottom) and the generally fewer low energy regions (see **Fig. 3.9**, top), the spectra for the Indian Ocean (**Fig. 5.5**, bottom) contain the highest energy level for both the geostrophic velocity components and for EKE. That is clearly visible for periods longer than 100 days. For shorter periods, the energy for the meridional velocity component is higher compared to the zonal velocity component as it was also true for the Atlantic basin-wide spectrum. The EKE frequency spectrum of the Indian Ocean shows higher energy levels than the global spectrum especially for periods longer than 100 days. The annual frequency contains the highest energies.

When comparing only the basin wide spectra of the three basins with each other (**Fig. 5.5**), several differences can be noticed, that are for example the meridional velocity component that is less pronounced in the Pacific Ocean over the complete frequency spectrum than it is for the other two basins. This is supported by the observation that in the Atlantic and Indian Ocean the meridional velocity component is more energetic than the zonal velocity component for periods shorter than 180 days, while both components show similar energy levels in the Pacific. The energy levels of the zonal and meridional velocity components in the Atlantic and Indian Ocean, on the other hand, stay closer together for periods longer than 180 days. In the Pacific, the energy levels of the zonal and meridional geostrophic velocity components show the largest energy differences. A possible explanation comes from the non-isotropic velocity field that has a stronger zonal and a less pronounced meridional alignment in the Pacific equatorial region than for the other basins. In the isotropy field shown in **Fig. 3.7** (top), the differences between the Pacific and the Atlantic/Indian Ocean can be seen. The larger differences for the annual frequency within the energy levels of both velocity components was discussed in Section 4.2.1 and can be seen in **Figs. 4.1** and **4.2**. In particular for the Indian Ocean the PSDs show the closest correspondence between both velocity components on the annual frequency. Furthermore, the frequency spectrum of both geostrophic velocity components in the Indian Ocean is the most energetic and the steepest of the three. This observation is supported by **Fig. 3.9** (top) where in contrast to the subtropical regions of the Pacific and Atlantic the Indian Ocean displays a large number of highly energetic areas raising the energy on longer periods while only a small number of small energy areas can be observed. However, the steeper slope for periods shorter than 60 days might be due to the scarce data in the Indian Ocean with an average number of only 47 values per time series (on average), compared with an average number of 65 and 71 values for the Pacific and Atlantic, respectively. Thus, the high frequencies are less well sampled in the Indian Ocean than in the other oceans.

Comparing the basin wide EKE frequency spectra (**Fig. 5.5**, right panels) with each other, the EKE spectra show similar shapes for periods smaller than 100 days but clearly differ for longer periods. The Atlantic shows lower PSDs than the Pacific and both show even lower PSDs compared to the Indian Ocean. As discussed before, the areas of very low energy in the subtropics are missing in the Indian Ocean. Therefore, the basin wide average spectrum is taken from high energy regions. The annual frequency is pronounced within all basins. Whereas in the Pacific, the spectrum shows more characteristics of a red spectrum for longer periods, the spectra in the Atlantic and Indian Ocean show more characteristics of a white spectrum. The peak in the Atlantic at about 125 days could be assigned to the equatorial Atlantic and westward propagating Rossby waves (e. g. CHELTON AND SCHLAX,

²The amount of measurements coming from the Indian Ocean is only $\sim 16\%$

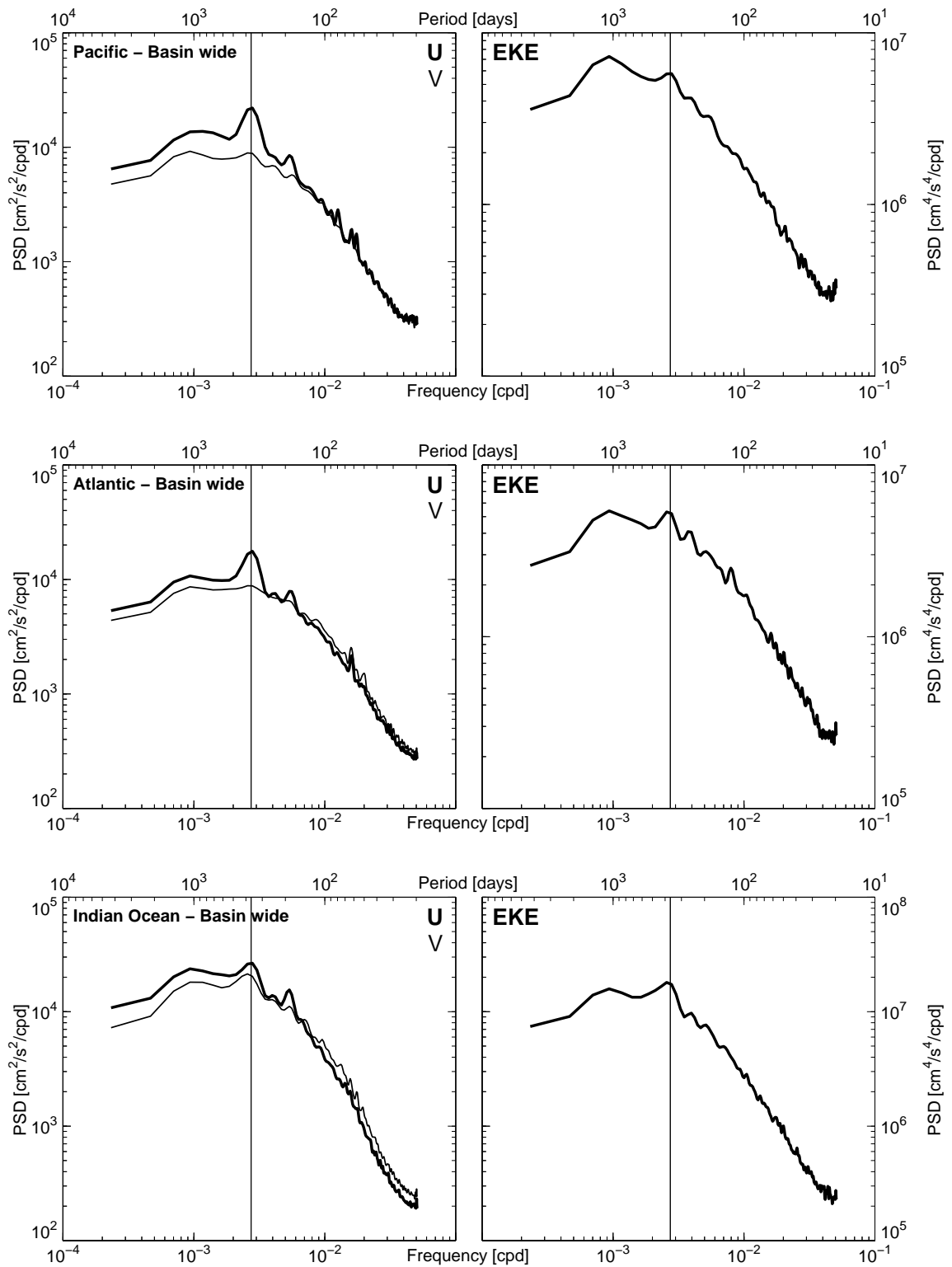


Figure 5.5.: Basin wide averaged frequency spectra for geostrophic velocity estimates [$\text{cm}^2/\text{s}^2/\text{cpd}$] (left) and EKE [$\text{cm}^4/\text{s}^4/\text{cpd}$] (right) for the Pacific (top), Atlantic (middle) and Indian Ocean (bottom). Note the different scale for the bottom right panel.

1996; CHELTON ET AL., 2003). The signal is most pronounced in the Atlantic. However, it exists throughout the whole global equatorial region. The signal can be seen in the spectra of geostrophic velocity estimates averaged over smaller scales ($2^\circ \times 1^\circ$ areas) as well.

5.2.2. Regional Frequency Spectra

In this section, the frequency spectra calculated for each measurement-point along the JTP virtual velocity track were averaged over all individual $2^\circ \times 1^\circ$, $5^\circ \times 5^\circ$ and $10^\circ \times 10^\circ$ areas. For an implementation of all subregion spectra into a global map, only the $10^\circ \times 10^\circ$ spectra are reasonable. Hence maps with all available frequency spectra averaged over $10^\circ \times 10^\circ$ areas are shown in **Fig. 5.6** for the zonal and meridional geostrophic velocity components (top, middle) and for the EKE (bottom). Although spectra are too small to investigate all frequency aspects within such a view, they are intended to give an overview of their global distribution in order to clearly identify the high and low energy areas. The equatorial region is well defined as a highly energetic region for all three quantities. While concentrating only on the equatorial regions, within all three basins the spectra show higher PSDs between 10° N and the equator than the respective spectra between 10° S and the equator. The annual frequency can be identified by eye even on these small subplots within the equatorial region. Despite the coarse resolution of $10^\circ \times 10^\circ$, one can easily follow the big current systems as the Kuroshio, Gulf Stream, Agulhas Retroflexion, Brazil Malvinas Confluence region and the ACC within all three quantities. The low energy regions, as can also be seen in the EKE from **Fig. 3.9** (top, indicated with blue colors), can be identified by a smaller PSD on longer periods, resulting in a white or even blue low frequency end of the spectrum for periods longer than a year. The spectra from the highly energetic regions, however, tend to a much slower decay for longer periods.

To get an idea of the latitudinal distribution of the PSDs for both the geostrophic velocity estimates and the resulting EKE, in **Fig. 5.7** the frequency spectra of globally averaged 10° zonal bands (center-latitudes are given in the plots) are shown for all different 10° latitude sections, on the left for the southern and on the right for the northern hemisphere. As in **Fig. 5.3** results are presented for the geostrophic u and v velocity components (left) and the EKE (right) and the annual frequency is marked as a thin black line. For both hemispheres, the equator is displayed in the bottom and the highest latitudes in the uppermost panels. For the velocity and EKE, the scales are equal for all sections.

Moving from the poles to the equator, the shape of the 65° (not shown), 55° and 45° band are very similar, showing a red spectrum for periods shorter than 365 days and a plateau up to periods of three years. In this latitude range, the southern hemisphere shows clearly higher PSDs. The main contributors are the ACC and partly the Agulhas Retroflexion that comprise more energy than the northern hemisphere in that latitude range. At 65° the zonal velocity component significantly exceeds the meridional component which can probably be partly attributed to the up to 1/3 higher error in the zonal velocity component poleward of 60° as is discussed in Section 2.2.2. In the 55° latitude band, both velocity components are highly isotropic over the complete frequency range, as can be seen from **Fig. 3.8** (blue curve).

At 45° the shape of the spectrum is still consistent with the observations described above, but now the northern hemisphere shows higher PSDs due to the very strong Kuroshio and Gulf Stream compared to the Agulhas Retroflexion, the Brazil Malvinas Confluence and the east Australian Current. For periods longer than a year, the meridional velocity component exceeds the zonal.

This becomes even more obvious at the 25° global latitude band. There, for periods longer

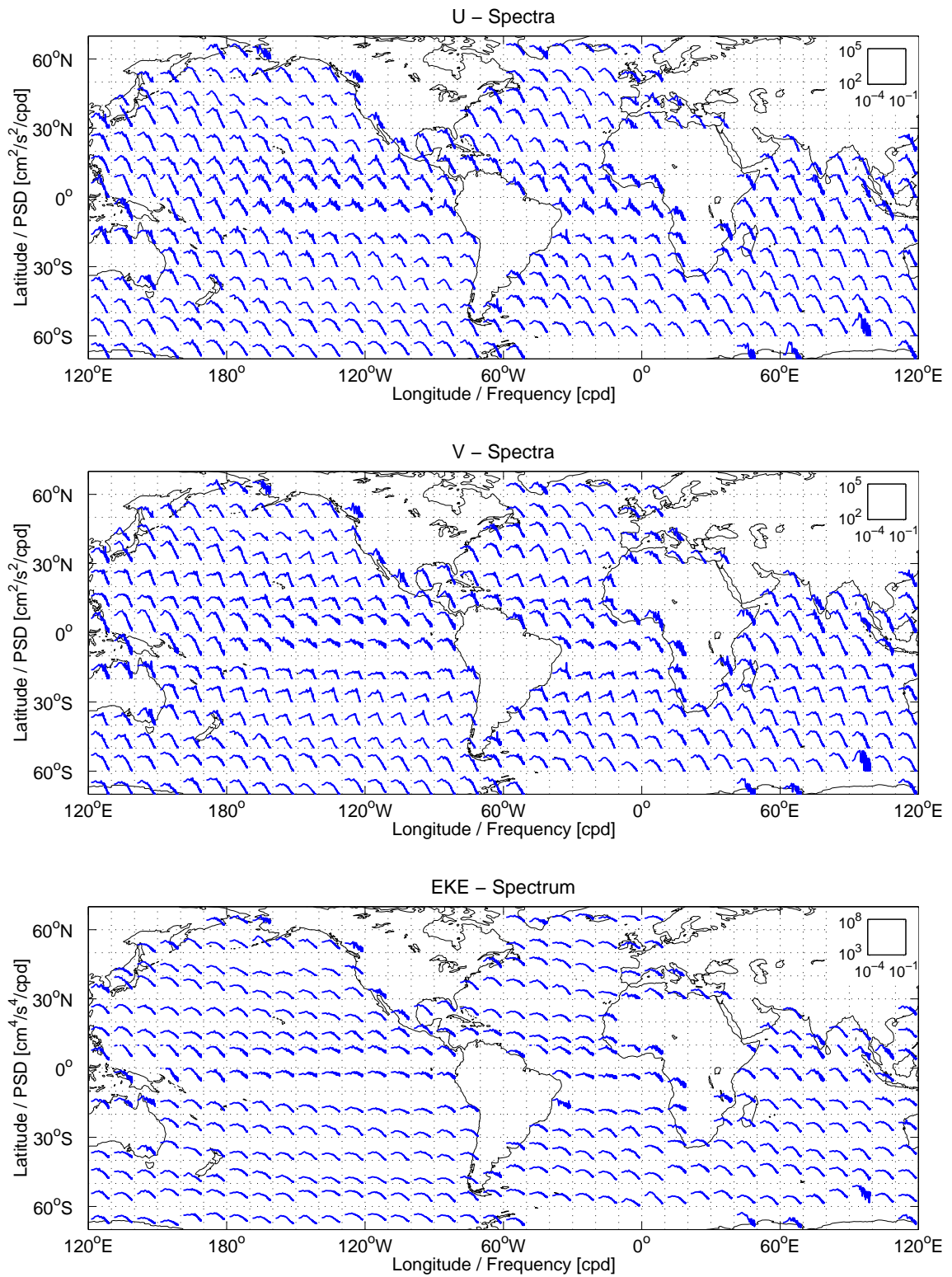


Figure 5.6.: Map with mean frequency spectra of the geostrophic u and v velocity component [$\text{cm}^2/\text{s}^2/\text{cpd}$] (top and middle) and the EKE [$\text{cm}^4/\text{s}^4/\text{cpd}$] (bottom). See text for the calculation of the spectra. The top right insets give the axis ranges of the displayed spectra.

than a year, the u -component has a steeper slope and the v -component behaves more like a white or even blue spectrum on these long periods. For periods shorter than 180 days, the meridional velocity component exceeds the u -component showing the maximum PSD at a cutoff period of about 100 days. Still, the northern hemisphere contains the higher PSDs. A related spectrum can be found at 25° . While the meridional velocity component still exceeds the zonal component for periods shorter than half a year and vice versa for longer periods, both show clear annual and semiannual peaks.

The 15° latitude band still has a steep slope for periods below ~ 60 days, however, the slope flattens towards the annual period. The annual period itself is pronounced and a plateau can be seen for the low frequency tail.

As close as 5° around the equator, the frequency spectra show the flattest, but still red slope for periods up to three years and the strongest annual and semiannual signal, compared to the other latitudes. The meridional velocity component contains slightly less energy and its annual and semiannual peaks are less pronounced. Within the EKE spectra a plateau is visible for periods longer than a year. Overall, the PSD is highest at the equator. Additionally, when concentrating at periods of smaller than 80 days, one can identify a higher noise level for the equatorial region (see Section 2.2.2) than for the other latitudes.

Previously, STAMMER (1997a) calculated averaged frequency spectra for SSH and slope (their **Fig. 10**) for different regional amplitudes of the RMS SSH variability according to σ_{SSH} , with $\sigma_{SSH} < 6$ cm for the very low energy regions, $6 \text{ cm} < \sigma_{SSH} < 15$ cm for the bulk of the oceans, $\sigma_{SSH} > 15$ cm for the high energy areas and for the tropical oceans between 15° S and 15° N. According to their assumptions, the RMS SSH variability in **Fig. 3.1** (top) thus leads to the distribution seen in **Fig. 5.8** for very low energetic regions (small grey dots), the bulk of the ocean (dark grey dots), highly energetic regions (black dots) and the equatorial region (open circles). In contrast to STAMMER (1997a), no overlap was applied for the calculation of the spectra. Thus, the tropical region here covers the latitude band between 10° S and 10° N. The corresponding averaged frequency spectra are shown in **Fig. 5.9** for the geostrophic velocity estimates (left) and the EKE (right), with the tropical region shown in blue.

While comparing the slope frequency spectra from STAMMER (1997a) with the geostrophic velocity frequency spectra (**Fig. 5.9**, left), similar features occur for all subregions. These features include the general slope of f^{-2} for the high frequency part of all spectra. However, the equatorial region has a slope of $f^{-3/2}$ in the velocity spectra, most likely due to the increasing error for the geostrophic velocity estimates (see Section 2.2.2). A f^{-2} relation has been observed from current meter moorings (WUNSCH, 1981; MÜLLER AND SIEDLER, 1992), that indicate a f^{-2} decay for periods up to 100 days. The same frequency range as for the current meter moorings of the f^{-2} decay is now visible for the frequency spectra of the geostrophic JTP velocity estimates. Furthermore, the peaks of the tidal aliasing periods of the M_2 and S_2 tides around 60 days (see discussion in Section 5.4) are pronounced in the tropical and low energetic regions, whereas the bulk of the oceans shows only a small peak and the highly energetic regions none at all. The low frequency end of all regions end within a white spectrum.

For the low energy regions (**Fig. 5.9**, light grey), the annual period is visible for both velocity components. For periods shorter than 180 days, the PSD is larger for the meridional component whereas for longer periods the PSD of the zonal component dominates. At the low frequency end, the meridional component exhibits white to blue spectral characteristics while the spectrum for the zonal component remains red with a slope of $f^{-1/2}$ between 200 and 1000 days.

The bulk of the ocean (dark grey) shows a red spectrum over the complete frequency range.

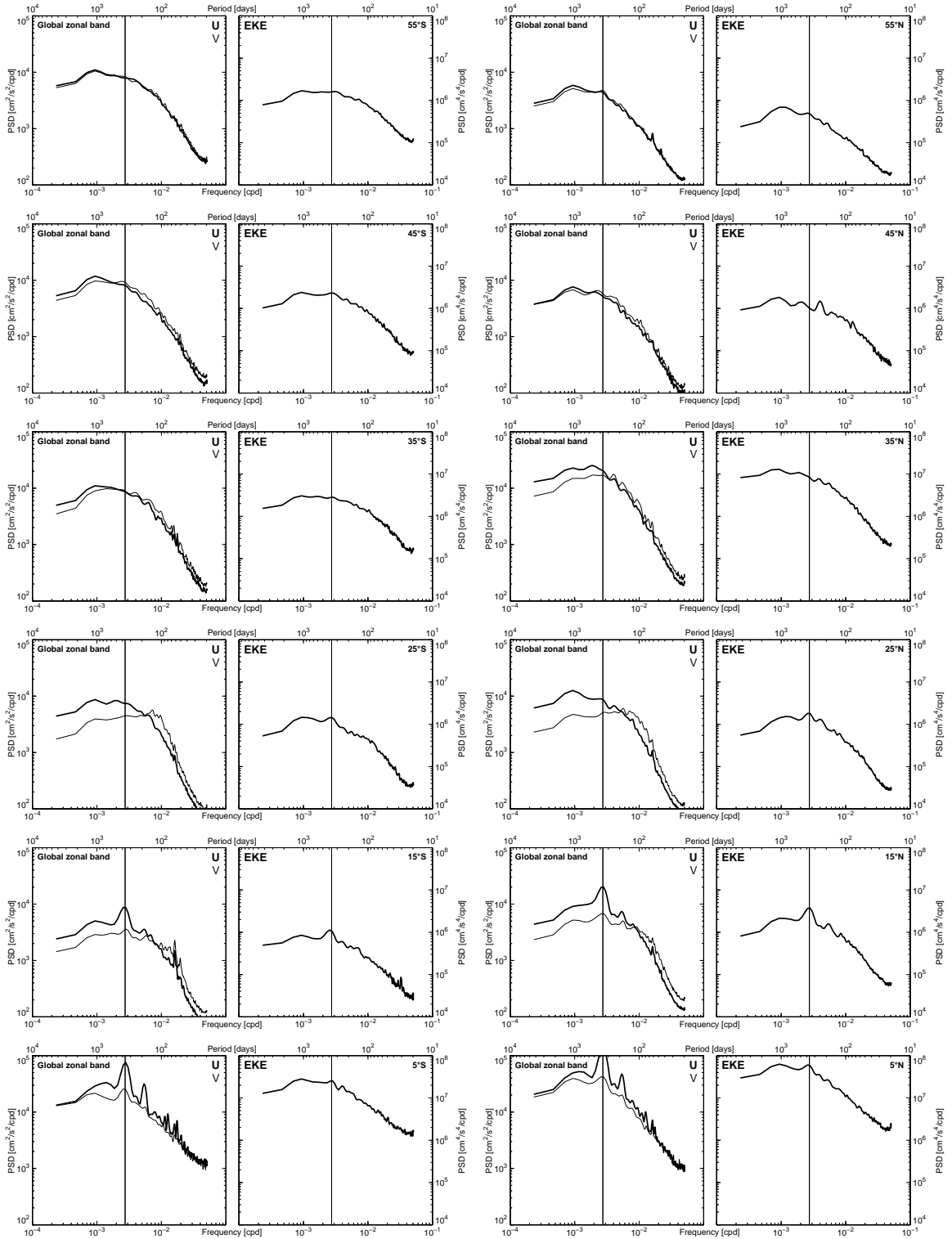


Figure 5.7.: Frequency spectra of globally averaged 10° zonal bands for different latitudes, left for the southern and right for the northern hemisphere. As in **Fig. 5.3** for the geostrophic u and v velocity components [$\text{cm}^2/\text{s}^2/\text{cpd}$] (left) and the EKE [$\text{cm}^4/\text{s}^4/\text{cpd}$] (right).

As for the low energy regions, the slope of the u -component follows a $f^{-1/2}$ relation for periods longer than 200 days. The v -component has lower PSDs and shows a $f^{-1/4}$ relation

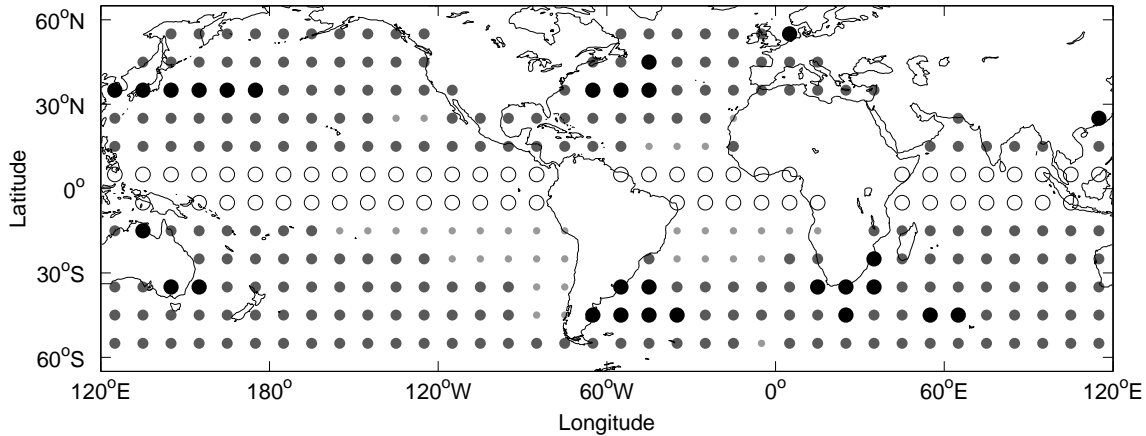


Figure 5.8.: Map of the $10^\circ \times 10^\circ$ areas over which the frequency (**Fig. 5.9**) and wavenumber spectra (**Fig. 5.17**) were averaged for different regional regimes according to their RMS SSH variability. For the very low energy regions with $\sigma_{SSH} < 6$ cm (small grey dots), the bulk of the oceans with $6 \text{ cm} < \sigma_{SSH} < 15$ cm (dark grey dots), the high energy areas with $\sigma_{SSH} > 15$ cm (black dots) and the tropical oceans between 10° S and 10° N (open circles).

within that frequency range. Similar to the low energy regions, the v -component has higher PSDs than the u -component for periods shorter than 180 days.

An equal slope of f^{-2} and $f^{-1/2}$ can be found for the highly energetic regions (black) for shorter and longer frequencies, respectively. However, the meridional component has higher PSDs for periods shorter than a year. Therefore, the zonal component continues as a red spectrum whereas the meridional component declines.

Different from the other three regions, the tropical ocean (blue) has the most pronounced annual peak for both velocity components as well as the most pronounced semiannual peak

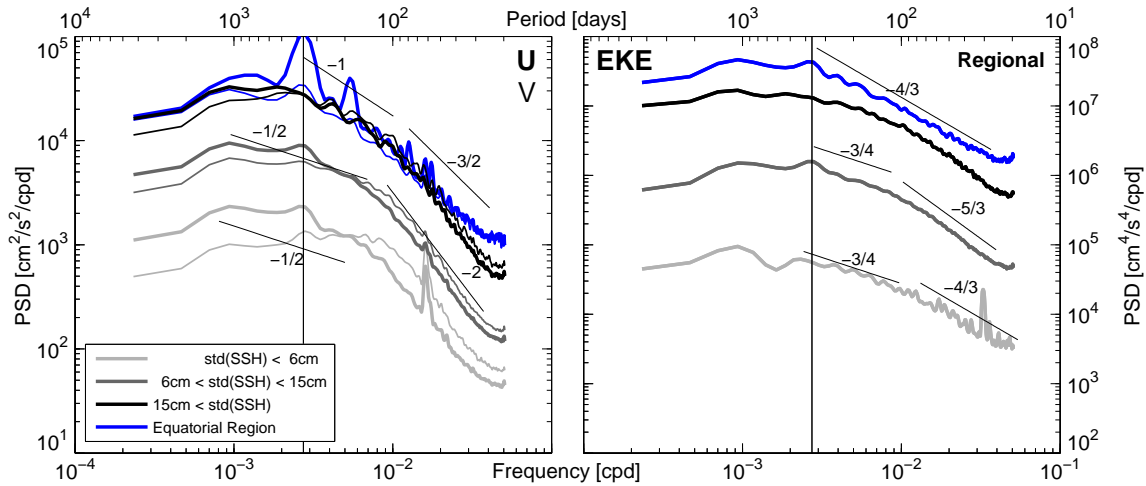


Figure 5.9.: Regional averaged frequency spectra of the geostrophic u and v velocity components [$\text{cm}^2/\text{s}^2/\text{cpd}$] (left) and of the EKE [$\text{cm}^4/\text{s}^4/\text{cpd}$] (right), for the tropical oceans (blue), the low energy regions (light grey), the bulk of the ocean (dark grey) and the high energy areas (black). Their respective geographical regions are marked in **Fig. 5.8** as open circles, small light grey-, dark grey- and large black-dots.

for the zonal velocity component. As mentioned before, the tropical ocean has a slope of $f^{-3/2}$ for periods shorter than 100 days and for longer periods a decay of f^{-1} . On periods longer than the tidal aliasing period of 60 days, the zonal velocity component comprises higher PSDs than the meridional component.

The regional averaged EKE frequency spectra (**Fig. 5.9**, right) can be described as red spectra with a nearly white low frequency end for periods longer than a year. Interestingly, the shape of the spectra from low energy regions (light grey) and the tropics (blue) show, despite their different PSD level, a similar slope of $f^{-4/3}$ for periods shorter than the semiannual and annual cycle. This will be mainly due to the small signal to error relation in those regions, that are in the equatorial regions determined by the larger errors, whereas in the low energy regions due to the only small signal. However, the spectra which represent the bulk of the ocean (dark grey) and the high energy regions (black) have slopes of $f^{-5/3}$ and $f^{-3/4}$ for periods shorter and longer than 100 days, respectively. A peak at 30 days is visible in the spectrum of the low energetic regions (light grey).

Only very few frequency spectra for geostrophic velocity measurements of sufficient length exist in the literature that can be compared directly to the JTP results. Therefore, as an example, the Recording Current Meter (RCM) record from the **Kiel276 mooring** described in MÜLLER AND SIEDLER (1992) provides a great opportunity to compare two completely independent data sets.

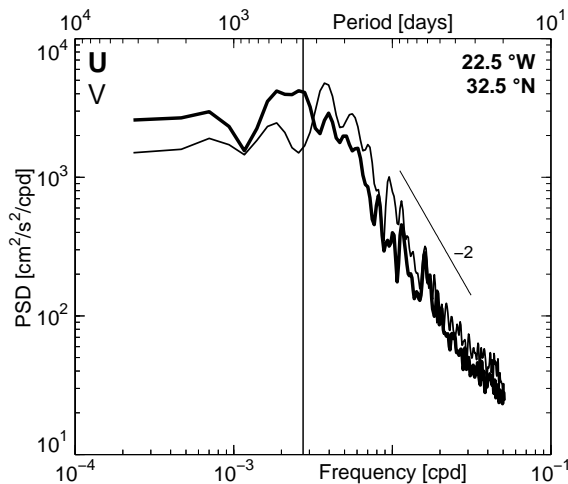


Figure 5.10.: Geostrophic velocity frequency spectrum [$cm^2/s^2/cpd$] of $5^\circ \times 5^\circ$ area in the North Atlantic.

v-component from JTP reverses to the same PSD level as the Kiel276 mooring. For periods longer than a year, both zonal velocity components exceed the meridional component. The current measurements from the Kiel276 mooring were point measurements whereas the spectrum in **Fig. 5.10** was averaged over $5^\circ \times 5^\circ$. However, both spectra picked up equal spectral behaviors of the ocean circulation. Results from the smaller $2^\circ \times 1^\circ$ areas close to the mooring site show similar shapes but with a larger noise level.

The Kiel276 mooring is located at $22^\circ W$ and $33^\circ N$ in the Canary Basin in the eastern subtropical North Atlantic. The site was chosen to measure the North Atlantic subtropical gyre within the Azores Current. The frequency spectra for the 9-year long time series (1977-1989) from a depth of 450 m (see **Fig. 5.1**) are very similar to the velocity spectra shown in **Fig. 5.10** from JTP. Both spectra have a slope of f^{-2} for periods between 20 and 100 days. Towards longer periods the flow gets anisotropic with the meridional component being more energetic than the zonal with a peak at the half year period. For longer periods the spectrum reverses for Kiel276 whereas it has a second even higher maximum at a period of 270 days in the JTP spectrum. Beyond that, the

5.3. Wavenumber Spectra

To obtain an overview of regional wavenumber characteristics in a global content, the wavenumber spectra of both the geostrophic velocity estimates and the EKE were calculated alongside the along-track positions using the Lomb periodogram. The details of computation for the Lomb periodogram are discussed in Appendix A.3. The wavenumber spectra are displayed in units of cycle per kilometer [cpkm] with the wavenumber $\tilde{\nu} = 1/\lambda$ (in contrast to the angular wavenumber $k = 2\pi/\lambda$), with λ denoting the wavelength. The JTP virtual ground tracks were divided into sections spanning 10° of latitude, ranging from 60° S to 60° N. Measurements from 65° to 60° are rejected. Due to the curvature of the JTP-tracks, arc-segments spanning different latitude ranges contain a different amount of measurements and therefore they comprise different distances (see **Fig. 5.16**). For the calculation of a global spectrum it is necessary to average all spectra. As the frequencies of the spectra have to be the same, the number of data points from the 10° arc-segment with most data points was set to be the necessary track length for the calculation of the periodogram. Shorter arc-segments were completed with dummy values that were treated as zero throughout the interpolation of the data (see Section A.3). The wavenumber spectra are available over $10^\circ \times 10^\circ$ areas. As the arc-segments spanning 10° in latitude do not only fall within one $10^\circ \times 10^\circ$ area in zonal direction, the location of each mid point of a single 10° arc-segment chooses whether the spectrum falls within the easterly or westerly box. Therefore, a single $10^\circ \times 10^\circ$ area can likewise contain wavenumber information both from its easterly and westerly neighboring areas.

For the discussion of the wavenumber spectra within this section, the resolution of the JTP data set becomes apparent. Due to the given separation of both satellite tracks of up to 157 km at the equator (see Section 2.2.2), only large mesoscale eddies can be resolved with the JTP tandem constellation. As previously estimated from LEEUWENBURGH AND STAMMER (2002), a closer track separation would have lead to smaller measurement errors allowing the resolution of smaller scaled eddies due to the estimation of geostrophic velocities over much smaller scales. The potential increase of knowledge from an evenly sampled global SSH cannot be doubted, but by only reducing the track separation, the SSH information from a two satellite constellation would have provided a drastically increased measurement density compared to a single satellite. For the estimation of geostrophic velocities, however, an increase in resolution by an order of magnitude would have been achieved!

Moreover, it is important to keep in mind that the wavenumber spectra were calculated along the JTP virtual velocity track that is displayed in **Fig. 2.2**. It can be seen, that different arc-segments ranging across 10° latitude have different elongations. Therefore, the path direction over which the zonal, meridional, and EKE wavenumber spectra were calculated extend neither only in zonal nor in meridional direction. As can be seen from **Fig. 2.2**, they are almost diagonally oriented, that is in N-E or S-W direction for ascending and descending arcs, respectively. The figure also demonstrates that ascending and descending wavenumber spectra were mixed while averaging over individual $10^\circ \times 10^\circ$ areas. In comparison to the along-track derived wavenumber spectra, ZANG AND WUNSCH (2001) have shown zonal wavenumber spectra for the zonal and meridional velocity components derived from model results (see **Fig. 5.2**). A direct comparison of both is not trivial as the wavenumber spectra were calculated in different directions across a non-isotropic ocean. However, as the assumption of isotropy is reasonable over most parts of the ocean (see Section 3.5), a comparison is worth a try. This has even been demonstrated by LE TRAON ET AL. (2008) who showed spectral estimates from different satellites (with different inclinations) that lead (next to other sources of error) to only small differences within their respective spectra.

5.3.1. Global and Basin Wide Wavenumber Spectra

A global wavenumber spectrum (**Fig. 5.12**) can now be obtained while averaging all along-track $10^\circ \times 10^\circ$ spectra in space and time. However, before starting the discussion about the global wavenumber spectrum, first the resolvable scales of the JTP tandem constellation should be considered. Therefore, **Fig. 5.11** shows the wavenumber spectra of the geostrophic velocity components that were estimated from the SSH measurements without Loess smoothing (see Section 2.2.2 for the Loess filter). For wavelength longer than about 200 km, a smooth spectrum (in shape) is visible, whereas for shorter wavelength an uncertainty range or noise level exists. To keep in mind,

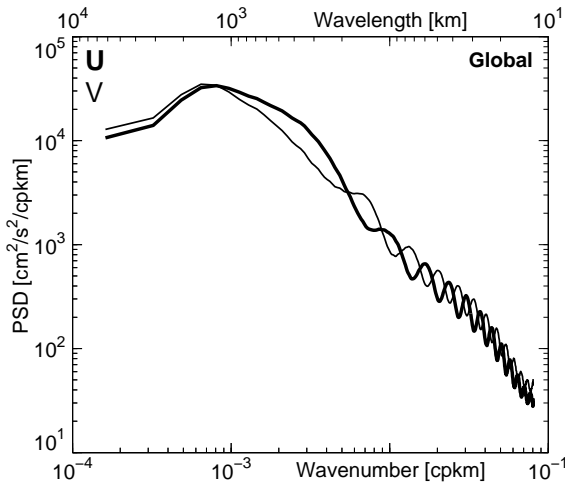


Figure 5.11.: As **Fig. 5.12** (left), but without Loess smoothing applied to the SSH measurements.

the along-track resolution of the analyzed variables is still on the order of 10 km whereas the distances $D_{1,2}$ and $D_{3,4}$ between the pairs of SSH-measurements (see **Fig. 2.3**, right) that were used for the calculation of the geostrophic velocities, and hence the EKE, are on the order of up to 220 km at the equator. Now it appears from **Figs. 5.11** that the resolved geostrophic velocity scales (order of 220 km) denote the transition between the “smooth” spectrum and the spectrum containing an uncertainty range, for wavelengths longer and shorter than 220 km. Looking at all unsmoothed wavenumber spectra zonally averaged over 10° latitude from 60° S to 60° N (not shown), the transition wavelength between the smooth part of the spectrum and the part containing an uncertainty range varies with latitude in the same way as the distances $D_{1,2}$ and $D_{3,4}$. The scales from **Fig. 2.3** (bottom left) have to be kept in mind while interpreting the Loess smoothed wavenumber spectra in the following section because of the vanished uncertainty range for the smoothed wavenumber spectra as a result of the reduced noise. See figures 5.11 and 5.12 (left) for a comparison between spectra from smoothed and unsmoothed SSH measurements.

The globally averaged wavenumber spectra of both velocity components are displayed in **Fig. 5.12** (left). Both components show equal PSDs for wavelengths shorter than 200 km with a slope of $\tilde{\nu}^{-2}$. However, for longer wavelengths both behave differently. The zonal component has a steeper slope of $\tilde{\nu}^{-3}$ for wavelengths of up to 300 km whereas the meridional component follows a $\tilde{\nu}^{-2}$ relation in that wavenumber range. In quantitative agreement with ZANG AND WUNSCH (2001, compare **Fig. 5.2**), the JTP results show a steeper slope for the zonal velocity component in contrast to the meridional, leading to higher PSDs for the zonal component in the 180 to 700 km wavelength range. The slopes of the zonal velocity component tend to be similar for both estimates. ZANG AND WUNSCH (2001) found slopes for the zonal (meridional) velocity component of $\tilde{\nu}^{-4}$ ($\tilde{\nu}^{-2}$), $\tilde{\nu}^{-5/2}$ ($\tilde{\nu}^{-1/2}$) and $\tilde{\nu}^{-1/2}$ ($\tilde{\nu}^{-1/2}$) for wavelengths up to 100, between 100 and 300 km and between 300 and 1000 km, respectively. The corresponding wavenumber spectra of the zonal (meridional) geostrophic velocity estimates from JTP (**Fig. 5.12**, left) have slopes of $\tilde{\nu}^{-2}$ ($\tilde{\nu}^{-2}$), $\tilde{\nu}^{-3}$ ($\tilde{\nu}^{-2}$) and $\tilde{\nu}^{-1/2}$ ($\tilde{\nu}^{-1}$) for for wavelengths up to 100 km, between 100 km and 300 km and for longer wavelengths of up to 1500 km. For wavelengths longer than 900 km, the meridional component

slightly exceeds the zonal component in the JTP estimates.

ZANG AND WUNSCH (2001) explained the different slopes between zonal- and meridional-wavenumber spectra, of zonal and meridional velocity to originate from geostrophy. However, as the JTP velocities were calculated along-track, they have to be somehow a mixture between the purely zonal- and meridional-wavenumber spectra.

For the globally averaged EKE wavenumber spectra different slopes can be found for wavelengths shorter and longer than 180 km. The shorter wavelengths follow a $\tilde{\nu}^{-2}$ relation whereas the longer wavelengths up to 1500 km follow a $\tilde{\nu}^{-6/5}$ relation.

The basin wide³ averaged wavenumber spectra can be seen in **Fig. 5.13**. As for the global JTP wavenumber spectra, one has to be aware of the fact that wavenumber spectra calculated on differently oriented JTP tracks (see **Fig. 2.2**) are averaged.

For the Pacific (**Fig. 5.13**, top), the wavenumber spectra are nearly indistinguishable from the global wavenumber spectra (**Fig. 5.12**) except for the zonal geostrophic velocity component for wavelengths longer than 400 km. In that range, the Pacific has higher PSDs than the global spectrum. For wavelengths longer than 1000 km, the spectra of both velocity components have the same PSD level for long wavelengths. Therefore, the slopes do not differ significantly from the global spectrum. The wavenumber spectrum of the EKE has slopes of $\tilde{\nu}^{-2}$ ($\tilde{\nu}^{-6/5}$) for wavelengths shorter (longer) than 200 km, equal to the global wavenumber spectrum.

In the Atlantic (**Fig. 5.13**, middle), the meridional component remains unchanged compared to the Pacific and the global estimates, whereas the zonal component show decreased PSDs for wavelengths longer than 400 km and hence a less steep slope of $\tilde{\nu}^{-1/6}$ within these wavelengths. The EKE wavenumber spectrum has slightly decreased PSDs compared to the global wavenumber spectrum of EKE with a relation of $\tilde{\nu}^{-3}$ between 100 and 200 km.

The wavenumber spectra for the geostrophic velocities in the Indian Ocean (**Fig. 5.13**, bottom) contain higher PSDs than the other basins. However, the slopes do not differ sig-

³Compare **Fig. 2.1** for the location of the separated basins.

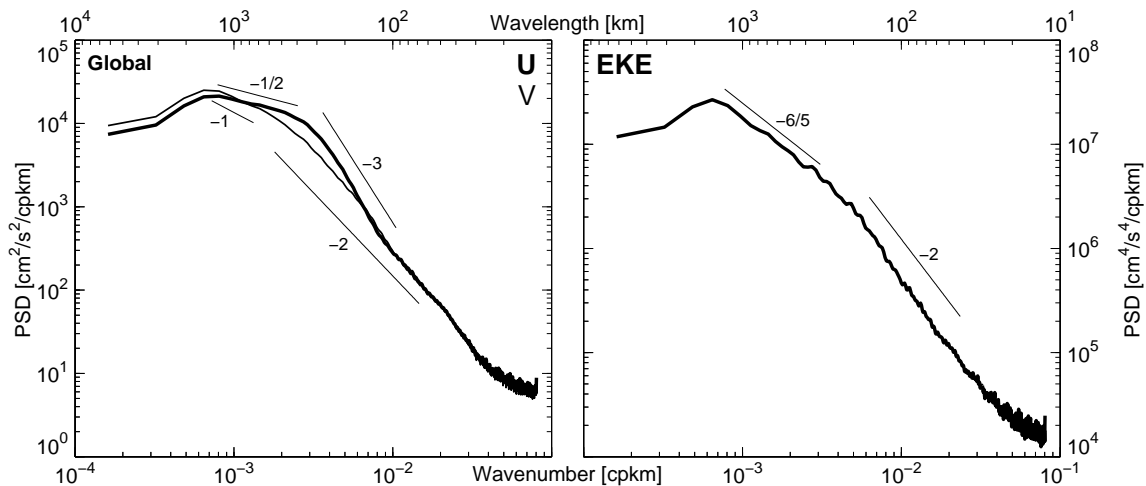


Figure 5.12.: Global-averaged wavenumber spectra of the geostrophic velocity components [$cm^2/s^2/cpkm$] (left) and of the EKE [$cm^4/s^4/cpkm$] (right). The left hand figure contains both velocity components with the u -component shown as bold and the v -component as thin line. The spectra were calculated for each arc segment spanning 10° in latitude. See text for details.

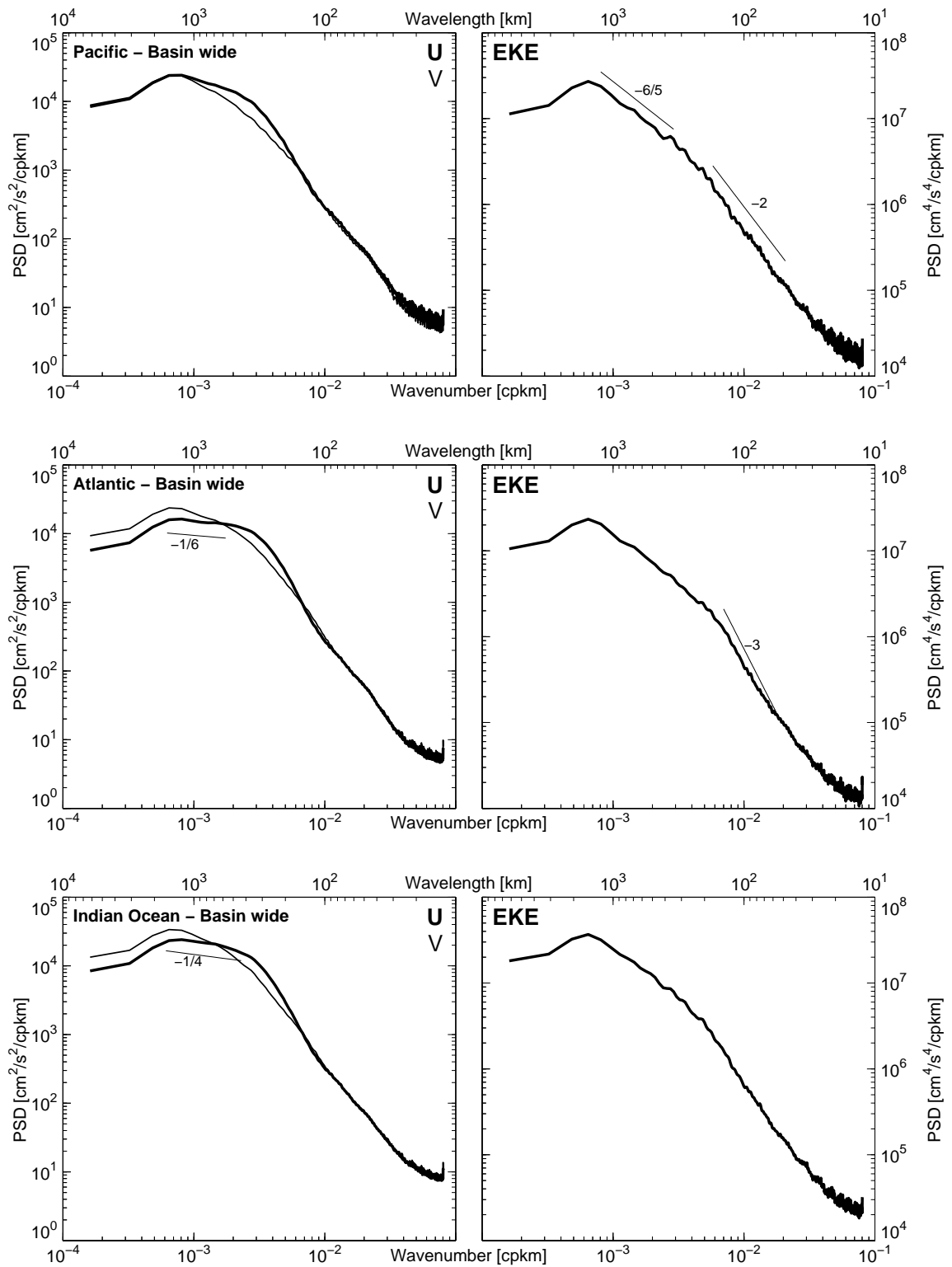


Figure 5.13.: Basin wide averaged wavenumber spectra for geostrophic velocity estimates $[\text{cm}^2/\text{s}^2/\text{cpkm}]$ (left) and EKE $[\text{cm}^4/\text{s}^4/\text{cpkm}]$ (right) for the Pacific (top), Atlantic (middle) and Indian Ocean (bottom). Note the different scale for the bottom right panel.

nificantly. The “plateau” in the zonal component between 300 and 1500 km has a slope of $\tilde{\nu}^{-1/4}$ and is therefore less steep than in the global spectrum. However, the meridional component has a steeper slope and thus higher PSDs than in the other ocean basins and in the global spectrum at a wavelength of 1500 km. This leads to an enhanced wavenumber spectrum of EKE over the complete wavenumber range.

Therewith it could be demonstrated again that the Indian Ocean is the most energetic ocean basin over the complete wavenumber range.

5.3.2. Regional Wavenumber Spectra

For a more detailed discussion of the wavenumber spectra, the along-track calculated wavenumber spectra are shown for each $10^\circ \times 10^\circ$ subregion in **Fig. 5.14** for the along-track zonal and meridional geostrophic velocity components (top, middle) and EKE (bottom).

For all quantities, the distribution of high and low energy regions are represented by the magnitude of the PSDs within each spectrum. As previously for the frequency spectra in **Fig. 5.6**, the highest PSDs can be found for example in the equatorial and boundary current regions. The regionally changing shapes of the spectra in **Fig. 5.14** indicate the change of the length-scale-distribution on which the geostrophic velocities and the EKE occur.

In the wavenumber spectra of the geostrophic velocity estimates (**Fig. 5.14**, top and middle), most of the high energy regions show a straight red spectrum with a single peak and a decrease for longer wavelengths. For some lower energy regions, however, a plateau is visible rather than a single peak, indicating a wider preferred wavelength range, as can be seen for example in the ACC for both components and in the very low energy regions for the zonal velocity component. While comparing different regions, different slopes can be recognized especially when comparing high and low energy regions. As indicated before for the global wavenumber spectra, the zonal and meridional components have different slopes especially in the low energetic regions.

The shape and hence the slopes of the EKE wavenumber spectra are very similar (**Fig. 5.14**, bottom) as could be seen before for the basin wide averages in **Fig. 5.13** (right). A generally red spectrum can be observed which mostly changes into a white spectrum for the long wavelength tail that only differs in the magnitudes of the PSDs for the different $10^\circ \times 10^\circ$ regions.

While looking at meridional sections in **Fig. 5.14**, the changing of the cutoff wavelength with latitude becomes obvious on every longitude. To shed light upon the latitude-dependent differences in the wavenumber spectra, the wavenumber spectra of global averaged 10° zonal bands are shown for all different latitudes in **Fig. 5.15**, as before on the left for the southern and on the right hand side for the northern hemisphere. The center latitudes of the 10° bands are given in each panel. The 10° equatorial bands for both hemispheres are shown in the bottom panels and the highest latitudes in the uppermost panels. The scales are equal for the velocity and the EKE panels, respective.

The largest PSDs for the wavenumber spectra of the v -component and of the EKE can be found at wavelengths corresponding to the length of the arc-segments spanning 10° in latitude. For the u -component this is only true for the 5° and 55° latitude band. The arc-segment-length varies between 1567 km for the 55° and 1185 km for the 5° latitude band, as can be seen in **Fig. 5.16**. Over this wavelength range, only three frequencies are estimated by the Lomb periodogram making it difficult to determine a latitudinal shift of that maximum. However, for the meridional velocity component the peak is confined at the wavelength of ~ 1550 km for the 55° and 45° latitudes and gets wider towards smaller wavelengths closer to the equator. For the EKE a shift of that peak is indeterminable.

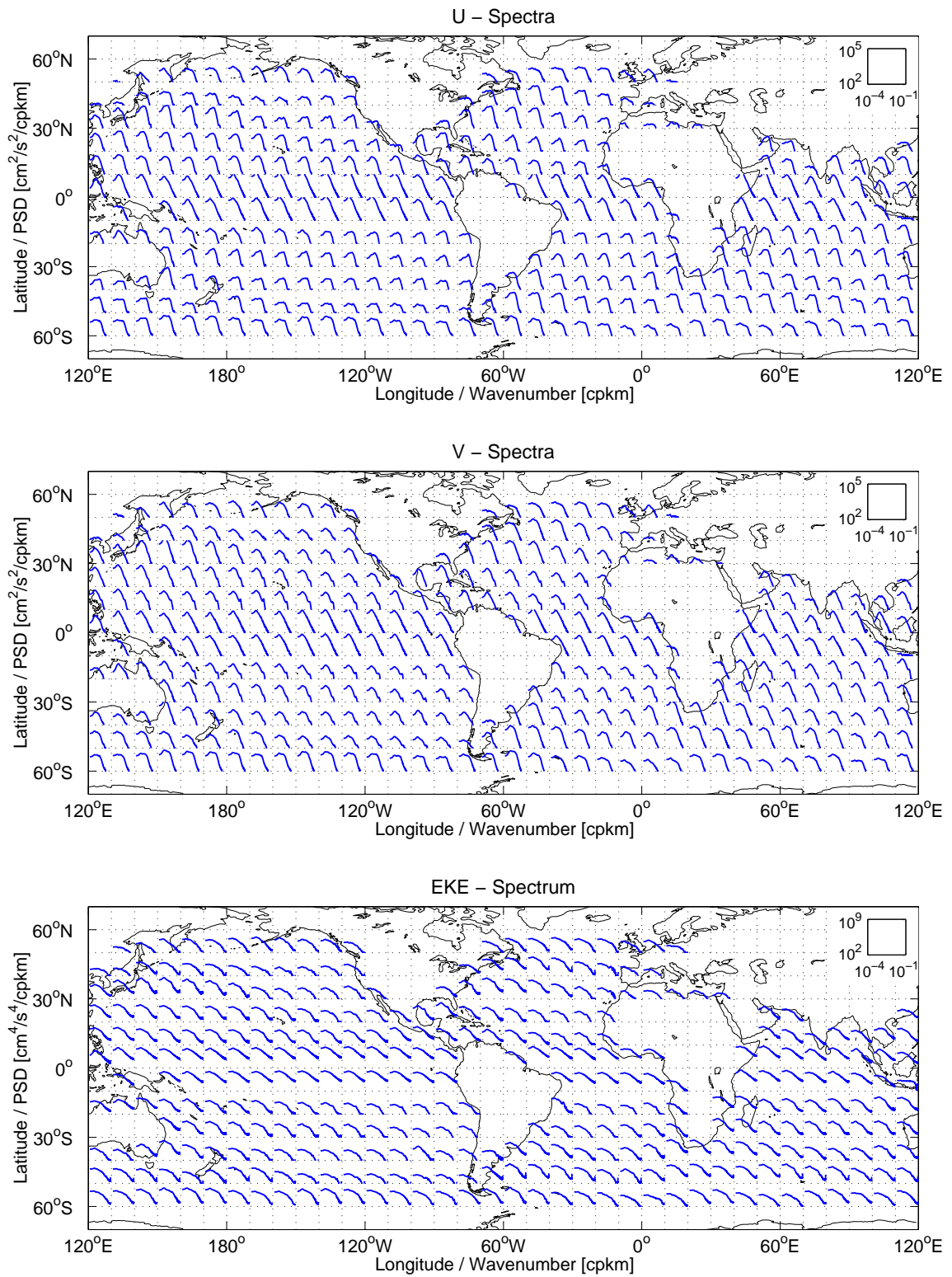


Figure 5.14.: Mean wavenumber spectra of the geostrophic *u*- and *v*-velocity component [cm²/s²/cpkm] (top, middle) and for the EKE [cm⁴/s⁴/cpkm] (bottom). See text for calculation of the spectra. Top right insets give the axis ranges of the displayed spectra.

Across all 10° latitude ranges, the slope of the zonal is steeper than the slope of the meridional velocity component for longer wavelengths, according to the wavelength of the uncertainty range displayed in **Fig. 5.11** and **2.3** (right). That leads to a shorter cutoff wavelength for the zonal velocity component in the range of 400/350 km at $15^\circ/35^\circ$ and down to 280 km at 55° latitude. For the meridional components, this cutoff is shifted to longer wavelength in lower latitudes, leading to 700/600 km at $15^\circ/35^\circ$ latitude and decreases to the same wavelengths of 280 km at 55° , as for the zonal component. For wavelengths longer than the cutoff wavelength, the spectra behave more like a white spectrum. However, a detectable peak is evident in the zonal velocity component for wavelengths on the order of the arc-segment-length. The findings about the variable cutoff wavenumber are in general agreement with the wavenumber spectra of the surface slope by STAMMER (1997a, their **Fig. 16**), i. e. a $\tilde{\nu}^{-3}$ relation for wavelengths shorter than the cutoff wavelength. That is the same slope as in the spectra for the zonal velocity component. While comparing both relations, one has to keep in mind that the former was calculated from an along-track slope spectrum of SSH and the latter from along-track geostrophic velocity estimates.

The cutoff wavelength in the EKE wavenumber spectrum again varies with latitude and is following the distances in **Fig. 2.3** (bottom, left) over which the geostrophic velocities were calculated from the SSH measurements, ranging from 200 km at 5° to 100 km at 55° latitude. The slopes of the EKE spectra are similar to each other excluding the equatorial region. The same holds for the slopes of both geostrophic velocity components which are similar in the latitude range between 15° and 45° latitude.

These results emphasize that over different ranges of 10° latitude, the track spacing as well as the arc-segment length significantly influence the shape of the wavenumber spectra for the JTP tandem data set.

The different PSD magnitudes in the wavenumber spectra (**Fig. 5.15**) between the northern and southern hemisphere follow the same explanations as for the frequency spectra in the previous Section 5.2.2 (**Fig. 5.7**). Therefore, they will only be described on the basis of the EKE spectra.

Going from the equator to the poles, the northern hemisphere has higher PSDs than the southern hemisphere at 5° N and S and is still true for latitudes of 15° N and S. That results from the stronger currents within the north-equatorial current system due to wind forcing. At 25° latitude both hemispheres have equal PSDs, whereas at 35° N higher PSDs can be seen as result of the strong Kuroshio and Gulf Stream boundary current regions. Further poleward, at 45° and 55° the southern hemisphere exceeds the northern one concerning their PSDs due to the Brazil Malvinas Confluence region and the ACC.

As before for the frequency spectra in Section 5.2.2, the regional wavenumber spectra were averaged for different regional scales (see **Fig. 5.8**) of the RMS SSH variability (σ_{SSH}). The division again is according to $\sigma_{SSH} < 6$ cm for the very low energy regions, $6 \text{ cm} < \sigma_{SSH} < 15$ cm for the bulk of the oceans, $\sigma_{SSH} > 15$ cm for the high energy areas and for the tropical oceans between 10° S and 10° N. The regional averaged spectra are displayed for the geostrophic velocity components and the EKE in **Fig. 5.17** (left and right, respectively). All wavenumber spectra in **Fig. 5.17** show a short scale noise for wavelengths shorter than 60 km.

The slope of the mean geostrophic velocity wavenumber spectrum across the equatorial region is close to $\tilde{\nu}^{-2}$ for wavelengths up to 200 km and rather $\tilde{\nu}^{-1}$ for longer wavelength. In that range, the zonal velocity component is only slightly steeper than the meridional. However, for the three off-equatorial subregions a slope of $\tilde{\nu}^{-3}$ can be found for wavelengths up to the cutoff wavelength of 300-400 km. Within the low energy regions (light grey) and the bulk of the ocean (grey), a flatter slope exist for the meridional velocity component on

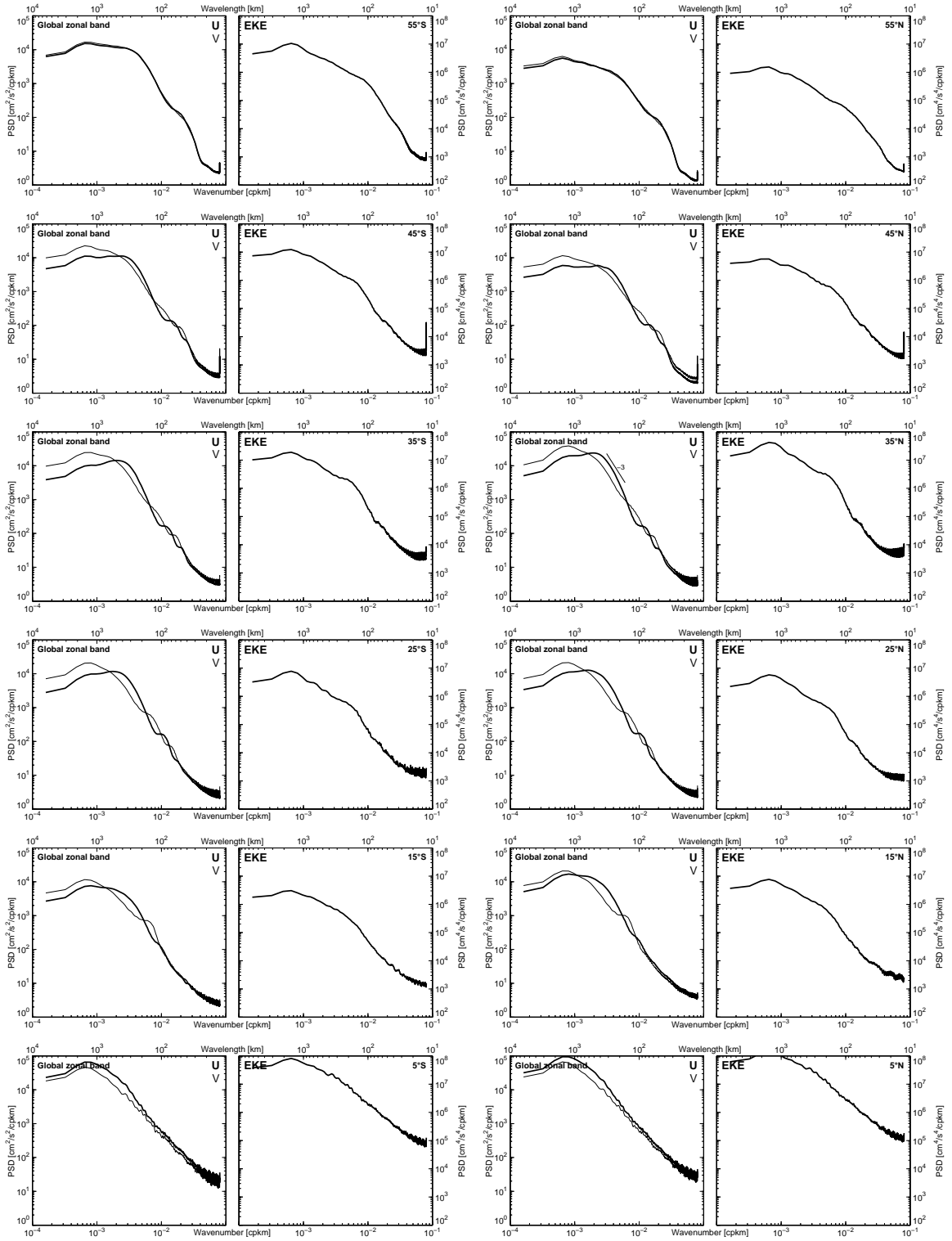


Figure 5.15.: Wavenumber spectra of 10° global averaged zonal bands for different latitudes. Left for the southern and right for the northern hemisphere. As in **Fig. 5.12**, for the geostrophic u - and v -velocity components [$cm^2/s^2/cpkm$] (left) and the EKE [$cm^4/s^4/cpkm$] (right).

5. The Spectral distribution

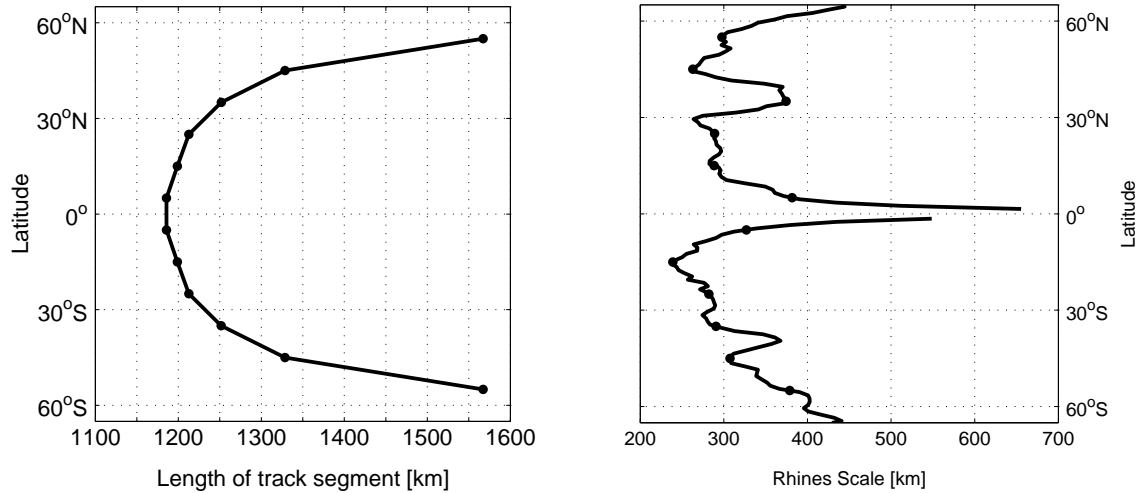


Figure 5.16.: Track-segment-length for the different 10° latitude ranges that was used for the calculation of the wavenumber spectra (right) and (left) an estimate of a “Rhines” scale (Eq. 5.1).

wavelengths longer than 200 km. The high energy regions have no decline in slope of the meridional component in that wavenumber range but rather a steeper slope of $\tilde{\nu}^{-5}$ for the zonal component.

In the wavenumber range between 500 km and 1500 km, the wavenumber spectra of the off-equatorial meridional components have a slope of $\tilde{\nu}^{-3/5}$ ($\tilde{\nu}^{-4/5}$, for the low energy regions), whereas the wavenumber spectra of the zonal components behave like a white spectrum.

The regional averaged off-equatorial (equatorial) wavenumber spectra of the EKE (Fig. 5.17, right) show, despite their different PSD level similar slopes of $\tilde{\nu}^{-5/4}$ (both) for wavelength longer than 120 km (300 km) and slopes of $\tilde{\nu}^{-3}$ ($\tilde{\nu}^{-2}$) for shorter.

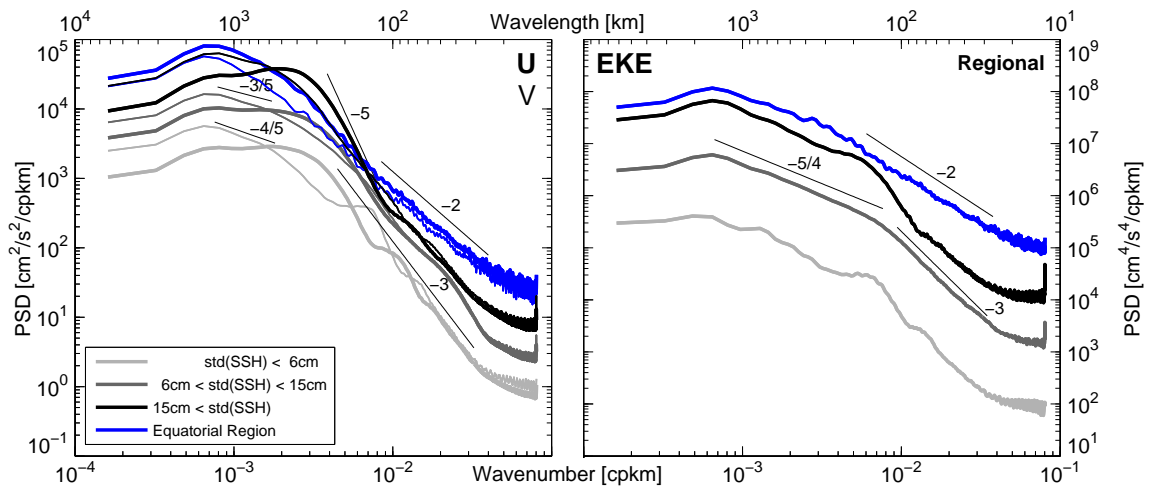


Figure 5.17.: Regional averaged wavenumber spectra of the geostrophic u and v velocity components [$\text{cm}^2/\text{s}^2/\text{cpkm}$] (left) and of the EKE [$\text{cm}^4/\text{s}^4/\text{cpkm}$] (right), for the tropical oceans (blue), the low energy regions (light grey), the bulk of the ocean (dark grey) and the high energy areas (black). Their respective geographical regions are marked in Fig. 5.8 as open circles, small light grey-, dark grey- and large black-dots, respectively.

In an ideal geostrophically turbulent flow field (KRAICHNAN, 1967; RHINES, 1979; STAMMER, 1997a) the wavenumber spectra of EKE should have slopes close to $\tilde{\nu}^{-5/3}$ and $\tilde{\nu}^{-3}$ for wavenumbers smaller and larger than the wavenumber of maximum instability. The maximum should show up at the ‘‘Rhines’’ scale L_{Rh} or ‘‘ β arrest’’ at which the red energy cascade comes to a halt as a result of Rossby wave dispersion. After RHINES (1975) the ‘‘Rhines’’ scale [km] (see **Fig. 5.16**, right) can be estimated as

$$L_{Rh} = \sqrt{\frac{U_{RMS}}{\beta}} \quad (5.1)$$

with β the meridional gradient of the Coriolis parameter and $U_{RMS} = \sqrt{2EKE}$ the RMS velocity. U_{RMS} can be estimated using the EKE (Equation 3.2) from **Fig. 3.9** (top), see STAMMER (1997a), DANILOV AND GURARIE (2002) and DANILOV AND GURARIE (2004). L_{Rh} was calculated for the zonal mean EKE. Over most parts of the ocean, L_{Rh} has a spatial scale of approximately 300 km. The scale reaches up to 400 km at latitudes where the big current systems as the Kuroshio, Gulf Stream and Agulhas Retroflexion play an important role for the magnitude of the EKE. Within the JTP wavenumber spectra the Rhines scale can be identified in the zonal velocity component only and at wavelengths of 300-400 km. For the meridional component, however, the cutoff can be found at wavelengths longer than 1000 km. The cutoff wavelength for all EKE spectra can be found on scales longer than 1000 km.

STAMMER (1997a) proposed a strikingly universal shape of the wavenumber spectra over the entire extra-tropical ocean, which would suggest that interior ocean dynamics are not significantly different from those near boundary currents. This finding can be supported by the JTP tandem data set but with the restrictions that the spectra of both velocity components have different slopes for wavenumbers larger than 100-200 km and that the predicted EKE wavenumber slope of $\tilde{\nu}^{-5/3}$ described by theory for an ideal geostrophically turbulent flow-field has a flattened slope of $\tilde{\nu}^{-5/4}$ for the JTP data.

Due to the scarce number of velocity wavenumber spectra in the literature only a few comparisons can be considered. Using the Geosat data set, LE TRAON AND ROUQUET (1990) calculated a transverse along-track geostrophic velocity wavenumber spectrum (their **Fig. 2 b**) for a region in the North Atlantic (30° - 40° N, 70° - 60° W). The wavelength range between 100 and 400 km shows a slope of $\tilde{\nu}^{-2}$. The equivalent wavenumber spectra, but now from the JTP data set can be seen in **Fig. 5.19** (middle, left). In the wavelength range between 100/200 and 400 km a slope of $\tilde{\nu}^{-3}$ and $\tilde{\nu}^{-5}$ rather than $\tilde{\nu}^{-2}$ (for Geosat) can be found for the meridional/zonal velocity component, respectively. For the zonal velocity component an even steeper slope of $\tilde{\nu}^{-6}$ can be found for the wavelength range between 100 and 200 km. Hence, the estimated slope from the Geosat data (LE TRAON AND ROUQUET, 1990, **Fig. 2 b**) of $\tilde{\nu}^{-2}$ is closer related to the meridional velocity component of the JTP data in **Fig. 5.19** (middle, right).

Within the same region, STAMMER (1997a, their **Fig. 13 b**) calculated cross-track velocity wavenumber spectra for several 10° boxes across the North Atlantic. As previously LE TRAON AND ROUQUET (1990), STAMMER (1997a) could identify the same slope of $\tilde{\nu}^{-2}$ for wavelengths between 100 and 400 km. For both estimates, the PSD declines for wavelengths longer than 400 km in consistency with the Rhines scale, whereas in the wavenumber spectra of the JTP data seen in **Fig. 5.18**, the PSD declines only slightly. Note that the center longitudes of the grid boxes are shifted by 5° for JTP in contrast to STAMMER (1997a). While moving from west to east and hence from the energetic boundary current towards a

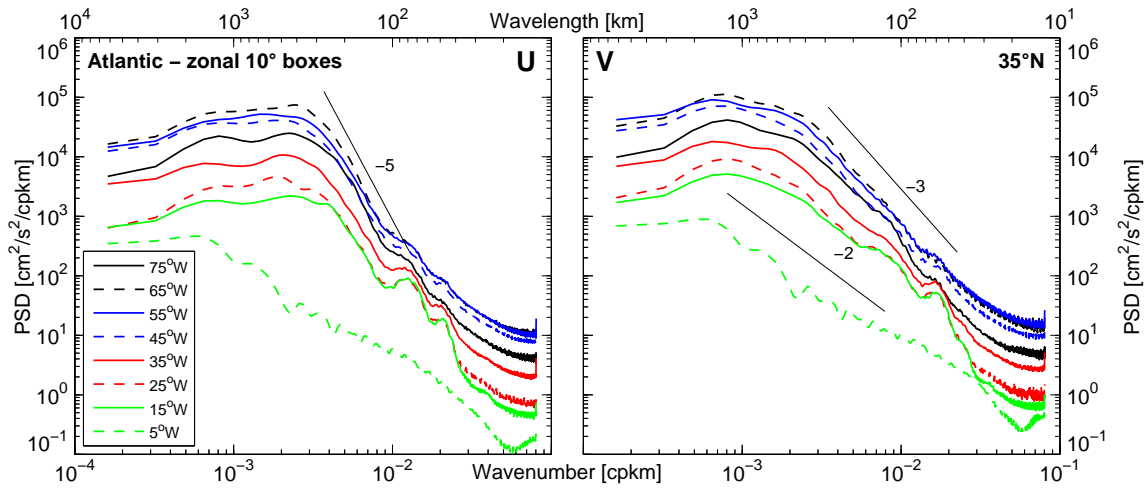


Figure 5.18.: Averaged wavenumber spectra from all $10^\circ \times 10^\circ$ areas in the latitude band of 30°N and 40°N in the North Atlantic (see **Fig. 5.14**), for the zonal (left) and meridional (right) geostrophic velocity component [$\text{cm}^2/\text{s}^2/\text{cpkm}$]. The center longitudes of the $10^\circ \times 10^\circ$ boxes are indicated in the figure.

less energetic region, a PSD decrease is evident and is accompanied by a decrease in slope from $\tilde{\nu}^{-3}$ to $\tilde{\nu}^{-2}$ for the meridional velocity component. However, the slope of $\tilde{\nu}^{-5}$ for the zonal velocity component stays unchanged across the basin in the wavenumber range of 100 to 300 km.

Recently, there has been a discussion about spectral wavenumber slopes and the underlying turbulence theory concerning whether the quasi geostrophic (QG) or the surface quasi geostrophic (SQG) theory yield a better description of the estimated wavenumber spectra seen for example within the SSH satellite data. The discussion goes back to the work of BLUMEN (1978, who proposed the SQG) and HELD ET AL. (1995), and has been revisited by LAPEYERE AND KLEIN (2006). In this discussion (TULLOCH AND SMITH, 2009; LAPEYERE, 2009; FERRARI AND WUNSCH, 2010), LE TRAON ET AL. (2008) show SSH (velocity⁴) wavenumber spectra in the highly energetic boundary current regions of the Kuroshio, Gulf Stream and Agulhas Retroflexion. They find slopes for the SSH (velocity) of $\tilde{\nu}^{-11/3}$ ($\tilde{\nu}^{-5/3}$) in the wavelength range between 100 and 300 km, rather than $\tilde{\nu}^{-5}$ ($\tilde{\nu}^{-3}$) as would be expected for QG turbulence. These slopes moreover indicate that the SQG turbulence theory yield a much better dynamical description in those regions. But questions remain as to the generality of the results (FERRARI AND WUNSCH, 2010). To compare their results with the wavenumber spectra derived from the JTP tandem mission, **Fig. 5.19** shows the $10^\circ \times 10^\circ$ averaged wavenumber spectra for the geostrophic velocity estimates (left) and the EKE (right). The spectra are shown for the Kuroshio (top), the Gulf Stream (middle) and the Agulhas Retroflexion (bottom). The slopes predicted by the QG turbulence theory ($\tilde{\nu}^{-3}$) and SQG theory ($\tilde{\nu}^{-5/3}$) are indicated in the velocity wavenumber spectra within the right panels of **Fig. 5.19**. One can easily see that the EKE wavenumber spectra follow slopes of $\tilde{\nu}^{-5/3}$ and $\tilde{\nu}^{-3}$ for wavelengths longer and shorter than ~ 150 km. According to LE TRAON ET AL. (2008) the SQG theory would better explain the variability seen in the JTP velocity estimates. However, a steep slope can be seen in the wavelength range between 80 and 150 km that arises mainly due to the resolvable spatial scales, i. e. the

⁴Which should be noted to be the absolute velocity or kinetic energy.

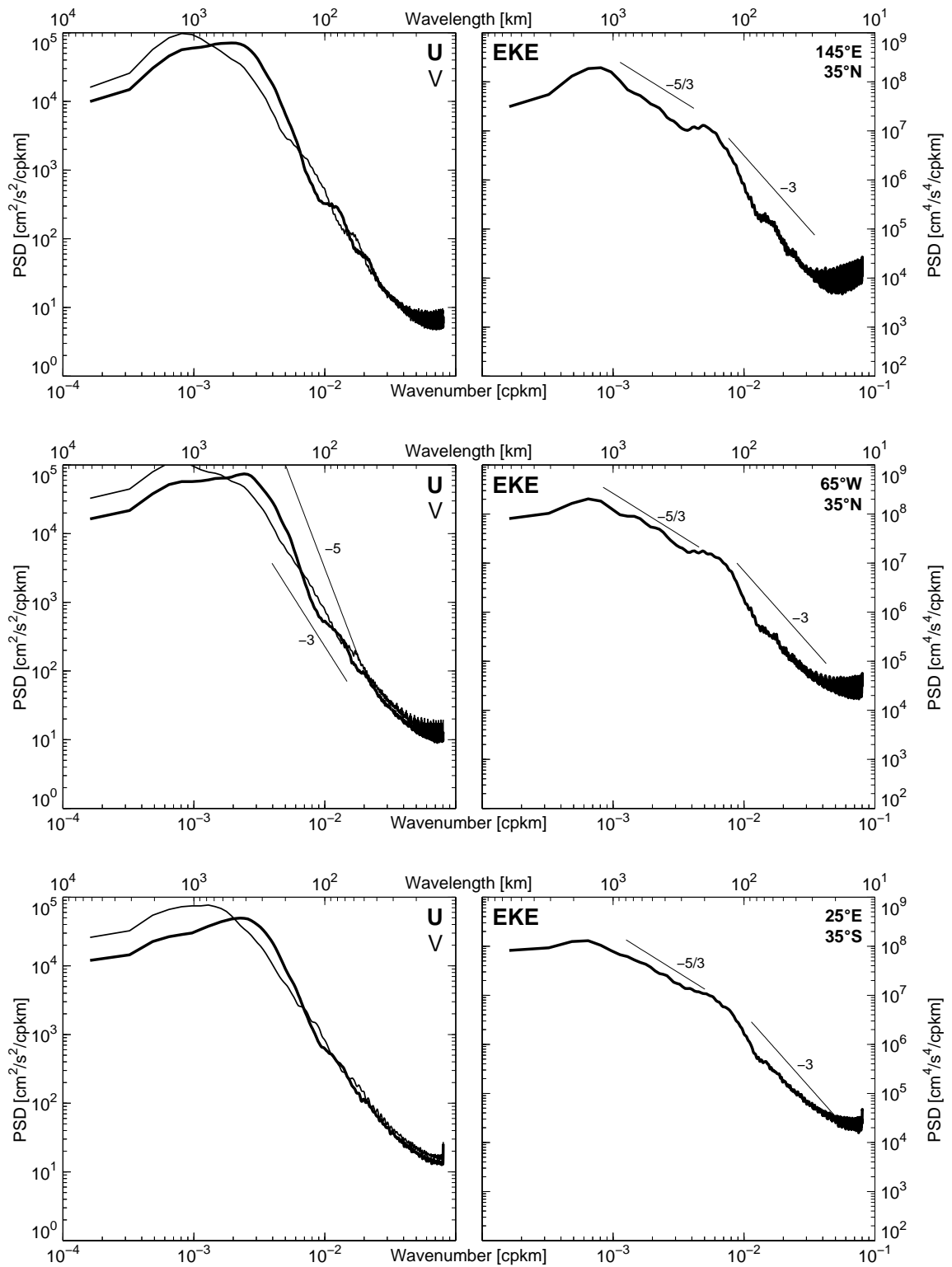


Figure 5.19.: $10^\circ \times 10^\circ$ averaged wavenumber spectra for geostrophic velocity estimates [$\text{cm}^2/\text{s}^2/\text{cpkm}$] (left) and EKE [$\text{cm}^4/\text{s}^4/\text{cpkm}$] (right) for the Kuroshio (top), Gulf Stream (middle) and Agulhas Retroflection (bottom).

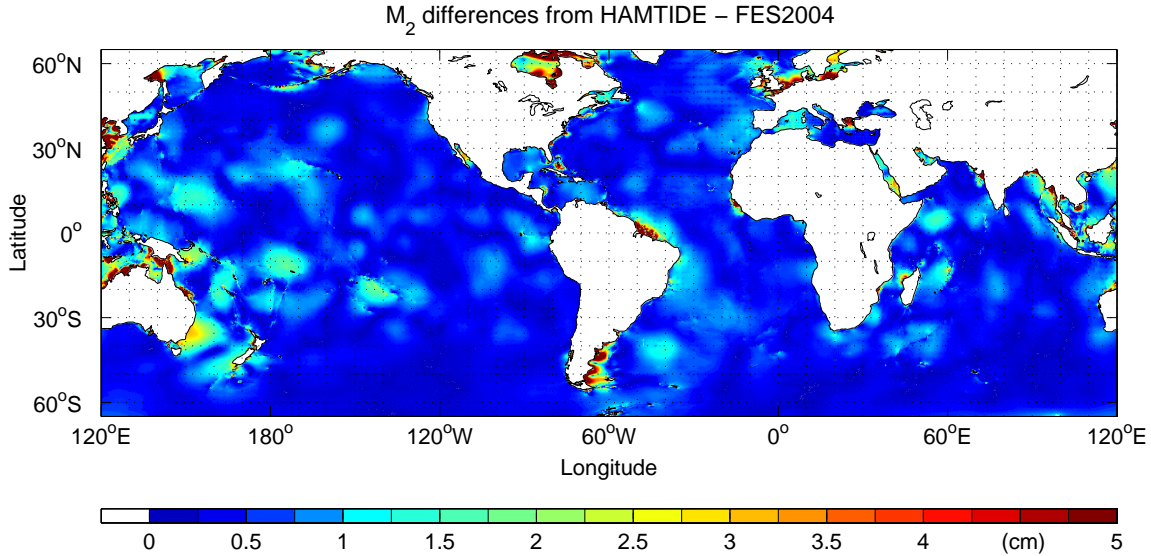


Figure 5.20.: Differences [cm] of the M_2 tide from the HAMTIDE and FES2004 models. The largest differences occur on the North-Brazilian shelf.

track spacing of the JTP tandem mission with the respective distances $D_{1,2}$ and $D_{3,4}$ over which the geostrophic velocities were calculated (see Section 2.2.1 and **Fig. 5.11**). A closer track-spacing during the JTP tandem mission would have minimized the uncertainties in that wavenumber range and therefore improved the knowledge about the wavenumber spectra on shorter wavelength, as to date (FERRARI AND WUNSCH, 2009) the observations on wavelengths of 200 km and shorter are particularly needed.

5.4. The aliasing frequencies of the M_2 and S_2 tides

In Section 5.2, the geostrophic surface currents estimated from the JTP tandem altimetric SSH data were used to calculate their frequency spectra.

The global frequency spectrum in **Fig. 5.21** (same as **Fig. 5.3**) shows peaks close to the M_2 and S_2 aliasing periods of 62.1 and 57.8 days (see SCHLAX AND CHELTON, 1994; RAY, 1998) indicated by the arrows. A regional analysis reveals that the signal originates from only a few regions on the continental shelves of the world ocean. The question arises whether those peaks describe ocean processes or emerge from the processing of the data set. It has to be noted that eddies can generate a signal with a ~ 60 day period. However, these regions coincide with areas for which large differences exist be-

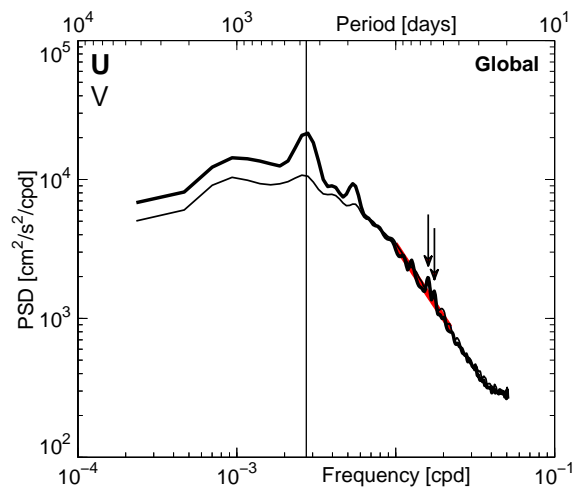


Figure 5.21.: Same figure as **Fig. 5.3** (left). The arrows indicate the periods of 62.1 and 58.7 days which are the aliasing periods of the M_2 and S_2 tides for the JTP satellites.

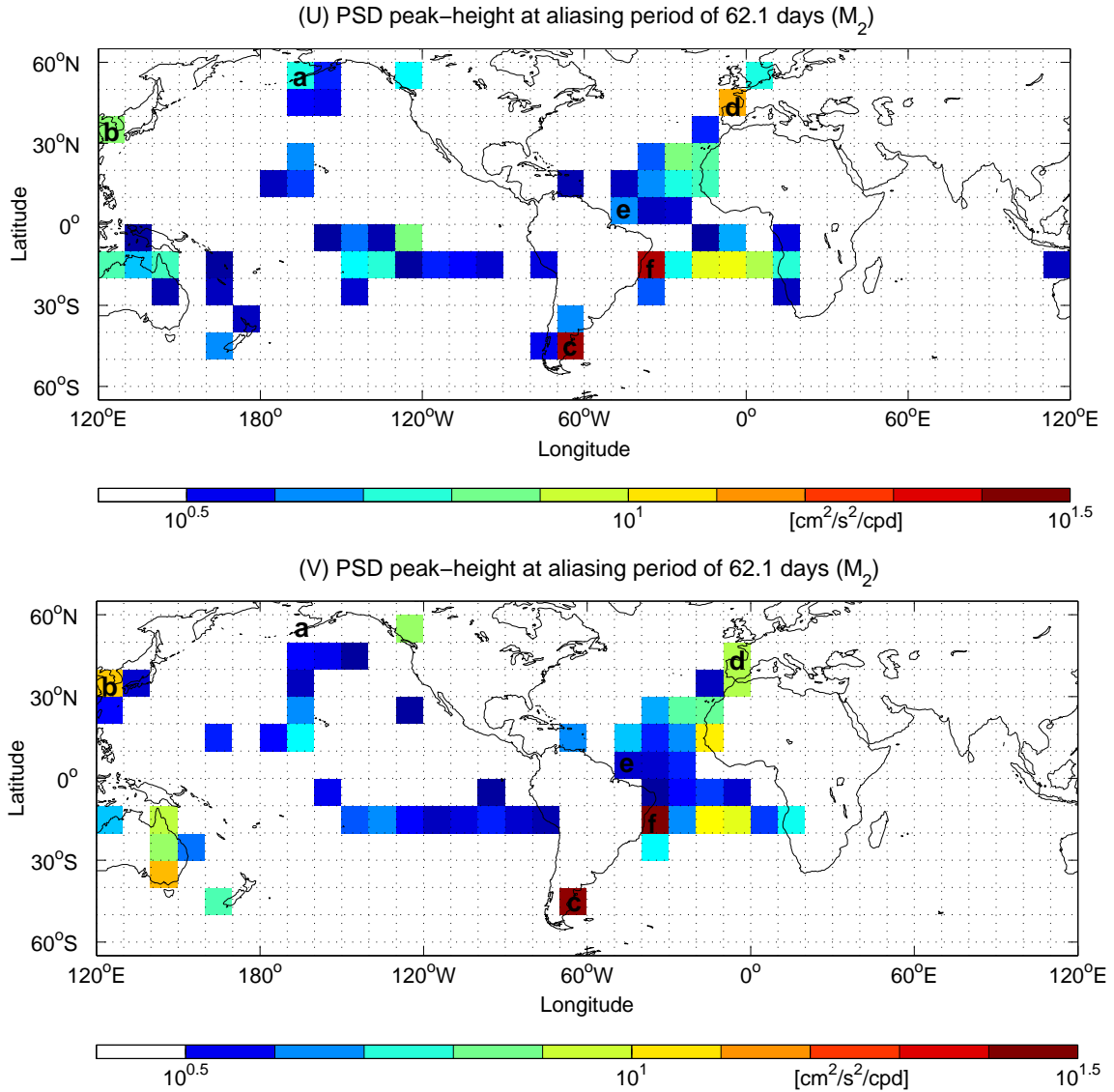


Figure 5.22.: PSD peak-height of the geostrophic velocity spectra (see **Fig. 5.6**) at the period of 62.1 days (which is the aliasing period for the M_2 tide), for the zonal (top) and meridional (bottom) velocity components [$cm^2/s^2/cpd$]. Shown are regions with a clear peak at the aliasing period of the M_2 tide. The letters from **a-f** correspond to the spectra in **Fig. 5.23**. Note the logarithmic scale.

tween the M_2 and the S_2 constituents that were provided by the finite element solutions (FES) FES2004 tidal model (LYARD ET AL., 2006) that was used to correct the ocean tides in the JTP altimeter data and is known to have difficulties within the tidal solutions in the coastal and shelf regions and those provided by the more recent Hamburg direct data Assimilation Methods for TIDES (HAMTIDE) tidal model (TAGUCHI AND STAMMER, 2010). The differences between both tidal models can be seen in **Fig. 5.20** for the M_2 aliasing period. Here, the differences are largest on the continental shelf and, albeit smaller, in the open ocean. The largest differences occur on the North-Brazilian shelf and reach values of more than 5 cm. The resulting velocity aberrations can reach values of 20 cm/s and more.

In order to check all frequency spectra averaged over $10^\circ \times 10^\circ$ regions (see **Fig. 5.6**, top and middle) for significant peaks at the aliasing periods of M_2 and S_2 , the regression slope and a corresponding noise-level were calculated for the period range between 45 and 100

5. The Spectral distribution

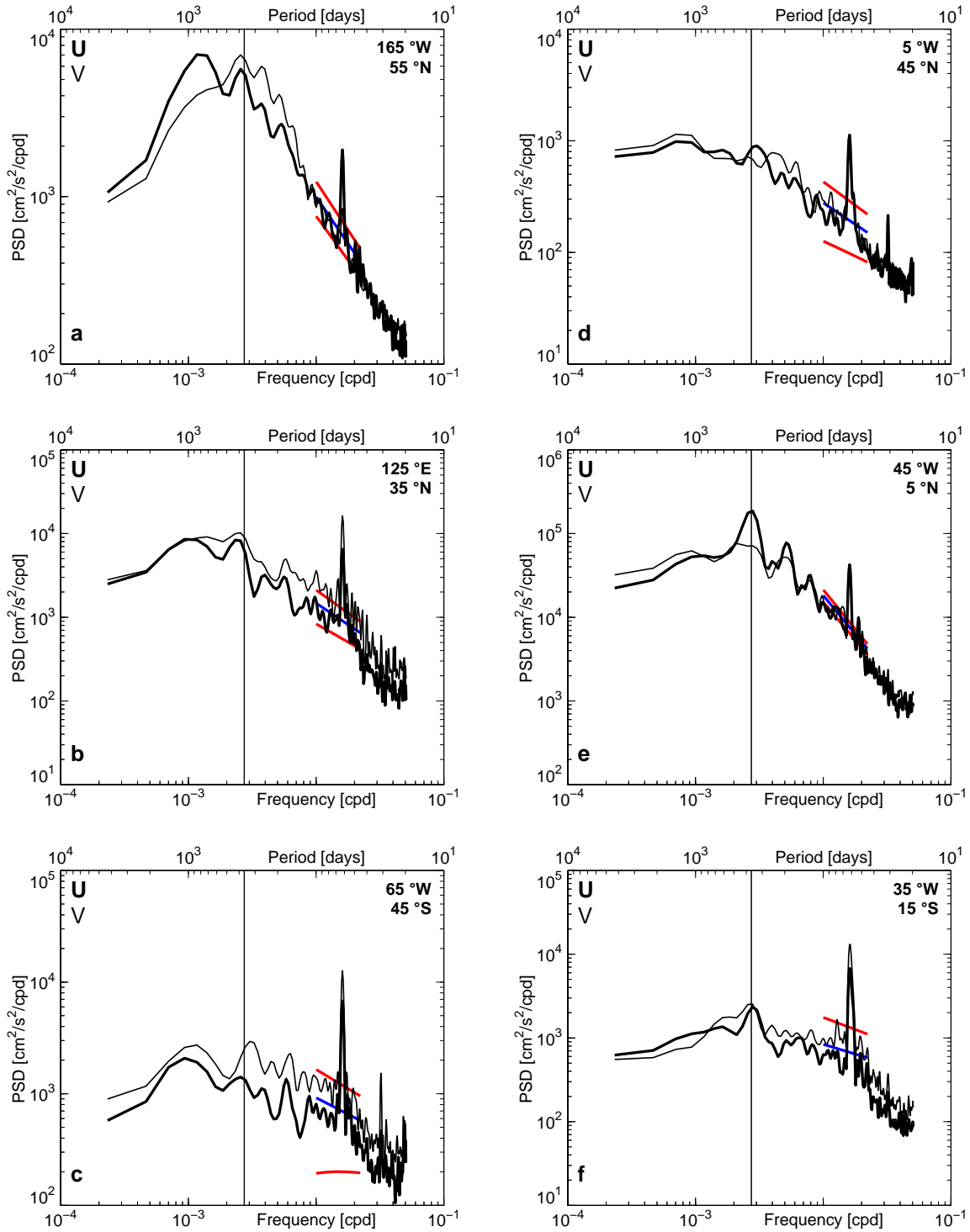


Figure 5.23.: $10^\circ \times 10^\circ$ averaged frequency spectra for geostrophic velocity estimates [$cm^2/s^2/cpkm$] for (left) **a** Alaskan Stream, **b** Yellow Sea, **c** Argentine Shelf and (right) **d** Bay of Biscay - European Shelf, **e** Amazon Shelf and **f** Abrolhos Bank east of Brazil. The spectra belong to the regions **a-f** in **Fig. 5.22**. The regression slope of the period range 45-100 days is indicated as blue and the according noise-level as red lines.

days. Exemplarily, six frequency spectra averaged over $10^\circ \times 10^\circ$ areas are displayed in **Fig. 5.23** for the zonal (bold) and meridional (thin) geostrophic velocity estimates. The spectra are shown (left) for **a** the Alaskan Stream, **b** the Yellow Sea, **c** the Argentine Shelf and again (right) for **d** the Bay of Biscay - European Shelf, **e** the Amazon Shelf and **f** the Abrolhos Bank east of Brazil. The associated geographic locations are marked in **Fig. 5.22**. The blue line denotes the regression slope whereas the red lines denotes the respective noise level⁵. A peak at one of those periods was chosen to be significant if it exceeded the noise level. Peaks exceeding the noise level by more than $10^{0.5}$ at the M_2 aliasing period are shown in **Fig. 5.22** for the frequency spectra of zonal (top) and meridional velocity (bottom). All locations with large differences between HAMTIDE (**Fig. 5.20**) and FES2004 (**Fig. 5.22**) show peaks at the M_2 aliasing period in the JTP velocity frequency spectra. Smaller less prominent peaks can be seen for the aliasing period of S_2 that are not shown here.

The results suggest that the “parallel-track-approach” to estimating instantaneous surface geostrophic currents is capable of detecting tidal currents over the global ocean. Further improved estimates of tidal constituents could be obtained through new models using data assimilation and a high horizontal resolution. To test the assumption, the FES2004 tide correction could be replaced by a newer version of tide models as the HAMTIDE tide model to verify whether the differences between both models as observed in **Fig. 5.20** can reduce the tide signal from the frequency spectra of geostrophic velocity.

5.5. Summary

Within this chapter, the spectral distribution in the frequency and in the wavenumber domain of the geostrophic flow-field and resulting EKE were presented. As the oceanic variability is broadband and comprises all time and spacial scales, the spectral frequency and wavenumber distributions clarified the impact of the different scales. The description of the seasonal cycle indeed implied important information, but reflected only a part of the oceanic variability. With the JTP tandem mission it was for the first time possible to calculate the frequency and wavenumber spectra for the zonal and meridional geostrophic velocity components separately and for the resulting EKE along the virtual velocity track.

The **frequency spectra** were calculated for each along-track position and subsequently gridded to obtain regional ($10^\circ \times 10^\circ$) and global mean frequency spectra of geostrophic velocity anomalies and of EKE.

Within the global mean frequency spectra, the annual peak was the most prominent followed by the peak at the half year period. At periods longer than half a year, the zonal velocity component was more energetic than the meridional and the the year- and half-year frequencies were far more pronounced. The geostrophic velocities showed relations of f^{-2} for periods shorter than 60 days, $f^{-3/2}$ for periods between 60 and 180 days and $f^{-1/2}$ within the range between 180 and 365 days.

The global mean EKE frequency spectrum showed a clear annual and 3-year peak and slopes of $f^{-3/2}$ were obtained for periods shorter than 100 days, f^{-1} for periods ranging from 100 up to 365 days and a white spectrum was seen on longer periods.

A comparison with the global mean velocity spectra obtained from the OSCAR data set showed an overall agreement, except for the under/overestimated meridional/zonal component in the OSCAR data for periods longer/shorter than 100 days. The amplitudes of the annual and semiannual peaks were most pronounced and sharpest for the 15-year OSCAR

⁵The lower noise level of **f** was omitted for display purposes as it ranges below a PSD of 10^{-1} .

time series where the energy decrease was shifted to longer periods.

The basin wide averaged frequency spectra contained an average number of 65, 71 and 47 values in time for the Pacific, Atlantic and Indian Ocean, respectively. The Pacific basin wide frequency spectra were nearly equal to the global mean spectra, whereas the spectra for the Atlantic contained less energy than the global spectra for periods longer than about half a year. The PSDs were the largest in the Indian Ocean due to the fewer low energy regions in the Indian Ocean and additionally a scarce data coverage. Only $\sim 16\%$ of all data came from the Indian Ocean. Hence, the high frequencies were less well sampled in the Indian Ocean compared to the Pacific and Atlantic. The comparison of the basin wide EKE frequency spectra revealed similar shapes for periods smaller than 100 days and a clear difference for longer periods. There, the Atlantic showed the lowest PSDs followed by the Pacific with PSDs close to the global mean and the Indian Ocean with the largest PSDs. The annual frequency, however, was pronounced in all basins. A peak at 125 days in the equatorial Atlantic could be identified by westward propagating Rossby waves (compare CHELTON AND SCHLAX, 1996).

Global maps, containing regional distributions across all $10^\circ \times 10^\circ$ areas of the frequency spectra for the geostrophic velocities and EKE emphasized the regional energy distribution in a global context. Therewith high and low energy areas could clearly be identified. Those were the equatorial regions, with larger PSDs north of the equator, as well as the big current systems as the Kuroshio, Gulf Stream, Agulhas Retroflexion, Brazil Malvinas Confluence region and the ACC. Thus, spectra calculated over high energy regions showed a red behavior and tended to a slow decay only for the longest periods, whereas the low energy regions can be identified by smaller PSD with white to even blue spectral behavior for the long period end of the spectra.

To highlight the latitudinal distribution, globally frequency spectra averaged over 10° latitude were discussed. Therewith the latitudinal differences got clearly visible, as there were for example the pronounced annual peak in the tropical regions and the larger PSD level for the zonal geostrophic velocity component in low latitudes ($15^\circ - 25^\circ$ N and S) compared to the meridional, for periods longer than half a year.

The spectral behavior of geostrophic velocities for diverse energetic regimes (low energy regions, bulk of the ocean, high energy regions, equatorial region) were characterized by different RMS SSH variabilities. In spite of different PSD levels, they showed similar slopes for all subregions. For the geostrophic velocities, thus, a general slope of f^{-2} was found for the high frequency part of all spectra and a slope of $f^{-1/2}$ could be attributed to periods longer than half a year for the zonal velocity component and a close to white spectral behavior for the meridional component. Only minor deviations were found within the equatorial spectral slopes, most likely due to the increased error level there, along with enhanced annual and semiannual peaks in the equatorial zonal component.

Similar shapes were also found within the regional averaged EKE frequency spectra. Beside a nearly white low frequency end for periods longer than a year, the extra-tropical regions had slopes of $f^{-5/3}$ and $f^{-3/4}$ for periods shorter and longer than 100 days, respectively. Interestingly, the high frequency part of the low energy regions and the equatorial region for periods shorter than a year showed, despite their different PSD level, an equal slope of $f^{-4/3}$ mainly due to the small signal to error relation in those regions.

A very regional comparison between a frequency spectrum derived from nine years (1977-1989) of RCM measurements (450 m depth) within the “Kiel276 mooring” in the Canary Basin and an average frequency spectrum over the according $5^\circ \times 5^\circ$ region⁶ from JTP

⁶To avoid the noise within the JTP spectra.

showed astonishingly similar behavior for both geostrophic velocity components as well as PSD levels at the same order of magnitude.

The **wavenumber spectra** of the geostrophic velocity estimates and EKE were calculated alongside the along-track JTP virtual ground track and were divided into sections spanning 10° of latitude ranging from 60° S to 60° N. However, one had to be aware of the JTP tandem mission conditions such as the distances between the pairs of SSH-measurements that were used to calculate the geostrophic velocities in the order of up to 220 km at the equator. They allowed only large mesoscale eddies to be resolved with the JTP tandem constellation. Moreover, the JTP track direction was shown to be almost diagonally oriented and therefore the spectral wavenumber information was calculated along those “diagonal” JTP tracks. But as both the ascending and descending arcs were averaged, wavenumber information from both directions was considered. The global wavenumber spectrum was obtained by averaging all along-track $10^\circ \times 10^\circ$ spectra in space and time.

The globally averaged wavenumber spectra of both velocity components showed equal PSDs for wavelengths shorter than 200 km with a slope of $\tilde{\nu}^{-2}$. This slope continued for the meridional component onto longer wavelengths. However, the zonal component followed a steeper slope of $\tilde{\nu}^{-3}$ up to a wavelength of 300 km. For wavelengths longer than 300 km, the zonal component then had a slope of $\tilde{\nu}^{-1/2}$. The different slopes between zonal- and meridional-wavenumber spectra of zonal and meridional velocity were shown before (ZANG AND WUNSCH, 2001) to follow from geostrophy. However, as the JTP velocities were calculated along-track, they had to be different from purely zonal- or meridional-wavenumber spectra.

For the globally averaged EKE wavenumber spectra, slopes of $\tilde{\nu}^{-2}$ and $\tilde{\nu}^{-6/5}$ were visible for wavelengths shorter and longer than 180 km, respectively.

The wavenumber spectra were averaged across each basin to highlight their differences. For the Pacific, the averaged spectra are nearly indistinguishable from the global wavenumber spectrum. The same was true for the Atlantic, only the zonal geostrophic velocity component has lower PSDs at wavelengths longer than 400 km and the PSD of the EKE wavenumber spectrum was slightly decreased. Compared to the other basins and to the global spectra, the wavenumber spectra of the Indian Ocean contained the highest PSDs. However, the slopes did not differ significantly.

Regional distributions across all $10^\circ \times 10^\circ$ areas of the wavenumber spectra for the geostrophic velocities and EKE were shown within global maps to emphasize the regional energy distributions in a global context. The highest PSDs were again found in the equatorial and boundary current regions. Within these highly energetic regions, a straight red spectrum was found for the geostrophic velocities with a single peak and a decrease towards longer wavelengths. In contrast, a few regions of lower energy exhibited a plateau rather than a single peak. Furthermore, the slopes differed significantly in the low energy regions between both velocity components.

Within all $10^\circ \times 10^\circ$ regions, generally red EKE wavenumber spectra were observed with a white long-wavelengths tail. However, they differed significantly in their magnitudes.

A change of the cutoff wavelength was seen within meridional sections. To emphasize the changing cutoff wavelengths, wavenumber spectra of global averaged 10° zonal bands were calculated. Within the wavenumber spectra of geostrophic velocities and EKE, a cutoff wavelength was determined by the length of the arc-segments spanning 10° in latitude. The arc-segment length varied between 1185 km and 1567 km for the 5° and 55° latitude band, respectively. However, a second cutoff wavelength was determinable. For the wavenumber spectra of zonal/meridional geostrophic velocity, the cutoff wavelength varied in the range of

400/700 km and 350/600 km down to 280/280 km, at 15°, 35° and 55° latitude, respectively. The cutoff wavelength in the EKE wavenumber spectrum varied according to the distances over which the geostrophic velocities were calculated from the SSH measurements, ranging from ~ 200 km at 5° to 100 km at 55° latitude.

It was proposed that the track spacing of the satellite track as well as the arc-segment length significantly influenced the shape of the wavenumber spectra for the JTP tandem data set.

Averaged wavenumber spectra were calculated over different energetic regions as the low energy, bulk of the ocean, high energy and equatorial regions. Except for the equatorial region with a general slope of $\tilde{\nu}^{-2}$, the spectral behaviors were equal for the other regions but with differing PSD levels. Hence, the wavenumber spectra of geostrophic velocity showed a general slope of $\tilde{\nu}^{-3}$ for wavelengths shorter than the cutoff wavelengths (300 km - 400 km). A flatter slope was found for the meridional component on wavelengths longer than 200 km and within the high and low energy regions a slope of $\tilde{\nu}^{-5}$ was evident between ~ 100 and ~ 300 km. For longer wavelengths, the meridional component had slopes close to $\tilde{\nu}^{-3/5}$ whereas the zonal component continued in a white spectral behavior.

For the different energetic regions, the wavenumber spectra of EKE had similar slopes of $\tilde{\nu}^{-5/4}$ and $\tilde{\nu}^{-3}$ for longer and shorter wavelengths than 150 km, except for low wavenumber end of the equatorial region which showed a slope close to $\tilde{\nu}^{-2}$.

As proposed before, the wavenumber spectra showed with some restrictions a strikingly universal shape over the entire extra-tropical ocean. The restrictions were namely the different slopes within the spectra for both velocity components and the slope of $\tilde{\nu}^{-5/4}$ for the EKE wavenumber spectrum being flatter than predicted by theory.

Two comparisons in the North Atlantic were examined, the first with transverse along-track geostrophic Geosat velocities (30° - 40° N, 70° - 60° W). In the wavelength range between 100 km and 400 km, the wavenumber spectrum obtained from Geosat was closer related to the wavenumber spectrum of the meridional velocity from JTP.

The second comparison was within the same latitude band but across all 10° sections in the North Atlantic from cross track T/P velocity estimates. In contrast, the JTP data did not show the PSD decrease for wavelengths longer than 400 km as for the T/P cross-track velocities. Further interesting features became evident such as the PSD-decrease moving from west to east (i. e. from the energetic boundary current towards a less energetic region) and the slope-decrease within the meridional component.

The recent discussion about the underlying turbulence theory behind the spectral wavenumber slopes was addressed. As in previous studies of SSH, the SQG theory could explain the spectral behavior ($\tilde{\nu}^{-5/3}$) on wavelengths longer than ~ 150 km within the regions of high eddy energy as the Kuroshio, Gulf Stream and Agulhas Retroflexion.

Finally, it was investigated whether the peaks close to the **M₂** and **S₂** aliasing periods of 62.1 and 57.8 days could have been related to oceanic processes or were rather not sufficiently corrected tidal signals. A regional study revealed that the signal originates from only a few regions on the continental shelves. Within these regions, the largest differences between the FES2004 and the HAMTIDE tidal model existed, which suggested that the peaks at the aliasing periods of the M₂ and S₂ tides could be explained due to difficulties in the tidal solutions of the FES2004 tidal model in the costal and shelf regions. Therefore, it was suggested to recalculate the JTP data set for a test of that assumption.

6. Conclusions and Outlook

The aim of this thesis is to investigate the basic statistics of the oceanic flow-field using the geostrophic current estimates available from the Jason-1 - TOPEX/Poseidon tandem mission covering three years of SSH data from September, 2002, to September, 2005. The satellites measured the SSH with an along-track resolution of 6.2 km, a track spacing of 157 km at the equator and an inclination of 66° . While the time covered by the data is still short (three years) for an elaborate evaluation of statistical quantities, the analysis demonstrates the value of geostrophic velocity estimates which can be computed from the JTP SSH fields. As previously demonstrated for the first month of the JTP tandem mission (STAMMER, 1997a), the data set gives the opportunity to calculate geostrophic velocities for the zonal and meridional velocity components separately and for each along-track position. Therefore, the JTP tandem mission was the first satellite observing system to obtain geostrophic velocities along track without the assumption of isotropy, turning the two altimeter satellites TOPEX/Poseidon and Jason-1 into a space born near real time current meter.

In order to describe the distribution of the geostrophic velocity anomalies, a global PDF is shown that has a clear exponential shape as a consequence of the significant variance of EKE over the global ocean. However, when the PDFs are calculated across smaller regions with only low variability, a clear Gaussian shape appears as shown before in GILLE AND SMITH (2000). Hence, the exponential shape is the result of averaging Gaussian PDFs with different PDF-width. Moreover, all PDFs have Gaussian shapes when normalized by their STD.

In particular, the study underlines the importance of the JTP velocity estimates for the understanding of the spatial structures of flow changes on the annual period (SCHARFFENBERG AND STAMMER, 2010). Results reproduce conclusions drawn from several studies which are available on a regional basis, as for example the clear dominance of the seasonal flow changes in low latitudes. However, they are extended to the basin-scale and into a global context. At the same time, complex structures of the seasonally changing flow-field are revealed. In the western Pacific, for instance, they appear as zonally coherent jet-like structures. Furthermore, complex phase structures are found in mid- and high latitudes. To what extent all of those structures represent the ocean still has to be investigated. However, it is reassuring in this context that similar structures could be reproduced while using the longer time series available from the OSCAR data set (JOHNSON ET AL., 2007). Moreover, first preliminary results that use model output from a $1/10^\circ$ global ocean circulation model also seem to reproduce the complex phase structures from altimetric data. Their dynamical causes could not be identified and next steps will need to use the model output for a better understanding of the dynamical processes leading to those complex structures of the seasonally changing flow-field.

Somewhat unexpected is the result of a slight excess of meridional eddy variability over most parts of the mid latitudes. From previous results (e.g. WUNSCH, 1997), an isotropic eddy field was expected. These results have to be revisited using model outputs to discriminate data uncertainties from dynamical principles responsible for the slightly enhanced

meridional eddy variance. The findings from the JTP tandem mission agree with a recent publication by SCOTT ET AL. (2008) who found an excess of meridional eddy variability in a numerical simulation of the mesoscale eddy field.

While still preliminary, the analysis reveals a very complex relation between the filtered large-scale EKE and the MKE in the ocean. As expected, for large parts of the ocean the EKE field is a factor of 10^2 to 10^3 larger than the MKE field. However, this certainly does not hold for all regions and in intense current regions the factor was only of the order of 1-10. The JTP results suggest that this holds particularly all along the ACC. On global average, a ratio of large-scale EKE/MKE of 6-7 is obtained. But for a more accurate investigation, results from the European Space Agency (ESA) GOCE gravity mission (JOHANNESSEN ET AL., 2003) and the wide-swath altimeter mission (SWOT, FU AND RODRIGUEZ, 2004; FU AND FERRARI, 2008) have to be awaited which will allow to recompute the MKE and EKE with an accuracy required to gain more insight into the spatial structures of the relation of MKE to EKE, respectively. Until now, both the fields of EKE and MKE are considered to be lower bound estimates. On the other hand, a much longer time series of altimetric geostrophic currents is required. Data sets like OSCAR or the AVISO objective analyses can serve as a basis to compute geostrophic currents. Nevertheless, the analysis reveals shortcomings in those data sets, for example in high latitudes where essentially most of the fast barotropic variability of the flow-field is filtered out through smoothing in time.

In contrast, the tandem velocities can be used to evaluate the annual cycle of the EKE without any temporal filtering and without the assumption of isotropy (SCHARFFENBERG AND STAMMER, 2010). All major current systems stand out in magnitude of their seasonal EKE changes. In particular, basic structures in the seasonal changes of the EKE field reproduce earlier results from STAMMER AND WUNSCH (1999). However, seasonal changes in the EKE field seem to be significant only in regions where seasonally modulated currents are prevailing (notably the low latitudes), and where seasonally varying wind fields lead to enhanced barotropic variability (notably the high latitudes). In general, the annual cycle is more significant in the northern hemisphere. In the Indian Ocean, an obvious westward moving annual EKE signal could be detected at 25° S that can be related to westward propagating Rossby waves, most likely generated at the western Australian shelf, or to large non-linear eddies. The Rossby waves could strengthen the eddy field within the SICC from where the signal moves on to the African coast joining the Mozambique Current until it gets to the Agulhas Retroflexion region. Another interesting annual EKE signal appears in the Gulf of Tehuantepec close to the Central American continent in the eastern equatorial Pacific this signal is related to the strong seasonal winds through the Isthmus of Tehuantepec that cause substantial EKE variability there.

The oceanic variability is broadband and comprises all temporal and spacial scales, hence spectral frequency and wavenumber distributions can clarify the impact of the different scales. This has been done in previous studies, however, with the JTP tandem mission it has been possible for the first time to calculate frequency and wavenumber spectra for the zonal and meridional geostrophic velocity components separately as well as for the resulting EKE along the satellite track. The opportunity to study each velocity component on its own yields an important increase in knowledge to the general spectral behavior of the ocean circulation.

Within the global mean frequency spectra of the geostrophic velocities and EKE, the annual peak is the most prominent. The peak becomes even more pronounced and sharper when looking at longer time series as the 15-year OSCAR data set. The separate ocean basins differ in the magnitude of their PSD. Out of there, the Atlantic is the least energetic basin,

followed by the Pacific with a PSD close to the global mean and the Indian Ocean which is the most energetic. The same holds for the basin wide EKE frequency spectra that indicate clear PSD-differences on longer periods. To emphasize the regional energy distributions of all spectra averaged over $10^\circ \times 10^\circ$ areas in a global context, they are displayed within global maps. Therewith high and low energy areas can be clearly identified due to the different shapes of the spectra. Furthermore, spectra calculated solely over high energy regions showed a red behavior and an only a slow decay for the longest periods, whereas the low energy regions can be identified by smaller PSD and white to even blue spectral behavior for the long period end of the spectra. Latitudinal differences exist such as the pronounced annual peak in the tropical regions and the larger PSD level for the zonal compared to the meridional geostrophic velocity component in low latitudes for periods longer than half a year, which is related to the excess of meridional eddy variability over most parts of the mid latitudes and will be revisited in that context. Spectra calculated over all low and high energy regions, over the bulk of the ocean and over the equatorial regions, respectively, show similar slopes for the geostrophic velocities in all subregions as well as different PSD levels according to their variability and enhanced annual and semiannual peaks in the equatorial zonal component. Similar shapes can also be found within the regional averaged frequency spectra of the EKE. A very regional comparison between a frequency spectrum from a mooring in the Canary Basin and JTP yield astonishingly similar behavior for both geostrophic velocity components and their respective PSDs.

In a few regions on the continental shelves, peaks close to the M_2 and S_2 aliasing periods of 62.1 and 57.8 days are evident and are most likely related to insufficiently removed tidal signals through the FES2004 tide model, which is known to have difficulties within the tidal solutions in the coastal and shelf regions (LYARD ET AL., 2006). The assumption that these peaks do not reflect ocean eddies is supported by the differences between the FES2004 and the more recent HAMTIDE tide models (TAGUCHI AND STAMMER, 2010) that appear in the same regions where the peaks in the aliasing frequencies are visible. Therefore, the JTP data will be recalculated in a future study using the recent HAMTIDE tide model to verify whether the peaks at the tidal aliasing frequencies in the spectra of the geostrophic velocities can be reduced.

There has been a long evolution of wavenumber spectra over the years since the pioneering work of FU (1983) who showed the first wavenumber spectra derived from Geosat data. The spacial resolution went to shorter wavelengths as the errors of the SSH measurements from the different satellites decreased. For the smoothed JTP wavenumber spectra, this range is now as small as 30 km. However, the resolved eddy scales are an order of magnitude larger due to the large track spacing of the JTP tandem mission and the concerning distances over which the geostrophic velocities have been estimated. The wavenumber spectra for the geostrophic velocity estimates and EKE are calculated alongside the along-track JTP virtual ground track within each $10^\circ \times 10^\circ$ area ranging from 60° S to 60° N. Therewith scales up to 1185 km in the 5° and 1567 km at 55° latitude band are resolved defining the cutoff wavelength for the calculated wavenumber spectra.

The global averaged geostrophic velocity wavenumber spectra show equal PSDs for both components on to wavelengths of 200 km with a slope of $\tilde{\nu}^{-2}$. This slope continues for the meridional component onto longer wavelengths. However, the the zonal component follows a steeper slope of $\tilde{\nu}^{-3}$ up to a wavelength of 300 km. The variance in slope between zonal- and meridional-wavenumber spectra of zonal and meridional velocity has been shown before (ZANG AND WUNSCH, 2001) to follow from geostrophy. However, as the JTP velocities are calculated along-track, they have to be different from purely zonal- or meridional-wavenumber spectra, and as their relation varies with latitude, the situation becomes com-

plex. The global averaged EKE wavenumber spectra have slopes of $\tilde{\nu}^{-2}$ and $\tilde{\nu}^{-6/5}$ for wavelengths shorter and longer than 180 km, respectively. The basin wide averaged spectra again display different energy levels as seen before in the frequency spectra. However, the shapes and slopes do not differ significantly between the three basins and are close to the global mean. In regional energy distributions for all wavenumber spectra averaged over $10^\circ \times 10^\circ$ areas, the highest PSDs can be seen in the equatorial and boundary current regions. These regions show a straight red spectrum for the geostrophic velocities in contrast to a few lower energetic regions that exhibit a plateau rather than a single peak. Furthermore, significantly different slopes exist for both velocity components in the low energy regions. There is a clear latitudinal dependence of the cutoff wavelength different for both velocity components that goes along with their different slopes on wavelengths longer than ~ 180 km and varies for the EKE wavenumber spectra according to the distances over which the geostrophic velocities are calculated. These results suggest that the track spacing of the satellite track as well as the arc-segment length have significant influence on the shape of the wavenumber spectra derived by the JTP tandem data set. Regional wavenumber spectra of geostrophic velocity that are averaged over all low and high energy regions, over the bulk of the ocean and over the equatorial regions, respectively, show the same spectral behavior for all extratropical regions, but on different PSD levels and with a change in slope in the meridional velocity component. The equatorial region itself has a general slope of $\tilde{\nu}^{-2}$ over all wavelengths. The same division for the wavenumber spectra of EKE results in nearly similar slopes of $\tilde{\nu}^{-5/4}$ and $\tilde{\nu}^{-3}$ for wavelengths longer and shorter than 150 km. Therewith the question of the generality of the spectral behavior (FERRARI AND WUNSCH, 2010) or, even more general, of the whole extra-tropical spectral behaviors can be answered by the strikingly universal shape of the wavenumber spectra show here with minor restrictions. These restrictions are the different slopes within the spectra from both velocity components and the slope of $\tilde{\nu}^{-5/4}$ for the EKE wavenumber spectrum which is flatter than predicted by theory.

Previous studies of SSH (LE TRAON ET AL., 2008) showed that the slopes derived from altimetry in high energy regions follow a relation that is in close agreement with the SQG theory. Kinetic energy spectra shown here for the same high energy regions indicate the proposed slope for the SQG theory of $\tilde{\nu}^{-5/3}$ on wavelengths longer than 150 km, whereas for shorter wavelength (< 100 km) a clear $\tilde{\nu}^{-3}$ relation is evident. Therewith, the spectra of the geostrophic velocities from the JTP tandem mission support the SQG theory but show clear deviations in the wavelength range shorter than 150 km. That range has been shown to have uncertainties due to the resolvable scales in the JTP measurement setup. Hence, a closer track separation would have increased the confidence in the smaller wavelength of the geostrophic velocity and EKE wavenumber spectra.

This thesis examines the increase of knowledge gained by the process of obtaining instantaneous velocity estimates through a “parallel-track-approach” that is an attractive procedure for observing ocean currents. Nevertheless, it should be recalled that due to the relatively wide track separation between the T/P and Jason-1 satellites only the variability of large eddies exceeding about 500 km in wavelength are investigated. To examine the variability down to shorter wavelength, the two tracks should be moved further together as suggested by LEEUWENBURGH AND STAMMER (2002). While it is unlikely that this will be established with two satellites in the near future (the follow on tandem mission of Jason-1 and Jason-2 is already in orbit with the same track separation as JTP), the anticipated SWOT mission (FU AND RODRIGUEZ, 2004; FU AND FERRARI, 2008) will provide measurements on spatial scales on the order of 10 km. With those novel data, it will finally be possible to investigate a large part of the eddy spectrum that could not be resolved with present technology. Next to the remaining questions that appeared within this thesis from JTP, a further step will

be to include the SSH data from the ongoing tandem mission of Jason-1 and Jason-2 to get an even longer time series. Unlikely both satellites fly with a five day offset making direct velocity calculations difficult. An interesting goal will thereby be the connection of both data sets that, are well separated in time, especially for the spectral frequency and wavenumber calculations.

References

- BALDWIN, M. P., P. B. RHINES, H.-P. HUANG and M. E. MCINTYRE, 2007: The Jet-Stream Conundrum. *Science*, **315**, 467–468.
- BIROL, F. and R. MORROW, 2003: Separation of quasi-semiannual Rossby waves from the eastern boundary of the Indian Ocean. *Journal of Marine Research*, **61** (6), 707–723.
- BLUMEN, W., 1978: Uniform Potential Vorticity Flow: Part I. Theory of Wave Interactions and Two-Dimensional Turbulence. *Journal of the Atmospheric Sciences*, **35**, 774–783.
- BONJEAN, F. and G. S. E. LAGERLOEF, 2002: Diagnostic Model and Analysis of the Surface Currents in the Tropical Pacific Ocean. *Journal of Physical Oceanography*, **32**, 2938–2954.
- BRACCO, A., J. H. LACASCE and A. PROVENZALE, 2000: Velocity Probability Density Functions for Oceanic Floats. *Journal of Physical Oceanography*, **30**, 461–474.
- BRANDT, P., F. A. SCHOTT, A. FUNK and C. S. MARTINS, 2004: Seasonal to interannual variability of the eddy field in the Labrador Sea from satellite altimetry. *Journal of Geophysical Research*, **109**, C02028.
- BRATH, M., 2007: Analysen von Wirbelenergie und Wirbeltransporten im sub-polaren Nordatlantik. Diploma thesis, University of Hamburg, Institut für Meereskunde, KlimaCampus Universität Hamburg, Germany.
- BRATH, M., M. G. SCHARFFENBERG, N. SERRA and D. STAMMER, under revision: Altimeter-based Estimates of Eddy Variability and Eddy Transports in the Sub-polar North Atlantic. *Marine Geodesy*.
- BUSALACCHI, A. J. and J. J. O'BRIEN, 1980: The Seasonal Variability in a Model of the Tropical Pacific. *Journal of Physical Oceanography*, **10**, 1929–1951.
- CAPET, X., P. KLEIN, B. L. HUA, G. LAPEYERE and J. C. MCWILLIAMS, 2008: Surface kinetic energy transfer in surface quasi-geostrophic flows. *Journal of Fluid Mechanics*, **604**, 165–174.
- CHELTON, D., M. SCHLAX, J. LYMAN and G. JOHNSON, 2003: Equatorially trapped Rossby waves in the presence of meridionally sheared baroclinic flow in the Pacific Ocean. *Progress in Oceanography*, **56**, 323–380.
- CHELTON, D. B., J. C. RIES, B. J. HAINES, L.-L. FU and P. S. CALLAHAN, 2001: *Satellite Altimetry and Earth Sciences*, Academic Press, Chapter Satellite Altimetry.
- CHELTON, D. B. and M. G. SCHLAX, 1996: Global Observations of Oceanic Rossby Waves. *Science*, **272**, 234–238.

- CHELTON, D. B., M. G. SCHLAX, R. M. SAMELSON and R. A. DE SZOEKE, 2007: Global observations of large oceanic eddies. *Geophysical Research Letters*, **34**, L15606.
- CHEN, S. and B. QIU, 2004: Seasonal variability of the South Equatorial Countercurrent. *Journal of Geophysical Research*, **109**, C08003.
- CHU, P. C., 2008: Probability distribution function of the upper equatorial Pacific current speeds. *Geophysical Research Letters*, **35**, L12606.
- CRAWFORD, W. R., J. Y. CHERNIAWSKY and M. G. G. FOREMAN, 2000: Multi-year meanders and eddies in the Alaskan Stream as observed by TOPEX/Poseidon altimeter. *Geophysical Research Letters*, **27** (7), 1025–1028.
- DANILOV, S. and D. GURARIE, 2002: Rhines scale and spectra of the b-plane turbulence with bottom drag. *Physical Review E*, **65**, 067301.
- DANILOV, S. and D. GURARIE, 2004: Scaling, spectra and zonal jets in beta-plane turbulence. *Physics of Fluids*, **16** (7), 25922603.
- DE RUIJTER, W. P. M., H. RIDDERINKHOF, J. R. E. LUTJEHARMS, M. W. SCHOUTEN and C. VETH, 2002: Observations of the flow in the Mozambique Channel. *Geophysical Research Letters*, **29** (10), 1502.
- DICKSON, R. R., W. J. GOULD, P. A. GURBUTT and P. D. KILLWORTH, 1982: A seasonal signal in ocean currents to abyssal depths. *Nature*, **295**, 193–198.
- DONG, S. and K. A. KELLY, 2003: Seasonal and interannual variations in geostrophic velocity in the Middle Atlantic Bight. *Journal of Geophysical Research*, **108** (C6), 3172.
- DOUGLASS, E., D. ROEMMICH and D. STAMMER, 2006: Interannual variability in northeast Pacific circulation. *Journal of Geophysical Research*, **111**, C04001.
- DUCET, N. and P.-Y. L. TRAON, 2001: A comparison of surface eddy kinetic energy and Reynolds stresses in the Gulf Stream and the Kuroshio Current systems from merged TOPEX/Poseidon and ERS-1/2 altimetric data. *Journal of Geophysical Research*, **106** (C8), 16,603–16,622.
- DUCET, N., P. Y. L. TRAON and G. REVERDIN, 2000: Global high-resolution mapping of ocean circulation from TOPEX/Poseidon and ERS-1 and -2. *Journal of Geophysical Research*, **105** (C8), 19,477–19,498.
- EDEN, C. and C. BÖNING, 2002: Sources of Eddy Kinetic Energy in the Labrador Sea. *Journal of Physical Oceanography*, **32**, 3346–3363.
- EMERY, W. J., 1983: On the Geographical Variability of the Upper Level Mean and Eddy Fields in the North Atlantic and North Pacific. *Journal of Physical Oceanography*, **13** (2), 269–291.
- FENG, M., G. MEYERS, A. PEARCE and S. WIJFFELS, 2003: Annual and interannual variations of the Leeuwin Current at 32° S. *Journal of Geophysical Research*, **108** (C11), 3355.
- FERRARI, R. and C. WUNSCH, 2009: Ocean Circulation Kinetic Energy: Reservoirs, Sources, and Sinks. *Annual Reviews of Fluid Mechanics*, **41**, 253–282.
- FERRARI, R. and C. WUNSCH, 2010: The Distribution of Eddy Kinetic and Potential Energies in the Global Ocean. *Tellus*, submitted.

- FLAGG, C. N., G. SCHWARTZE, E. GOTTLIEB and T. ROSSBY, 1998: Operating an Acoustic Doppler Current Profiler aboard a Container Vessel. *Journal of Atmospheric and Oceanic Technology*, **15**, 257–271.
- FU, L.-L., 1983: On the Wave Number Spectrum of Oceanic Mesoscale Variability Observed by the SEASAT Altimeter. *Journal of Geophysical Research*, **88** (C7), 4331–4341.
- FU, L.-L. and A. CAZENAVE, Hg., 2001: *Satellite Altimetry and Earth Sciences*. Academic Press.
- FU, L.-L., E. J. CHRISTENSEN, C. A. YAMARONE JR., M. LEFEBVRE, Y. MNARD, M. DORRER and P. ESCUDIER, 1994: TOPEX/POSEIDON Mission Overview. *Journal of Geophysical Research*, **99** (C12), 24,369–24,381.
- FU, L.-L. and R. FERRARI, 2008: Observing Oceanic Submesoscale Processes From Space. *EOS, Transactions, American Geophysical Union*, **89** (48), 488.
- FU, L.-L. and E. RODRIGUEZ, 2004: Observing the Ocean with a Wide Swath Altimeter. *AVISO*, (10), 15–17.
- FUENZALIDA, R., W. SCHNEIDER, J. GARCÉS-VARGAS and L. BRAVO, 2008: Satellite altimetry data reveal jet-like dynamics of the Humboldt Current. *Journal of Geophysical Research*, **113**, C07043.
- GILLE, S. T. and S. G. L. SMITH, 2000: Velocity Probability Density Functions from Altimetry. *Journal of Physical Oceanography*, **30**, 125–136.
- GODFREY, J. S. and K. R. RIDGWAY, 1985: The Large-Scale Environment of the Poleward-Flowing Leeuwin Current, Western Australia: Longshore Steric Height Gradients, Wind Stresses and Geostrophic Flow. *Journal of Physical Oceanography*, **15**, 481–495.
- GREENSLADE, D. J. M., D. B. CHELTON and M. G. SCHLAX, 1997: The Midlatitude Resolution Capability of Sea Level Fields Constructed from Single and Multiple Satellite Altimeter Datasets. *Journal of Atmospheric and Oceanic Technology*, **14**, 849–870.
- HELD, I. M., R. T. PIERREHUMBERT, S. T. GARNER and K. L. SWANSON, 1995: Surface quasi-geostrophic dynamics. *Journal of Fluid Mechanics*, **282**, 1–20.
- HOLLAND, C. L. and G. T. MITCHUM, 2001: Propagation of Big Island eddies. *Journal of Geophysical Research*, **106** (C1), 935–944.
- HUA, B. L., M. D'ORGEVILLE, M. D. FRUMAN, C. MENESGUEN, R. SCHOPP, P. KLEIN and H. SASAKI, 2008: Destabilization of mixed Rossby gravity waves and the formation of equatorial zonal jets. *Journal of Fluid Mechanics*, **610**, 311–341.
- HUANG, H.-P., A. KAPLAN, E. N. CURCHITSER and N. A. MAXIMENKO, 2007: The degree of anisotropy for mid-ocean currents from satellite observations and an eddy-permitting model simulation. *Journal of Geophysical Research*, **112**, C09005.
- JOHANNESSEN, J. A., G. BALMINO, C. LE PROVOST, R. RUMMEL, R. SABADINI, H. SÜNKEL, C. C. TSCHERNING, P. VISSER, P. WOODWORTH, C. W. HUGHES, P. LEGRAND, N. SNEEUW, F. PEROSANZ, M. AGUIRRE-MARTINEZ, H. REBHAN and M. R. DRINKWATER, 2003: The European Gravity Field and Steady-State Ocean Circulation Explorer Satellite Mission: Its Impact on Geophysics. *Surveys in Geophysics*, **24** (4), 339–386.

- JOHNSON, E. S., F. BONJEAN, G. S. E. LAGERLOEF, J. T. GUNN and G. T. MITCHUM, 2007: Validation and Error Analysis of OSCAR Sea Surface Currents. *Journal of Atmospheric and Oceanic Technology*, **24**, 688–701.
- JOHNSON, G. C., B. M. SLOYAN, W. S. KESSLER and K. E. MCTAGGART, 2002: Direct measurements of upper ocean currents and water properties across the tropical Pacific during the 1990s. *Progress in Oceanography*, **52**, 31–61.
- JOHNSON, T. J., R. H. STEWART, C. SHUM and B. D. TAPLEY, 1992: Distribution of Reynolds Stress carried by mesoscale variability in the Antarctic Circumpolar Current. *Geophysical Research Letters*, **19** (12), 1201–1204.
- KAMENKOVICH, I., P. BERLOFF and J. PEDLOSKY, 2009: Role of Eddy Forcing in the Dynamics of Multiple Zonal Jets in a Model of the North Atlantic. *Journal of Physical Oceanography*, **39**, 1361–1379.
- KELLY, K. A., R. C. BEARDSLEY, R. LIMBURNER, K. H. BRINK, J. D. PADUAN and T. K. CHERESKIN, 1998: Variability of the near-surface eddy kinetic energy in the California Current based on altimetric, drifter, and moored current data. *Journal of Geophysical Research*, **103** (C6), 13,067–13,08.
- KELLY, K. A. and S. T. GILLE, 1990: Gulf Stream Surface Transport and Statistics at 69° W from the Geosat Altimeter. *Journal of Geophysical Research*, **95** (C3), 3149–3161.
- KESSLER, W. S., 2006: The circulation of the eastern tropical Pacific: A review. *Progress in Oceanography*, **69** (2-4), 181–217.
- KESSLER, W. S. and L. GOURDEAU, 2006: Wind-driven zonal jets in the South Pacific Ocean. *Geophysical Research Letters*, **33**, L03608.
- KLEIN, P., B. L. HUA, G. LAPEYERE, X. CAPET, S. LE GENTIL and H. SASAKI, 2008: Upper Ocean Turbulence from High-Resolution 3D Simulations. *Journal of Physical Oceanography*, **38**, 1748–1763.
- KNUTSEN, Ø., H. SVENDSEN, S. ØSTERHUS, T. ROSSBY and B. HANSEN, 2005: Direct measurements of the mean flow and eddy kinetic energy structure of the upper ocean circulation in the NE Atlantic. *Geophysical Research Letters*, **32**, L14604.
- KRAICHNAN, R. H., 1967: Inertial Ranges in Two-Dimensional Turbulence. *Physics of Fluids*, **10** (7), 1417–1423.
- LAGERLOEF, G. S. E., G. T. MITCHUM, R. B. LUKAS and P. P. NIILER, 1999: Tropical Pacific near-surface currents estimated from altimeter, wind, and drifter data. *Journal of Geophysical Research*, **104** (C10), 23,313–23,326.
- LAPEYERE, G. and P. KLEIN, 2006: Dynamics of the Upper Oceanic Layers in Terms of Surface Quasigeostrophy Theory. *Journal of Physical Oceanography*, **36**, 165–176.
- LAPEYRE, G., 2009: What Vertical Mode Does the Altimeter Reflect? On the Decomposition in Baroclinic Modes and on a Surface-Trapped Mode. *Journal of Physical Oceanography*, **39**, 2857–2874.
- LE TRAON, P.-Y., 1993: Comments on "Mesoscale Variability in the Atlantic Ocean from Geosat Altimetry and WOCE High-Resolution Numerical Modeling". *Journal of Physical Oceanography*, **23**, 2729–2732.

- LE TRAON, P.-Y. and G. DIBARBOURE, 1999: Mesoscale Mapping Capabilities of Multiple-Satellite Altimeter Missions. *Journal of Atmospheric and Oceanic Technology*, **16**, 1208–1223.
- LE TRAON, P. Y., P. KLEIN and B. L. HUA, 2008: Do Altimeter Wavenumber Spectra Agree with the Interior or Surface Quasigeostrophic Theory? *Journal of Physical Oceanography*, **38**, 1137–1142.
- LE TRAON, P.-Y. and J.-F. MINSTER, 1993: Sea Level Variability and Semiannual Rossby Waves in the South Atlantic Subtropical Gyre. *Journal of Geophysical Research*, **98** (C7), 12,315–12,326.
- LE TRAON, P.-Y. and M. C. ROUQUET, 1990: Spatial Scales of Mesoscale Variability in the North Atlantic as Deduced From Geosat Data. *Journal of Geophysical Research*, **1995** (C11), 20,267–20,285.
- LE TRAON, P.-Y., J. STUM, J. DORANDEU, P. GASPARD and P. VINCENT, 1994: Global statistical analysis of TOPEX and POSEIDON data. *Journal of Geophysical Research*, **99** (C12), 24,619–24,31.
- LEBEN, R. R. and B. S. POWELL, 2003: Accuracy Assessment of Jason-1 and TOPEX/POSEIDON Along-Track Sea Surface Slope. *Marine Geodesy*, **26**, 355–366.
- LEEUWENBURGH, O. and D. STAMMER, 2002: Uncertainties in altimetry-based velocity estimates. *Journal of Geophysical Research*, **107** (C10), 3175.
- LEMOINE, F. G., D. E. SMITH, L. KUNZ, R. SMITH, E. C. PAVLIS, N. K. PAVLIS, S. M. KLOSKO, D. S. CHINN, M. H. TORRENCE, R. G. WILLIAMSON, C. M. C. K. E. RACHLIN, Y. M. WANG, S. C. KENYON, R. SALMAN, R. TRIMMER, R. H. RAPP and R. S. NEREM, 1998: The Development of the joint NASA GSFC and National Imagery and Mapping Agency (NIMA) Geopotential Model EGM96l. Technical Report, NASA/TP-1998-206861, NASA Goddard Space Flight Center, Greenbelt, Md.
- LEULIETTE, E. W., R. S. NEREM and G. T. MITCHUM, 2004: Calibration of TOPEX/Poseidon and Jason Altimeter Data to Construct a Continuous Record of Mean Sea Level Change. *Marine Geodesy*, **27**, 79–94.
- LEWELLYN SMITH, S. G. and S. T. GILLE, 1998: Probability Density Functions of Large-Scale Turbulence in the Ocean. *Physical Review Letters*, **81** (23), 5249–5252.
- LOMB, N. R., 1976: Least-Squares Frequency Analysis of Unequally Spaced Data. *ASS*, **39** (2), 447–462.
- LYARD, F., F. LEFEVRE, T. LETELLIER and O. FRANCIS, 2006: Modelling the global ocean tides: modern insights from FES2004. *Ocean Dynamics*, **56**, 394–415.
- MALTRUD, M. E. and J. L. MCCLEAN, 2005: An eddy resolving global 1/10 ocean simulation. *Ocean Modelling*, **8**, 31–54.
- MALTRUD, M. E., A. J. SEMTNER and R. C. MALONE, 1998: Global eddy-resolving ocean simulation driven by 1985-1995 atmospheric winds. *Journal of Geophysical Research*, **103** (C13), 30,825–30,853.
- MAXIMENKO, N. A., B. BANG and H. SASAKI, 2005: Observational evidence of alternating zonal jets in the world ocean. *Geophysical Research Letters*, **32**,1-4, L12607.

- MAXIMENKO, N. A., O. V. MELNICHENKO, P. P. NILER and H. SASAKI, 2008: Stationary mesoscale jet-like features in the ocean. *Geophysical Research Letters*, **35**, L08603.
- MENARD, Y., L.-L. FU, P. ESCUDIER, F. PARISOT, J. PERBOS, P. VINCENT, S. DESAI, B. HAINES and G. KUNSTMANN, 2003: The Jason-1 Mission. *Marine Geodesy*, **26**, 131–146.
- MENEMENLIS, D., J.-M. CAMPIN, P. HEIMBACH, C. HILL, T. LEE, A. NGUYEN, M. SCHODLOK and H. ZHANG, 2008: ECCO2: High Resolution Global Ocean and Sea Ice Data Synthesis. *Mercator Ocean Quarterly Newsletter*, **31**, 13–21.
- MESTAS-NUÑEZ, A., D. B. CHELTON and R. A. DESZOEKE, 1991: Evidence of Time-dependent Sverdrup Circulation in the South Pacific from the Seasat Scatterometer and Altimeter. *Journal of Physical Oceanography*, **22**, 934–943.
- MORROW, R., R. COLEMAN, J. CHURCH and D. CHELTON, 1994: Surface Eddy Momentum Flux and Velocity Variances in the Southern Ocean from Geosat Altimetry. *Journal of Physical Oceanography*, **24**, 2050–2071.
- MÜLLER, T. J. and G. SIEDLER, 1992: Multi-year current time series in the eastern North Atlantic Ocean. *Journal of Marine Research*, **50** (1), 63–98.
- NADIGA, B. T., 2006: On zonal jets in oceans. *Geophysical Research Letters*, **33**, L10601.
- NAKANO, H. and H. HASUMI, 2005: A Series of Zonal Jets Embedded in the Broad Zonal Flows in the Pacific Obtained in Eddy-Permitting Ocean General Circulation Models. *Journal of Physical Oceanography*, **35**, 474–488.
- OLLITRAULT, M., M. LANKHORST, D. FRATANTONI, P. RICHARDSON and W. ZENK, 2006: Zonal intermediate currents in the equatorial Atlantic Ocean. *Geophysical Research Letters*, **33**, L05605.
- PALACIOS, D. M. and S. J. BOGRAD, 2005: A census of Tehuantepec and Papagayo eddies in the northeastern tropical Pacific. *Geophysical Research Letters*, **32**, L23606.
- PALASTANGA, V., P. J. VAN LEEUWEN, M. W. SCHOUTEN and W. P. M. DE RUIJTER, 2007: Flow structure and variability in the subtropical Indian Ocean: Instability of the South Indian Ocean Countercurrent. *Journal of Geophysical Research*, **112**, C01001.
- PARK, Y.-H. and L. GAMBÉRONI, 1995: Large-scale circulation and its variability in the south Indian Ocean from TOPEX/POSEIDON altimetry. *Journal of Geophysical Research*, **100** (C12), 24,911–24,929.
- PEDLOSKY, J., 1987: *Geophysical Fluid Dynamics*. Springer, second edition Vol.
- PRESS, W. H., S. A. TEUKOLSKI, W. T. VETTERLING and B. P. FLANNERY, 2001: *Numerical Recipes in Fortran 77: The Art of Scientific Computing (Vol. 1 of Fortran Numerical Recipes)*, Cambridge University Press, Cambridge, UK, 1–933.
- PROVOST, C. and P.-Y. LE TRAON, 1993: Spatial and Temporal Scales in Altimetric Variability in the Brazil-Malvinas Current Confluence Region: Dominance of the Semiannual Period and Large Spatial Scales. *Journal of Geophysical Research*, **98** (C10), 18,037–18,051.
- QIU, B., 1992: Recirculation and Seasonal Change of the Kuroshio from Altimetry Observations. *Journal of Geophysical Research*, **97** (C11), 17,801–17,811.

- QIU, B., 1999: Seasonal Eddy Field Modulation of the North Pacific Subtropical Counter-current: TOPEX/Poseidon Observations and Theory. *Journal of Physical Oceanography*, **29**, 2471–2486.
- QIU, B. and S. CHEN, 2004: Seasonal Modulations in the Eddy Field of the South Pacific Ocean. *Journal of Physical Oceanography*, **34**, 1515–1527.
- QIU, B., K. A. KELLY and T. M. JOYCE, 1991: Mean Flow and Variability in the Kuroshio Extension From Geosat Altimetry Data. *Journal of Geophysical Research*, **96** (C10), 18,491–18,507.
- RAY, R. D., 1998: Spectral analysis of highly aliased sea-level signals. *Journal of Geophysical Research*, **113** (C11), 24,991–25,000.
- REIGBER, C., P. SCHWINTZER, K.-H. NEUMAYER, F. BARTHELMES, R. KÖÖNIG, C. FÖRSTE, G. BALMINO, R. BIANCALE, J.-M. LEMOINE, S. LOYER, S. BRUINSMA, F. PEROSANZ and T. FAYARD, 2003: The CHAMP-only Earth Gravity Field Model EIGEN-2. *Advances in Space Research*, **31** (8), 1883–1888.
- REVERDIN, G., C. FRANKIGNOUL, E. KESTENARE and M. J. MCPHADEN, 1994: Seasonal variability in the surface currents of the equatorial Pacific. *Journal of Geophysical Research*, **99** (C10), 20,323–20,344.
- RHINES, P. B., 1975: Waves and turbulence on a beta-plane. *Journal of Fluid Mechanics*, **69** (3), 417–443.
- RHINES, P. B., 1979: Geostrophic Turbulence. *Annual Reviews of Fluid Mechanics*, **11**, 401–441.
- RHINES, P. B., 1994: Jets. *Chaos*, **4** (2), 313–339.
- RIDDERINKHOF, H. and W. DE RUIJTER, 2003: Moored current observations in the Mozambique Channel. *Deep-Sea Research II*, **50**, 1933–1955.
- RIDGWAY, K. R. and J. S. GODFREY, 1997: Seasonal cycle of the East Australian Current. *Journal of Geophysical Research*, **102** (C10), 22,921–22936.
- RIO, M.-H. and F. HERNANDEZ, 2004: A mean dynamic topography computed over the world ocean from altimetry, in situ measurements, and a geoid model. *Journal of Geophysical Research*, **109**, C12032.
- ROMERO-CENTENO, R., J. ZAVALA-HIDALGO, A. GALLEGOS and J. J. O'BRIEN, 2003: NOTES AND CORRESPONDENCE Isthmus of Tehuantepec Wind Climatology and ENSO Signal. *Journal of Climate*, **16**, 2628–2639.
- ROSSBY, T. and E. GOTTLIEB, 1998: The Oleander Project: Monitoring the Variability of the Gulf Stream and Adjacent Waters between New Jersey and Bermuda. *Bulletin of the American Meteorological Society*, **79** (1), 5–18.
- ROSSBY, T. and H.-M. ZHANG, 2001: The near-surface velocity and potential vorticity structure of the Gulf Stream. *Journal of Marine Research*, **59** (6), 949–975.
- SCARGLE, J. D., 1982: Studies in Astronomical Time Series Analysis. II. Statistical Aspects of Spectral Analysis of Unevenly Spaced Data. *The Astrophysical Journal*, **263**, 835–853.

- SCHARFFENBERG, M. G. and D. STAMMER, 2010: Seasonal variations of the large-scale geostrophic flow-field and of eddy kinetic energy inferred from the TOPEX/Poseidon and Jason-1 Tandem Mission Data. *Journal of Geophysical Research*, **115**, C02008.
- SCHLAX, M. G. and D. B. CHELTON, 1992: Frequency Domain Diagnostics for Linear Smoothers. *Journal of the American Statistical Association*, **87** (420), 1070–1081.
- SCHLAX, M. G. and D. B. CHELTON, 1994: Aliased tidal errors in TOPEX/POSEIDON sea surface height data. *Journal of Geophysical Research*, **99** (C12), 24,761–24,775.
- SCHLAX, M. G. and D. B. CHELTON, 2003: The Accuracies of Crossover and Parallel-Track Estimates of Geostrophic Velocity from TOPEX/Poseidon and Jason Altimeter Data. *Journal of Atmospheric and Oceanic Technology*, **20**, 1196–1211.
- SCHLAX, M. G. and D. B. CHELTON, 2008: The influence of mesoscale eddies on the detection of quasi-zonal jets in the ocean. *Geophysical Research Letters*, **35**, L24602.
- SCHORGHOFER, N. and S. T. GILLE, 2002: Statistics of velocity gradients in two-dimensional Navier-Stokes and ocean turbulence. *Physical Review E*, **65**, 026307.
- SCHOTT, F. A. and J. P. MCCREARY JR., 2001: The monsoon circulation of the Indian Ocean. *Progress in Oceanography*, **51**, 1–123.
- SCHOUTEN, M. W., W. P. M. DE RUIJTER, P. J. VAN LEEUWEN and H. RIDDERINKHOF, 2003: Eddies and variability in the Mozambique Channel. *Deep-Sea Research II*, **50**, 1987–2003.
- SCOTT, R. B., B. K. ARBIC, C. L. HOLLAND, A. SEN and B. QIU, 2008: Zonal versus meridional velocity variance in satellite observations and realistic and idealized ocean circulation models. *Ocean Modelling*, **23**, 102–112.
- SEMTNER JR., A. J. and R. M. CHERVIN, 1992: Ocean General Circulation From a Global Eddy-Resolving Model. *Journal of Geophysical Research*, **97** (C4), 5493–5550.
- SIEDLER, G., M. ROUAULT and J. R. E. LUTJEHARMS, 2006: Structure and origin of the subtropical South Indian Ocean Countercurrent. *Geophysical Research Letters*, **33**, L24609.
- SMITH, R. D., M. E. MALTRUD, F. O. BRYAN and M. W. HECHT, 2000: Numerical Simulation of the North Atlantic Ocean at 1/10. *Journal of Physical Oceanography*, **30**, 1532–1561.
- SMITH, R. L., A. HUYER, J. S. GODFREY and J. A. CHURCH, 1991: The Leeuwin Current off Western Australia, 1986–1987. *Journal of Physical Oceanography*, **21**, 323–345.
- STAMMER, D., 1997a: Global Characteristics of Ocean Variability Estimated from Regional TOPEX/POSEIDON Altimeter Measurements. *Journal of Physical Oceanography*, **27**, 1743–1769.
- STAMMER, D., 1997b: Steric and wind-induced changes in TOPEX/POSEIDON large-scale sea surface topography observations. *Journal of Geophysical Research*, **102** (C9), 20,987–21,009.
- STAMMER, D., C. BÖNING and C. DIETERICH, 2001: The role of variable wind forcing in generating eddy energy in the North Atlantic. *Progress in Oceanography*, **48**, 289–311.

- STAMMER, D. and C. W. BÖNING, 1992: Mesoscale Variability in the Atlantic Ocean from Geosat Altimetry and WOCE High-Resolution Numerical Modeling. *Journal of Physical Oceanography*, **22**, 732–752.
- STAMMER, D. and C. W. BÖNING, 1993: Reply. *Journal of Physical Oceanography*, **23**, 2733–2735.
- STAMMER, D. and C. DIETERICH, 1999: Space-Borne Measurements of the Time-Dependent Geostrophic Ocean Flow Field. *Journal of Atmospheric and Oceanic Technology*, **16**, 1198–1207.
- STAMMER, D. and J. THEISS, 2004: Velocity Statistics Inferred from the TOPEX/Poseidon-Jason-1 Tandem Mission Data. *Marine Geodesy*, **27**, 551–575.
- STAMMER, D. and C. WUNSCH, 1994: Preliminary assessment of the accuracy and precision of TOPEX/POSEIDON altimeter data with respect to the large-scale ocean circulation. *Journal of Geophysical Research*, **99** (C12), 24,584–24,604.
- STAMMER, D. and C. WUNSCH, 1999: Temporal changes in eddy energy of the oceans. *Deep-Sea Research II*, **46**, 77–108.
- STAMMER, D., C. WUNSCH and R. M. PONTE, 2000: De-Aliasing of Global High Frequency Barotropic Motions in Altimeter Observations. *Geophysical Research Letters*, **27** (8), 1175–1178.
- STAMMER, D., C. WUNSCH and K. UEYOSHI, 2006: NOTES AND CORRESPONDENCE Temporal Changes in Ocean Eddy Transports. *Journal of Physical Oceanography*, **36**, 543–550.
- STEWART, R. H., T. J. JOHNSON, L. JI, C. SHUM and B. D. TAPLEY, 1993: Structure of space-time variability of Geostrophic Currents in the Southern Ocean. *Recent advances in Marine Science and Technology*, **92**, 127–138.
- SWALLOW, J., M. FIEUX and F. SCHOTT, 1988: The Boundary Currents East and North of Madagascar 1. Geostrophic Currents and Transports. *Journal of Geophysical Research*, **93** (C5), 4951–4962.
- TAGUCHI, E. and D. STAMMER, 2010: HAMTIDE: High-resolution global and regional data assimilation for ocean tides. To be submitted.
- TULLOCH, R. and K. S. SMITH, 2009: A Note on the Numerical Representation of Surface Dynamics in Quasigeostrophic Turbulence: Application to the Nonlinear Eady Model. *Journal of the Atmospheric Sciences*, **66**, 1063–1068.
- VANÍČEK, P., 1971: Further Development and Properties of the Spectral Analysis by Least-Squares. *ASS*, **12** (1), 10–33.
- VAZQUEZ, J., V. ZLOTNICKI and L.-L. FU, 1990: Sea Level Variabilities in the Gulf Stream Between Cape Hatteras and 50° W: A Geosat Study. *Journal of Geophysical Research*, **95** (C10), 17,957–17,964.
- VINAYACHANDRAN, P. N., Y. MASUMOTO, T. MIKAWA and T. YAMAGATA, 1999: Intrusion of the Southwest Monsoon Current into the Bay of Bengal. *Journal of Geophysical Research*, **104** (C5), 11,077–11,085.

- VINAYACHANDRAN, P. N. and T. YAMAGATA, 1998: Monsoon Response of the Sea around Sri Lanka: Generation of Thermal Domes and Anticyclonic Vortices. *Journal of Physical Oceanography*, **28**, 1946–1960.
- WEBB, D. J., 2000: Evidence for Shallow Zonal Jets in the South Equatorial Current Region of the Southwest Pacific. *Journal of Physical Oceanography*, **30**, 706–720.
- WHITE, M. A. and K. J. HEYWOOD, 1995: Seasonal and interannual changes in the North Atlantic subpolar gyre from Geosat and TOPEX/POSEIDON altimetry. *Journal of Geophysical Research*, **100** (C12), 24,931–24,941.
- WILLETT, C. S., R. R. LEBEN and M. F. LAVÍN, 2006: Eddies and Tropical Instability Waves in the eastern tropical Pacific: A review. *Progress in Oceanography*, **69**, 218–238.
- WUNSCH, C., 1981: *Evolution of Physical Oceanography*, The MIT Press, Chapter Low-frequency variability in the sea., 342–374. *Evolution of Physical Oceanography*.
- WUNSCH, C., 1997: The Vertical Partition of Oceanic Horizontal Kinetic Energy. *Journal of Physical Oceanography*, **27**, 1770–1794.
- WUNSCH, C. and D. STAMMER, 1995: The global frequency-wavenumber spectrum of oceanic variability estimated from TOPEX/POSEIDON altimetric measurements. *Journal of Geophysical Research*, **100**, 24,895–24,910.
- WUNSCH, C. and D. STAMMER, 1998: Satellite Altimetry, the Marine Geoid, and the Oceanic General Circulation. *Annual Review Earth Planet Sciences*, **26**, 219–253.
- WYRTKI, K., L. MAGAARD and J. HAGER, 1976: Eddy Energy in the Oceans. *Journal of Geophysical Research*, **81** (15), 2641–2646.
- YU, X. and M. J. MCPHADEN, 1999: Seasonal Variability in the Equatorial Pacific. *Journal of Physical Oceanography*, **29**, 925–947.
- ZANG, X. and C. WUNSCH, 2001: Spectral Description of Low-Frequency Oceanic Variability. *Journal of Physical Oceanography*, **31**, 3073–3095.
- ZLOTNICKI, V., 1991: Sea Level Differences across the Gulf Stream and Kuroshio Extension. *Journal of Physical Oceanography*, **21**, 599–609.
- ZLOTNICKI, V., L.-L. FU and W. PATZERT, 1989: Seasonal Variability in Global Sea Level Observed With Geosat Altimetry. *Journal of Geophysical Research*, **94** (C12), 17,959–17,969.

A. Main Equations

Within this chapter the basic equations are described that are used for the computations in this study. Section A.1 comments on the geostrophic balance that forms the basis of the calculation of geostrophic velocities (Section 2.2.1) based on the equations of motion. An important part of this study is the description of seasonal variations within the JTP tandem data set for geostrophic velocities and for EKE. The description of the least-squares fit used for the computation of the annual signal is hence given in Section A.2. To furthermore quantify the complete spectral range that is covered by the 3-year JTP data set, a spectral analysis using the Lomb periodogram is performed that is explained in Section A.3.

A.1. Geostrophic Velocities

The equations of motion (PEDLOSKY, 1987) can be written as:

$$\frac{d\vec{u}}{dt} + 2\vec{\Omega} \times \vec{u} = \frac{1}{\rho} \left[-\nabla p + \rho \nabla \Phi + \vec{F}r \right] \quad (\text{A.1})$$

with $\vec{u} = (u, v, w)$ being the velocity of a fluid parcel, $\vec{\Omega}_E$ Earth angular velocity, Φ the combined gravitational and zentripetal potential, ρ the water density and $\vec{F}r$ the friction and other forces. With $\frac{d}{dt} = \frac{\delta}{\delta t} + \vec{u} \cdot \nabla$ the total derivative with time t (A.1) can be written as

$$\frac{\partial \vec{u}}{\partial t} + \vec{u} \cdot \nabla \vec{u} + 2\vec{\Omega} \times \vec{u} = \frac{1}{\rho} \left[-\nabla p + \rho \nabla \Phi + \vec{F}r \right]. \quad (\text{A.2})$$

The continuity equation accounts for the conservation of mass and can be written as

$$\frac{\partial \rho}{\partial t} + \nabla \cdot (\rho \vec{u}) = \frac{\partial \rho}{\partial t} + \vec{u} \cdot \nabla \rho + \rho \nabla \cdot \vec{u} = 0. \quad (\text{A.3})$$

These equations can be simplified with a few assumptions. Not looking at sound waves, seawater can be treated as incompressible. Thus (A.3) can be written as

$$\nabla \cdot \vec{u} = 0. \quad (\text{A.4})$$

Now typical length scales can be taken into account. Geostrophy can be assumed if the Rossby number $Ro \ll 1$, which is the ratio of inertial to Coriolis force:

$$\frac{\vec{u} \cdot \nabla \vec{u}}{2\vec{\Omega} \times \vec{u}} \sim \frac{\frac{\partial \vec{u}}{\partial t}}{2\vec{\Omega} \times \vec{u}} \sim \frac{U U}{2\Omega U}, \quad \frac{U}{fL} = Ro \ll 1. \quad (\text{A.5})$$

The typical length scales L were taken from STAMMER (1997a). Their **Fig. 22** shows the eddy scales estimated from the zonally averaged TOPEX SSH autocorrelations, see open circles in **Fig. A.1**. The eddy scales range from 50 (60) km at 55° N (S) up to 110 km at the equator

and typical velocity scales U were taken from the standard deviations of the geostrophic velocity estimates in **Fig. 3.2**. In **Fig. A.1**, the Rossby number is shown exemplarily for the northern hemisphere. It can clearly be seen that the geostrophic approximation breaks at the equator where $Ro \gg 1$. Up to a latitude of 5° , the geostrophic approximation is valid for the complete range of velocities and up to a latitude of 2° it is valid for velocities in the order of 20 cm/s. The order W of the vertical velocity component w is much smaller than the order U of the horizontal velocity components u and v so that

$$\frac{W}{U} \ll 1 \quad (\text{A.6})$$

is true over the whole ocean. The same holds for the Ekman number Ek which gives the ratio of viscous forces to the Coriolis force:

$$Ek = \sqrt{\frac{Ro}{Re}} \quad (\text{A.7})$$

$$\text{with (A.5) and } Re = \frac{UL}{\nu_{EK}}, \quad (\text{A.8})$$

where Re is the Reynolds number, which is the ratio of inertial forces to viscous forces.

Ek can be written as

$$Ek = \frac{\nu_{EK}}{\tilde{f}L^2}. \quad (\text{A.9})$$

Here ν_{EK} denotes the kinematic viscosity of the order of $10^{-3} \text{ m}^2/\text{s}$ which is defined as $\nu_{EK} = \eta_{EK}/\rho$. With the dynamic viscosity η_{EK} in the order of 1 kg/m/s and ρ in the order of 10^3 kg/m^3 , Ek is in the order of 10^{-7} to 10^{-9} at the equator and at high latitudes, respectively. Using a local cartesian coordinate system in the way that $\vec{\Omega}$ has only a z -component $2\vec{\Omega} = (0, 0, f)$ the equations of motion can be written as

$$\tilde{f}u = -\frac{1}{\rho} \frac{\delta p}{\delta y}, \quad (\text{A.10})$$

$$\tilde{f}v = \frac{1}{\rho} \frac{\delta p}{\delta x}, \quad (\text{A.11})$$

$$pg = -\frac{\delta p}{\delta z}, \quad (\text{A.12})$$

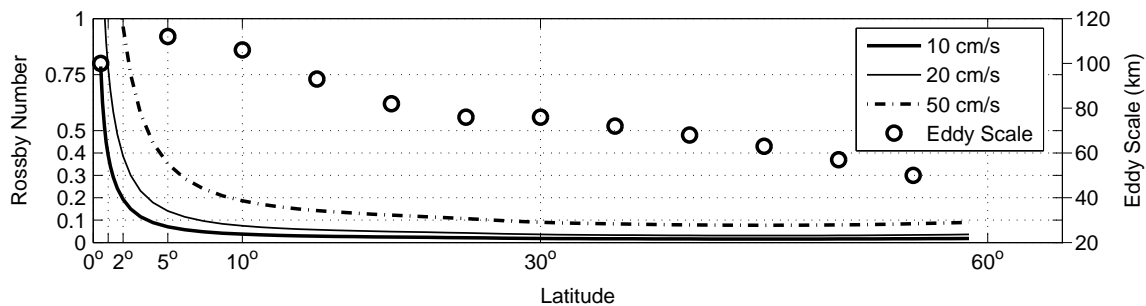


Figure A.1.: Eddy scale [km] from STAMMER (1997a, **Fig. 22**) (right axis) and Rossby Number (A.5) calculated for geostrophic velocities of 10 cm/s, 20 cm/s and 50 cm/s (compare also **Fig. 3.2**) from the equator to 55° N (left axis).

with u and v the zonal and meridional velocity components, z the depth, ρ the density of seawater, $g = \frac{\delta\Phi}{\delta z}$ the gravitational acceleration, $f = 2|\vec{\Omega}_E| \sin \phi$ the Coriolis parameter, $\vec{\Omega}_E$ the Earth angular velocity, ϕ the latitude and p the pressure. This approximation is called the geostrophic approximation. The pressure is given as $p = \rho g \eta$, with η SSH. Thus with the deviation of the sea surface at two positions the geostrophic velocity normal to their connecting line can be estimated. For u and v follows

$$u = -\frac{g}{\tilde{f}} \frac{\delta\eta}{\delta y}, \quad (\text{A.13})$$

$$v = \frac{g}{\tilde{f}} \frac{\delta\eta}{\delta x}, \quad (\text{A.14})$$

The balance of terms in (A.10, A.11) and (A.13, A.14) is the geostrophic approximation and the hydrostatic approximation is given in (A.12). As demonstrated in **Fig. A.1**, the geostrophic approximation breaks down at the equator due to the vanishing coriolis parameter. Even though the geostrophic balance holds only for velocities smaller than 10 cm/s for as close as 1° latitude around the equator and in general as close as 5° N and S, all calculations within this work are performed down to $\pm 1^\circ$ around the equator. So as can be seen from **Fig. 2.6**, the errors of the geostrophic velocity estimates are largest at the equator. Nevertheless, the results close to the equator seem to be acceptable.

A.2. Seasonal Harmonic Analysis

To investigate the annual cycle in the JTP flow-field and EKE field of Chapter 4, the along-track velocity components u and v were first averaged in $2^\circ \times 1^\circ$ geographic boxes to reduce noise effects and to avoid phase aberrations due to the averaging. Subsequently, a least-squares fit was applied to the data and an annual harmonic was fitted independently to each velocity component. The resulting annual harmonic amplitudes X_{ann} of the time series in x , at time steps t with a period of $T = 365, 25$ days can be written as

$$X_{ann} = \frac{\sum cx}{\sum c^2} + \frac{\sqrt{-1} \sum sx}{\sum s^2} \quad (\text{A.15})$$

$$\text{with } c = \cos\left(\frac{2\pi(t - t_0)}{T}\right)$$

$$\text{and } s = \sin\left(\frac{2\pi(t - t_0)}{T}\right)$$

c and s being the cosine and sine fit for the real and imaginary part of (A.15). The phase of the annual signal Φ_{ann} can then be calculated as

$$\Phi_{ann} = \arctan(X_{ann}) \frac{T}{2\pi}. \quad (\text{A.16})$$

A phase of zero would denote that the maximum positiv amplitude is at January 1st, whereas a phase of 182.5 would denote July 1st. A minimum number of 10 data points in time was set as threshold to be necessary for the computation of an annual harmonic of a time series. With both values X_{ann} and Φ_{ann} the time series of the annual harmonic signal can be recomputed as

$$x_{ann} = |X_{ann}| \cos\left(\frac{2\pi(t - \Phi_{ann} - t_0)}{T}\right), \quad (\text{A.17})$$

where x_{ann} are the recomputed amplitudes of the annual harmonic signal from time series x . With the extracted annual part of the time series the evolution of seasonal phenomena can be displayed.

A.3. Lomb Periodogram

The Lomb periodogram (LOMB, 1976; SCARGLE, 1982; VANÍČEK, 1971) was used for a complete spectral analysis of the JTP data in time and space. The following computations are based on the code described in PRESS ET AL. (2001) with minor modifications.

The advantage of the Lomb periodogram is its capability to analyze unevenly sampled data. Thus no interpolation prior to the spectral analysis was necessary, as it would have been required for an Fast Fourier Transformation (FFT) analysis. To test the Lomb periodogram, data with different amounts of missing values ranging from 5% up to 60% were analyzed. With an increasing number of missing values the Lomb periodogram loses energy at the low frequencies whereas it gains energy at higher frequencies. To overcome the problem of too scarce data, an interpolation of the data was applied. As was previously estimated by STAMMER (1997a) for an FFT analysis, a linear interpolation was applied but no extrapolation. Instead, missing values at the beginning and end of the data were treated as zero. STAMMER (1997a) filled only gaps smaller than 20 days in time and 30 km in space by linear interpolation, and data with larger gaps were rejected. A test showed that even interpolation over much larger gaps in space and time produced no major divergencies between the spectra calculated from data with and without interpolated gaps. Therefore all existing time series could be taken into account and all gaps in space and in time were interpolated. A comparison of the spectra calculated with the Lomb periodogram and with an FFT analysis both calculated from the interpolated data showed an overall good agreement. From these simple tests it is thus recommended to use the Lomb periodogram for evenly sampled data with a percentage of data gaps below 10%. Otherwise an interpolation of the data gaps is recommended. When interpolating the gaps the faster FFT analysis could be used for the calculation instead. However, as the Lomb periodogram is able to calculate significance levels for each frequency and to fit frequencies up to 1/4 of a wavelength into the data compared to 1/2 of a wavelength for an FFT, the Lomb periodogram was used in this study instead of an FFT analysis, knowing that the capabilities of the Lomb periodogram are disregarded due to the previous interpolation of the data.

Instead of a Fourier analysis the Lomb algorithm uses the least squares method. The Lomb periodogram $P(\tilde{\omega})$ as a function of angular velocity $\tilde{\omega} = 2\pi f$ is then given as

$$P(\tilde{\omega}) = \left\{ \frac{\left[\sum_{j=1}^N (x_j - \bar{x}) \cos \tilde{\omega}(t_j - \tau) \right]^2}{\sum_{j=1}^N \cos^2 \tilde{\omega}(t_j - \tau)} + \frac{\left[\sum_{j=1}^N (x_j - \bar{x}) \sin \tilde{\omega}(t_j - \tau) \right]^2}{\sum_{j=1}^N \sin^2 \tilde{\omega}(t_j - \tau)} \right\} \quad (\text{A.18})$$

after PRESS ET AL. (2001, Chapter 13.8). Here \bar{x} represents the mean of values x_j of time series x , N the number of samples, t time and τ the time shift

$$2\omega\tau = \arctan \left(\frac{\sum_{j=1}^N \sin(\tilde{\omega}t_j)}{\sum_{j=1}^N \cos(\tilde{\omega}t_j)} \right). \quad (\text{A.19})$$

An oversampling (OS) of 4 was applied to the Lomb algorithm which results in

$$F = \frac{N}{2} OS \quad (\text{A.20})$$

frequencies with F_{max} being the maximum number of frequencies.

The amplitude spectrum is calculated from the Lomb periodogram that is in the form (A.18) a one sided spectrum. Therefore the factor $\frac{1}{2}$ accounts for the correct amplitudes as they would be seen from a two sided spectrum. Thus the amplitude spectrum $A(\tilde{\omega})$ is calculated as

$$A(\tilde{\omega}) = \frac{1}{2} \sqrt{P(\tilde{\omega})}, \quad (\text{A.21})$$

whereas the energy conserving Power Spectral Density $PSD(\tilde{\omega})$ spectrum for the Lomb periodogram is given as

$$PSD(\tilde{\omega}) = \Delta t P(\tilde{\omega}), \quad (\text{A.22})$$

with $\Delta t = 1/f_s$ and f_s being the sampling frequency. The units for the PSD are in [1/cpd] (cycle per day) for the frequency spectra and in [1/cpkm] (cycle per kilometer) for the wavenumber spectra. The appropriate significance level can be calculated using the variance (σ^2) normalized spectrum

$$P_{normalized}(\tilde{\omega}) = \frac{1}{\sigma^2} P(\tilde{\omega}) \quad (\text{A.23})$$

$P_{normalized}(\tilde{\omega})$ is an exponential probability distribution with mean 1. Therefore the significance α_{sig} is given as

$$\alpha_{sig} = 1 - (1 - e^{-P_{normalized}(\tilde{\omega})})^{F_i}, \quad (\text{A.24})$$

with F_i the number of independent frequencies which is approximately the number of sampled frequencies ν . In Chapter 5 the significance for each spectrum is plotted only for regions up to a $2^\circ \times 1^\circ$ grid. Due to averaging it is not useful to display the significance for larger areas.

For the calculation of the Power Spectral Density (PSD) it is necessary to satisfy Parseval's theorem. For a Fourier Transform of discretely sampled data, the discrete form of Parseval's theorem (PRESS ET AL., 2001, Chapter 12.1) can be written as

$$\Delta t \sum_{t=0}^{N-1} |x_t|^2 = \frac{1}{N \Delta t} \sum_{j=0}^{N-1} |X_j|^2. \quad (\text{A.25})$$

Where X_j is the Discrete Fourier Transform (DFT) of the time series x_t . Looking at a normalized Power Spectrum estimation the total power under the PSD spectrum has to be equal to the corresponding mean squared amplitude of the function x_t (PRESS ET AL., 2001, Chapter 13.4):

$$\frac{1}{N} \sum_{t=1}^N |x_t|^2 = \Delta f \sum_{j=1}^F PSD. \quad (\text{A.26})$$

Here Δf is the frequency interval of the PSD spectrum. Due to the applied oversampling, the number of data points N is not equal to the number of sampled frequencies F .

The the PSD periodograms calculated with the Lomb algorithm were tested against spectra calculated with the Welch method, i. e. using an FFT. Both methods showed similar results with slightly enhanced amplitudes within the Lomb PSD-spectrum.

The alongtrack frequency and wavenumber spectra were then averaged over $2^\circ \times 1^\circ$ and $10^\circ \times 10^\circ$ boxes, respectively.

B. Glossary

Acronym	Meaning
ACC	Antarctic Circumpolar Current
ADCP	Acoustic Doppler Current Profiler
AVHRR	Advanced Very High Resolution Radiometer
COAPS	Center for Ocean-Atmospheric Prediction Studies
CRD	Costa Rica Dome
DFT	Discrete Fourier Transform
EAC	East Australian Current
EKE	Eddy Kinetic Energy
ENSO	El Niño Southern Oscillation
EQ	Equatorial Region
ERS1/2	European Remote Sensing Satellites
ESA	European Space Agency
EUC	Equatorial Undercurrent
FES2004	Finite Element Solutions FES2004 Tidal Model
FFT	Fast Fourier Transformation
Geosat	Geodetic Satellite
GOCE	Gravity-field and steady-state Ocean Circulation Explorer
GS	Gulf Stream
GW	Great Whirl
HAMTIDE	Hamburg direct data Assimilation Methods for TIDEs tidal model
IFREMER	Institut Français de Recherche pour l'Exploration de la MER
ITCZ	Intertropical Convergence Zone
JTP	Jason-1 - TOPEX/Poseidon tandem mission (altimeter satellites)
MDTP	Mean Dynamic Topography
MKE	Mean Kinetic Energy
NEC	North Equatorial Current
NECC	North Equatorial Counter Current
NEMC	North East Madagascar Current
NEUC	North Equatorial Undercurrent
nSEC	Northern branch of the South Equatorial Current
OS	Oversampling
OSCAR	Ocean Surface Current Analyses - Real time velocity estimates
PDF	Probability Density Function
POP	Los Alamos National Lab distribution of Parallel Ocean Program model
PSD	Power Spectral Densities
QG	Quasi Geostrophic
RCM	Recording Current Meter
RMS	Root mean square
SEC	South Equatorial Current
SECC	South Equatorial Counter Current
SEMC	Southeast Madagascar Current

Acronym	Meaning
SICC	South Indian Ocean Countercurrent
SISMER	Système d'Informations Scientifiques pour la Mer
SLD	Sri Lanka Dome
SP	Subpolar region
SQG	Surface Quasi Geostrophic theory
SSH	Sea Surface Height
SSM/I	Special Sensor Microwave Imager
ST	Subtropical region
STCC	South Tropical Countercurrent
STD	Standard deviation
SVP	Surface Velocity Program
SWOT	Surface Water Ocean Topography (altimeter satellite)
TAO	Tropical Atmosphere Ocean array
TB	Tehuantepec Bowl
TOGA	Tropical Ocean and Global Atmosphere
T/P	TOPEX/Poseidon (altimeter satellite)
XBT	Expendable Bathythermograph
WGC	West Greenland Current
WOCE	World Ocean Circulation Experiment

C. Constants and Variables

Constants

Symbol		Meaning	Page
g	$= 9.81 \text{ ms}^{-2}$	Gravitational Constant	113
$\vec{\Omega}_E$	$= 7.29 \times 10^{-5} \text{ s}^{-1}$	Earth Angular Velocity of planetary rotation	113
π	$= 3.14159$	Pi	113

Variables

Symbol	Unit	Meaning	Page
α	-	Significance	114
$A(\tilde{\omega})$	misc.	Amplitude spectrum	115
β	s^{-1}	Meridional gradient of the Coriolis parameter f	85
c	misc.	Cosine fit for real and imaginary part of X_{ann}	113
Ek	-	Ratio of viscous forces to the Coriolis force	112
EKE	$cm^2 s^{-2}$	Eddy Kinetic Energy	30
η	m	Sea Surface Height (SSH)	112
η_{Ek}	$kg m^{-1} s^{-1}$	Dynamic viscosity of a fluid	112
\tilde{f}	s^{-1}	Coriolisparameter, $f' = 2\Omega_E \sin\varphi$	113
f	s^{-1}	Frequency	65
f_s	s^{-1}	Sampling Frequency	115
F	-	Number of Frequencies	115
F_i	-	Number of independent Frequencies	115
Fr	$kg s^{-2} m^{-2}$	Friction	111
k	$rad m^{-1}$	Angular wavenumber	76
λ	km	Wavelength	76
L	km	A typical length scale	111
L_{Rh}	km	Rhines scale	85
MKE	$cm^2 s^{-2}$	Mean Kinetic Energy	33
N	-	Number of samples	114
$\tilde{\nu}$	m^{-1}	Wavenumber	76
ν_{Ek}	$m^2 s^{-1}$	Kinematic viscosity of a fluid, $\nu_{Ek} = \frac{\eta_{Ek}}{\rho}$	76
$\tilde{\omega}$	s^{-1}	Angular frequency	114
ϕ	$^\circ$	Geographical Latitude	113
Φ	$kg s^{-2} m^{-2}$	Combined gravitational and zentripetal potential	111
Φ_{ann}	$^\circ$	Phase of annual signal	113
p	$kg s^{-2} m^{-2}$	Pressure gradient	111
$P(\tilde{\omega})$	misc.	Lomb Periodogram	114

Symbol	Unit	Meaning	Page
$PSD(\tilde{\omega})$	$1/cpd, 1/cpkm$	Power Spectral Density for frequency or wavenumber	115
Re	-	Reynolds number	112
ρ	$kg\ m^{-3}$	Density	111
Ro	-	Rossby number	111
s	misc.	Sine fit for real and imaginary part of X_{ann}	113
σ	misc.	Standard deviation	12
σ^2	misc.	Variance	115
σ_{SSH}	cm	RMS SSH variability	82
t	s	Time	111
τ	s	Timeshift	114
U	$m\ s^{-1}$	Aa typical velocity scale	112
U_{RMS}	$m\ s^{-1}$	RMS velocity	85
u	$m\ s^{-1}$	Zonal velocity component in x direction	111
v	$m\ s^{-1}$	Meridional velocity component in y direction	111
W	$m\ s^{-1}$	Order of the vertical velocity component w	112
w	$m\ s^{-1}$	Velocity in z direction	111
$w - PDF$	$m\ s^{-1}$	PDF width	25
X_{ann}	misc.	Annual harmonic amplitudes	113
x_{ann}	misc.	Reconstructed annual harmonic time series	113
x	m	Horizontal coordinate W-E	113
y	m	Horizontal coordinate S-N	113
z	m	Vertical coordinate	113

Acknowledgements

Many people have helped to make this dissertation possible and supported my work during the last years. This thesis was supported by Prof. Dr. Detlef Stammer who provided the opportunity for a dedicated Ph.D research in the remote sensing group at the Center for Marine and Atmospheric Research, the Institute for Marine Research in Hamburg. I would like to thank Prof. Stammer for his continuous support and helpful scientific advice, for providing several opportunities and opening doors thanks to his far-reaching connection for the time beyond the Ph.D. phase.

I want to thank Charmaine King who helped with the processing of the T/P and Jason-1 altimeter data, F. Bonjean and G. Lagerloeff for providing the Ocean Surface Current Analyses (OSCAR) real time current fields and Tom Rossby for providing the MV OLEANDER ADCP data. Furthermore, I am thankful to Eifu Taguchi who provided data from the Hamburg direct data Assimilation Methods for TIDEs (HAMTIDE) tidal model, Dr. Frank O'Bryan who provided output of the Los Alamos National Lab distribution of POP/CCSM.3(POP) model and D. Menemeis for providing output of the Estimating the Circulation and Climate of the Ocean (ECCO2) model that I used for comparisons during my Ph.D, however, the CCSM and ECCO2 models do not appear within this thesis. Valuable comments from D. Chelton and an anonymous referee helped to improve a paper (SCHARFFENBERG AND STAMMER, 2010) which covers Chapters 2, 3 and 4 of this thesis.

Working in a remote-sensing research group at the Institute for Marine Research in Hamburg provided unique opportunities for my Ph.D. research. I have benefited from the knowledge of several colleagues. I want to express my gratitude to Rolf Käse, Manfred Brath, Steffan Kern, Ulrich Körner and Armin Köhl. Besides science, this group also provided significant moral support. Therefore I am especially thankful to my office members Anne-Kristin Anweiler and Patrick Rosendahl as well as Steffen Grünler and Malte Heinemann.

I want to express my deep gratitude to an anonymous referee who has devoted a significant portion of his time for reading and improving my thesis.

Very special thanks are to my family, in particular to my parents. They enabled my education and gave me and my family their encouragement. Most of all I gratefully thank my wife and my daughter. This thesis could not have been completed without their patience and continuous support.